ISSN 2542-1565

Vol. 17 2024 No. 01

GEOGRAPHY ENVIRONMENT SUSTAINABILITY

«The journal GEOGRAPHY, ENVIRONMENT, SUSTAINABILITY was founded in 2008 by Russian Geographical Society, the Lomonosov Moscow State University Geography Department, and the Russian Academy of Sciences Institute of Geography. Since that time the journal publishes **4 issues per year**, containing original research papers and reviews. The journal issues are open source and distributed through subscriptions, library exchanges of leading universities, and via the website through the world»

FOUNDERS OF THE JOURNAL: Russian Geographical Society, Faculty of Geography, Lomonosov Moscow State University and Institute of Geography of the Russian Academy of Sciences

The journal is published with financial support of the Russian Geographical Society.

The journal is registered in Federal service on supervision of observance of the legislation in sphere of mass communications and protection of a cultural heritage. The certificate of registration: ПИ № ФС77-67752, 2016, December 21.

PUBLISHER
Russian Geographical Society
Moscow, 109012 Russia
Novaya ploshchad, 10, korp. 2
Phone 8-800-700-18-45
E-mail: press@rgo.ru
www.rgo.ru/en

EDITORIAL OFFICE
Lomonosov Moscow State University
Moscow 119991 Russia
Leninskie Gory, 1,
Faculty of Geography, 1806a
Phone 7-495-9391552
Fax 7-495-9391552
E-mail: ges-journal@geogr.msu.ru
www.ges.rgo.ru

DESIGN
Layout designer: Tereshkin Anton
Moscow, 115088,
26 Simonovsky Val str., bldg. One
Phone: +7 (903) 108-04-44
E-mail: smile.tai@gmail.com

DOI prefix: 10.24057

Format A4 (210x297mm)

"GEOGRAPHY, ENVIRONMENT, SUSTAINABILITY" is the only original English-language journal in the field of geography and environmental sciences published in Russia. It is supposed to be an outlet from the Russian-speaking countries to Europe and an inlet from Europe to the Russian-speaking countries regarding environmental and Earth sciences, geography and sustainability. The main sections of the journal are the theory of geography and ecology, the theory of sustainable development, use of natural resources, natural resources assessment, global and regional changes of environment and climate, social-economical geography, ecological regional planning, sustainable regional development, applied aspects of geography and ecology, geoinformatics and ecological cartography, ecological problems of oil and gas sector, nature conservations, health and environment, and education for sustainable development.

Date of publication: March 31st, 2024.

CONTENTS

Disclaimer:

The information and opinions presented in the Journal reflect the views of the authors and not of the Journal or its Editorial Board or the Publisher. The GES Journal has used its best endeavors to ensure that the information is correct and current at the time of publication.

RESEARCH PAPER

SPATIO-TEMPORAL HETEROGENEITY AND POTENTIAL DRIVERS OF HUMAN TICK-BORNE ENCEPHALITIS IN THE SOUTH OF RUSSIAN FAR EAST

Natalia V. Shartova[1], Fedor I. Korennoy[2], Tamara V. Vatlina[3], Dmitry S. Orlov[4], Varvara A. Mironova[4*], Hairong Lee[5], Wang Li[5], Svetlana M. Malkhazova[4]

[1]International Laboratory of Landscape Ecology, Higher School of Economics, Moscow, Russia. Pokrovsky bvd, 11, Moscow 109028

[2]FGBI Federal Center for Animal Health (FGBI ARRIAH), Vladimir, Russia, mkr. Yurevets, Vladimir 600901

[3]Faculty of Natural Geography, Smolensk State University, Smolensk, Russia, Przhevalsky st., 4, Smolensk 214000

[4]Lomonosov Moscow State University, Russian Federation, Geography faculty, department of biogeography. Leninskie Gory 1, Moscow 119991

[5]Institute of Geographic Sciences and Natural Resources Research, Chinese Academy of Sciences, Beijing

*Corresponding author: mironova.va@gmail.com

Received: November 11th, 2023 / Accepted: December 7th, 2023 / Published: March 31st, 2024

https://DOI-10.24057/2071-9388-2023-3117

ABSTRACT. The south of the Russian Far East is distinguished by diversity of natural conditions for the presence of vectors and circulation of pathogens, primarily tick-borne infections. Despite the relatively low proportion of tick-borne encephalitis in the structure of tick-borne infections and the rather low incidence rate compared to other Russian regions, the disease here has epidemiological significance, which is associated with its severe course. Therefore, it is important to identify local areas of greatest epidemic manifestation of the disease and potential drivers influencing the spread of tick-borne encephalitis.

This study uses data on population incidence in the municipal districts of Khabarovsk Krai, Amur Oblast, Jewish Autonomous Oblast and Zabaikalsky Krai between 2000 and 2020. Based on Kulldorf spatial scanning statistics, a temporally stable cluster of virus circulation in the population in the southwest of Zabaikalsky Krai was identified, which existed during 2009-2018. Regression modeling using zero-inflated negative binomial regression based on a set of environmental and socio-economic predictors allowed to identify variables determining the probability of infection: the share of forest, the amount of precipitation in the warm period, population density, as well as variables reflecting population employment and socio-economic well-being.

Despite the fact that tick-borne encephalitis is a natural focal disease and may be characterized by natural periods of increased incidence, the influence of the social component can have a strong impact on the epidemiological manifestation. The identified spatio-temporal differences within the study region and potential drivers must be taken into account when developing a set of preventive measures.

KEYWORDS: SatScan, GeoDa, endemic areas, space-time clusters, modeling, GIS

CITATION: N. V. Shartova, F. I. Korennoy, T. V. Vatlina, D. S. Orlov, V. A. Mironova, H. Lee, W. Li, S. M. Malkhazova (2024). Spatio-temporal heterogeneity and potential drivers of human tick-borne encephalitis in the south of Russian Far East. Geography, Environment, Sustainability, 1(17), 6-15

https://DOI-10.24057/2071-9388-2023-3117

ACKNOWLEDGEMENTS: Spatio-temporal and regression analyzes were carried out with the support of a grant from the Russian Science Foundation (project No. 21–47–00016) and preliminary data analysis was carried out at the expense of the Moscow State University Development Program (P. 1220).

Conflict of interests: The authors reported no potential conflict of interest.

INTRODUCTION

Tick-borne infections are caused by pathogens that are transmitted through tick bites. These infections include a wide range of diseases, some of which can pose a serious threat to human health. Regarding the variety of environmental factors that contribute to the existence of vectors and the spread of infections, the south of the Russian Far East region is especially significant. The structure of incidence of natural focal diseases in the region is dominated by pathologies transmitted by ixodid ticks: tick-borne rickettsioses, primarily Siberian tick-borne typhus (STT), account for about 40% of all registered cases; 30% of the overall incidence structure are ixodid tick-borne borrelioses (TBB), while tick-borne encephalitis (TBE) accounts for 13%. Human granulocytic anaplasmosis (HGA) and human monocytic ehrlichiosis (HME) are less frequent (Malkhazova et al., 2023). Because a single tick can harbor more than one pathogenic agent, the population may be infected with more than one pathogen simultaneously, adding to the challenges of diagnosis and treatment. As the incidence of tick-borne diseases increases and the geographic areas in which they occur expand, healthcare providers are increasingly required to distinguish between the diverse and often overlapping clinical manifestations of these diseases.

In most regions in the southern part of the Russian Far East, the incidence of the three predominant tick-borne infections is observed annually, with the highest rates recorded in Primorsky and Khabarovsk krais. At the same time, there is a geographic heterogeneity in the spread of tick-borne infections in the region (Fig. 1). For example, in Zabaikalsky and Primorsky krais, the predominance of TBB in the morbidity structure is noticeable, while in Amur Oblast, Khabarovsk Krai, and Jewish Autonomous Oblast, STT is more frequent. Over the years, there is a discernible shift in the severity of morbidity manifestations, which is particularly noticeable in TBE.

Despite the low share of TBE in the structure of tick-borne infections and the rather low incidence rate in the south of the Far East compared to other regions of the country, the long-term average rate is 1.4 per 100 thousand population. This number approximately corresponds to the national average (1.34) and falls behind the most affected areas of the Urals and Southern Siberia (8-12 per 100 thousand population (On the state.., 2023). This indicates that the disease is of great epidemiological significance. TBE is caused by the TBE virus (TBEV) belonging to the genus *Flavivirus* of the family *Flaviviridae*, and consists of three main subtypes: European, Siberian, and Far Eastern TBEV (Ecker et al., 1999; Lindquist, Vapalahti, 2008). In the Far East, the infection is especially severe, with a large number of adverse outcomes, which is associated with the high virulence of the Far Eastern subtype virus (Andaev et al., 2021). Retrospective analysis revealed that TBE cases were recorded in the southern region of the Far East in the late 19th and early 20th centuries. Over the past 30 years, there have been significant fluctuations in the incidence rate (Leonova, 2020). The spread of the infection is confined to the south of the Far East within the range of the main vector, the tick *Ixodes persulcatus*, whose habitat belongs to taiga landscapes (Korenberg et al., 2013). In addition, *I. pavlovskyi* may play a role in the transmission of infection as well, but its significance has not been sufficiently studied (Chicherina et al., 2015). The TBE virus has also been isolated from ticks of the genus *Dermacentor, D. nuttalli*, and *D. silvarum*, which are native to open steppe and forest-steppe biotopes (Dampilova, Turanov, 2014; Shchuchinova et al., 2015; Kholodilov et al., 2019).

The aims of this study were to identify the geographical heterogeneity of TBE distribution within the endemic region and to define the main drivers that can be used in creating preventive strategies. In this study, we investigated spatio-temporal patterns as well as potential drivers of TBE using incidence data (2000–2020) from the south of Russian Far East. First, we identified areas with high and low clustering of TBE incidence within the region. Then we explored whether various environmental and social conditions, including climatic, landscape and socio-economic variables, can explain the spatial patterns of TBE.

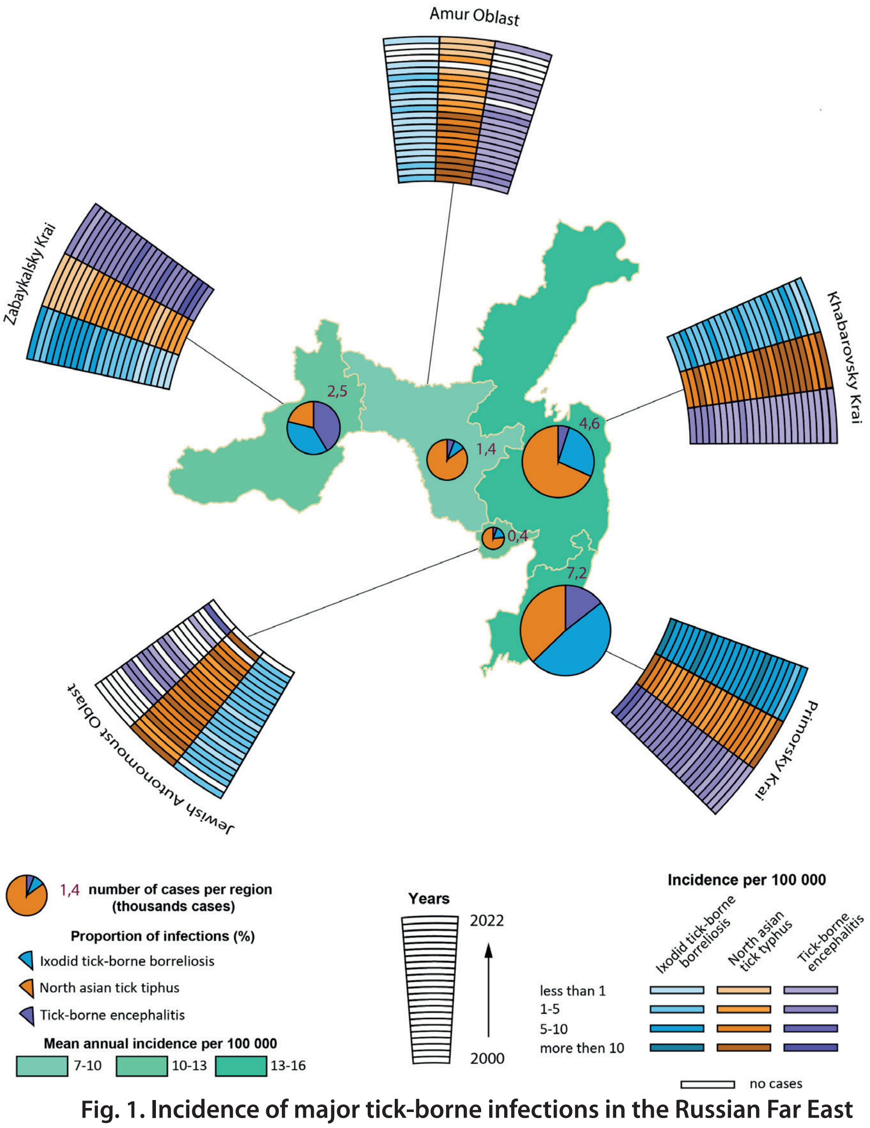

Fig. 1. Incidence of major tick-borne infections in the Russian Far East

Materials and methods

Study area

The study area includes four federal entities of the Russian Federation located in the south of the Far East: Zabaikalsky Krai, Khabarovsk Krai, Amur Oblast, and Jewish Autonomous Oblast. Three northern municipal districts of the Khabarovsk Krai (Okhotsky, Ayano-Maisky, and Tuguro-Chumikansky districts), extending beyond the ranges of ixodid ticks, were excluded from the analysis. The region under study is characterized by a variety of climatic and physical-geographical conditions. According to the Köppen-Geiger classification, most of the territory is influenced by warm humid continental climate (Dfb) and subarctic climate (Dfc), with the inclusion of a cold semi-arid climate (Bsk) in Zabaikalsky Krai, as well as hot humid continental climate (Dfa) in Jewish Autonomous Oblast (Beck et al., 2018). The territory is dominated by mountainous terrains. The relief of Zabaikalsky Krai presents itself in a form of elongated low and medium-high ridges, with the highest peak at 3067 m, while Amur Oblast is characterized by an alternation of medium-high and low ridges with plains, lowlands, and depressions. The vegetation is represented by taiga complexes of coniferous, coniferous-deciduous, and broad-leaved forests and forest steppe landscapes (National Atlas of Russia, vol. 2, 2007). This creates different habitat conditions for the tick population and functioning of the natural TBE foci. The socioeconomic conditions in the study region differ significantly, which could have an impact on the population's TBE circulation.

TBE data

Initial TBE incidence data were presented as absolute (annual number of cases) and relative (annual number of cases per 100,000 population) indicators aggregated by municipal units for the period from 2000 to 2020. A total of 85 municipal districts were included in the analysis. The data were officially sourced from the regional departments of the Federal Service for Supervision of Consumer Rights Protection and Human Welfare (Rospotrebnadzor).

Environmental and socio-economic data

Variables reflecting the effects of natural and socioeconomic conditions on the possible spread of tick-borne encephalitis are presented in Table 1. The choice of variables is determined by the environmental requirements of vectors, primarily climate, vegetation, and topography, as well as the peculiarities of the epidemiology of TBE and the possible influence of the socioeconomic component. Ixodid ticks are sensitive to humidity and temperature conditions (Burri et al., 2011, Tokarevich et al., 2017); therefore the distribution of natural foci of TBE is determined by the sum of temperatures for a period with a stable average daily temperature above 5 °C of at least 1600 °, with a moisture index varying from 0.15 to 0.60 and even slightly higher (Korenberg, Kovalevsky, 1985). Ixodid tick habitats are largely determined by forest structure (Daniel et al., 1998). Altitude can also potentially influence the distribution of various tick species (Kholodilov et al., 2019).

Information about natural conditions was obtained using a digital elevation model, ERA5 climate reanalysis data aggregated by month, and data on land use and surface temperature presented in the Google Earth Engine catalog (https://earthengine.google.com). After downloading the calculated variables (altitude, share of forest territories, precipitation in the warm period, land surface temperature for the warm period, and depth of snow cover) in raster format with the spatial resolution of the original datasets, the most represented pixel value was then recalculated to municipal units.

Human activity and behavior can significantly affect the spread of TBE. For example, the use of forest resources, changes in agriculture, or other types of anthropogenic activities may be reasons for the increase in the incidence of TBE (Kriz et al., 2004; Stefanoff et al., 2012; Panatto et al., 2022). These changes may be influenced by differences in broader socioeconomic circumstances (Randolf, 2008).

Data on socio-economic conditions (population density; share of people employed in agriculture, hunting, and forestry; fishing and fish farming; share of people employed in mining; share of the total area of residential premises equipped with sewerage; share of dilapidated housing; and density of paved roads) were obtained from open sources of the Federal State Statistics Service (Rosstat). The listed indicators characterize both the employment and living conditions, can generally reflect the socio-economic development of the municipality and the well-being of the population living in it, and indirectly influence the possibility of the spread of infection.

Data on natural and socio-economic conditions were limited to the period from 2016 to 2020. The primary processing and preparation of data for subsequent analysis were performed using the JavaScript Earth Engine API on the Google Earth Engine platform as well as the mapping service QGIS.

Spatio-temporal statistical analysis

Kulldorff spatial scan statistics implemented in SaTScan 9.6 software (Kulldorff, 2018) were used to identify possible spatio-temporal clusters of high TBE incidence in the study area during the period from 2000 to 2020. This approach is based on moving a cylindrical scanning window across the area of interest. The vertical dimension of the cylinder represents time. The radius and height of the cylinder varied from zero to 50% of the size of the study area and study period, respectively. Those cylinders within which there was a statistically significant excess of the observed number of cases over the expected number were then represented as spatio-temporal clusters. The expected number of cases was estimated based on the hypothesis of its Poisson distribution depending on the population in the municipal area using a discrete Poisson model (Kulldorff, 1997).

Spatial scan statistics were applied to the annual number of TBE cases assigned to municipal centroids. The model also uses municipal population data for the period from 2000 to 2020 (data is sourced from Rosstat). The use of this method made it possible to obtain spatial clusters of municipalities for a specific period of time, where the observed number of TBE cases statistically exceeds the expected number of cases.

To examine overall spatial clustering of TBE incidence, Global Moran's I spatial autocorrelation tool was additionally used. TBE incidence data were also tested for the presence of local spatial autocorrelation using Getis-Ord Statistics (Getis and Ord, 1992). Calculations were implemented in GeoDa software (Anselin et al., 2006). As a result, spatial clusters with high and low incidence could be identified and compared to the spatio-temporal clusters that had already been found.

Table 1. Environmental and socio-economic variables

Drivers	Variable	Data source
Natural	Altitude (m)	ALOS World 3D - 30m (AW3D30) is a global digital surface model (DSM) dataset
	Share of forest territories (%)	Dynamic World (a 10m near-real-time (NRT) Land Use/ Land Cover (LULC) dataset) (Brown et al., 2022)
	Precipitation in the warm period, (May — September, °C)	Copernicus Climate Change Service (C3S) (2017): ERA5: Fifth generation of ECMWF atmospheric reanalyses of the global climate. Copernicus Climate Change Service Climate Data Store (CDS), (date of access 08-10-2023), https://cds.climate.copernicus.eu/cdsapp#!/home
	Depth of snow cover (mm)	
	Air temperature for the cold period (November — March, °C)	
	Land surface temperature for the warm period (May — September, °C)	MODIS daily Land-surface Temperature at 1 km grids https://doi.org/10.5067/MODIS/MOD11A1.061
Socio-economic	Population density (people per sq. km)	Federal State Statistics Service (Rosstat)
	Share of people employed in agriculture, hunting, and forestry; fishing and fish farming (%)	
	Share of people employed in mining (%)	
	Share of the total area of residential premises equipped with sewerage (%)	
	Share of dilapidated housing (%)	
	Density of paved roads (km per 1000 sq. m)	

Regression analysis

Due to the fact that the incidence rate is highly biased and does not correspond to a normal distribution, which makes it difficult to use multiple linear regression, the number of years of registration of TBE cases in the municipality was used as the dependent variable. This approach seems justified, since the number of cases in the study area is usually no more than 1–2 per year, with rare exceptions of up to 10–15 cases (maximum 18) confined to cities. In addition, in a number of municipalities, TBE was not registered at all during the study period, which creates a significant number of zero values in the sample. In contrast to the incidence rate, there were no outliers for the variable of the number of years of registration.

We used zero-inflated negative binomial regression, which is appropriate for modeling count variables with excessive zeros that may be overdispersed (the count mean was 5.76, with a variance of 28.64, indicating overdispersion). According to theory, the count values and excess zeros are produced by different processes and can be represented separately (Hilbe, 2011).

Zero-inflated negative binomial regression models have two sets of predictors. One is used in a negative binomial model that predicts counts of the years of TBE registration and other is used in a logistic model to predict zero values (current absence of TBE registration in municipality). In that case we used a set of environmental and social predictors as the share of forest area, precipitation during warm period, population density, the share of population employed in mining. All variables were tested for multicollinearity by with the variance inflation factor (VIF < 5 that indicated moderate correlation). The goodness of regression model fit was assessed by an adjusted R-squared (R^2_{adj}) – a coefficient of determination adjusted for the number of predictions in the model, and a Root Mean Square Error (RMSE) - an average difference between values predicted by a model and the actual values. Regression analysis was carried out using R packages *ggplot2, car, pscl, easystats, sjPlot*.

Regression residuals were tested for the absence of spatial autocorrelation using Anselin Local Moran's I test (Anselin, 1995). This test is aimed at finding clusters of polygons with increased/decreased residual values based on the local Moran's I index and its statistical significance metrics (z-score and p-value). Statistical significance was assessed using 999 random permutations, and FDR correction was applied to eliminate the influence of multiple testing. Moran's I index values close to 1 or -1 and having a p-value<0.05 indicate the presence of clustering.

Results

Spatio-temporal clusters

Spatio-temporal analysis of TBE incidence allowed us to identify several statistically significant clusters. The most stable spatio-temporal cluster occurred between 2009 and 2018, and was characterized by a high relative risk of incidence (RR = 24.9), observed in the southwest of Zabaikalsky Krai (Fig. 2). The cluster includes two municipal districts, Krasnochikoisky and Petrovsk-Zabaikalsky. The remaining statistically significant spatio-temporal clusters belong to the period from 2000 to 2002, and are confined to the entire study area.

When considering the time dynamics for the entire study period, it was revealed that the period from 2000 to 2002 was characterized by a high incidence rate, after which the number of cases in the region stabilized (Fig. 3). It should be noted that in these years, no increase in incidence was observed in the Krasnochikoysky and Petrovsk-Zabaykalsky districts.

The Global Moran's I test for overall spatial clustering of incidence indicated the existence of a possible positive spatial autocorrelation (0.375, p-value<0.001) in the region. A spatial cluster of high incidence was identified in Zabaikalsky Krai, more specifically, in the central (Sretensky, Shelopogunsky) and southwestern (Kyrinsky, Krasnochikoysky, Petrovsk-Zabaikalsky, Khiloksky, Uletovsky) districts, while a low incidence cluster, including areas where the incidence was not recorded at all, was recorded in the southern districts of Amur Oblast (Fig. 4).

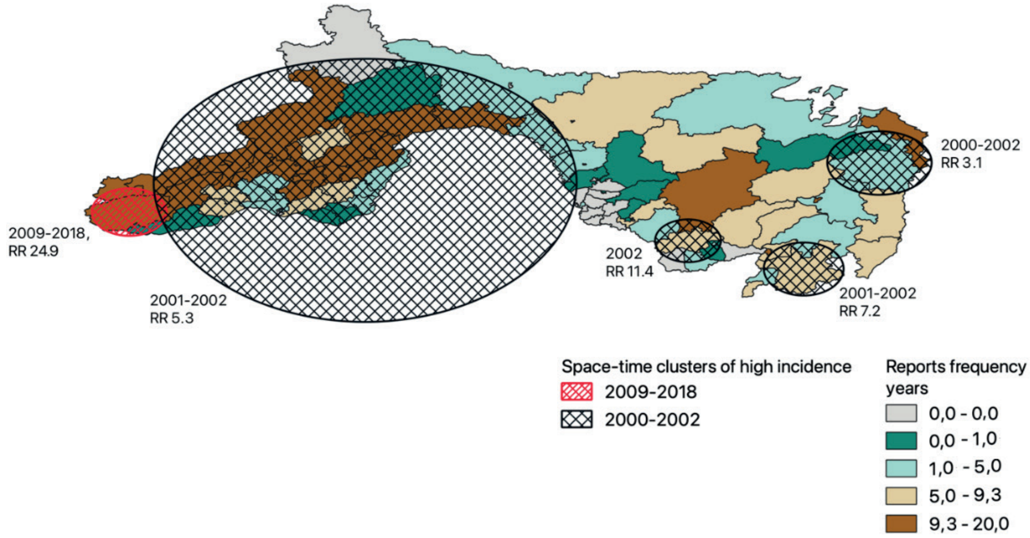

Fig. 2. Spatio-temporal patterns of TBE incidence (retrospective Space-Time analysis scanning for clusters with high rates using the Discrete Poisson model, RR – relative risk, cluster p-value < 0.05)

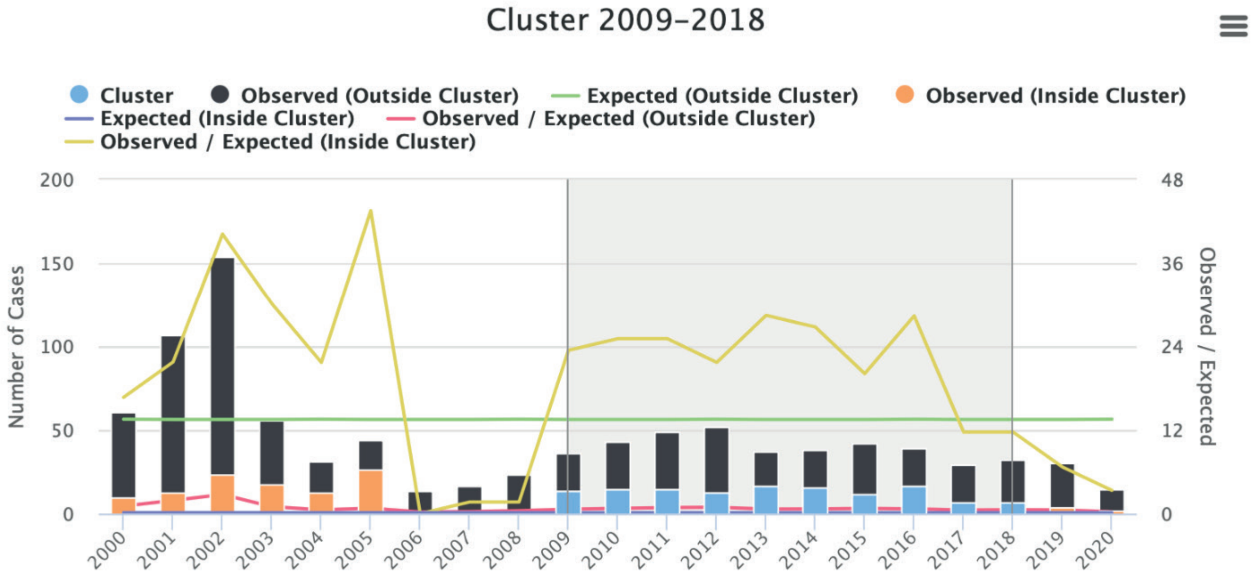

Fig. 3. TBE incidence dynamic (2000-2020) inside and outside of incidence cluster 2009-2018

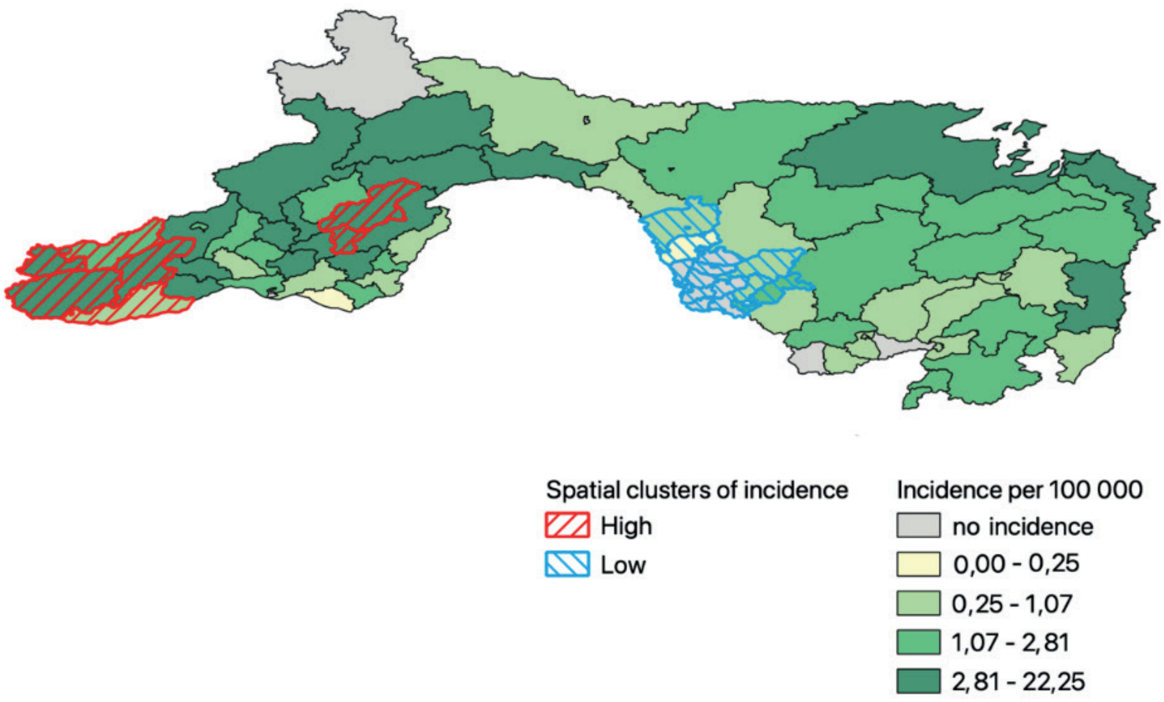

Fig. 4. Spatial patterns of high and low TBE incidence, 2000-2009 (Getis-Ord Statistics, cluster p-value < 0.05)

Potential drivers of TBE distribution

The results of Zero-inflated negative binomial regression showed good explanatory power of the TBE model (R2adj=0.90, RMSE =3.28). No overdispersion in the model, nor clustering of residuals were recorded. Registration of TBE on the territory was significantly related to such indicators as altitude, the share of forests, precipitation for the warm period, population density, the share of people employed in agriculture, hunting and forestry, fishing and fish farming, the share of people employed in mining, the share of dilapidated housing. Table 2 summarizes the model coefficients with their 95% confidence intervals, as well as statistical significance metrics (p-value) indicating a performance of particular variable as an explanatory factor in the regression. (Table 2).

Discussion

Population morbidity in 85 municipalities in the southern part of the Russian Far East for the period between 2000 and 2020 was analyzed, and a set of potentially influencing factors that shape the spatial heterogeneity of the distribution of TBE were identified.

In the study region, there are two focal territories: the Central Siberian-Transbaikal region, which includes Zabaikalsky Krai, and the Khingano-Amur region, which ties all other territories together (Korenberg and Kovalevsky, 1981). The results of the analysis showed that currently these focal areas are characterized by different intensities of the epidemic process. The territory where the epidemic process has been most active and stable for a long time is the southwest of Zabaikalsky Krai. This includes the Krasnochikoisky and Petrovsk-Zabaikalsky districts, that are forming a stable spatio-temporal cluster. This conclusion coincides with the results of other studies, where these two areas are classified as areas with high epidemiological risk (Turanov et al., 2020). This may be due both to the most favorable environmental conditions for tick populations represented in mid-mountain cedar-larch forests (National Atlas of Russia, vol. 2, 2007), and the influence of the peculiarities of economic activities carried out by residents

Table 2. Results of zero-inflated negative binomial regression models

Variables	Model coefficients	CI 95%	Std. Error	z value	Pr(>|z|)
Truncated poisson with log link					
(Intercept)	1.306	–0.527, 3.138	0.935	1.397	0.163
Altitude (m)	0.000	0.000, 0.001	0.000	2.557	0.011*
Share of forest territories (%)	0.016	0.009, 0.022	0.003	4.872	<0.001***
Precipitation in the warm period, (May — September, °C)	–13.266	–20.001, –6.531	3.436	-3.861	<0.001***
Depth of snow cover (mm)	–0.133	–2.025, 1.758	0.965	-0.138	0.890
Air temperature for the cold period (November — March, °C)	0.011	–0.043, 0.065	0.027	0.403	0.687
Land surface temperature for the warm period (May — September, °C)	0.020	–0.017, 0.057	0.019	1.042	0.298
Population density (people per sq. km)	0.001	0.001, 0.002	0.000	5.531	<0.001***
Share of people employed in agriculture, hunting, and forestry; fishing and fish farming (%)	–0.095	–0.136, –0.055	0.021	-4.634	<0.001***
Share of people employed in mining (%)	–0.171	–0.310, –0.032	0.071	-2.412	0.016*
Share of the total area of residential premises equipped with sewerage (%)	0.001	–0.005, 0.008	0.003	0.345	0.730
Share of dilapidated housing (%)	0.039	0.010, 0.068	0.015	2.628	0.009**
Density of paved roads (km per 1000 sq. m)	–0.002	–0.010, 0.006	0.004	-0.546	0.585
Zero hurdle model coefficients (binomial with logit link)					
(Intercept)	6.214	2.513, 9.914	1.888	3.291	<0.001***
Share of forest territories (%)	0.067	0.025, 0.108	0.021	3.147	0.002**
Precipitation in the warm period, (May — September, °C)	–78.206	–125.583, –30.829	24.172	-3.235	0.001**
Population density (people per sq. km)	0.005	0.000, 0.009	0.002	1.949	0.051
Share of people employed in mining (%)	–1.197	–1.911, –0.483	0.364	-3.285	0.001**

Signif. codes: 0 '***' 0.001 '**' 0.01 '*' 0.05 '.' 0.1 ' ' 1

Testing of regression residuals revealed no clusters or outliers.

of the areas associated with active interaction with natural environment.

Residents of the Krasnochikoysky district are mainly engaged in agricultural production (livestock raising), wood processing and procurement of wild plants: mushrooms, berries, pine nuts, wild garlic (Official portal of the Trans-Baikal Territory. Krasnochikoysky district. https://chikoy.75.ru/o-rayone/168914 -description). Labor employment of the population is low, which is why there are high risks of people coming into contact with the vector, especially during the period of active taiga fishing (Turanov et al., 2020). The metallurgical plant in the Petrovsk-Zabaikalsky district ceased its operation in 2002 (Rogov, 2023), which could also have contributed to a decrease in employment and people switching to actively visiting natural biotopes for hunting, fishing and collecting wild plants.

It should be noted that the administrative units neighboring the Krasnochikoisky and Petrovsk-Zabaikalsky districts form a spatial cluster of high incidence, which can also serve as confirmation of an active epidemic process in this territory.

Areas with low activity of the epidemic process include districts of the south of Amur Oblast, where a cluster of low incidence was identified, including areas with zero registration of TBE cases. This is the most populated and developed territory of the region, located in the landscape zone of deciduous forests on the Zeya-Bureya Plain and the southern part of the Amur-Zeya Plain. Natural conditions are less favorable for the circulation of the virus compared to the rest of the study region, which is mainly determined by the low proportion of forests in these districts (no more than 40%). The low activity of the epidemic process is confirmed by the lowest detection rates of antibodies to the TBE virus in the population (Dragomeretskaya et al., 2018).

A distinctive feature of the 2000–2002 clusters was the even distribution throughout the study region. In general, TBE is characterized by periodic cycles of rising incidence, usually occurring every 3–5 years (Korenberg et al., 2013). However, these clusters are, apparently, an echo of the deterioration of the epidemic situation with TBE throughout the entire focal territory of the Eurasian continent in 1990–1999, when there was a multifold increase in incidence rates not only in Western and Eastern Siberia, but also in the European and Far Eastern parts of the country (Zlobin et al., 2015; Leonova, 2020). The deterioration of the epidemiological situation could be caused by both the increased risk of infection of urban residents and the almost complete absence of methods and opportunities for mass prevention during the years of the socio-economic crisis (Voronkova, Zakharycheva, 2007; Korenberg et al., 2013). In subsequent years, on the contrary, there was a persistent trend towards a pronounced decrease in the incidence of TBE.

It should be noted that the Russian focal area of TBE continues into China, covering the northeast of the country and the provinces of Inner Mongolia, Heilongjiang, and Jilin, taking that that Heilongjiang is of the foremost priority (Yi et al., 2017) . Approximately 99% of cases have been reported in forested areas with mixed broadleaf-coniferous forests as the dominant vegetation, as well as in mixed broadleaf-coniferous forests and broadleaf forests. Moreover, most cases were in farmers or forestry workers (Sun et al., 2017; Chen et al., 2019).

The results of the regression analysis contribute to the understanding of the distribution of TBE in the study region, as well as the location of the identified spatio-temporal clusters. The spread of infection is the result of both natural and social factors; however, the role of the latter cannot be underestimated. According to the regression model, factors influencing the likelihood of infection primarily include the share of forest, the amount of precipitation during the warm season, population density, and employment in the mining industry.

The share of forests in the territory of a municipality is one of the main drivers, as it determines the possibility of the existence of the main vector of the virus, *I. persulcatus*. This is supported by consistent results from both spatio-temporal cluster analysis and regression model analysis. This is one of the most influential factors associated with the vector ecology.

The amount of precipitation during the warm period was also a significant variable in the model: the higher the amount of precipitation, the lower the probability of the spread of TBE. However, the influence of this factor should be interpreted with caution. Several other studies have also shown mixed results regarding the nature of the influence of precipitation (Brabec et al., 2017; Li et al., 2017). For example, in northeastern China, the risk of TBE infection in southwestern Heilongjiang Province was found to decrease with increasing precipitation, whereas in the center, it intensified along with increasing precipitation (Li et al., 2017). Ticks are sensitive to humidity, and increased humidity caused by increased precipitation helps to maintain optimal conditions in tick refuges, reduces moisture loss during hunting, improves their survival, and lengthens hunting periods (Uusitalo et al., 2020). However, the mechanism for synchronizing the complex life cycle of ixodid ticks under natural conditions is based on the reaction to day length. Therefore, the most generally important hydrothermal conditions are those under which ticks can receive an amount of heat and moisture that guarantees the completion of a certain developmental stage within a strictly defined time frame (Korenberg et al., 2013).

The lack of significance of the temperature factor in the model is probably explained by fairly favorable temperature conditions for the tick population and virus circulation throughout the entire study area; therefore, it is not limiting and does not appear on the regional scale of the study. In addition, it should be noted that little studies have been made about the impact of temperature or other meteorological factors directly on the TBE virus population (Korenberg et al., 2013).

Among other natural factors that significantly influence the spread of TBE, is altitude that can also reflect the environmental requirements of ticks. However, as in the case of the relationship with precipitation, the threshold values may be important when assessing the influence of a factor on the distribution of TBE. In northeast China, a non-monotonic and segmental effect of altitude was shown, with the highest risk of infection at altitudes of 400–600 m, then 1400–1700 m and 2000–3000 m (Sun et al., 2017). The affinity of *I. persulcatus* to medium and low altitudes has been noted in studies on Altai (Shchuchinov et al., 2015) and Tuva (Kholodilov et al., 2019).

Among socio-economic factors, the greatest influence was found for indicators of population density and employment, as well as the share of dilapidated housing. High population density appears to be a factor contributing to the spread of TBE. It is often associated with a high proportion of urban areas and a large population, which naturally increases the risk of TBE (Uusitalo et al., 2020). Employment of the population, which in our case was characterized by the share of people employed in agriculture, hunting, forestry, fishing, and fish farming, as well as in mining, probably restrained the spread of taiga foraging among the population and, accordingly, caused less contact with natural biotopes. In addition, those formally employed in hunting and forestry are more likely to be vaccinated, which also limits the spread of the disease. The influence of the share of dilapidated housing and the share of the total area of residential premises equipped with sewerage, as an indirect indicators of the socio-economic well-being of the population, support the hypothesis that one of the main factors in the spread of TBE in districts may be the lack of employment of the population or low level of income. The finding of the impact of unemployment and low-wage work on forest visits to gather resources for sale is in agreement with other studies (Stefanoff et al., 2012; Stefanoff et al., 2018).

Thus, the analysis not only made it possible to identify territories with different levels of manifestation of the epidemic process and determine the factors influencing the formation of a spatially heterogeneous picture in the spread of TBE, but also led to an indirect conclusion about the most vulnerable group: the economically marginalized population living in areas that are depressed in the socio-economic context. At the same time, the rest of the sick population might be vacationers resting in nature or working on private plots of land. These differences can be illustrated by the example of larger cities of the region (Chita, Khabarovsk, and Komsomolsk-on-Amur), where cases of TBE are recorded almost annually; however, taking into account population density and socio-economic characteristics, the likelihood of population contact with a vector and the risk of TBE infection cannot be considered together with districts included in the stable spatio-temporal cluster of Krasnochikoisky and Petrovsk-Zabaikalsky districts.

The identified spatio-temporal differences within the study region and their potential drivers must be considered when carrying out preventive measures, including vaccine prevention, anti-tick treatments, health education, and informing the population about personal protection. Despite the fact that at least 95% of the child and adult populations living in endemic areas are subject to mandatory vaccination, as well as the entire population that is exposed to occupational risks or travels to areas endemic for TBE (Sanitary Rules..., 2022), the vaccination plan is not completely fulfilled. The information on the partial volume of the vaccination campaign carried out is available in the reports "On the state of sanitary and epidemiological well-being of the population" for all subjects studied. Immunization coverage of TBE among the population living in endemic areas was no more than 10%. In addition, there are problems in evaluating the epidemiological effectiveness of vaccine prevention (Pen'evskaya et al., 2018). To improve the vaccine prevention program and analyze its effectiveness, a wider use of assessing the seroprevalence of IgG antibodies to the tick-borne encephalitis virus is necessary (Tokarevich et al., 2022). Despite the existence of natural cycles in the epidemiological manifestations of TBE, the influence of socio-economic components can have a strong impact on the incidence rate. A clear confirmation of this is the rise in incidence in the 1990s. Therefore, a set of preventive measures should be developed with consideration for the socio-economic characteristics of districts.

Strengths and limitations

The research carried out has certain limitations. Firstly, due to the lack of data, the influence of such factors as the size of tick populations, species composition and the level of their infestation in the study area, as well as the presence of rodents and large mammals that act as feeders for a significant number of both immature and adult stages were not considered (Cagnacci et al., 2012). Secondly, we were unable to compile a cohesive picture of the south of the Far East due to the absence of publicly available statistical data for Primorsky Krai. Lastly, the accuracy of threshold estimations for the response of influencing factors is limited by statistics that are combined across municipal units. However, the set of methods used allowed us to obtain consistent results regarding the spatial picture and potential drivers in the spread of TBE.

CONCLUSION

The study's findings allowed for the identification of two distinct clusters: one in the south of Amur Oblast, which was non-endemic and had a low incidence rate, and the other in the southwest of Zabaikalsky Krai, which showed a temporally stable cluster of active TBE viral circulation among the population. Simultaneously, various drivers in the creation of these spatial clusters can be identified. While the lack of ideal conditions for the virus vector, primarily caused by a small percentage of forests, determines a cluster of non-endemic areas, the socio-economic component plays a major role in the formation of a cluster of active virus circulation among the population. Despite the fact that TBE is a natural focal disease (as evidenced by the identified influence of the proportion of forests, the amount of precipitation in the warm season and altitude), the socio-economic parameters, such as population density, employment and financial well-being of the population, might also have quite the impact on the viral processes of TBE. Therefore, the underestimation of the socio-economic components may negatively affect the effectiveness of preventive measures.

REFERENCES

Andaev E.I., Nikitin A.Y., Yatsmenko E.V., Verigina E.V., Tolmacheva M.I., Ayugin N.I., Matveeva V.A., Balakhonov S.V. (2021). Tendencii razvitiya epidemicheskogo processa kleshchevogo virusnogo encefalita v Rossijskoj Federacii, laboratornaya diagnostika, profilaktika i prognoz na 2021 g. (Trends in Epidemic Process Development of Tick-Borne Encephalitis in the Russian Federation, Laboratory Diagnosis, Prophylaxis and Forecast for 2021). Problemy osobo opasnyh infekcij, 1:6-16. DOI:10.21055/0370-1069-2021-1-6-16 (in Russian).

Anselin L. (1995). Local Indicators of Spatial Association – LISA. Geographical Analysis, 27(2): 93–115.

Anselin L., Ibnu S., Youngihn K. (2006). GeoDa: An Introduction to Spatial Data Analysis. Geographical Analysis, 38 (1), 5-22.

Beck H., Zimmermann N., McVicar T. et al. (2018). Present and future Köppen-Geiger climate classification maps at 1-km resolution. Sci Data 5, 180214, DOI: 10.1038/sdata.2018.214.

Brabec M, Daniel M, Malý M, Danielová V, Kříž B, et al. (2017). Analysis of meteorological effects on the incidence of tickborne encephalitis in the Czech Republic over a thirty-year period. Virol Res Rev, 1(1): 1-8. DOI: 10.15761/VRR.1000103.

Brown C.F., Brumby S.P., Guzder-Williams B. et al. (2022). Dynamic World, Near real-time global 10 m land use land cover mapping. Sci Data 9, 251. DOI:10.1038/s41597-022-01307-4.

Burri C., Bastic V., Maeder G., Patalas E., Gern L. (2011). Microclimate and the zoonotic cycle of tick-borne encephalitis virus in Switzerland. J Med Entomol, 48: 615–627.

Cagnacci F., Bolzoni L., Rosà R., Carpi G., Hauffe H.C. et al. (2012). Effects of deer density on tick infestation of rodents and the hazard of tick-borne encephalitis. I: Empirical assessment. Int J Parasitol, 42: 365–372.

Chen X, Li F, Yin Q, Liu W, Fu S, He Y, et al. (2019). Epidemiology of tick-borne encephalitis in China, 2007- 2018. PLoS ONE 14(12): e0226712. https://doi.org/10.1371/journal. pone.0226712

Chicherina G.S., Morozova O.V., Panov V.V., Romanenko V.N., Bahvalov S.A., Bahvalova V. N. (2015). Osobennosti infekcii virusom kleshchevogo encefalita Ixodes persulcatus Schulze i Ixodes pavlovskyi Pomerantsev v period rosta chislennosti i transformacii vidovoj struktury soobshchestva iksodid (Features of the tick-borne encephalitis virus infection of Ixodes persulcatus Shulze и Ixodes pavlovskyi Pomerantsev 1946 during period of growth and transformation of species structure of the ixodids community). Voprosy virusologii, 60 (5): 42-46 (in Russian).

Dampilova, I.G., Turanov, A.O. (2014). Voprosy epidemiologicheskogo nadzora za kleshchevym virusnym encefalitom v Zabajkal'skom krae (Issues of epidemiologic surveillance of tick-borne viral encephalitis in Transbaikal Territory). Nacional'nye prioritety Rossii, 3 (13), 33-36 (in Russian).

Daniel M., Kolar J., Zeman P., Pavelka K., Sadlo J. (1998). Predictive map of Ixodes Ricinus high-incidence habitats and a tick-borne encephalitis risk assessment using satellite data. Exp. Appl. Acarol, 22: 417–433.

Dragomeretskaya A.G., Kurganova O.P., Trotsenko O.E., Mzhelskaya T.V., Romanova A.P., Perepelitsa A.A., Korotkoruchko O.I., Makeeva L.S. (2018). Ocenka sostoyaniya estestvennogo populyacionnogo immuniteta k virusu kleshchevogo encefalita u naseleniya Amurskoj oblasti (Assessment of innate immune response to tick-borne encephalitis vims of the Amur region population). Zdorov'e naseleniya i sreda obitaniya – ZNiSO, (3):38-42 (in Russian).

Ecker M., Allison S. L., Meixner T., Heinz F. X. (1999). Sequence analysis and genetic classification of tick-borne encephalitis viruses from Europe and Asia. J. Gen. Virol., 1:179-185. DOI: 10.1099/0022-1317-80-1-179.

Getis A., Ord J.K. (1992). The Analysis of Spatial Association by Use of Distance Statistics. Geographical Analysis, 24: 189–206.

Hilbe J. (2011). Negative binomial regression: Modeling. In Negative Binomial Regression. Cambridge: Cambridge University Press, 221-283. DOI:10.1017/CBO9780511973420.010.

Kholodilov I., Belova O., Burenkova L., Korotkov Y., Romanova L., Morozova L., Kudriavtsev V., Gmyl L., Belyaletdinova I., Chumakov A., Chumakova N., Dargyn O., Galatsevich N., Gmyl A., Mikhailov M., Oorzhak N., Polienko A., Saryglar A., Volok V., Yakovlev A., Karganova G. (2019). Ixodid ticks and tick-borne encephalitis virus prevalence in the South Asian part of Russia (Republic of Tuva). Ticks Tick Borne. Dis., 10(5):959-969. DOI: 10.1016/j.ttbdis.2019.04.019.

Korenberg E. I., Kovalevsky Yu. V. (1985). Taezhnyĭ kleshch Ixodes persulcatus Schulze (Acarina, Ixodidae). Morfologiya, sistematika, ekologiya, medicinskoe znachenie (Taiga tick Ixodes persulcatus Schulze (Acarina, Ixodidae). Morphology, systematics, ecology, medical importance). Nauka. Leningrad, 193 (in Russian).

Korenberg E.I., Kovalevsky Yu.V. (1981). Rayonization of the tick-borne encephalitis areal (Raionirovanie areala kleshchevogo entsefalita). In: Itogi nauki i tekhnika: Meditsinskaya geografiya. M.: VINITI, 11: 148 (in Russian).

Korenberg E.I., Pomelova V.G., Osin N.S. (2013). Prirodnoochagovye infekcii, peredayushchiesya iksodovymi kleshchami (Naturally occurring infections transmitted by ixodal ticks). Moskva, Kommentarij, 463 (in Russian).

Kriz B., Benes C., Danielová V., Daniel M. (2004). Socio-economic conditions and other anthropogenic factors influencing tick-borne encephalitis incidence in the Czech Republic. Int J Med Microbiol, 37:63-8. DOI: 10.1016/s1433-1128(04)80010-x.

Kulldorff M. (1997). A spatial scan statistic. Communications in Statistics: Theory and Methods, 26:6, 1481-1496. DOI: 10.1080/03610929708831995.

Kulldorff M. and Information Management Services (2018). Inc. SaTScan™ v9.6: Software for the spatial and space-time scan statistics [online]. Available at: www.satscan.org.

Leonova G.N. (2007). Problema kleshchevogo encefalita na yuge Dal'nego Vostoka: ot otkrytiya do nastoyashchego vremeni (Problem of Tick-Borne Encephalitis in the south of The Far East from opening till now). Sibirskij nauchnyj medicinskij zhurnal, 4: 7-13 (in Russian).

Leonova G.N. (2015). Dinamika epidemicheskoj situacii po kleshchevomu encefalitu na Dal'nem Vostoke (The Dynamics of the Epidemiological Situation of Tick Borne Encephalitis in the Far East). Epidemiologiya i vakcinoprofilaktika, 14(3):17-22. DOI: 10.31631/2073-3046-2015-14-3-17-22 (in Russian).

Leonova G.N. (2020). Kleshchevoj encefalit v dal'nevostochnom ochagovom regione evrazijskogo kontinenta (Tick-borne encephalitis in the Far East focal region of the Eurasian continent). ZHurnal mikrobiologii, epidemiologii i immunobiologii, 97: 150-158. DOI: 10.36233/0372-9311-2020-97-2-150-158 (in Russian).

Li Y., Wang J., Gao M., Fang L., Liu C., Lyu X., Bai Y., Zhao Q., Li H., Yu H., Cao W., Feng L., Wang Y., Zhang B. (2017). Geographical Environment Factors and Risk Assessment of Tick-Borne Encephalitis in Hulunbuir, Northeastern China. Int J Environ Res Public Health, 26; 14(6):569. DOI: 10.3390/ijerph14060569.

Lindquist L., Vapalahti O. (2008). Tick-borne encephalitis. Lancet, 31;371(9627):1861-71. DOI: 10.1016/S0140-6736(08)60800-4.

Malkhazova, S. M., Mironova, V. A., Vatlina, T. V., Vladimirov, I. V., Zelikhina, S. V., Orlov, D. S. (2023). Aktual'nye prirodnoobuslovlennye zabolevaniya na yuge Dal'nego Vostoka Rossii (Actual natural diseases in the south of the Russian Far East). Voprosy geografii, 156: 273-293. DOI: 10.24057/probl.geogr.156.17 (in Russian).

National Atlas of Russia. (2007). Vol. 2 (in Russian). https://nationalatlas.ru/tom2/328-330.html (accessed 20.11.2023)

On the state of sanitary and epidemiological well-being of the population in the Russian Federation in 2022: State report. M.: Federal Service for Supervision of Consumer Rights Protection and Human Welfare, 2023. 368 p. (in Russian).

Panatto D., Domnich A., Amicizia D., Reggio P., Iantomasi R. (2022). Vaccination against Tick-Borne Encephalitis (TBE) in Italy: Still a Long Way to Go. Microorganisms, 10(2):464. DOI: 10.3390/microorganisms10020464.

Pen'evskaya N.A., Rudakov N.V., Rudakova S.A. (2018). Problemnye aspekty ocenki epidemiologicheskoj effektivnosti vakcinoprofilaktiki kleshchevogo encefalita (Problematic Aspects of the Evaluation of the Epidemiological Effectiveness of Vaccination against Tick-Borne Encephalitis). Epidemiologiya i vakcinoprofilaktika, 5: 102 (in Russian).

Randolph S.E. (2008) Tick-borne encephalitis incidence in Central and Eastern Europe: consequences of political transition. Micr Infect, 10: 209-216. DOI: 10.1016/j.micinf.2007.12.005.

Rogov V.YU. (2023). Stanovlenie chyornoj metallurgii Bajkal'skogo regiona na osnove innovacionnyh reshenij (Stanovlenie ferrous metallurgy of the Baikal region on the basis of innovative solutions. Stanovlenie ferrous metallurgy of the Baikal region on the basis of innovative solutions.). Vestnik Zabajkal'skogo gosudarstvennogo universiteta, 29(2): 164-175 (in Russian).

Sanitarnye pravila i normy SanPiN 3.3686-21. «Sanitarno-epidemiologicheskie trebovaniya po profilaktike infekcionnyh boleznej» (Sanitary and epidemiological requirements for the prevention of infectious diseases) [online]. Available at: https://docs.cntd.ru/document/573660140?marker=6580IP (in Russian).

Shchuchinova L.D., Kozlova I.V., Zlobin V.I. (2015). Influence of altitude on tick-borne encephalitis infection risk in the natural foci of the Altai Republic, Southern Siberia. Ticks Tick Borne Dis, 6(3):322-9. DOI: 10.1016/j.ttbdis.2015.02.005.

Stefanoff P., Rosinska M., Samuels S., White D.J., Morse D.L. et al. (2012). A National Case- Control Study Identifies Human Socio-Economic Status and Activities as Risk Factors for Tick-Borne Encephalitis in Poland. PLOS ONE 7(9): e45511. DOI: 10.1371/journal.pone.0045511.

Stefanoff P., Rubikowska B., Bratkowski J., Ustrnul Z., Vanwambeke S.O., Rosinska M. A. (2018). Predictive Model Has Identified Tick-Borne Encephalitis High-Risk Areas in Regions Where No Cases Were Reported Previously, Poland, 1999-2012. Int J Environ Res Public Health, 15(4):677. DOI: 10.3390/ijerph15040677.

Sun R.X., Lai S.J., Yang Y., Li X.L., Liu K., Yao H.W., Zhou H., Li Y., Wang L.P., Mu D., Yin W.W., Fang L.Q., Yu H.J., Cao W.C. (2017). Mapping the distribution of tick-borne encephalitis in mainland China. Ticks Tick Borne Dis., 8(4):631-639. DOI: 10.1016/j.ttbdis.2017.04.009.

Tokarevich N., Blinova O., Stoyanova N. et al. (2022). Seroprevalence of tick-borne diseases in the Northwest Federal District of the Russian Federation. Russian Journal of Infection and Immunity, 12(5):891-901. DOI: 10.15789/2220-7619-SOT-1953.

Tokarevich N., Tronin A., Gnativ B., Revich B., Blinova O., Evengard B. (2017). Impact of air temperature variation on the ixodid ticks habitat and tick-borne encephalitis incidence in the Russian Arctic: the case of the Komi Republic, International Journal of Circumpolar Health, 76:1 . DOI: 10.1080/22423982.2017.1298882.

Turanov A.O., Nikitin A.YA., Andaev E.I., Balahonov S.V., SHashina N.I. (2020). Differenciaciya territorii Zabajkal'skogo kraya po zabolevaemosti kleshchevym virusnym encefalitom (Differentiation of Transbaikal Territory by Tick-Borne Viral Encephalitis Incidence). Problemy osobo opasnyh infekcij, 2:108-114. DOI: 10.21055/0370-1069-2020-2-108-114 (in Russian).

Uusitalo R., Siljander M., Dub T., Sane J., Sormunen J.J., Pellikka P., Vapalahti O. (2020). Modelling habitat suitability for occurrence of human tick-borne encephalitis (TBE) cases in Finland. Ticks Tick Borne Dis., 11(5):101457. DOI: 10.1016/j.ttbdis.2020.101457.

Voronkova G. M., Zakharycheva T. A. (2007). Sostoyanie problemy kleshchevyh infekcij v Habarovskom krae (State of the problem of tick-borne infections in Khabarovsk Krai). Sibirskij nauchnyj medicinskij zhurnal, 4:82-88 (in Russian).

Yi Xing, Heinz-Josef Schmitt, Adriano Arguedas, Junfeng Yang (2017). Tick-borne encephalitis in China: A review of epidemiology and vaccines. Vaccine, 35, 9, 1227-1237. https://doi.org/10.1016/j.vaccine.2017.01.015.

Zlobin V.I., Rudakov N.V., Malov I.V. (2015). Kleshchevye transmissivnye infekcii (Tick-borne vector-borne infections). Novosibirsk: Nauka, 224 (in Russian).

RESEARCH PAPER

MAPPING SEAGRASS PERCENT COVER AND BIOMASS IN NUSA LEMBONGAN, BALI, INDONESIA

Devica Natalia Br Ginting[1], Pramaditya Wicaksono[1*], Nur Mohammad Farda[1]
[1]Faculty of Geography, Gadjah Mada University, Yogyakarta, 55281, Indonesia
***Corresponding author:** prama.wicaksono@ugm.ac.id
Received: May 11th, 2023 / Accepted: February 7th, 2024 / Published: March 31st, 2024
https://DOI-10.24057/2071-9388-2023-2886

ABSTRACT. Seagrass meadow is one of the blue-carbon ecosystems capable of absorbing and storing carbon more effectively in the bodies and sediments than terrestrial ecosystems. However, nationwide data on its carbon stock remains elusive due to limitations and challenges in data collection and mapping. Seagrass percent cover and biomass, which were closely related with above-ground carbon stock, can be effectively mapped and monitored using remote sensing techniques. Therefore, this study aimed to compare the accuracy of 4 scenarios as well as assess the performance of random forest and stepwise regression methods, for mapping seagrass percent cover and biomass in Nusa Lembongan, Bali, Indonesia. The scenarios were experimented using only atmospherically corrected images, sunglint, water, as well as sunglint and water column corrected images. Furthermore, WorldView-3 images and in-situ seagrass data were used, with the image corrected by applying the scenarios. Random forest and stepwise regression methods were adopted for mapping and modelling. The optimum mapping scenario and method were chosen based on R^2, RMSE, and seagrass spatial distribution. The results show that the atmospherically corrected image produced the best seagrass percent cover and biomass map. Range of R^2 using random forest and stepwise regression model was 0.49–0.64 and 0.50–0.58, with RMSE ranging from 18.50% to 21.41% and 19.36% to 20.72%, respectively. Based on R^2, RMSE, and seagrass spatial distribution, it was concluded that the random forest model produced better mapping results, specifically for areas with high seagrass percent cover.

KEYWORDS: WorldView-3, Percent cover, Biomass, Random forest, Stepwise

CITATION: D. N. Br Ginting, P. Wicaksono, N. M. Farda (2024). Mapping Seagrass Percent Cover And Biomass In Nusa Lembongan, Bali, Indonesia. Geography, Environment, Sustainability, 1(17), 16-27
https://DOI-10.24057/2071-9388-2023-2886

ACKNOWLEDGEMENTS: The authors are grateful to Ignatius Salivian Wisnu Kumara for providing the insitu data. The authors are also thankful to the National Research and Innovation Agency and the Program "Rekognisi Tugas Akhir" (RTA) UGM 2022, for supporting and facilitating this study.

Conflict of interests: The authors reported no potential conflict of interest.

INTRODUCTION

Seagrass is an ecosystem with numerous benefits, including protection services, serving as primary producers, providing habitats for marine biota, and carbon storage (Duarte and Tomas 2013; Macreadie et al. 2017; Sjafrie et al. 2018; Macreadie et al. 2019; Duarte et al. 2020). Compared to terrestrial vegetation, it can store more CO_2 in the bodies and sediments (Mcleod et al. 2011). Despite these benefits, seagrass is experiencing a decline of 2-5% annually on a global scale (Duarte and Dennison, 2008). This ecosystem is vulnerable to damage and degradation due to increased coastal development and activities (Grech et al. 2012; Yaakub et al. 2014; Holon et al. 2015), as well as changes in environmental conditions that lead to the extinction of certain species (Strydom et al. 2017). According to study conducted by P2O-LIPI through the COREMAP-CTI project between 2015 – 2017, seagrass beds in Indonesia were in poor condition (Sjafrie et al. 2018). Given this situation, the significance of the mapping and obtaining up-to-date information on the extent and condition of seagrass is increasing (UNEP, 2020).

Remote sensing technology is an efficient and effective tool for monitoring seagrass beds due to its ability to provide both spatial and temporal information (Koedsin et al. 2016; Fauzan et al. 2017; Effrosynidis et al. 2018). Various method can be used to analyze remote sensing data (Effrosynidis et al. 2018; Pham et al. 2019), enabling the provision of information on seagrass extent and changes, species distribution, percent cover (Roelfsema et al. 2014; Fauzan et al. 2021), and biomass (Lyons et al. 2015; Koedsin et al. 2016; Wicaksono et al. 2021).

Seagrass mapping using remote sensing comprises various processes, contributing to producing accurate maps, such as atmospheric, sunglint, and water column correction, as stated in previous studies (Bukata et al. 1995; Hedley et al. 2005). While some investigations suggested that correction can improve accuracy (Tamondong et al. 2013; Anggoro et al. 2016), others indicated the opposite (Zhang et al. 2013). In addition to correction-related reports, data analysis is another critical process in remote sensing, facilitating data interpretation and visualization (Lillesand et al. 2015). The commonly used approach is stepwise regression method, as it enables the selection of an independent variable based on a significant relationship

(Thompson 1995; Smith 2018). This approach accelerates the selection and analysis of the most influential independent variables (Wang and Jain 2003; Khogkhao et al. 2017; Wicaksono et al. 2021). The application of linear regression is challenging due to the complexity of seagrass with diverse habitats and varying density. Alternatively, random forest regression method is a machine learning approach that builds decision trees based on random vectors with independently sampled data. It can unveil more complex relationships and process data quickly and accurately (Salford Systems, 2014; Genuer and Poggi, 2020; Zhang and Xie, 2012; Zhang et al., 2013; Effrosynidis et al., 2018; Maxwell et al., 2018; UNEP 2020).

The study specifically focuses on percent cover and biomass mapping, with previous investigation presenting these parameters as crucial indicators for estimating carbon stocks in seagrass beds (Wahyudi et al., 2019). Remote sensing techniques have been adopted for the mapping process, as showed by Roelfsema et al. (2014), Koedsin et al. (2016), Fauzan et al. (2021), and Wicaksono et al. (2021). Given the importance of seagrass beds in mitigating climate change by sequestering carbon, there is a growing need for data and knowledge on these variables (Duarte and Tomas, 2013; Fourqurean et al., 2013). Therefore, using remote sensing technology to obtain information on percent cover and biomass is crucial. This study aimed to examine various correction methods and compare the effectiveness of the random forest and stepwise regression methods for mapping percent cover and seagrass biomass in Nusa Lembongan Island.

MATERIALS AND METHODS

Study Area

Nusa Lembongan, an island in the Klungkung Regency, Bali, Indonesia (Fig. 1), is geographically located at 08° 30´ 40´´ - 08° 41´ 43´´ S, and 115° 25´ 36´´ E - 115° 28´ 20´´ E. The island has a flat topography with northward and southward slopes of 0–3% and 3–8%, respectively. The study area had a coastline of 16.3 km and comprised of mud, rock, and mangrove (Kumara 2018). Nusa Lembongan has a semi-diurnal tide pattern, resulting in two high and two low tides in a day. The current patterns in its waters were influenced by the movement of water masses from the Bali Strait, Lombok Strait, and the Indonesian sea, while tides have a more significant impact on current types in shallow waters (Prasetia et al., 2017).

According to field observations made by the Coral Triangle Center and Udayana University, the Nusa Penida Marine Protected Area has an area of 108 hectares covered by eight species of seagrass, namely *Thalassia hemprichii, Halophila decipiens, Halophila ovalis, Enhalus acoroides, Cymodocea rotundata, Syringodium isoetifolium, Cymodocea serrulata, and Halodule uninervis* (Kabupaten Klungkung, 2012). The seagrass ecosystem in the study area comprised of sand and muddy sand substrate types (Negara et al., 2020). However, Negara et al. (2020) stated that seagrass beds in the area were mainly used for tourism purposes, with the majority of the seagrass region serving as docking points for ships.

Field Data

The field data used in this study was sourced from Kumara (2018), who conducted a survey on benthic habitat and seagrass percent cover on Nusa Lembongan Island from June 12 to 19, 2017. This dataset comprised information related to various benthic types, such as coral, seagrass, macroalgae, and bare substrate, with data points distribution of 155, 450, 17, and 194, respectively.

The photo-transect method, which adopted underwater cameras and quadrants, was applied to collect the seagrass percent cover data. The photos taken contained coordinate information as the camera time is synchronized with GNSS. Furthermore, the receiver tracking interval is one second,

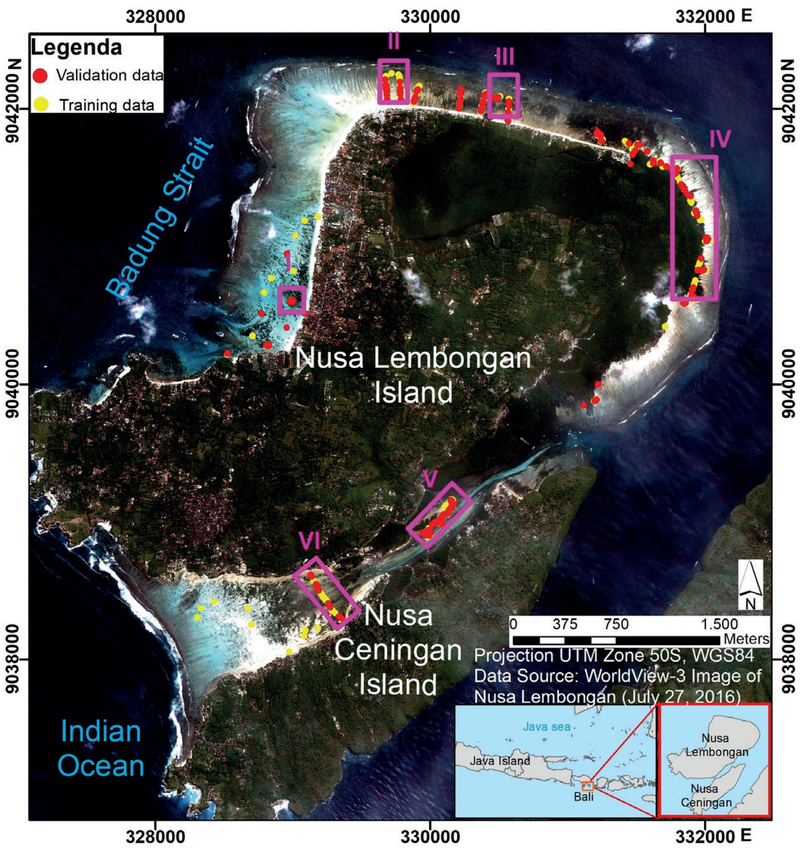

Fig. 1. The study site on Nusa Lembongan Island, as captured by WorldView-3 image. The purple rectangles on the figure represent the various coastal typology zones, while the points indicate the locations of the sample sites

ensuring precise geotagging. Quadrants measuring 0.5 × 0.5 m were used, and photos were captured at 2 m intervals. These quadrants served as a tool for scaling objects in photos or determining the percentage of seagrass cover. The classification of seagrass percent cover was established according to Fig. 2. For example, when the seagrass covers the entire area of the quadrat, it is labelled as 100%.

Each transect, ranging from 100-150 m long, was divided according to the coastal typology zones, comprising Zone I to VI, namely deep rocky, deep sandy, sandy sloping, muddy sloping, strait sloping, and sandy zones with high currents, respectively. This partitioning facilitated the identification of areas where specific seagrass species were predominantly discovered in each zone. The percent cover on each zone is presented in Table 1. Each zone consisted of 4-6 transect lines, determined by the level of species diversity observed. The field data was divided into two sets. One and one part was used to train the classification and regression models, while the other set was reserved for accuracy assessment.

WorldView-3 Image

DigitalGlobe launched WorldView-3 in 2014 as a commercial high-resolution image. It captures 8 multispectral bands with a spatial resolution of 1.24 m and 8 short infrared bands at 3.7 m resolution, alongside 12 Cavis bands at 30 m resolution, as presented in Table 2. The panchromatic band has a resolution of 0.31 m, and according to Kovacs et al. (2018), high spatial resolution imagery offers increased detail and is commonly regarded as more representative for mapping purposes. This image can capture up to 680,000 km^2 per day and has been corrected for sensor distortion. The received pixels were in radiometrically calibrated digital number (DigitalGlobe, 2014). The Worldview-3 image used in this study was captured on July 27, 2016, at 10:00:00 AM, when the waters in Nusa Lembongan Island were in low tide. As a result, several benthic objects were visible above the surface at the time of capture. This study used only the visible and near-infrared bands.

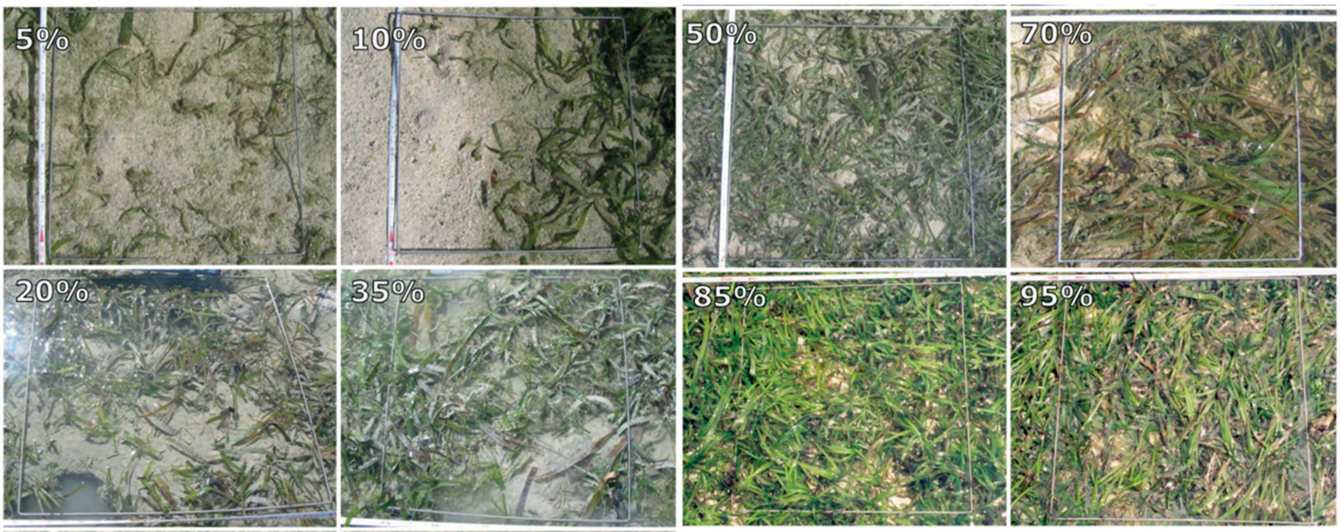

Fig. 2. Seagrass percent cover interpretation guide (seagrasswatch.org, accessed April 10, 2022)

Table 1. Seagrass percent cover on each zone

Zone	Total number of field data	Average (%)
1	49	74.59
2	65	26.17
3	36	47.92
4	84	73.57
5	180	51.75
6	22	55.45

Table 2. WorldView-3 specification

Band	Wavelength (nm)	Band	Wavelength (nm)
Coastal	400 - 450	Red	630 - 690
Blue	450 - 510	Red edge	705 - 745
Green	510 - 580	Near-IR1	770 - 895
Yellow	585 - 625	Near-IR2	860 - 1040
Spatial resolution	1.24 m		
Radiometric resolution	11-bit		
Temporal resolution	Daily		

Image Processing

The initial phase of image processing comprises masking, followed by correction using Scenario 1 - atmospheric, Scenario 2 - sunglint, Scenario 3 - water column, as well as Scenario 4 - sunglint and water column corrections. The corrected image is then used to create maps of benthic habitat and percent cover. Furthermore, the benthic habitat was characterized based on random forest classification algorithm. Pixel values within the seagrass and substrate classes were analyzed using both random forest and stepwise regression methods to produce percent cover map. This percent cover was further transformed into biomass map through the application of equation developed by Wicaksono (2015). The flowchart showing the methodology of this study is presented in Fig. 3.

Image Masking

The process of image masking was adopted to eliminate unnecessary pixels. This includes masking out land, optically deep water, and wave breaking pixels. To achieve land masking, the threshold value of the NIR band was used, enabling the differentiation of water and land pixels. Similarly, water column-corrected bands were used to identify threshold values for deep water pixels, thereby masking out optically deep waters (Wicaksono et al. 2021).

Atmospheric Correction

Atmospheric correction was conducted to obtain the surface reflectance values. The method for removing path radiance in images is the dark object subtraction (DOS) technique developed by Chavez (1996), which is applied to the TOA reflectance of the WorldView-3 image (Equation 1).

$$\rho_{BOA} = \rho_{TOA} - \rho_e \quad (1)$$

where:

ρ_{BOA}: surface reflectance,
ρ_e: reflectance of dark object,
ρ_{TOA}: reflectance on top of atmosphere

Sunglint Correction

In this study, the method developed by Hedley et al. (2005), was applied to reduce sunglint by leveraging the linear relationship between the NIR and visible bands in a training area with various sunglint levels. The required inputs for this correction include the visible band to be corrected, the slope of the linear regression, the NIR band, and the minimum value of the NIR band in an area unaffected by sunglint, as shown in Equation 2. The correction process engaged 968 samples obtained from affected deep-water areas. The slope of the linear regression was obtained from a training area of pixels in deep waters with varying sunglint intensities, as determined by Hochberg et al. (2003). The minimum value of the NIR band in the region

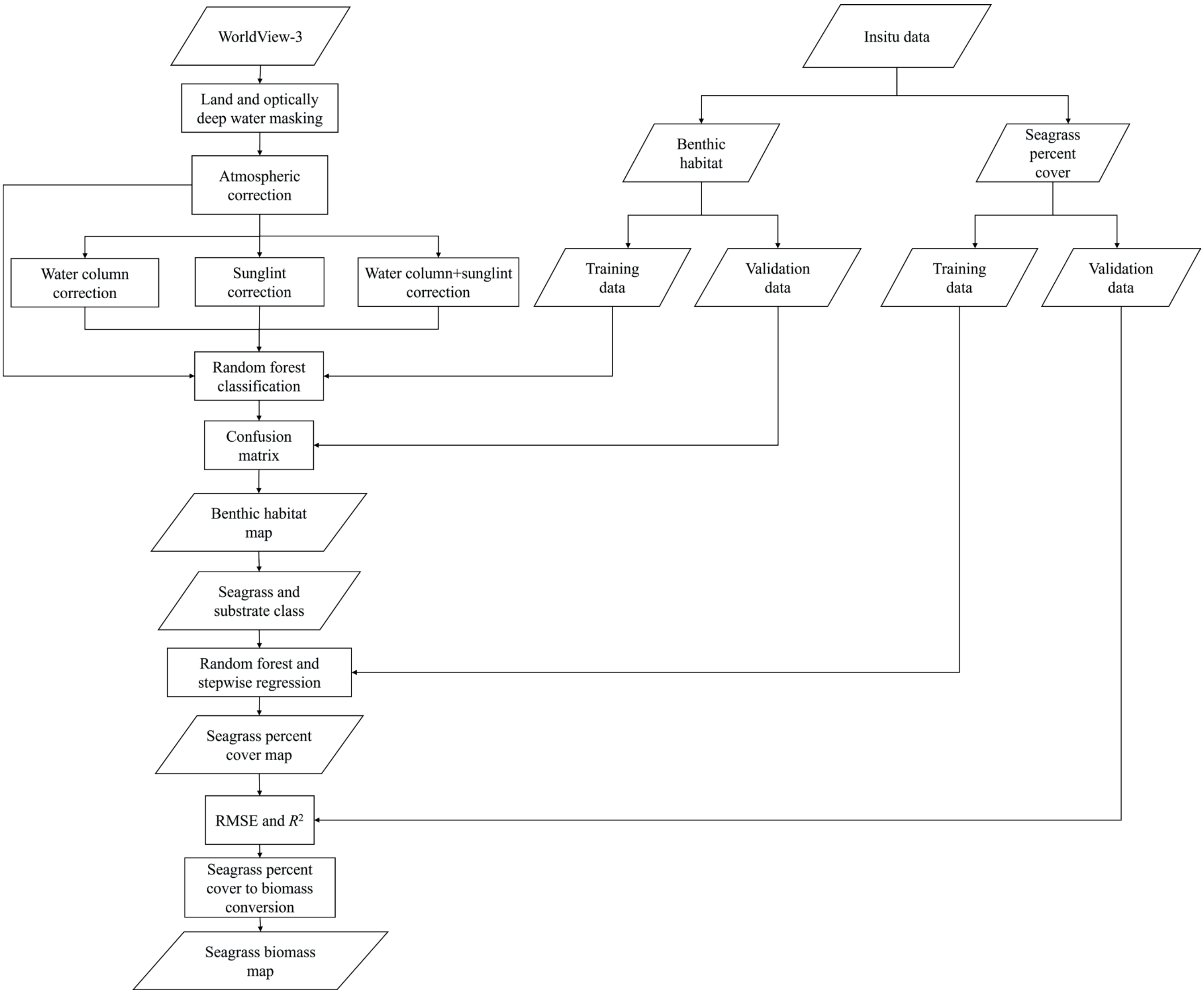

Fig. 3. The study flowchart

without sunglint was calculated by applying the following equation.

$$\rho_i' = \rho_i - b_i(\rho_{NIR} - \rho Min_{NIR}) \quad (2)$$

where:

ρ_i = reflectance of visible band i
b_i = slope between visible and NIR
ρ_{NIR} = reflectance of band NIR
ρMin_{NIR} = minimum reflectance of NIR band
ρ_i' = reflectance of sunglint corrected band

Water Column Correction

This study used the water column correction method developed by Lyzenga (1978), as described in Green et al. (2000). The method adopted a pair of visible bands to generate a new band where the energy attenuation effect from the water column has been minimised. To perform the necessary corrections, reflectance values of the same benthic object at different depths were required (Equation 3). Meanwhile, sand was chosen for this study, as it is easily visible and distinguishable at different depths, with the reflectance value decreasing as depth increases. A total of 217 samples of sand were collected at various depths.

$$Y = In(L_i) - \left[(\frac{ki}{kj}) xIn(L_j) \right] \quad (3)$$

where:

Y = depth invariant index
L_i = reflectance of band i
L_j = reflectance of band j
k_i / k_j = ratio of coefficient attenuation for band i dan j

Mapping Methods

Random Forest

Random forest is a machine learning approach that builds decision trees based on random vectors with independently sampled data (Salford Systems, 2014; Genuer and Poggi, 2020). Its classification and regression was used for benthic habitat and seagrass percent cover mappings, respectively. In random forest regression, n_{tree} (the number of trees) and m_{try} (the number of variables randomly selected at each node) parameters were also set. Furthermore, n_{tree} used factors of 100 and 500, while for m_{try}, the total of input variables was divided by 3 (Genuer and Poggi, 2020) and the lowest error from out-of-bag (OOB). The first m_{try} was the initial m_{try} in R software, and second mtry OOB was chosen because OOB samples help evaluate misclassification as well as estimate the importance of variables (Eisavi et al., 2015).

Stepwise Regression

Stepwise regression is an analysis method used to determine the relationship between independent and dependent variables. This was achieved analysing the sequence of significant relationships among the independent variables (Thompson, 1995; Smith, 2018). In this study, stepwise regression was used to determine the relationship between reflectance value of the image and the in-situ data on the percent cover. The equation obtained from this analysis was then adopted to generate a spatial distribution of the percent cover on the WorldView-3 image.

Seagrass Biomass

The seagrass biomass map was derived through the conversion of percent cover using the equation provided by Wicaksono (2015). A regression analysis was conducted on in-situ data, establishing a relationship between percent cover and biomass with an R^2 value of 0.4399 and a standard error (SE) ranging from 30 to 40 g/m^2, as shown in Equation 4. Seagrass PC was the most efficient method for estimating biomass due to its quick and non-destructive nature (Wicaksono, 2015). The following represent the equation adopted.

$$AGB_{seagrass} = 1.2712(PCy) + 6.6016 \quad (4)$$

With PCv is seagrass percent cover

Accuracy Assessment

Benthic habitat mapping accuracy assessment was performed using the confusion matrix method. This approach adopted a table that evaluates the classification algorithm performance (Ting, 2017). The overall accuracy was determined by calculating the number of pixels accurately classified against the field data. In testing empirical modelling for percent cover and biomass, the coefficient of determination (R^2) and root mean square error (RMSE) were used. The R^2 measures the goodness-of-fit of the model to the data (Ozer, 1985). On the other hand, the RMSE is a statistical method that assesses the model accuracy (Chai and Draxler, 2014). The error value represented the difference between the model results and the in-situ data. This assessment is essential in evaluating the accuracy of each scenario and the results obtained was compared using the random forest and stepwise regression methods.

RESULTS

Benthic habitat Mapping

Benthic habitat maps were generated using random forest classification in atmospheric scenario, which showed the highest accuracy and spatial distribution in Nusa Lembongan Island (Ginting et al., 2023). The classification outcomes showed the ability to map fringing reef formations, despite the misclassification of seagrass as coral, as indicated by the red circle in Fig. 4.

In atmospheric scenario, the accuracy was 73.00%, while for coral, seagrass, substrate, and macroalgae, the user's accuracies were 83.33%, 71.94%, 69.84%, and 0%, respectively. The corresponding producer's accuracies for the same classes were 56.45%, 87.36%, 57.14%, and 0%. When comparing the user's and producer's accuracies, the results suggest that the reef and substrate classes were underestimated, and the spatial distribution of this ecosystem exceeded estimation. However, due to a lack of field data and the absence of macroalgae in the study area, accurate mapping was not possible.

Seagrass Percent Cover Mapping

The spatial distribution of percent cover in each scenario was analyzed based on the levels specified in the Decree of the Minister of Environment No. 200 of 2004 (Kepmen LH, 2004), which include low (29.9%), medium (30.0–59.9%), and high (> 60%). The analysis was focused on 6 zones, as described in Fig. 1. Seagrass dominated in Zone I and IV, seagrass dominated, showing high percent cover, while Zone II had a low percent cover. Finally, the percent cover in III, V, and VI was moderate.

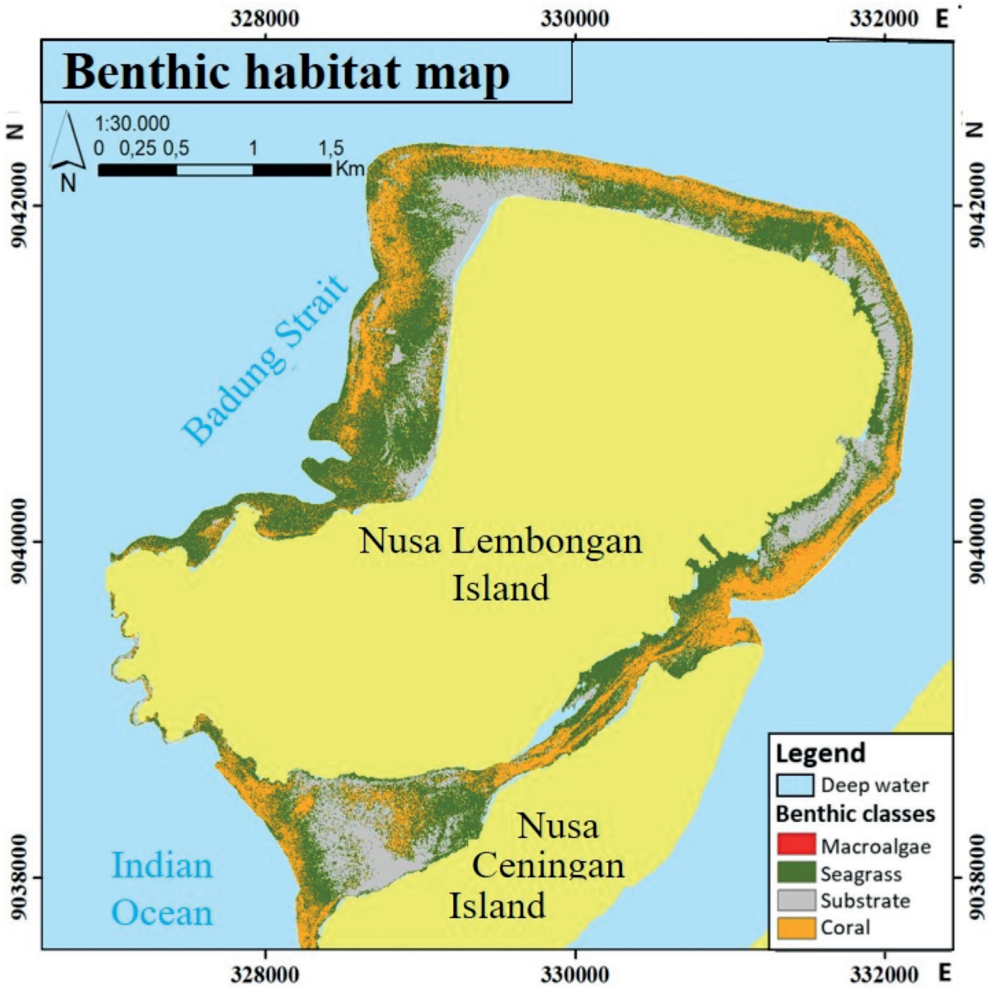

Fig. 4. Benthic habitat map obtained from random forest classification based on atmospheric correction scenario

In random forest regression, parameter tuning is conducted to analyze the effect of each parameter (n_{tree} and m_{try}) on the mapping of percent cover. The R^2 did not show a significant difference between parameter tuning, as indicated by the small variation in its values (0-0.2), as presented in Table 3. Based on RMSE, the error difference between mtry ranged from 0.03-0.31%, while n_{tree} was spanned between 0.09-0.76%. The initial m_{try} showed the lowest RMSE among all m_{try} parameter tuning. This study concluded that the n_{tree} parameter had the most influence on the accuracy of the percent cover map, with the lowest RMSE observed at n_{tree} 500. The range of R^2 and RMSE in the 4 scenarios are 0.49–0.64 and 18.50–21.41%, respectively. The ranking of R^2 from highest to lowest include Scenario 2, Scenario 4, Scenario 1, and Scenario 3. On the other hand, the best RMSE was indicated by the lowest value, observed in Scenario 4, followed by Scenario 2, Scenario 3, and Scenario 1.

In Scenario 1, based on random forest regression, seagrass with medium-to-high percent cover can be mapped as apposed to those with low cover percent, as shown in Fig. 5. On the other hand, Scenario 2 is unable to map high percent cover in coastal areas near mangroves (Zone IV) due to the pixel value loss caused by the sunglint correction process (marked by white on the map). Analyzing the distribution in each zone showed that Scenario 2 adequately maps the percent cover of zones III, V, and VI. However, misclassifications occurs in Zone II, where low percent cover is classified as a medium cover.

Table 3. R^2 and RMSE based on random forest regression

Scenario	n_{tree}							
	100				500			
	R^2	RMSE (%)	R^2	RMSE (%)	R^2	RMSE (%)	R^2	RMSE (%)
1	0.61	21.41	0.61	21.35	0.61	21.07	0.61	21.10
2	0.63	19.50	0.64	19.60	0.63	19.34	0.62	19.41
3	0.51	21.4	0.49	21.22	0.50	21.06	0.51	21.13
4	0.62	19.08	0.62	19.26	0.63	18.81	0.62	18.50
	Initial		OOB		Initial		OOB	
	m_{try}							

Scenario 3 had the lowest R^2 and higher error compared to the others, indicating a higher level of misclassification due to the correction process. Examining the spatial distribution in each zone show that this scenario is effective at mapping the percent cover in Zones I, and IV, which have a high percent cover. Scenario 4 had similar classification with 2, with missing pixel values denoted by white markings resulting from sunglint correction. This scenario was effective at mapping moderate percent cover but is less effective for low percent cover.

Each scenario was compared using 3 metrics, namely R^2, RMSE, and spatial distribution, to determine the optimal scenario for mapping biomass. Analysis showed that Scenario 1 (Zones I, II, IV, and VI) and Scenario 3 (zones III and IV) had the best performance, with the highest R^2 and lowest error, as detailed in Fig. 6. Specifically, Scenario 1 proved effective for mapping seagrass with a high percent cover, while 2 was more suitable for objects that are often submerged in water and the ecosystem with a medium percent cover. Based on these results, Scenario 1 was the optimal choice for mapping purposes, considering R^2, RMSE, and spatial distribution.

Based on the stepwise regression in Table 4, Scenario 1, 2, 3, and 4 had R^2 and RMSE values of 0.53 and 20.65%, 0.58 and 19.36%, 0.50 and 20.72%, as well as 0.56 and 20.61%, respectively. These values showed that Scenarios 2, 4, 1, and 3 were ranked from the best to the worst.

Fig. 7 contains a map showing the percent cover obtained through stepwise regression. While Scenario 1 is proficient in mapping from low to high, it misclassifies the percent cover of seagrass. The distribution in zones I, II, IV, V, and VI, was accurately mapped by this scenario, except for zone III dominated by high cover. On the other hand, Scenario 2 maps the percentage of cover in zones I, II, III, V, and VI accurately, except for zone IV due to the loss of seagrass pixel caused by the sunglint correction process. In the mapping process, Scenario 3 also shows the same pattern as Scenario 1. However, certain areas marked as having high percent cover in the Scenario 1 are classified as medium in Scenario 3.

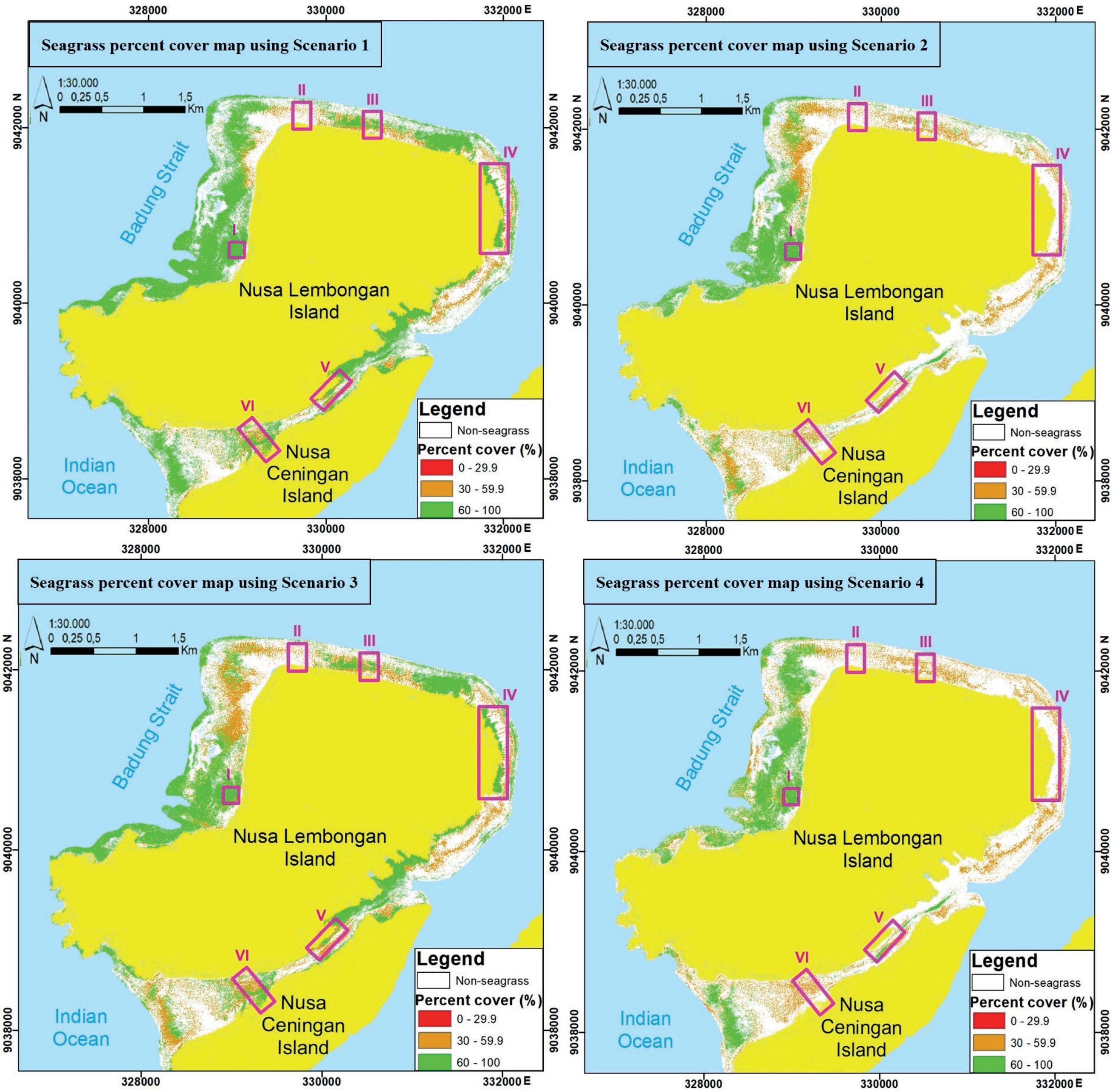

Fig. 5. Seagrass percent cover map based on random forest regression. Red boxes indicate coastal typology zones. The figures illustrate variations in seagrass percent cover based on the four scenarios

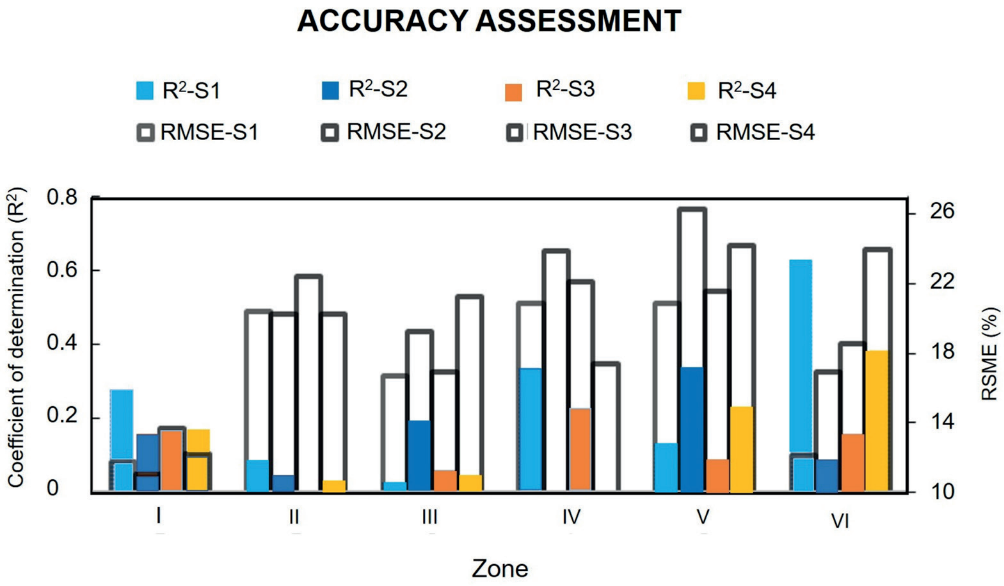

Fig. 6. The accuracy assessment of seagrass percent cover map based on the random forest method for each scenario and zone. The R^2 is represented by the coloured boxes, while the scenarios are distinguished by their respective colours. Boxes with a thick outline indicate the RMSE

Table 4. The R^2 and the RMSE of each scenario

Scenario	R^2	RMSE (%)
1	0.53	20.65
2	0.58	19.36
3	0.50	20.72
4	0.56	20.61

Comparison of seagrass percent cover map using random forest and stepwise regression

Based on the scenario analysis, the random forest regression outperformed the stepwise regression method in terms of the R^2 (Fig. 8) and RMSE values. To compare the spatial distribution of the results obtained from both methods, the scenarios with the highest R^2 and the lowest RMSE were selected. Scenario 1 was chosen for the random forest regression, while Scenario 2 was selected for the stepwise regression. The results showed that the random forest regression provided better spatial distribution of seagrass percent cover. This shows that the method was selected based on its accuracy and spatial distribution of seagrass percent cover.

Seagrass Biomass

In this study, biomass map was obtained by using an equation developed by Wicaksono (2015). This equation demonstrated that mapping seagrass aboveground biomass (g/m^2) can be accomplished by applying information on percent cover. To generate the biomass map, the best value of R^2, RMSE, and spatial distribution was selected. The accuracy assessment showed that random forest method was most effective for mapping. The results of the biomass map can be viewed in Fig. 9, where high aboveground biomass is located in zones I and IV.

The field data was converted to a percentage of cover for validation using the Wicaksono (2015) equation to assess the accuracy of the aboveground biomass. The atmospheric scenario biomass was compared with that of validation data. Finally, the comparison yielded R^2 and RMSE of 0.38 and 24.33 g/m^2, respectively.

DISCUSSION

This study aims to examine various correction and compare the effectiveness of the random forest and stepwise regression methods for mapping percent cover and seagrass biomass in Nusa Lembongan Island. Initially, benthic habitats were classified, achieving an accuracy of over 60%, which met the Indonesian National Standard 7716:2011 (BSN 2011). The classification effectively mapped fringing reef formations and seagrass meadow ecosystems in the study area, as shown in the study by Prasetia et al. (2017) and Negara et al. (2020). However, macroalgae objects were not mapped due to the low cover, as presented in the report by Munir and Wicaksono (2019).

Seagrass and sand pixels from benthic habitat were selected to examine various correction and methods to extract seagrass percent cover. Based on the analysis of all data, both the random forest and stepwise regression methods indicate that Scenario 2 had the highest R^2 and the lowest RMSE. However, a closer examination of coastal typology zones shows that the random forest method performs better with Scenario 1, particularly in zones of high seagrass cover. This approach outperforms the stepwise regression method in terms of R^2 and RMSE, both overall and per-zone. Furthermore, an analysis was conducted related to tuning parameters, such as n_{tree} and m_{try}. The random forest method parameter settings indicated that n_{tree} had a more significant effect on RMSE than m_{try} for mapping percent cover. The number of trees is directly proportional to the stability of the model (Dai et al. 2018; Genuer and Poggi 2020).

Scenario 1 was chosen for several reasons. Firstly, the image was captured during low tide, eliminating the

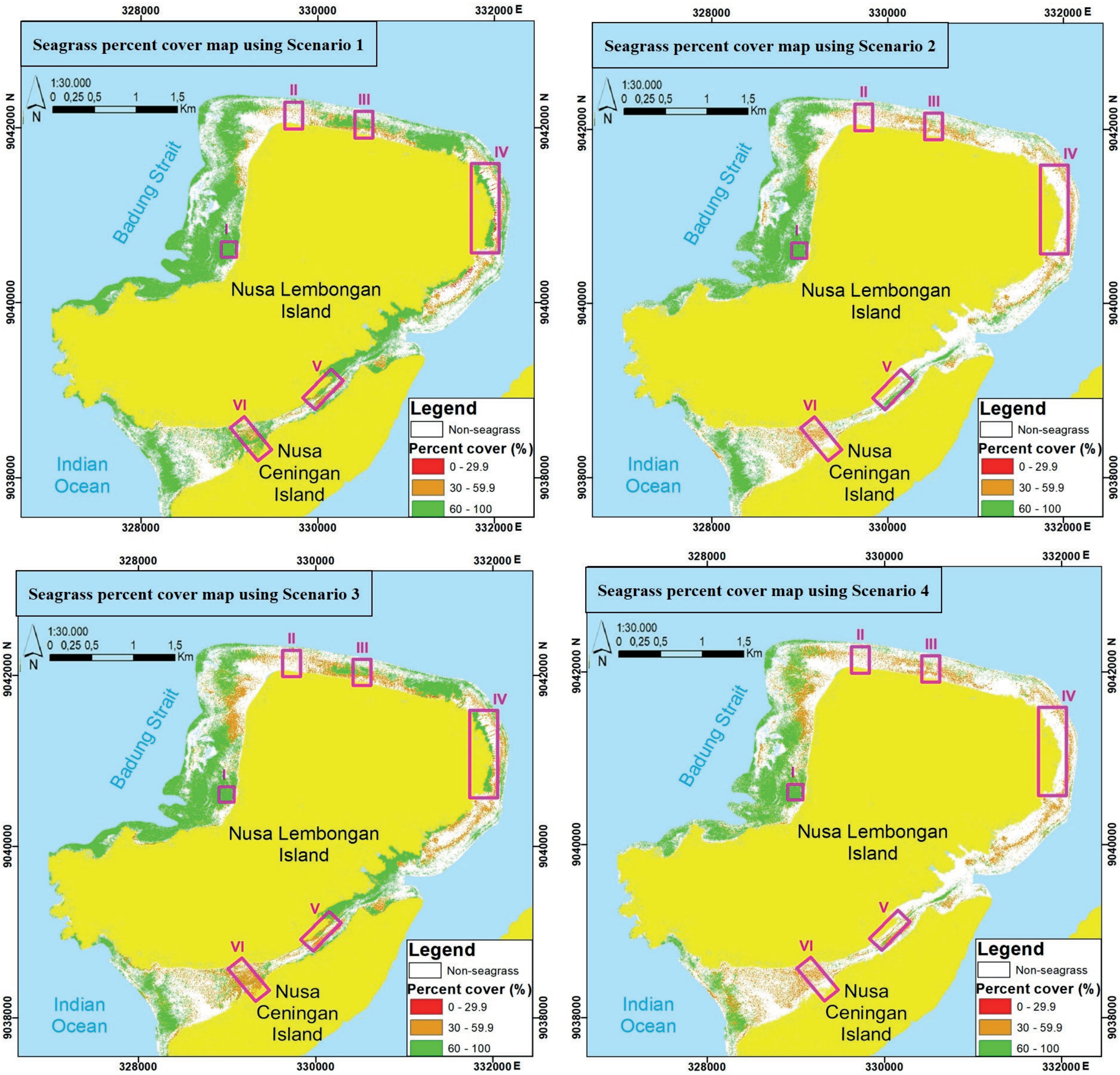

Fig. 7. The map of seagrass percent cover obtained using stepwise regression. Purple boxes indicate the coastal typology zones. The figures display the variation of seagrass percent cover based on four mapping scenarios

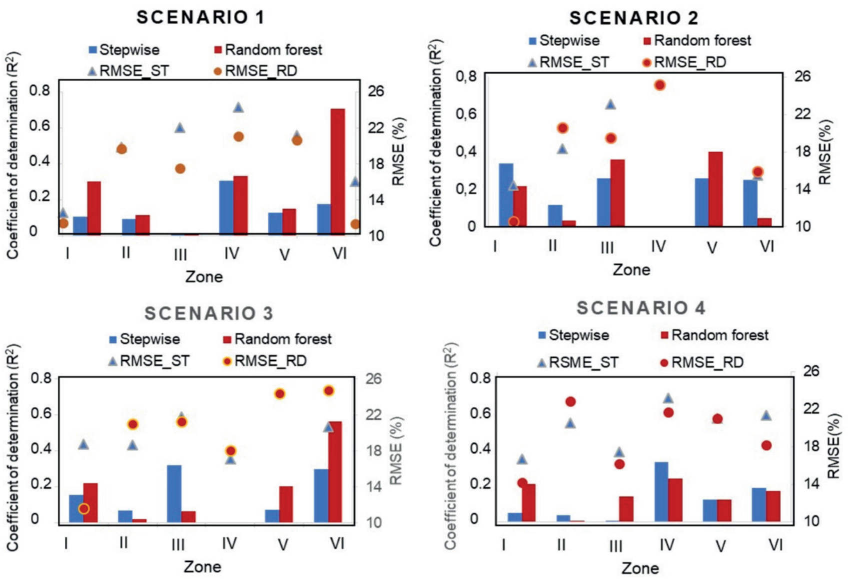

Fig. 8. Comparison of seagrass percent cover map accuracy assessment in each zone for all scenarios, using both random forest and stepwise regression. The rectangles in the figure represent the R^2, while triangles and circles represent RMSE values

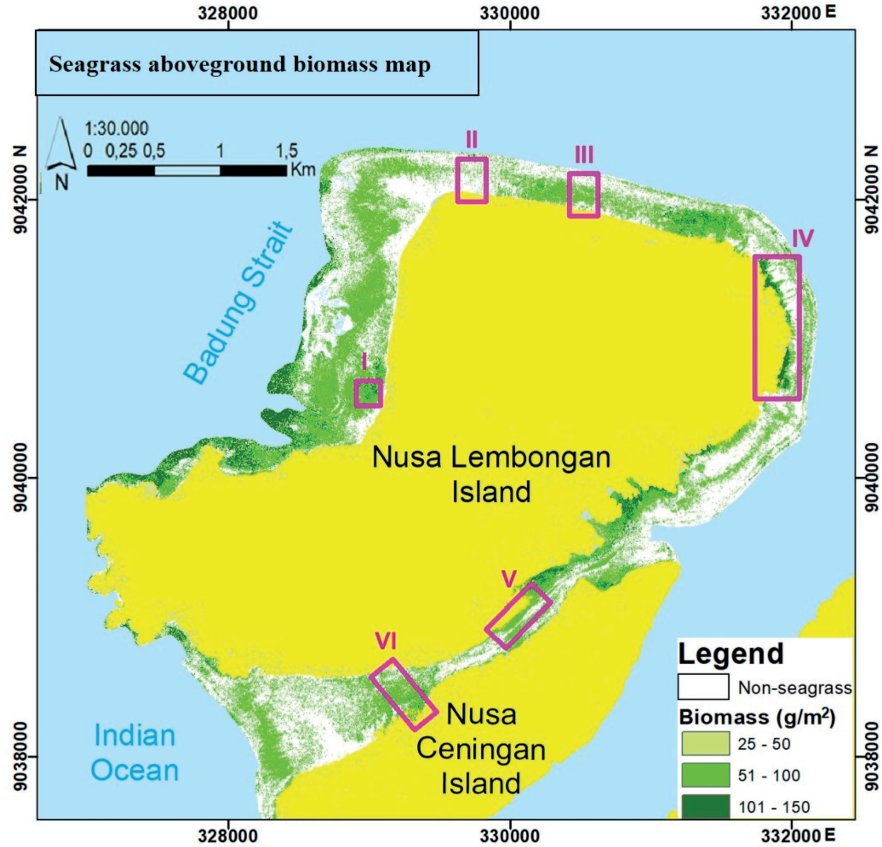

Fig. 9. Seagrass aboveground biomass map

need for water column correction. This was in line with the study of Zoffoli et al. (2014), where it was concluded that the Lyzenga method cannot be used for very shallow waters. Moreover, the images used were recorded at low tide and dominated by field data on reef flats. Secondly, despite sunglint scenario yielding the highest R^2, it resulted in the loss of pixels above the water surface, particularly seagrasses, after correction. This suggested that atmospheric correction was the best input data for percent cover mapping. Finally, according to Wicaksono et al. (2019), atmospheric correction produced relatively stable values depending on atmospheric conditions.

Compared to the previous investigation on mapping seagrass percent cover, this study indicates better performance than the R^2 generated in Labuan Bajo using Planetscope data and the Support Vector Machine method (Munir et al. 2019). However, the model accuracy was lower than in the study of Ariasari et al. (2019), where Planetscope data and principal component analysis were used on the image to generate input data for random forest regression. Future study should consider the principal component analysis process to improve the accuracy of mapping the percent cover in the study area.

Seagrass percent cover map was adopted to estimate above-ground biomass using the equation from Wicaksono (2015). The result showed that the equation can be used to map above-ground biomass up to 131 g/m^2. Based on field data collected in 2019 by Negara et al. (2020), the biomass at the study site ranged from 157.38 to 310.75 g/m^2, covering 3 zones. This difference in value was due to the equation by Wicaksono (2015) being developed in areas with lower biomass values compared to Nusa Lembongan Island. Despite this, the R^2 results are not significantly different from those of Wicaksono (2015).

The success of WorldView-3 imagery in producing a representative map is attributed to its high spatial and spectral resolution, making it particularly suitable for mapping seagrass ecosystems. These ecosystems are characterized by diverse species, benthic types, and present at varying density. However, WorldView-3 has limitations when applied to large areas or time series analysis. This is primarily due to a lack of scheduled and regular acquisition frequency, thereby making it expensive.

CONCLUSIONS

In conclusion, this study successfully documented the optimal data input for mapping seagrass percent cover based on image and site conditions. The most effective input data for mapping seagrass percent cover using WorldView-3 imagery, recorded at low tide, in a small island and dominated by field data in reef flat areas, was the atmospheric scenario, yielding R^2 and RMSE values of 0.61 and 21.07%, respectively. The random forest algorithm showed superior accuracy compared to the stepwise regression method.

REFERENCES

Anggoro, A., Siregar, V. P., & Agus, S. B. (2016). The Effect of Sunglint on Benthic Habitats Mapping in Pari Island Using Worldview-2 Imagery. Procedia Environmental Sciences, 33, 487–495. https://doi.org/10.1016/j.proenv.2016.03.101

Ariasari, A., Hartono, & Wicaksono, P. (2019). Random forest classification and regression for seagrass mapping using PlanetScope image in Labuan Bajo, East Nusa Tenggara. Proceedings of SPIE - The International Society for Optical Engineering, 11174, 1117407. https://doi.org/10.1117/12.2541718

Badan Standarisasi Nasional. (2011). SNI 7716/2011: Pemetaan habitat perairan laut dangkal. Jakarta.

Bukata, R. P., Jerome, J. H., Kondratyev, A. S., & Pozdnyakov, D. V. (1995). Optical Properties and Remote Sensing of Inland and Coastal Waters. CRC Press LLC.

Chai, T., & Draxler, R. R. (2014). Root mean square error (RMSE) or mean absolute error (MAE)? -Arguments against avoiding RMSE in the literature. Geoscientific Model Development, 7(3), 1247–1250. https://doi.org/10.5194/gmd-7-1247-2014

Chavez, P. S. (1996). Image-based atmospheric corrections - Revisited and improved. Photogrammetric Engineering and Remote Sensing, 62(9), 1025–1036.

Dai, B., Gu, C., Zhao, E., & Qin, X. (2018). Statistical model optimized random forest regression model for concrete dam deformation monitoring. Structural Control and Health Monitoring, 25(6), 1–15. https://doi.org/10.1002/stc.2170

DigitalGlobe. (2014). World View-3 Design and Specifications. Www.Digitalglobe.Com, 1–2.

Duarte, C. M., Dennison, W. C., Orth, R. J. W., & Carruthers, T. J. B. (2008). The Charisma of Coastal Ecosystems: Addressing the Imbalance. Estuaries and Coasts: J CERF (2008) 31:233–238. DOI 10.1007/S12237-008-9038-7.

Duarte, C. M., Tomas, S., & Nuria, M. (2013). Assessing the CO2 capture potential of seagrass restoration projects. Journal of Applied Ecology, 50, 1341–1349. https://doi.org/10.1111/1365-2664.12155

Duarte, C. M., Agusti, S., Barbier, E., Britten, G. L., Castilla, J. C., Gattuso, J. P., Fulweiler, R. W., Hughes, T. P., Knowlton, N., Lovelock, C. E., Lotze, H. K., Predragovic, M., Poloczanska, E., Roberts, C., & Worm, B. (2020). Rebuilding marine life. Nature, 580(7801), 39–51. https://doi.org/10.1038/s41586-020-2146-7

Effrosynidis, D., Arampatzis, A., & Sylaios, G. (2018). Seagrass detection in the Mediterranean: A supervised learning approach. Ecological Informatics, 48, 158–170. https://doi.org/10.1016/j.ecoinf.2018.09.007

Eisavi, V., Homayouni, S., Yazdi, A. M., & Alimohammadi, A. (2015). Land cover mapping based on random forest classification of multitemporal spectral and thermal images. Environmental Monitoring and Assessment, 187(5), 1–14. https://doi.org/10.1007/s10661-015-4489-3

Fauzan, M. A., Kumara, I. S. W., Yogyantoro, R., Suwardana, S., Fadhilah, N., Nurmalasari, I., Apriyani, S., & Wicaksono, P. (2017). Assessing the Capability of Sentinel-2A Data for Mapping Seagrass Percent Cover in Jerowaru, East Lombok. Indonesian Journal of Geography, 49(2), 195–203.

Fauzan, M. A., Wicaksono, P., & Hartono. (2021). Characterizing Derawan seagrass cover change with time-series Sentinel-2 images. Regional Studies in Marine Science, 48, 102048. https://doi.org/10.1016/j.rsma.2021.102048

Fourqurean, J. W., Duarte, C. M., Kennedy, H., Marbà, N., Holmer, M., Mateo, M. A., Apostolaki, E. T., Kendrick, G. A., Krause-Jensen, D., McGlathery, K. J., & Serrano, O. (2012). Seagrass ecosystems as a globally significant carbon stock. Nature Geoscience, 5, 505–509.

Genuer, R., & Poggi, J.-M. (2020). Random Forests with R. In Use R!. Springer. https://doi.org/10.1007/978-3-030-56485-8

Grech, A., Chartrand-Miller, K., Erftemeijer, P., Fonseca, M., McKenzie, L., Rasheed, M., Taylor, H., & Coles, R. (2012). A comparison of threats, vulnerabilities and management approaches in global seagrass bioregions. Environmental Research Letters, 7(2). https://doi.org/10.1088/1748-9326/7/2/024006

Green, E. P., Mumby, P. J., Edwards, A. J., & Clark, C. D. (2000). Remote Sensing Handbook for Tropical Coastal Management. In Coastal Management Sourcebooks 3 (Issue January 2000).Ginting, D. N. B., Wicaksono, P., & Farda, N. M. (2023). Mapping Benthic Habitat From Worldview-3 Image Using Random Forest Case Study: Nusa Lembongan, Bali, Indonesia. International Archives of the Photogrammetry, Remote Sensing and Spatial Information Sciences - ISPRS Archives, 48(4/W6-2022), 123–129. https://doi.org/10.5194/isprs-archives-XLVIII-4-W6-2022-123-2023

Hedley, J. D., Harborne, A. R., & Mumby, P. J. (2005). Simple and robust removal of sun glint for mapping shallow-water benthos. International Journal of Remote Sensing, 26(10), 2107–2112. https://doi.org/10.1080/01431160500034086

Hedley, J. D., Roelfsema, C. M., Chollett, I., Harborne, A. R., Heron, S. F., Weeks, S. J., Skirving, W. J., Strong, A. E., Mark, E. C., Christensen, T. R. L., Ticzon, V., Bejarano, S., & Mumby, P. J. (2016). Remote sensing of coral reefs for monitoring and management: A review. Remote Sensing, 8(2). https://doi.org/10.3390/rs8020118

Hochberg, E. J., Andréfouët, S., & Tyler, M. R. (2003). Sea surface correction of high spatial resolution ikonos images to improve bottom mapping in near-shore environments. IEEE Transactions on Geoscience and Remote Sensing, 41(7 PART II), 1724–1729. https://doi.org/10.1109/TGRS.2003.815408

Holon, F., Boissery, P., Guilbert, A., Freschet, E., & Deter, J. (2015). The impact of 85 years of coastal development on shallow seagrass beds (Posidonia oceanica L. (Delile)) in South Eastern France: A slow but steady loss without recovery. Estuarine, Coastal and Shelf Science, 165(May), 204–212. https://doi.org/10.1016/j.ecss.2015.05.017

Kabupaten Klungkung. (2012). Rencana Pengelolaan KKP Nusa Penida. Kabupaten Klungkung, Provinsi Bali.

Khogkhao, C., Hayashizaki, K. I., Tuntiprapas, P., & Prathep, A. (2017). Changes in seagrass communities along the runoff gradient of the Trang river, Thailand. ScienceAsia, 43(6), 339–346. https://doi.org/10.2306/scienceasia1513-1874.2017.43.339

Koedsin, W., Intararuang, W., Ritchie, R. J., & Huete, A. (2016). An integrated field and remote sensing method for mapping seagrass species, cover, and biomass in Southern Thailand. Remote Sensing, 8(4). https://doi.org/10.3390/rs8040292

Kovacs, E., Roelfsema, C., Lyons, M., Zhao, S., Phinn, S. Seagrass habitat mapping: How do landsat 8 OLI, sentinel-2, ZY-3A, and worldview-3 perform? Remote Sens Lett [Internet]. 2018;9(7):686–95. Available from: https://doi.org/10.1080/2150704X.2018.1468101

Kumara, I. S. W. (2018). Pemetaan spesies lamun melalui integrasi citra multispektral dan pola respon spektral di Nusa Lembongan, Bali. (Skripsi yang tidak dipublikasikan). Universitas Gadjah Mada, Indonesia.

Lillesand, T. M., Kiefer, R. F., & Chipman, J. W. (2015). Remote Sensing and Image Interpretation (7th ed.). Photogrammetric Engineering and Remote Sensing, 81(8). https://doi.org/10.14358/pers.81.8.615

Lyons, M., Roelfsema, C., Kovacs, E., Samper-Villarreal, J., Saunders, M., Maxwell, P., & Phinn, S. (2015). Rapid monitoring of seagrass biomass using a simple linear modelling approach, in the field and from space. Marine Ecology Progress Series, 530, 1–14. https://doi.org/10.3354/meps11321

Macreadie, P. I., Serrano, O., Maher, D. T., Duarte, C. M., & Beardall, J. (2017). Addressing calcium carbonate cycling in blue carbon accounting. Limnology And Oceanography Letters, 2(6), 195–201. https://doi.org/10.1002/lol2.10052

Lyzenga, D. R. (1978). Passive remote sensing techniques for mapping water depth and bottom features. Applied Optics, 17(3), 379. https://doi.org/10.1364/ao.17.000379

Macreadie, P. I., Anton, A., Raven, J. A., Beaumont, N., Connolly, R. M., Friess, D. A., Kelleway, J. J., Kennedy, H., Kuwae, T., Lavery, P. S., Lovelock, C. E., Smale, D. A., Apostolaki, E. T., Atwood, T. B., Baldock, J., Bianchi, T. S., Chmura, G. L., Eyre, B. D., … Duarte, C. M. (2019). The Future of Blue Carbon Science. Nature Communications, 10(1), 1–13. https://doi.org/10.1038/s41467-019-11693-w

Maxwell, A. E., Warner, T. A., & Fang, F. (2018). Implementation of machine-learning classification in remote sensing: An applied review. International Journal of Remote Sensing. Taylor and Francis Ltd. https://doi.org/10.1080/01431161.2018.1433343

McLeod, E., Chmura, G. L., Bouillon, S., Salm, R., Bjork, M., Duarte, C. M., Lovelock, C. E., Schlesinger, W. H., & Silliman, B. R. (2011). A Blueprint For Blue Carbon: Toward An Improved Understanding Of The Role Of Vegetated Coastal Habitats in Sequestering CO2. Frontiers in Ecology and the Environment, 9, 552–260.

Munir, M., & Wicaksono, P. (2019). Support vector machine for seagrass percent cover mapping using PlanetScope image in Labuan Bajo, East Nusa Tenggara. December, 112. https://doi.org/10.1117/12.2541849

Negara, I. K. S., Astawa Karang, I. W. G., & Giri, P. I. N. (2020). Simpanan karbon padang lamun di Kawasan Pantai Nusa Lembongan, Klungkung, Bali. Journal of Marine Research and Technology, 3(2), 82. https://doi.org/10.24843/jmrt.2020.v03.i02.p04

Ozer, D. J. (1985). Correlation and the coefficient of determination. Psychological Bulletin, 97(2), 307–315. https://doi.org/10.1037/0033-2909.97.2.307

Pham, T., Xia, J., Thang Ha, N., Tien Bui, D., Nhu Le, N., & Tekeuchi, W. (2019). A review of remote sensing approaches for monitoring blue carbon ecosystems: Mangroves, sea grasses and salt marshes during 2010–2018. Sensors (Switzerland), 19(8). https://doi.org/10.3390/s19081933

Prasetia, D., Supriharyono, M., Anggoro, S., & Sya'Rani, L. (2017). Coral bleaching on Lembongan Island, Nusa Penida, Bali. 134 (Icirad), 66–72. https://doi.org/10.2991/icirad-17.2017.13

Roelfsema, C. M., Lyons, M., Kovacs, E. M., Maxwell, P., Saunders, M. I., Samper-Villarreal, J., & Phinn, S. R. (2014). Multi-temporal mapping of seagrass cover, species and biomass: A semi-automated object based image analysis approach. Remote Sensing of Environment, 150, 172–187. https://doi.org/10.1016/j.rse.2014.05.001

Salford Systems. (2014). Random Forests for Beginners. Salford Systems, 71.

Seagrass Watch. Percent Cover Standards. Online at https://www.seagrasswatch.org/manuals/, accessed April 10, 2022

Sjafrie, N. D. M., Hernawan, U. E., Prayudha, B., Supriyadi, I. H., Iswari, M. Y., Rahmat, & Anggaraini, K. (2018). Status Padang Lamun Indonesia. P2OLIPI.

Smith, G. (2018). Step away from stepwise. Journal of Big Data, 5(1). https://doi.org/10.1186/s40537-018-0143-6

Strydom, M., Veldtman, R., Ngwenya, M. Z., & Esler, K. J. (2017). Invasive Australian Acacia seed banks: Size and relationship with stem diameter in the presence of gall-forming biological control agents. PLoS ONE, 12(8), 1–16. https://doi.org/10.1371/journal.pone.0181763

Tamondong, A. M., Blanco, A. C., Fortes, M. D., & Nadaoka, K. (2013). Mapping of seagrass and other benthic habitats in Bolinao, Pangasinan using Worldview-2 satellite image. In Proceedings of the IGARSS 2013—2013 IEEE International Geoscience and Remote Sensing Symposium, Melbourne, VIC, Australia, 21–26 July 2013; Pp. 1579–1582. https://doi.org/10.1109/IGARSS.2013.6723091

Ting, K. M. (2017). Confusion Matrix. In Encyclopedia of Machine Learning and Data Mining. Encyclopedia of Machine Learning and Data Mining. https://doi.org/10.1007/978-1-4899-7687-1

Thompson, B. (1995). Stepwise regression and stepwise discriminant analysis need not apply here: A guidelines editorial (Educational Researcher, pp. 525–534). Sage Publications, Inc.

UNEP. (2020). Out of Blue: The value of seagrasses to the environment and to people.

Wahyudi, A. J., Rahmawati, S., Irawan, A., Hadiyanto, H., Prayudha, B., Hafizt, M., Afdal, A., Adi, N. S., Rustam, A., Hernawan, U. E., Rahayu, Y. P., Iswari, M. Y., Supriyadi, I. H., Solihudin, T., Ati, R. N. A., Kepel, T. L., Kusumaningtyas, M. A., Daulat, A., Salim, H. L., … Kiswara, W. (2020). Assessing Carbon Stock and Sequestration of the Tropical Seagrass Meadows in Indonesia. Ocean Science Journal, 55(1), 85–97. https://doi.org/10.1007/s12601-020-0003-0

Wang, G., & Jain, W. (2003). Regression Analysis Modeling dan Forecasting. Graceway Publishing Company.

Wicaksono, P., Danoedoro, P., Hartono, Nehren, U., Maishella, A., Hafizt, M., Arjasakusuma, S., & Harahap, S. D. (2021). Analysis of field seagrass percent cover and aboveground carbon stock data for non-destructive aboveground seagrass carbon stock mapping using worldview-2 image. International Archives of the Photogrammetry, Remote Sensing and Spatial Information Sciences - ISPRS Archives, 46(4/W6-2021), 321–327. https://doi.org/10.5194/isprs-Archives-XLVI-4-W6-2021-321-2021

Wicaksono, P., Lazuardi, W., & Munir, M. (2019). Integrating image at different spatial resolutions and field data for seagrass percent cover mapping. International Archives of the Photogrammetry, Remote Sensing and Spatial Information Sciences - ISPRS Archives, 42(4/W19), 487–492. https://doi.org/10.5194/isprs-archives-XLII-4-W19-487-2019

Wicaksono, P. (2015). Remote sensing model development for seagrass and mangroves carbon stock mapping. (Unpublished doctoral dissertation). Universitas Gadjah Mada, Indonesia.

Wicaksono, P., & Lazuardi, W. (2019). Random forest classification scenarios for benthic habitat mapping using planetscope image. International Geoscience and Remote Sensing Symposium (IGARSS), 346, 8245–8248. https://doi.org/10.1109/IGARSS.2019.8899825

Yaakub, S. M., McKenzie, L. J., Erftemeijer, P. L. A., Bouma, T., & Todd, P. A. (2014). Courage under fire: Seagrass persistence adjacent to a highly urbanised city-state. Marine Pollution Bulletin, 83(2), 417–424. https://doi.org/10.1016/j.marpolbul.2014.01.012

Zhang, C., & Xie, Z. (2012). Combining object-based texture measures with a neural network for vegetation mapping in the Everglades from hyperspectral imagery. Remote Sensing of Environment, 124, 310-320. https://doi.org/10.1016/j.rse.2012.05.021

Zhang, C., Selch, D., Xie, Z., Roberts, C., Cooper, H., & Chen, G. (2013). Object-based benthic habitat mapping in the Florida Keys from hyperspectral imagery. Estuarine, Coastal and Shelf Science, 134, 88-97. https://doi.org/10.1016/j.ecss.2013.07.017

Zoffoli, M. L., Frouin, R., & Kampel, M. (2014). Water column correction for coral reef studies by remote sensing. Sensors, 14(9), 16881-16901. https://doi.org/10.3390/s140916881

RESEARCH PAPER

ASSESSMENT OF REMOTE SENSING APPROACH FOR URBAN ECOLOGICAL QUALITY EVALUATION IN PEKANBARU CITY, RIAU PROVINCE INDONESIA

Eggy Arya Giofandi[1*], Idrus Syahzaqi[2], Dhanu Sekarjati[3], Assyaroh Meidini Putriana[4], Heni Marta Diana Matita Putti[3], Cipta Estri Sekarrini[5]

[1] Master Program of Regional Planning Sciences, IPB University, Raya Dramaga Street, Bogor, 16680, Indonesia
[2] Master Program of Statistics, Institut Teknologi Sepuluh November, Teknik Kimia Street, Surabaya, 60111, Indonesia
[3] Amcolabora Institute, Boulevard Street, Depok, 16421, Indonesia
[4] Ministry of Agrarian Affairs and Spatial Planning/National Land Agency, Asahan Street, Pematang Siantar, 21136, Indonesia
[5]Doctoral Program of Geography Education, Universitas Negeri Malang, Semarang Street, Malang, 65145, Indonesia

*Corresponding author: eggyarya@apps.ipb.ac.id
Received: October 10th, 2022 / Accepted: December 12th, 2023 / Published: March 31st, 2024
https://DOI-10.24057/2071-9388-2023-2640

ABSTRACT. There are obstacles in estimating environmental dynamics behind its convenience, beginning with the development of effective policies for sustainable urban development. The objectives of this research were to comprehend the ability and performance of ecological indices integration and to identify the spatial distribution of changes from 2018 to 2021 in Pekanbaru City, Riau province, Indonesia. This study employed remote sensing data to create ecological parameters including the build-up index, vegetation index, soil index, and moisture index, as well as principal component analysis to generate ecological index integration. The findings indicate a correlation of over 90% among these parameters from 2018 to 2021. Overall, there has been a significant decrease in the ecological quality index's high-quality categories, such as good and excellent, covering a total of 19.6% over 127 km^2. Conversely, the poor ecological quality category increased to 2.2%, encompassing an area of 15 km^2, up from the initial 21.2% covering 122 km^2. Additionally, the fair and moderate categories also experienced increases of 4% and 13.4%, respectively, reaching 28 km^2 and 84 km^2. The study area's ecological quality is largely affected by increased anthropogenic activities, leading to a drastic decrease in the presence of ecological quality in the good and excellent categories. The importance of spatial planning is emphasized to incorporate aspects of ecological assessment rather than solely focusing on increasing economic activity. This outcome can be used to respond to the concept of sustainable development by caring for the ecological environment, particularly in urban areas, and mitigating ecological damage.

KEYWORDS: Assessment, urban ecology, remote sensing, geographic information system, ecosystem, ecological modelling, restoration, sustainability

CITATION: E. A. Giofandi, I. Syahzaqi, D. Sekarjati, A. M. Putri, H. Marta, C. E. Sekarrini (2024). Assessment Of Remote Sensing Approach For Urban Ecological Quality Evaluation In Pekanbaru City, Riau Province Indonesia. Geography, Environment, Sustainability, 1(17), 28-35
https://DOI-10.24057/2071-9388-2023-2640

Conflict of interests: The authors reported no potential conflict of interest.

INTRODUCTION

Environmental ecology is one of the scientific disciplines that examine alterations in land configuration resulting from human spatial activities, with the objective of managing environmental quality dynamics (Wiyono and Sunarto 2016). Human activity has had a considerable direct and indirect impact on natural landscapes by growing built-up areas (L. Sun et al. 2021). One of the planning scientists' goals is to develop policies that may improve environmental ecological quality monitoring by incorporating sustainable development into community spatial planning (Xu et al. 2019). Sustainable community development may be carried out in several stages by paying more attention to remote sensing (Zheng et al. 2022).

The concept of urban ecology that we aim to develop focuses on environmental quality through a regional characteristics approach, environmental comfort, and human ecology (J. Wang et al. 2022). One crucial aspect of the viability of urban ecology is considering the physical qualities of urban environments that are conducive to sustaining ecological systems (Liu and Shi 2019; Yu et al. 2022). The potential for ecological vulnerability is determined by the characteristics of the stratified ecosystem (C. Sun et al. 2020), and addressing this vulnerability can involve a series of intellectual conceptual flows, such as ecological vulnerability zoning (Amri et al. 2017).

When external demands exceed an ecosystem's carrying capacity, a state of instability arises, threatening ecosystem development and resilience (Liao and Jiang 2020). This explains why the assessment of ecological quality serves not only as scientific evidence for conservation (Bobby Rahman et al. 2019) but also as a valuable starting point for addressing sustainable development and impartiality towards industries inflicting environmental damage.

Numerous theorists and practitioners in urban ecology have explored the impact of land development on urban ecological environments using remote sensing data (Safitri and Giofandi 2019; Giofandi et al. 2020). An obvious advantage of environmental monitoring is the constituent elements of primary analytical methods, such as drought index, greenness index, humidity and ecosystem heat (Muhlisin et al., 2021). However, certain thresholds may face data restrictions on specific indicators and challenges in defining the hierarchy. According to research by (X. Wang et al. 2018; Shi and Li 2021), different vegetation densities with the corresponding vegetation indices can serve as environmental ecological quality variables, containing three aspects: changes in external disturbances, production capacity, and the impact of human social and economic development.

The evaluation of ecological quality aims to assess the state of the environment and the ecosystem health. It aids in understanding the impact of various factors on vegetation coverage and the overall ecological conditions (Y. G. Gao et al. 2022). In this study, the Remote Sensing Ecological Index (RSEI) is used to assess the ecological quality in Pekanbaru City, Riau province, Indonesia. RSEI, a model utilizing remote sensing data, combines multiple index factors to provide a quick and easy evaluation of regional ecological quality. RSEI avoids the artificial setting of weights by using the contribution rate of each index to the first principal component. It facilitates an objective coupling of indices and provides a comprehensive assessment of the ecological environment (Jiang et al. 2020). RSEI has been proven effective in analyzing ecological quality changes across various areas, and its reliability and applicability make it a suitable choice for regional ecological quality assessment (Shi and Li 2021).

Based on this, the paper evaluates remote sensing by proposing the combined use of several indices, such as NDBI (Build-up index), SAVI (Vegetation index), NDSI (Soil index), and NDMI (Moisture Index), amalgamated into an Ecological Index to measure urban ecological quality. The effectiveness of the ecological system is gauged by an objective ecological index based on a multidimensional and multi-method long-time series approach spanning from 2018 to 2021. This study seeks to address the following questions: (i) whether spatial factors can explain the capability and efficacy of integrated ecological indices in the context of environmental management, and (ii) whether ecological indices can be classified and explained concerning changes in spatial distribution. These findings aim to improve the urban ecology evaluation system for restoration success, offering enduring insights for construction ecology practitioners in the research area.

MATERIALS AND METHODS

Study Area

Pekanbaru City is one of the fastest-growing areas on the island of Sumatra, especially when compared to other cities. In the 2020 population census, researchers conducted a temporally spanning ecological quality assessment covering a total area of approximately 402.32 km^2, with a total population of 983,356 individuals (BPS 2021). Given the increasing urban and economic expansion, it is vital to assess spatial aspects to comprehend the environmental dynamics (Giofandi and Sekarjati 2020), and spatial-temporal ecological evolution in Pekanbaru City (Fig. 1).

Data Sources and Pre-Processing

This observation utilizes multi-temporal remote sensing data acquired by Landsat 8 Operational Land Imager (OLI) in June 2018 and July 2021. The selection of the acquisition date is based on the availability of satellite imagery with the least cloud cover and the use of the same month to minimize seasonal differences at the observation site. Pekanbaru is located on the Landsat 8 OLI image line for study area 127/060 using the World Geodetic System 1984 – Universal Transverse Mercator 47 South projection at 30 m resolution. The data was downloaded from the United States Geological Survey platform (www.earthexplorer.usgs.gov), which is OpenSources, to obtain ecological index maps for 2018 and 2021. Before further processing the image, the first step is pre-processing using remote sensing software with processing specifications including radiometric calibration chosen to convert the digital number (DN) value of the multispectral band to the reflectance value of the Earth's surface, and atmospheric correction using the Fast Line of sight Atmospheric Analysis of Spectral Hypercubes (FLAASH) approach as the data process to reduce the effects of weather and cloud cover. The next step is to crop the image based on the observation location.

Vegetation index, soil condition index, moisture index, and human activity index from Landsat 8 OLI image are the selected bands for developing an index adapted to the Landsat image channel, retrieved, and used as a reference for band calculation to obtain remote sensing dataset values such as Normalized Difference Build-up Index (NDBI), Normalized Difference Soil Index (NDSI), Normalized Difference Moisture Index (NDMI), and Soil Adjusted Vegetation Index (SAVI). The SAVI index is an algorithm that improves upon the Normalized Difference Vegetation Index (NDVI) by mitigating the impact of background soil on canopy brightness. The vegetation line equation (representing vegetation with uniform density and a consistent background) is derived through the estimation of canopy reflectance using a first-order photon interaction model, which simulates the interaction between the canopy and the ground layer. In addition, the indicators for the ecological index were selected based on the representation of the ecological environment, which includes vegetation, moisture, presence of buildings, and soil condition, which are the characteristics of the urban environment. Finally, an ecological index is created, which is geometrically combined with the previous indicators to reflect and evaluate the ecological quality of the city.

The ecological index is formed from four components: NDBI, NDSI, SAVI, and NDMI. These components are analyzed using the Principal Component Analysis (PCA) method to form an equation, along with the eigenvalue contribution rate, which indicates the ability of principal components (PCs) to explain the characteristics of the data. The PCA method aims to simplify the observed variables by reducing their dimensions, achieved by eliminating correlations between independent variables by transforming the original variables into new uncorrelated ones. It is assumed that k principal components are created from the p variables (with $k \le p$), where these principal components are linear combinations of the original p

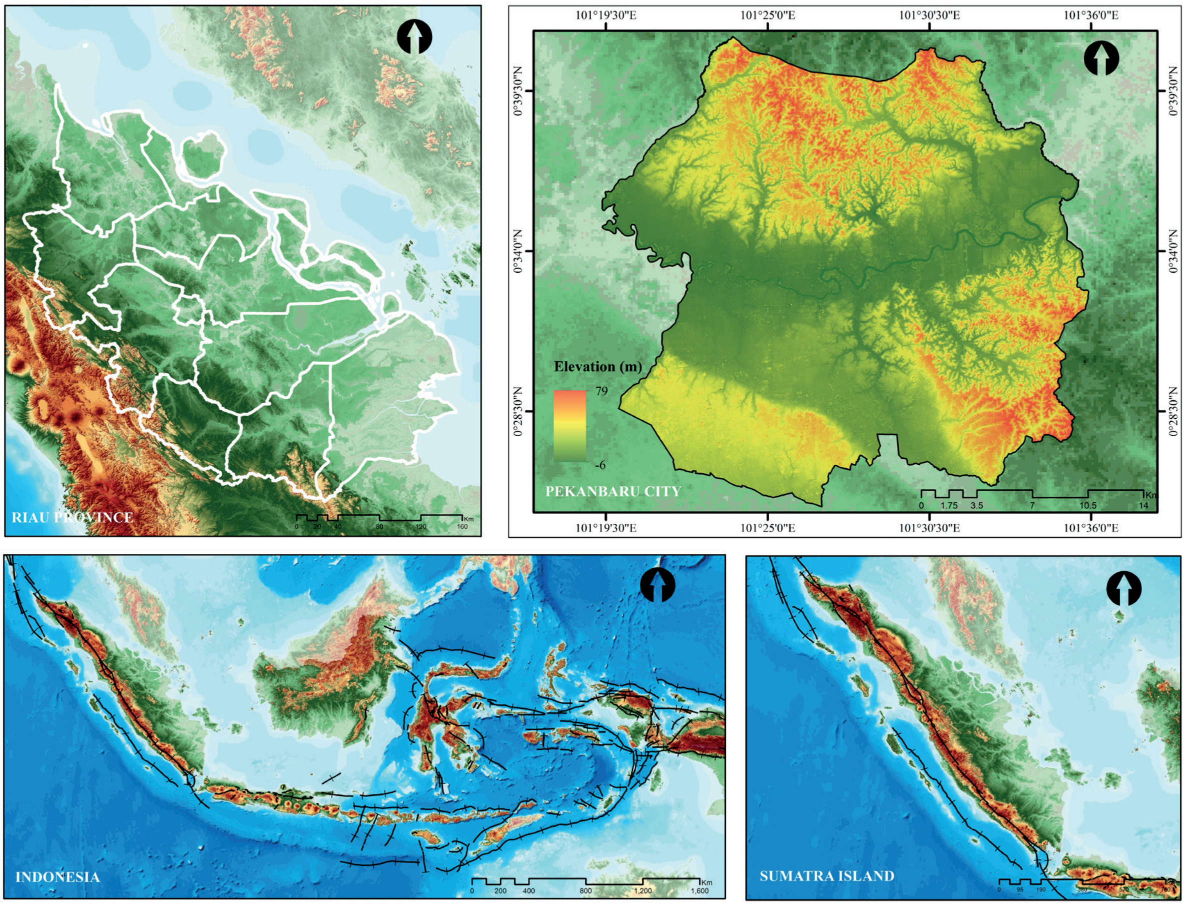

Fig. 1. Research site

variables. The advantages of the PCA method include the removal of correlations without losing a significant amount of information about all variables. PCA analysis was conducted using Minitab 21 software.

Development of Ecological Index Remote Sensing Data

The ecological index based on remote sensing is developed to quantify ecological quality by integrating four ecological factors: SAVI, NDBI, NDSI, and NDMI. These factors were selected based on a review of existing research (Jiang et al. 2020; Lian et al. 2022). Firstly, the dynamics of land use change, particularly in urban settings, alter the conditions and procedures of ecological study. Changes in landscape conditions initially influenced by human activities are obtained. As a result, the NDBI technique can be used to demonstrate the expansion of human activities under environmental conditions. Secondly, the vegetation indicator aims to reflect the environment and the quality of the ecological habitat as a green condition, while the soil condition is represented by the NDSI algorithm chosen to explain the ecological condition. In response to ecological changes, the NDMI method provides complete information on surface climatic change circumstances, such as air humidity.

The development of the ecological index involves several key processes, starting with the selection of ecological environmental characteristics and concluding with the integration of the ecological index. The physical ecological quality of the existing conditions in the study area is represented by four ecological parameters: SAVI, NDBI, NDSI, and NDMI. These parameters include the ecological quality of vegetation on the soil surface regarding greenery, human activity levels from the building perspective, soil conditions, and humidity conditions (Table 1). The comprehensive ecological indicator was then developed using the PCA regression. In this case, the following formula is employed to calculate the integrated ecological index with four ecological factors for ecological evaluation.

Table 1. Case studies and used methods

No	Formula	Parameter	Source
1	$NDBI = \dfrac{SWIR - NIR}{SWIR + NIR}$	Build-up Index	(Zha et al. 2003)
2	$NDSI = \dfrac{BSI + NDISI}{2}$	Soil Index	(Deng et al. 2015)
3	$SAVI = \dfrac{NIR - RED}{NIR + RED + L}(1 + L)$	Vegetation Index	(Huete, 1988)
4	$NDMI = \dfrac{NIR - SWIR}{NIR - SWIR}$	Moisture Index	(B.-C. Gao, 1995)

Ecological Index Integration

The four normalized ecological parameters generated from the previous technique are critical in this study since they can be used to construct a comprehensive ecological index that incorporates information from the four parameters. The PCA regression was used to create the ecological composite index. As one of the multidimensional technical approaches, PCA can eliminate the effect of collinearity among distinct variables (Xu et al. 2019; Liao and Jiang 2020; Hao et al. 2022). PCA captures the most information from all factors and is utilized to construct an ecological index image. The ecological index can be expressed by equation (1):

$$Ecology\ Index = f\,(NDBI, NDSI, SAVI, NDMI) \tag{1}$$

Finally, the value of the ecological quality images can be compared between different years. Therefore, the higher the ecological index value, the higher the ecological quality, and vice versa (Chen et al. 2020).

RESULTS

Capabilities and Performance of the Ecological Index Integration

Four ecological parameters are integrated by PCA, from 2018 and 2021 (Fig. 2). According to the PCA results of the four parameters used, the first principal component (PC1) has the highest contribution rate from the eigenvalues in 2018 and 2021, exceeding 76 %. The first PCA component typically explains more than 80% of the dataset characteristics, and is used to represent the ecological index (Yue et al. 2019). This indicates that PC1 represents the primary information and characteristics of the dataset (Table 2). Therefore, the results derived from PC1 can effectively contain most of the information from the four parameters.

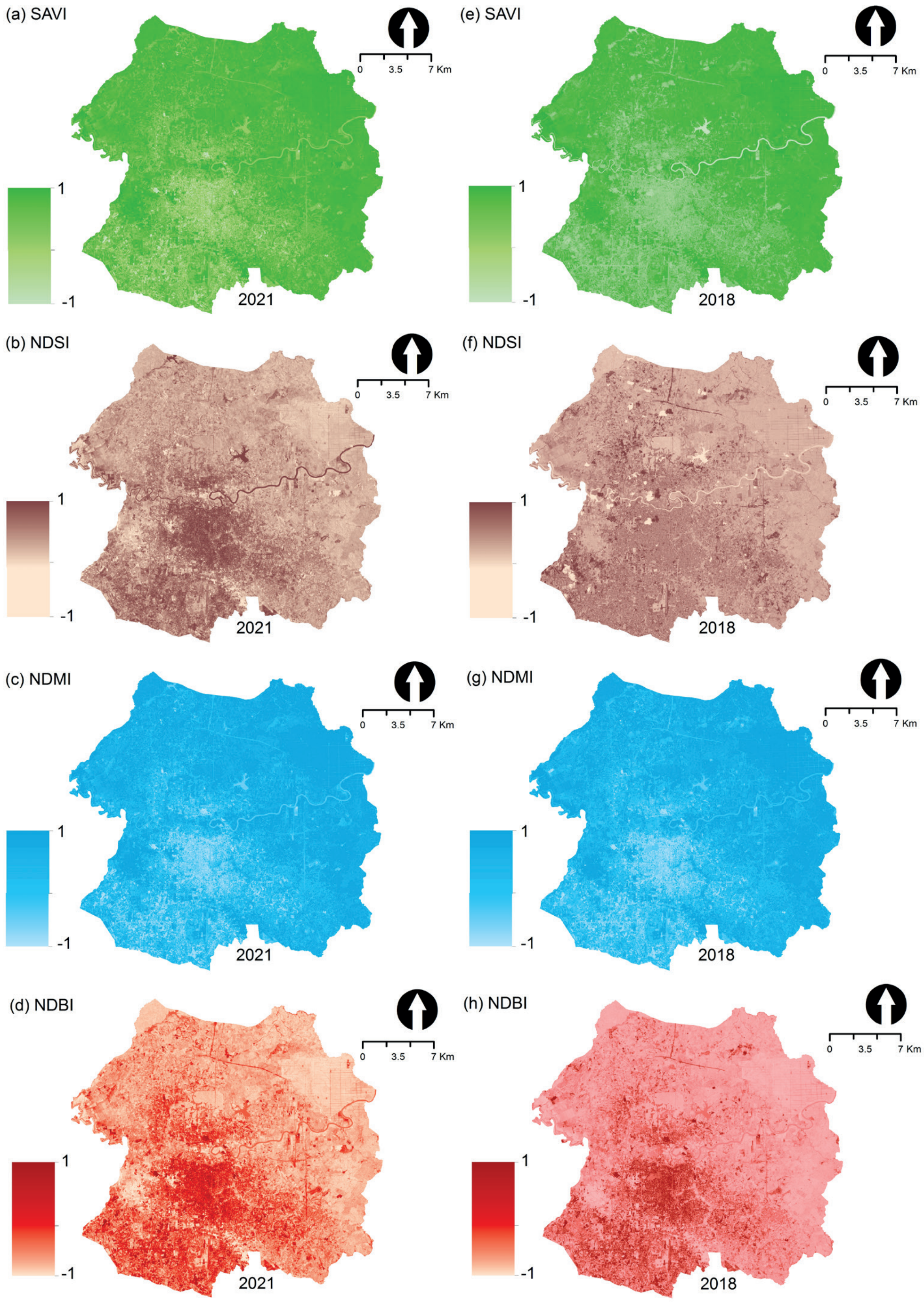

Source: Primary data processing

Fig. 2. Four parameters index (SAVI, NDSI, NDMI, NDBI) from 2018 and 2021

Table 2. Remote sensing ecological index calculation based on Landsat 8 OLI

Year	Indicator	PC 1	PC 2	PC 3	PC 4
2021	SAVI	-0,508	-0,181	-0,517	0,665
	NDBI	0,500	0,392	-0,765	-0,106
	NDSI	0,484	-0,865	-0,132	0,031
	NDMI	-0,509	-0,255	-0,361	-0,739
	Eigenvalues	3,656	0,1973	0,0938	0,0523
	Eigenvalue contribution rate	91,4%	4,9%	2,3%	1,3%
2018	SAVI	-0,522	-0,383	-0,491	0,582
	NDBI	0,548	-0,056	-0,804	-0,224
	NDSI	0,373	-0,874	0,310	0,021
	NDMI	-0,536	-0,293	-0,127	-0,781
	Eigenvalues	30,510	0,7373	0,1181	0,0936
	Eigenvalue contribution rate	76,3%	18,4%	3%	2,3%

Source: Primary data processing

The primary components explaining the dynamic variations in the index values of the first four main component ecological elements from 2018 and 2021 can be examined using the information provided in (Table 2). Among the four factors, SAVI, NDBI, and NDMI contributed the most absolute value. The SAVI parameter contributed to the index reaching -0.522 in 2018, which then increased to -0.508 in 2021. The NDBI parameter contributed to the index reaching 0.548 in 2018, which then declined to 0.500 in 2021. Meanwhile, the NDMI parameter contributed to the index reaching -0.536 in 2018, which then increased to -0.509 in 2021. A drawback of sensitivity to the scaling of variables is found in PCA. If the variables are not on the same scale, the results can be skewed, and only linear relationships in the data may be captured. Non-linear relationships are not suitable for capture by PCA.

Correlation analysis is necessary to determine the relationship between variables in 2018 and 2021. If the correlation coefficient is positive, it indicates a unidirectional relationship, while a negative coefficient signifies a non-unidirectional correlation (opposite direction). In this study, we used the Pearson correlation method because of the interval-ratio scale data. (Fig. 3) shows that the correlation between parameters in 2018 has the same sign as the correlation in 2021. This indicates that the correlation results between parameters align with the ecological meaning expressed by each of the four parameters, thus confirming the applicability. and effectiveness of the ecological index for the assessment of ecological quality. This finding is in line with the research by (Hui et al. 2021), which states that the ecological index has a significant positive correlation with ecological quality.

(Fig. 3-a) shows the correlation between the four parameters (SAVI, NDBI, NDSI, and NDMI) in 2018, while (Fig. 3-b) represents the correlation in 2021. It is evident from the graph above that NDSI and NDBI do not correlate with SAVI and NDMI. NDSI and NDBI have a negative association with the SAVI, but a positive correlation with the NDMI. Between 2018 and 2021, the correlation coefficient between SAVI and NDMI exceeds 90%, indicating\ a strong relationship between them. This finding is consistent with the results of (Y. G. Gao et al. 2022), who found that the average value of the Ecological Index increased in the Wugong Mountain region from 2015 to 2019, with the greenness and humidity indices positively impacting ecological quality. Meanwhile, \NDBI correlates negatively with NDMI but positively with NDSI, while NDSI has a negative correlation with NDMI.

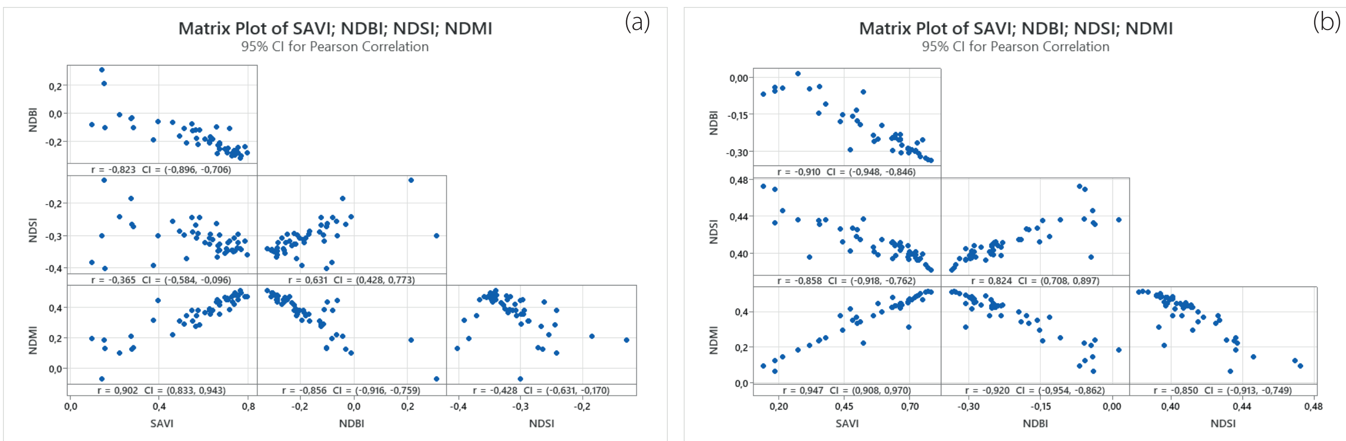

Source: Primary data processing

Fig. 3. Correlations among four parameters

Ecological Quality Classification and Spatial Change from 2018 to 2021

In Pekanbaru City, the ecological quality is generally higher in the suburbs and lower in the center/core area. Areas with poor environmental quality are becoming more common, particularly in the center of Pekanbaru. Meanwhile, decent environmental quality continues to degrade and is mostly found on the outskirts of Pekanbaru (Fig. 4).

The classification of the ecological index utilizing remote sensing is divided into five sorts of landscapes: poor, fair, moderate, good, and excellent. In this study, the images were classed into five levels of ecological quality based on the mean and standard deviation. (Fig. 5) and (Table 3) present the results of the ecological quality classification in Pekanbaru City from 2018 to 2021. Based on the processed data, there was a considerable decrease in the value of the ecological quality index Between 2018 and 2021, there was an increase in the proportion of 0.212% with an area

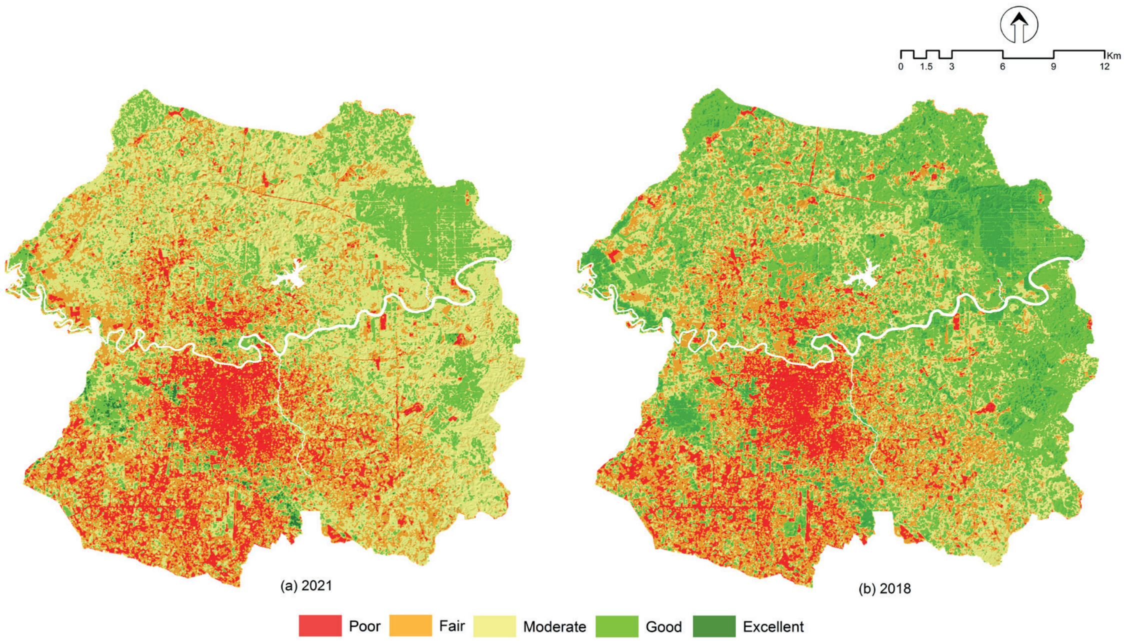

Fig. 4. Ecological index changes of Pekanbaru

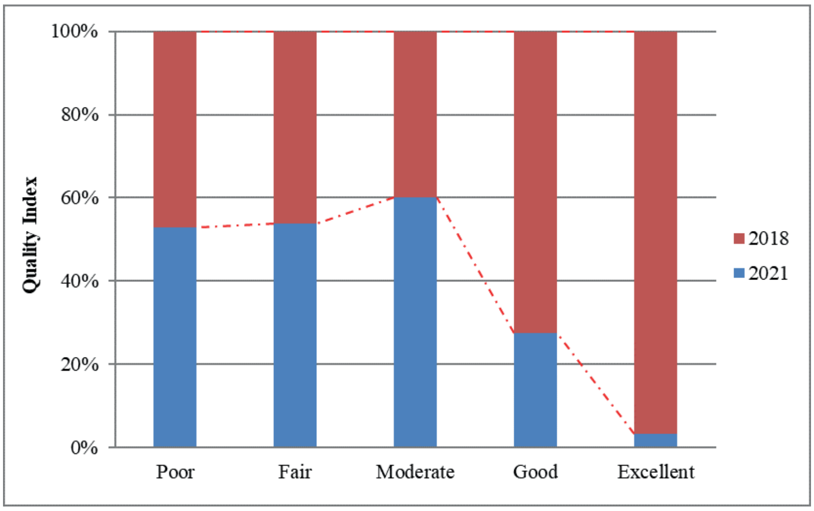

Fig. 5. Percentage accumulation chart of ecological index

Table 3. Remote sensing ecological index calculation based on Landsat 8 OLI

Quality Index	2021		2018	
	Area (Km^2)	Percentage (%)	Area (Km^2)	Percentage (%)
Poor	137	21.2	122	19
Fair	192	30.3	164	26.3
Moderate	249	38.9	165	25.5
Good	61	9.4	161	24.9
Excellent	1	0.2	28	4.3

Source: Primary data processing

of 137 km^2 in the category of poor ecological quality from the initial proportion of 0.190% with an area of 122 km^2 in 2018. Meanwhile, the proportion of the excellent category declined significantly from 0.043% with an area of 28 km^2 to 0.002% with an area of just 1 km^2.

DISCUSSION

The advantages of remote sensing can depict the ecological quality of the area at amicro level, and the spatial distribution of the ecological index through remote sensing can aid in understanding environmental ecological patterns. The analysis results of the four ecological index indicators via remote sensing and PC1 correlation have a high contribution rate of eigenvalues exceeding 90% in 2021. This study framework is oriented toward assessing changes in ecological configurations in urban areas through site-specific implementation, optimizing multi-temporal remote sensing data to understand changes in ecological landscapes in a sustainable manner.

Utilizing spatial and temporal characteristics of ecological status is crucial for enhancing accuracy and efficiency in assessment and monitoring. Several studies have developed design concepts using ecological indicators, diverse parameters, and systematic models to evaluate changes in ecological landscape configuration. This research is of great importance for developing an efficient model using a remote sensing approach for urban ecological quality assessment. This study derives from four various environmental parameters that can guide a simple, comprehensive ecological quality assessment. All the various parameters for the ecological quality index are easily available and applicable to other regions, facilitated by different databases. The ecological quality index needs four environmental parameters as an assessment input; all parameters are constructed from remote sensing data (Table 1). Overall parameters can be quickly calculated with Landsat images, and the urban ecological index is a key application of ecology from remote sensing.

The study discovered that the ecological condition in the Pekanbaru area had degraded over three years (Fig.4). This degradation is evidenced by a decrease in the vegetation index and normalized soil fluctuations, while SAVI, which mitigates the loss of vegetation index response, remains ineffective in altering vegetation canopy measurements (Indrawati et al. 2020). According to the correlation results, the SAVI indicator reflects the influence of surface vegetation on the ecological environment, specifically humidity and vegetation cover on soil quality, as well as the expansion of human activities as seen through changes in landscape use. The two indicators are negatively correlated, suggesting that the surface of vacant or construction landis not vast enough to harm the ecological environment. However, local climatic conditions (such as surface temperature and air humidity) are positively correlated in responding to environmental changes that occur and cause damage to the ecological environment. The indicators of ground surface moisture and heat were represented respectively by moisture and land surface temperature, which reveal climate changes responding to the ecosystem state alterations (Yue et al. 2019). Environmental quality is generally higher in the suburbs and lower in the city center or core area, with poor environmental quality becoming more common, especially in the Pekanbaru city center. Conversely, the "good" environmental quality category continues to deteriorate and is found mainly in the periphery of Pekanbaru. This shows how certain human activities harm the surrounding natural environment. As the impact of human activities on the natural environment increases, the complexity of the changes that occur intensifies.

The green indicator parameter represented by SAVI is employed in this study to measure the ecological state before and after changes in anthropogenic land surface functions. Meanwhile, humidity and building density are represented by NDMI and NDBI values, respectively, revealing climatic change as a response to changes in existing ecosystem circumstances. (Zhang et al. 2020) conducted a similar study with the same variables with the addition of land surface temperature. The utilization of results from the urban ecological quality index is rational and effective. This finding gives information about the dynamics of the environment from four ecological parameters, and the urban ecological quality evaluation index is expressed by the ecological index. Furthermore, the urban ecological quality index can be considered a four-aspect condition of urban ecology (such as soil condition, moisture, greenery, and human activities), a guide effective in helping a selected parameter with the assumption of ecological existence, and a tool to assess or evaluate the quality of urban ecology comprehensively.

There are some limitations to the assessment of the urban ecological quality index. Firstly, the medium-resolution data quality deteriorates information accuracy, necessary for the calculation of the ecological quality index. Regarding complex urban surface conditions using high-quality data (hyperspectral and high-resolution spatial imagery) provides more accurate information. Next, the observation time is relatively short, and it is necessary to conduct a long-term study, for instance of about 20 years. Such study will better explain the drivers that influence the ecological landscape dynamics by involving the factors (hydro climatology, anthropogenic influence, social economics, community mobility, and land use planning) that aim to determine the impact of surface activities. A combination of multiple remote sensing data sources, statistical data, geospatial data, and big data based on open sources can provide various types of data for research. Finally, the effect composition of the thermal environment should be studied in other metropolitan areas for proper decision-making in the management and protection of the sustainable ecological environment.

CONCLUSIONS

The results of the study obtained using the urban ecology approach revealed that the deteriorating trend. This is inextricably linked to the role of human land use in urban development, as well as the current state of land characteristics represented by soil index, moisture, and vegetation distribution. Given the complexity of the urban environmental system influenced by anthropogenic activities, research involving a longer time span is necessary to comprehensively understand the ecological spatial patterns. This condition has the potential to reduce the ecological index over the last three years while increasing the number of poorly categorized zones. The future handling required to be able to comprehend this challenge and establish a sustainable development concept that cares about the natural landscape, particularly in urban areas, as a kind of ecological harm anticipation and control. Further research is also needed to better understand the effects of ecological composition on the thermal environment in various situations and metropolitan areas.

REFERENCES

Amri S.N., Adrianto L., Bengen D.G. and Kurnia R. (2017). Spatial Projection of Land Use and Its Connection With Urban Ecology Spatial Planning in the Coastal City, Case Study in Makassar City, Indonesia. International Journal of Remote Sensing and Earth Sciences (IJReSES), 14(2), 95–110. DOI: 10.30536/j.ijreses.2017.v14.a2715

Bobby Rahman M., Nurhasanah I.S., Nugraha E. and Harahap T. (2019). Applying the Urban Political ecology (UPE) Framework to Re-Visit Disaster and Climate change Vulnerability-Risk Assessments. Journal of Regional and City Planning, 30(3), 224–240. DOI: 10.5614/jpwk.2019.30.3.4

BPS. (2021). Hasil Sensus Penduduk 2020 Kota Pekanbaru.

Chen Y., Gong A., Zeng T. and Yang Y. (2020). Evaluation of water conservation function in the Xiongan New Area based on the comprehensive index method. PLoS ONE, 15(9), 1–19. DOI: 10.1371/journal.pone.0238768

Deng Y., Wu C., Li M. and Chen R. (2015). RNDSI: A ratio normalized difference soil index for remote sensing of urban/suburban environments. International Journal of Applied Earth Observation and Geoinformation, 39, 40–48. DOI: 10.1016/j.jag.2015.02.010

Gao B.-C. (1995). Normalized Difference Water Index for Remote Sensing of Vegetation Liquid Water from Space. Proc. SPIE, 225–236.

Gao Y.G., Li Y.H. and Xu H.Q. (2022). Assessing Ecological Quality Based on Remote Sensing Images in Wugong Mountain. Earth and Space Science, 9(e2021EA001918), 1–22. DOI: 10.1029/2021EA001918

Giofandi E.A. and Sekarjati D. (2020). Persebaran Fenomena Suhu Tinggi melalui Kerapatan Vegetasi dan Pertumbuhan Bangunan serta Distribusi Suhu Permukaan. Jurnal Geografi : Media Informasi Pengembangan Dan Profesi Kegeografian, 17(2), 56–62. DOI: 10.15294/jg.v17i2.24486

Giofandi E.A., Sekarjati D. and Riyadhno F.A. (2020). Pemantauan Dan Mitigasi Tingkat Potensi Bencana Kekeringan Di Kota Dumai. GEOGRAPHY: Jurnal Kajian, Penelitian Dan Pengembangan Pendidikan, 8(2), 88–97.

Hao H., Lian Z., Zhao J., Wang H. and He Z. (2022). A Remote-Sensing Ecological Index Approach for Restoration Assessment of Rare-Earth Elements Mining. Computational Intelligence and Neuroscience, 2022, 1–14.

Huete A.R. (1988). A Soil-Adjusted Vegetation Index (SAVI). Remote Sensing of Environment, 25, 295–309.

Hui J., Bai Z. and Ye B. (2021). Eco-Environment Evaluation of Grassland Based on Remote Sensing Ecological Index : A Case in Hulunbuir Area , China. Journal of Computer and Communications, 9, 203–213. DOI: 10.4236/jcc.2021.96012

Indrawati L., S S.H.M.B. and Rachmawati R. (2020). Integrated ecological index (IEI) for urban ecological status based on remote sensing data : a study at Semarang – Indonesia. IOP Conf. Series: Earth and Environmental Science, 1–9. DOI: 10.1088/1755-1315/500/1/012074

Jiang Y., Jia D., Li K. and Zhao C. (2020). Remote Sensing Evaluation of Urban Ecological Changes in Arid Region Oasis: A Case Study in Liangzhou District of Wuwei, Chin. IOP Conf. Series: Earth and Environmental Science, 1–9. DOI: 10.1088/1755-1315/546/3/032011

Lian Z., Hao H., Zhao J., Cao K., Wang H. and He Z. (2022). Evaluation of Remote Sensing Ecological Index Based on Soil and Water Conservation on the Effectiveness of Management of Abandoned Mine Landscaping Transformation. International Journal of Environmental Research and Public Health, 19(9750), 1–15.

Liao W. and Jiang W. (2020). Evaluation of the Spatiotemporal Variations in the Eco-environmental Quality in China Based on the Remote Sensing Ecological Index. Remote Sensing, 12(2462), 1–18.

Liu Q. and Shi T. (2019). Spatiotemporal Di ff erentiation and the Factors of Ecological Vulnerability in the Toutun River Basin Based on Remote Sensing Data. Sustainability, 11(4160), 1–19.

Muhlisin, Iskandar J., Gunawan B. and Cahyandito M.F. (2021). Vegetation diversity and structure of urban parks in Cilegon City, Indonesia, and local residents' perception of its function. Biodiversitas, 22(7), 2589–2603. DOI: 10.13057/biodiv/d220706

Safitri Y. and Giofandi E.A. (2019). Pemanfaatan Citra Multi Spektral Landsat OLI 8 dan Sentinel-2A (Studi Kasus : Cagar Alam Rimbo Panti , Pasaman). Swarnabhumi, 4(2), 115–121.

Shi F. and Li M. (2021). Assessing Land Cover and Ecological Quality Changes under the New-Type Urbanization from Multi-Source Remote Sensing. Sustainability, 13(11979), 1–21.

Sun C., Li X., Zhang W. and Li X. (2020). Evolution of Ecological Security in the Tableland Region of the Chinese Loess Plateau Using a Remote-Sensing-Based Index. Sustainability, 12(3489), 1–17.

Sun L., Yu Y., Gao Y., He J., Yu X. and Malik I. (2021). Remote Sensing Monitoring and Evaluation of the Temporal and Spatial Changes in the Eco-Environment of a Typical Arid Land of the Tarim Basin in Western China. Land, 10(868), 1–18.

Wang J., Li G. and Chen F. (2022). Eco-Environmental Effect Evaluation of Tamarix chinesis Forest on Coastal Saline-Alkali Land Based on RSEI Model. Sensors, 22(5052), 1–19.

Wang X., Liu C., Fu Q. and Yin B. (2018). Construction and Application of Enhanced Remote Sensing Ecological Index. The International Archives of the Photogrammetry, Remote Sensing and Spatial Information Sciences, XLII–3, 1809–1813.

Wiyono J. and Sunarto. (2016). Regional Resource Management Based on Landscape Ecology in Northern Muria Peninsula, Central Java. Indonesian Journal of Geography, 48(1), 57–64. DOI: 10.22146/ijg.12467

Xu H., Wang Y., Guan H., Shi T. and Hu X. (2019). Detecting Ecological Changes with a Remote Sensing Based Ecological Index (RSEI) Produced Time Series and Change Vector Analysis. Remote Sensing, 11(2345), 1–24.

Yu J., Li X., Guan X. and Shen H. (2022). Geo-spatial Information Science A remote sensing assessment index for urban ecological livability and its application. Geo-Spatial Information Science, 1–22. DOI: 10.1080/10095020.2022.2072775

Yue H., Liu Y., Li Y. and Lu Y. (2019). Eco-Environmental Quality Assessment in China 's 35 Major Cities Based On Remote Sensing Ecological Index. IEEE Access, 7, 51295–51311. DOI: 10.1109/ACCESS.2019.2911627

Zha Y., Gao J. and Ni S. (2003). Use of normalized difference built-up index in automatically mapping urban areas from TM imagery. International Journal of Remote Sensing, 24(3), 583–594. DOI: 10.1080/01431160304987

Zhang X., Xie H., Shi J., Lv T., Zhou C. and Liu W. (2020). Assessing changes in ecosystem service values in response to land cover dynamics in jiangxi province, china. International Journal of Environmental Research and Public Health, 17(3018), 1015. DOI: 10.3390/ijerph17093018

Zheng X., Zou Z., Xu C., Lin S., Wu Z., Qiu R., Hu X. and Li J. (2022). A New Remote Sensing Index for Assessing Spatial Heterogeneity in Urban Ecoenvironmental-Quality-Associated Road Networks. Land, 11(46), 1–16.

RESEARCH PAPER

NUMERICAL HYDRODYNAMIC MODELLING AS A TOOL FOR RESEARCH AND USE OF TIDAL RIVERS

Evgeniya D. Panchenko[1,2*], Andrei M. Alabyan[2,1], Tatiana A. Fedorova[1]
[1] Water Problems Institute of RAS, Gubkina str., 3, 117971, Moscow, Russia
[2] Lomonosov Moscow State University, Leninskie Gory, 1, 119991, Moscow, Russia
*Corresponding author: panchenko.zhe@gmail.com
Received: November 16th, 2023 / Accepted: December 12th, 2023 / Published: March 31st, 2024
https://DOI-10.24057/2071-9388-2023-3122

ABSTRACT. Tidal estuaries play a crucial role, serving as major hubs for economic activities while also contributing to the preservation of natural diversity and bioproductivity. In Russia, these estuaries are primarily located in remote regions of the European North and the Far East, making them vital for energy and transportation usage as they essentially form the 'cores' of territorial development along the Northern Sea Route.

To facilitate the development of energy and navigation infrastructure in tidal estuaries, as well as to plan and implement environmental protection measures, it is essential to have a comprehensive understanding of their hydrological regime. Unlike regular river flow, tidal estuaries exhibit more complex hydrodynamics, influenced by both river and marine factors. Due to the considerable challenges of conducting field hydrological studies in remote areas, numerical hydrodynamic modelling has emerged as a valuable method for obtaining information on the flow and water level regime in tidal estuaries. This paper presents an application of one-dimensional HEC-RAS and two-dimensional STREAM_2D CUDA numerical models to investigate the parameters of reverse currents in the hypertidal Syomzha estuary flowing into the Mezen Bay of the White Sea. The limitations and accuracy of the models are discussed, along with the potential for their improvement considering recent advancements in understanding the hydraulics of reverse currents.

KEYWORDS: tidal estuary, reverse current, energy potential, mathematical model, White Sea, Syomzha river

CITATION: E. D. Panchenko, A. M. Alabyan, T. A. Fedorova (2024). Numerical Hydrodynamic Modelling As A Tool For Research And Use Of Tidal Rivers. Geography, Environment, Sustainability, 1(17), 36-43
https://DOI-10.24057/2071-9388-2023-3122

ACKNOWLEDGEMENTS: The authors are grateful to the participants of fieldwork – N.A. Demidenko, M. Leummens, L. Leummens, A. Popryadukhin, E. Fingert.

The work was supported by Russian Science Foundation project №22-29-01184, https://rscf.ru/project/22-29-01184/.

Conflict of interests: The authors reported no potential conflict of interest.

INTRODUCTION

Estuaries have always been important to people as transport links between the sea and river, providing shelter for sailors, recreation opportunities, and resources for fishing and hunting. The flora and fauna of estuarine areas are incredibly diverse; fertile soils, flat terrain, and abundant freshwater resources offer excellent potential for agriculture. Hence it is no surprise that some of the world's most densely populated coastal areas are located near estuaries, and it is even more pronounced along the Russian Arctic coast, where all major cities and essential towns are situated at the mouths of large or small rivers. In addition, in the case of tidal estuaries, the problem of energy supply even to remote settlements can be successfully solved owing to the development of several innovative solutions for the use of tidal energy (Khare et al. 2019; Neill and Hashemi 2018). The modern designs of in-channel units that do not require the construction of dams and barrages make tidal power plants even more economical and environmentally friendly.

At the same time, settlements along estuarine shores are not without their challenges and can face specific hazards, such as storm-surge floods or brackish water intrusions into water intakes. Navigational conditions in estuarine aquatories, especially in tidal ones, can significantly differ from those in rivers and the open sea due to reverse tidal currents and unpredictable channel deformations caused by intensive sediment transport. Estuarine hydrodynamics play a crucial role in shaping these natural processes, influenced by river and marine characteristics.

Tidal estuaries exhibit the most complex hydrodynamic features, which are characterized by rapid variations of flow structures and properties during the tidal cycle. Although essential estuarine hydrodynamics is well explained with field surveys and conceptual mathematical descriptions (Mikhailov 1971; McDowell and O'Connor 1977; Savenije 2012; Hoitink and Jay 2016), collecting high-resolution spatial and temporal data along the entire estuary from the river mouth to the adjacent section of the tidal river reach is laborious, time-consuming, and expensive (Miskevich et.al. 2018b; Veerapaga 2019). In many cases, numerical models offer the most effective alternative for complicated field campaigns and comprehensive analyses of the hydrodynamic measurements (Abreu et.al. 2020; Matte et.al. 2017).

Worldwide, a large number of hydrodynamic models of estuaries have been developed both for various economic purposes and to address different scientific questions (Alabyan et.al. 2022). These estuarine models are used to study the interaction of river flow with tidal and surge waves, to forecast floods and other hazards (Zheng et.al. 2020; Lyddon et.al. 2018; Ward et.al. 2018), and to assess the impact of current and expected climate change on estuarine flow dynamics (Chen et.al. 2015; Iglesias et.al. 2022; Panchenko et.al. 2020b; Anh et.al. 2018). Some models are specifically developed for monitoring estuarine processes such as salt intrusion (Mills et.al. 2021; Chen et.al 2015; Veerapaga et.al. 2019) and sediment transport (Jiang et.al. 2013; Yin et.al. 2019; Rahbani 2015). Hydrodynamic modelling is also used to determine optimal locations for the construction of engineering structures, to study currents for tidal energy utilization (Rtimi et.al. 2021), and to ensure favorable conditions for navigation (Jouanneau et.al. 2013).

While these models often reproduce the general features of the hydrodynamic regime, there can be significant quantitative differences between the modelling results and actual flow parameter values. Every model simplifies reality and comes with its strengths and weaknesses. Therefore, modelling results have a wide range of uncertainties related to errors, calibration parameters, model assumptions, and approximations used for initial conditions and forcing characteristics (Iglesias et.al. 2022; Khanarmuei et.al. 2020). Sometimes it is difficult to understand the main factor affecting modelling quality. Part of the errors stem from inaccuracies in channel and floodplain topography and boundary conditions (Khanarmuei et.al. 2020; Matte et.al. 2017), which, in turn, are linked to the practical difficulties of carrying out fieldwork in large estuaries and obtaining the full set of field data necessary for model construction and calibration.

The model dimensioning (1D, 2D or 3D) is still problematic and questionable (Samarasinghe et.al. 2022; Veerapaga et.al. 2019), depending on the research purpose, the object size and geometry, and the availability and accuracy of field data. When the primary aim of a study is to analyze changes in the hydrodynamic characteristics along a small tidal river, and the length of the study area exceeds the river width by two orders or more, it is preferable to use one-dimensional (1D) models. Such models require significantly fewer measurement data and less computational power and time for calculations compared to two-dimensional (2D) and three-dimensional (3D) models. Moreover, in a small estuary, owing to its size and relatively simple morphology and bed topography, it is possible to obtain highly accurate field data, allowing us to assess the actual capabilities of hydrodynamic models and to analyze the factors contributing to modelling errors.

Previously, estuarine hydrodynamics of small tidal rivers was investigated using one-dimensional models in the White Sea region, where tidal wave heights can vary from less than 1 m in the Laya River (a Northern Dvina delta branch tributary) to 9 m in the Syomzha River (a Mezen estuary tributary) (Panchenko 2023). For the hypertidal Syomzha estuary, differences between measured and modeled values of high and low water levels, as well as flood and ebb water discharges, ranged from 10 to 20%, even with high-accuracy bathymetry and boundary data available (Panchenko and Alabyan 2022). Similar results were reported by(Mohammadian et.al. 2022) for a 3D model of a hypertidal estuary, where despite accurate boundary conditions based on in-situ measurements, the best water level calibration results were of the same order of inaccuracy. This was attributed to the fact that hypertidal estuaries are characterized by extremely high variations in tidal depths over ebb-flood cycles, caused by significant spatial flow variations and interactions of complex currents with bathymetric features.

Previous research on the large mesotidal Onega estuary (Panchenko et.al. 2020c), undertaken on the background of reliable field data, demonstrated good agreement of 1D model calculations with both results of the 2DH (depth-averaged 2D model) and measured values of water levels and flow parameters, only when focusing on averaged values across the cross-section. This research aims to compare 1D and 2DH modelling results for a very different environment – the small hypertidal estuary – where all hydrodynamic processes are much more rapid and pronounced throughout the tidal cycle. The Syomzha estuary was selected as the research object, with fieldwork held in the summer low water periods of 2015 and 2018 to ensure a sufficient dataset for model construction, calibration and validation (Panchenko et.al. 2020a; Panchenko and Alabyan 2022).

MATERIALS AND METHODS

The study area

The study object is the Syomzha estuary. The Syomzha River meets the Mezen estuary near its mouth (Fig.1, 2). The Syomzha is 63 km long and has a catchment area of 490 km^2. The average slope of the river is 0.61‰, and the average slope of the estuary bottom is three times less at 0.26‰. There are no gauging stations along the river, but estimates suggest that an average summer low-water river runoff is about 5 m^3/s, with a maximum spring snow-melt flood discharge of 5% probability reaching around 200 m^3/s, nearly equivalent to the maximum flood and ebb tidal flow at the river mouth during the low-water period.
The tide in the White Sea is semidiurnal of regular sinusoidal shape in the open sea. At the Syomzha mouth, the spring tidal range exceeds 8.5 m, increasing relative to the open sea due to the confusor effect along the narrowing Mezen Bay and the Mezen estuary. Under summer low-water conditions, the tidal stretch of the river spans approximately 23–25 km, constituting roughly one-third of the total river length.

In lower cross-sections, the maximum flow depth fluctuates between 1 and 10 m, with the river bed primarily composed of loess and mud, while sand and gravel accumulative forms concentrate along the dynamic axis of the tidal currents. The tidal wave decreases in height upstream to approximately 5–6 m at 4 km and 3–4 m at 8 km.

The river channel is characterized by a meandering pattern. The width of the estuary changes significantly during the tidal cycle. At the mouth, it widens to 90 m at high water and contracts to 30 m at low water (Fig. 2). Further upstream, the range of river width and depth tidal oscillation declines, along with the corresponding decrease in tidal wave height. At 10 km upstream from the mouth, the channel width ranges from 20 to 30 m, and at 21 km, it narrows to 10–15 m regardless of the tidal cycle phase. The depth at low tide averages around 0.8 meters, dropping to 0.3–0.5 m at gravel ripples and rising to 1.5–2.0 m in pools.

The methodology

To explore the hydraulic regime of the Syomzha estuary and to gather the necessary data for numerical modelling, field campaigns were carried out in August

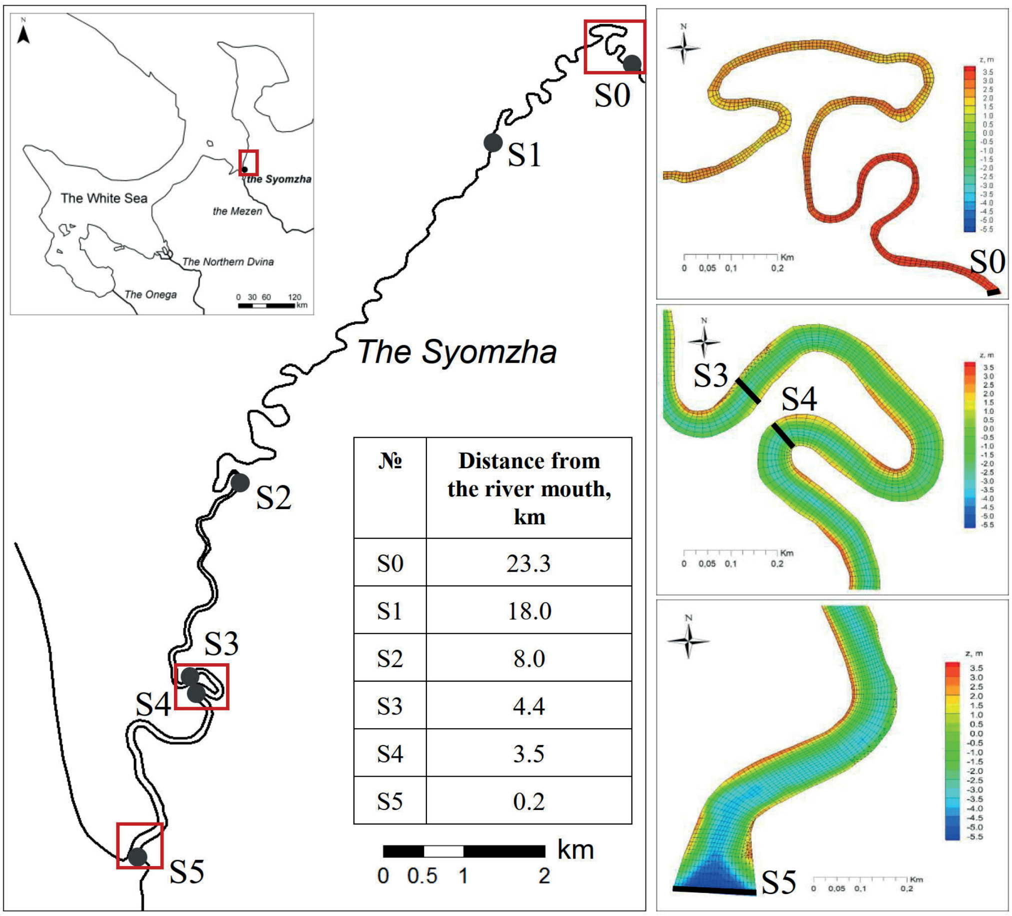

№	Distance from the river mouth, km
S0	23.3
S1	18.0
S2	8.0
S3	4.4
S4	3.5
S5	0.2

Fig. 1. Location of the study area and the Syomzha River section under modelling with enlarged fragments of key sections

Fig. 2. The Syomzha River mouth at (a) high and (b) low water

2015 and August 2018. These measurements took place during the summer low-flow period when the river runoff was around 5–7 m^3/s. In 2015, water levels were recorded by barometric loggers at points S1, S2, and S5 (Fig. 1), while flow measurements with an Acoustic Doppler Current Profiler (ADCP) were undertaken at S2, specifically during flood flow (not covering the full tidal cycle). Tidal water level oscillations were deemed negligible at point S0.

The 2018 surveys were more extensive: water levels were measured at five points (S1–S5) with the unified zero-mark, and runoff and flow velocity were measured with two ADCPs concurrently at cross-sections S3 and S4 throughout the entire tidal cycle (Panchenko et.al. 2020a; Panchenko and Alabyan 2022). Simultaneously, a bottom relief survey was undertaken together with an examination of brackish water intrusion from the Mezen estuary and its mixing with the freshwater of the Syomzha River.

The obtained data on the detailed channel bathymetry served as the foundation for the digital elevation model (DEM) used in both the 1D and 2DH hydrodynamic models. Non-stationary low boundary conditions for the models were formed based on records from a level logger located at the lowest point, S5. The upper boundary condition was a stationary inflow discharge of 7 m^3/s at point S0, located 23.5 km upstream from the mouth, where the flow dynamics is no longer affected by sea level tidal oscillations. The HEC-RAS software (Brunner 2016), solving the full one-dimensional Saint-Venant equations, was used for 1D modelling of the hydrodynamic regime of the Syomzha estuary. The geometry cross-sections in the 1D model were defined with a step of 100–150 m (147 cross-sections in total).

The 2DH model was developed using the STREAM 2D CUDA package, based on shallow water equations and their numerical solution for shallow water flows with shoaling areas and bottom discontinuities (Aleksyuk and

Belikov 2017a,b). The mesh of 2DH model consisted of 17,602 rectangular cells with varying sizes, ranging from 10 to 20 m in length and 5 m in width. The bottom bathymetry in both models was kept consistent.

The calibration of the 1D and 2D models was conducted for the hydrological situation during two tidal cycles of August 13–14, 2018. The only calibrating parameter for both models was the Manning's roughness coefficient. By adjusting its values along the river sections, the goal was to achieve the best model results compared to measured water levels and discharges. The data collected on August 6, 2015, were used to validate the models (model test on the independent dataset not used for the calibration routine).

RESULTS

Following the calibration routine of both models, the Syomzha River stretch covered by the modelling was divided into three zones with varying roughness coefficient values: 1) n = 0.015 up to 5 km from the mouth cross-section; 2) n = 0.02 between 5 and 10 km; 3) n = 0.03 upstream of 10 km. This division enabled the attainment of realistic results for all measurement sites in terms of both water level and flow oscillations during the tidal cycle (Fig.3, 4), as well as facilitated the termination of water level fluctuations at the upper boundary of the model.

Following the calibration, both the 1D and 2D models showed nearly identical results in terms of predicted water levels (Fig. 3). At the S4 location, the actual range of water level changes was 6.2 m, whereas in the 1D model, it was 5.8 m, and in the 2D model it was 5.7 m (with modeled ranges being 6–8% lower). At the same time, at the S4 location, where the measured tidal range was 3.72 m, the modeled value in both models was 3.12 m (15% less). At the S1 location, the measured range was 1.1 m, while the simulated ranges were 1.05 m and 0.9 m in the 1D and 2D models, respectively.

At S2, the minimum water levels before the tidal rise were modeled with high accuracy (2–5 cm difference), but the maximum water level in the models was lowered by more than 0.5 m (Fig. 3, b). The modeled maximum level nearly coincided with the maximum level set at the lower boundary. However, according to the measurement data from both expeditions, the maximum water level in this section exceeded the maximum at the lower boundary by about 0.8 m.

Conversely, ebb water levels were less accurately modeled at locations S3 and S4. At S4, ebb water levels in the models were overestimated relative to actual levels by 0.54 and 0.78 m (1D and 2D, respectively), while the maximum levels differed only by 0.18 m. Although the difference in tidal range did not exceed 15% at S4, the difference in minimum levels was significant and comparable with the low water depth at the cross-section (Fig. 3, a). Nonetheless, this inaccuracy is not of critical importance when analyzing the pattern of tidal wave propagation and transformation.

The timing of tidal peaks and troughs was reproduced quite accurately by both models, with a difference of no more than 10 minutes in all locations (which is comparable to the accuracy of visually registering the time of a current slowing down at the beginning of the tide). In other words, the tidal propagation velocity was modeled very accurately. At calibration points S3 and S4, changes in water discharges during the tidal cycle were closely reproduced by both models (Fig. 4), but the difference between 1D and 2D results increased with distance from the lower boundary. The ebb discharge during the tide was accurately computed by both models. For peak flood and ebb discharges, the difference between measured and modelled values at both locations did not exceed 30 m^3/s, which was less than 10% of the discharge range.

The availability of measured water levels and discharges for another period during the summer of 2015 allowed for the validation of the selected roughness characteristics on

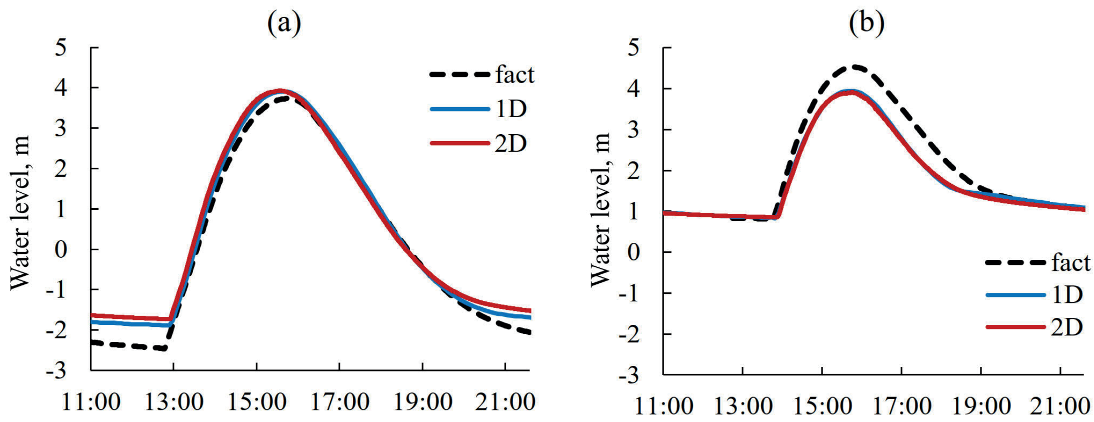

Fig. 3. Model calibration results: water levels at (a) the S4 location; (b) the S2 location on August 14, 2018

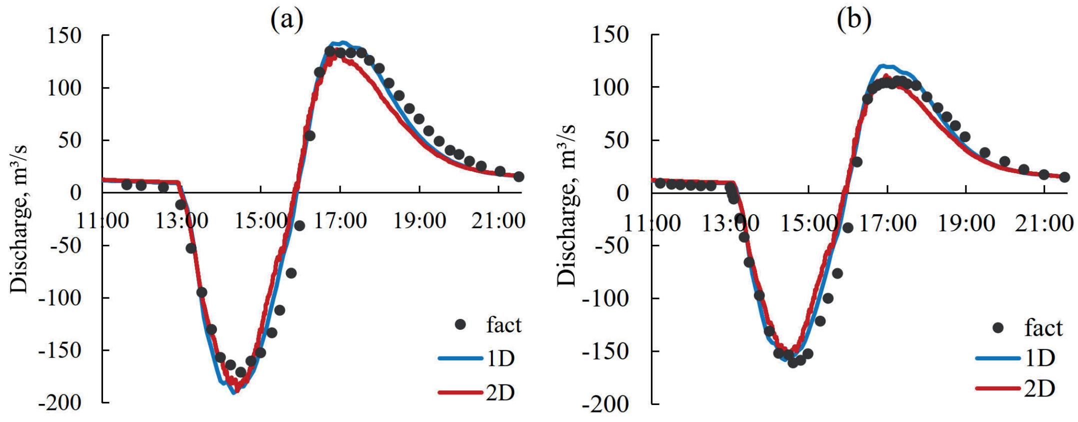

Fig. 4. Model calibration results: discharges at (a) the S4 location; (b) the S3 location on August 14, 2018

independent data. A pattern similar to what was observed during the calibration process can also be seen for the model validation.

At the S2 location, the measured tidal range was 3.07 m, and the simulated ranges were 2.43 m and 2.36 m in 1D and 2D, respectively (the modeled values were 20 – 23% lower) with the largest difference for the maximum level (Fig. 5). The times of the maximum flood tide discharge (negative value) and current reversal during tide at S2 were accurately predicted by both models. However, both models underestimated the value of the peak flood discharge: 46.6 m^3/s and 39.7 m^3/s for the 1D and 2D models, respectively, compared to the measured 56 m^3/s.

The slightly better results of the 1D model compared to the 2D one can be explained by the fact that the calibration was performed on the one-dimensional model, and the selected roughness values were used in both cases. If there were enough field data to calibrate the 2D model, this contradiction could be eliminated.

The tidal wave propagation celerity was 1.3 m/s between points S2 and S5 and 1.5 m/s between points S1 and S2, which corresponded to reality for both models.

Thus, we can assume that in cases where it is necessary to calculate flow characteristics averaged over the cross-section of the channel, the use of a one-dimensional model is preferable since it has an accuracy that is at least no less than that of a two-dimensional model and requires much less labor and machine time.

The use of a two-dimensional model provides an advantage when analyzing changes in the flow velocity spatial distribution during the tidal cycle. For instance, in Fig. 6, an example is presented of how, at the same water discharge of 100 m^3/s (in different directions), the flow concentrates along its dynamic axis as the tidal flood and ebb currents develop.

Such an analysis may be necessary when calculating the trajectories of sediment and pollutants, bed deformations, and projecting the location and design of water intakes and dispersing water outlets. Of particular interest is the velocity field of the slack water period when the water masses do not stand still, but form a complex system of large-scale eddies, constantly transforming and migrating across the water area (Fig. 7).

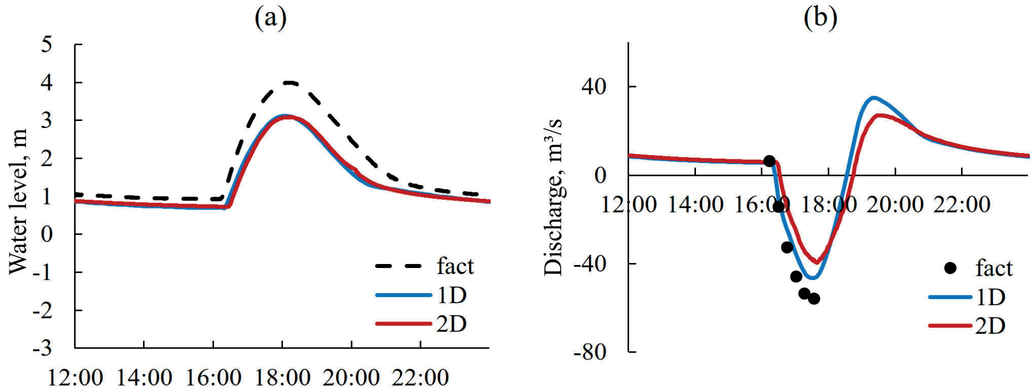

Fig. 5. Model validation results: (a) water levels and (b) discharges at the S2 location on August 6, 2015

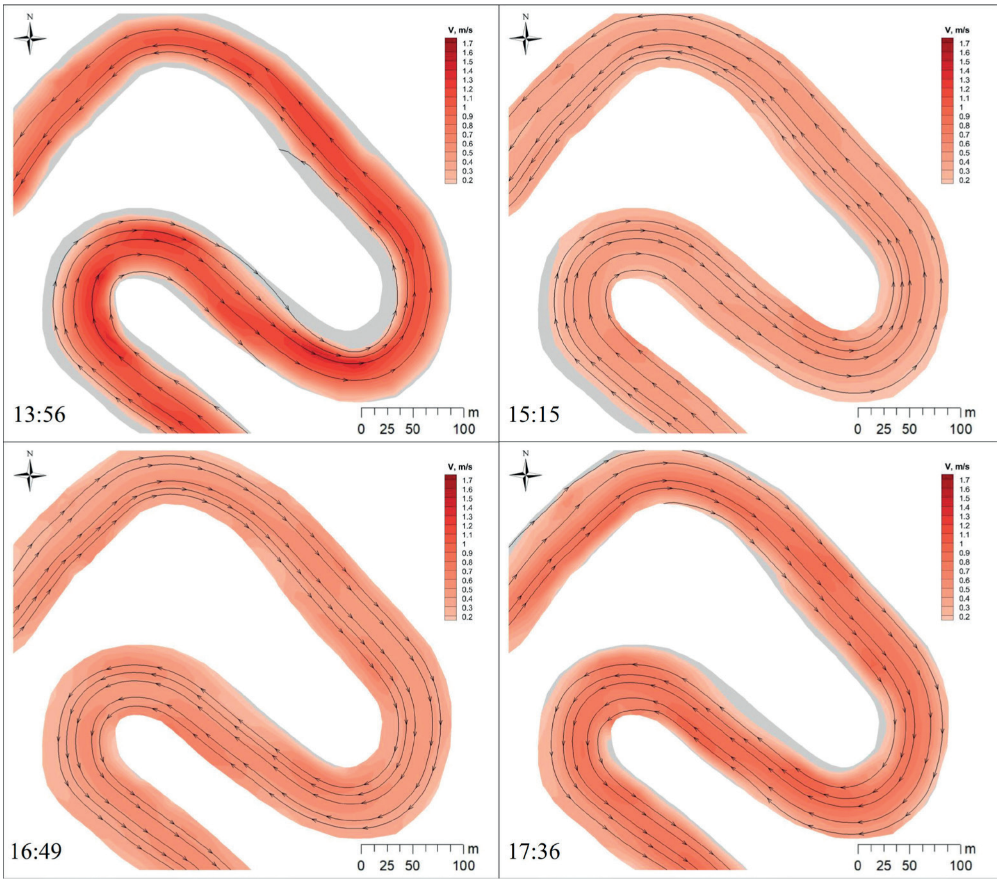

Fig. 6. 2D simulated flow velocity spatial distribution on August 14, 2018

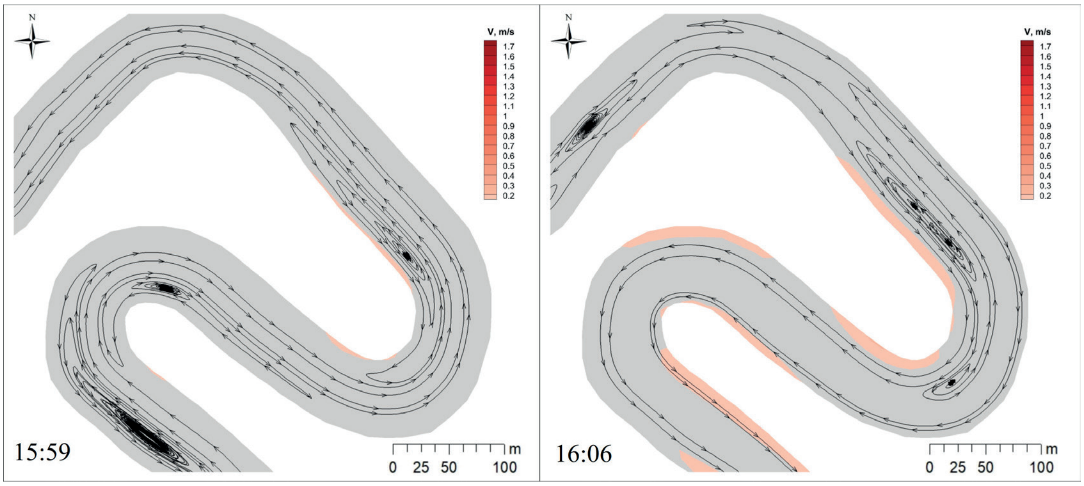

Fig. 7. 2D simulated flow velocity fields near slack water on August 14, 2018

DISCUSSION

The use of numerical hydrodynamic models to study the regime of the hypertidal Syomzha estuary made it possible, based on point hydrological measurements, to demonstrate a continuum picture of hydrodynamic processes throughout the full tidal cycle along the estuary. At the same time, the results of field measurements were used to calibrate and validate the models.

The transformation pattern of the tidal wave, as well as the order of occurrence of water level and flow peaks during the tidal cycle on the Syomzha, are quite consistent with the main patterns established on other tidal rivers during similar, but more detailed and lengthy field measurements (Miskevich et.al. 2018a, Panchenko et.al. 2020). The modelling inaccuracies may be associated both with the insufficient detail of the bottom relief pattern and with the underestimation of some features of the reverse flow hydraulics identified in recent studies (Panchenko and Alabyan 2022). The possibility of taking into account changeable hydraulic resistance and eddy viscosity when modelling may represent a way to improve the reverse flow simulation results. Since the river runoff in August 2018 was comparable to the inaccuracy in tidal flow modelling, its influence can be considered insignificant, at least for the summer low-water period.

On a tidal estuary, during semidiurnal tides during low water, the direction of the river flow changes four times a day. In this case, the values of maximum water flow rates at high and low tides can be quite comparable with the flow rate of spring floods caused by snowmelt. Unlike snowmelt and rain floods, tidal floods repeat with a certain periodicity, determined solely by astronomical factors. Their predictability is an important positive aspect when planning and carrying out activities related to ensuring safe navigation and fishing, the operation of water intakes and dispersing water outlets, as well as other activities related to the sustainable use of water resources. Since tides are more predictable than the wind and the sun, tidal power is considered to be the most preferable renewable energy source in the environment of the Russian Arctic and Far East. Even on such a small river as the Syomzha, a chain of in-channel units, switched on as the tidal wave passes, can provide a stable energy supply to the surrounding area.

CONCLUSIONS

Both one-dimensional and two-dimensional models can be successfully used to study the regime of tidal rivers: determining the tidal wave celerity and transformation when propagating upstream, the time of high and low water, and the moment of slack water and current reversal; maximum tidal flood and ebb flow at different distances from the river mouth are less accurately reproduced, but with an acceptable accuracy of about 20%. The advantage of a one-dimensional model is that it requires less labor to prepare the initial data and significantly reduces computer calculation time. The use of two-dimensional models is necessary in cases where the research object is not only the flow parameters averaged over the cross-section but also their distribution over the channel width and the aquatory as a whole. A necessary condition for the use of numerical hydrodynamic modelling to solve engineering and environmental issues is their calibration and validation based on reliable field data.

REFERENCES

Abreu C., Barros M., Brito D., Teixeira M., Cunha A. (2020). Hydrodynamic Modeling and Simulation of Water Residence Time in the Estuary of the Lower Amazon River. Water, 12(3), 660, DOI:10.3390/w12030660.

Alabyan A., Panchenko E., Alekseeva A. (2018). Hydrodynamic features of small tidal estuaries of the White Sea basin // Vestnik Moskovskogo Universiteta, Seria 5 Geographia, 4, 39–48. (in Russian with English summary).

Alabyan A., Krylenko I., Lebedeva S., Panchenko E. (2022). World experience in numerical simulation of flow dynamics at river mouths. Water Resources, 49 (5), 766–780. DOI: 10.1134/S0097807822050025.

Aleksyuk A., Belikov V. (2017). Simulation of shallow water flows with shoaling areas and bottom discontinuities. Computational Mathematics and Mathematical Physics, 57 (2), 318–339, DOI: 10.1134/S0965542517020026.

Aleksyuk A., Belikov V. (2017). STREAM 2D CUDA program complex for calculation of currents, bottom deformations and pollution transport in open streams using CUDA technology (on NVIDIA GPUs). Software Registration Certificate No. 2017660266. (in Russian).

Anh D., Hoang L., Bui M., Rutschmann P. (2018). Simulating Future Flows and Salinity Intrusion Using Combined One- and Two-Dimensional Hydrodynamic Modelling—The Case of Hau River, Vietnamese Mekong Delta. Water, 10(7), 897, DOI:10.3390/w10070897.

Brunner G. (2016). HEC-RAS River Analysis System User's Manual. Version 5.0. US Army Corps of Engineers, Institute for Water Resources, Hydrologic Engineering Center, Davis, CA, USA. 960 p.

Chen W., Chen K., Kuang C., Zhu D., He L., Mao X., Liang H., Song H. (2016). Influence of sea level rise on saline water intrusion in the Yangtze River Estuary, China. Applied Ocean Research, 54, 12–25, DOI: 10.1016/j.apor.2015.11.002.

Hoitink A., Jay D. (2016). Tidal river dynamics: Implications for deltas. Rev. Geophys., 54, 240–272, DOI:10.1002/2015RG000507.

Iglesias I., Bio A., Melo W., Avilez-Valente P., Pinho J., Cruz M., Gomes A., Vieira J., Bastos L., Veloso-Gomes F. (2022). Hydrodynamic Model Ensembles for Climate Change Projections in Estuarine Regions. Water, 14, 1966, DOI: 10.3390/w14121966.

Jiang A., Ranasinghe R., Cowell P. (2013). Contemporary hydrodynamics and morphological change of a microtidal estuary: a numerical modelling study. Ocean Dynamics, 63(1), 21–41, DOI:10.1007/s10236-012-0583-z.

Jouanneau N., Sentchev A., Dumas F. (2013). Numerical modelling of circulation and dispersion processes in Boulogne-sur-Mer harbour (Eastern English Channel): Sensitivity to physical forcing and harbour design. Deutsche Hydrographische Zeitschrift, 63 (11–12), 321–1340, DOI:10.1007/s10236-013-0659-4.

Khanarmuei M., Suara K., Sumihar J., Brown R.J. (2020). Hydrodynamic modelling and model sensitivities to bed roughness and bathymetry offset in a micro-tidal estuary. Journal of Hydroinformatics, 22 (6), 1536–1553, DOI:10.2166/hydro.2020.102.

Khare V., Khare C., Nema S., Baredar P. (2019). Tidal Energy Systems. Design, Optimization and Control. Elsevier. DOI: 10.1016/C2017-0-02279-6.

Lyddon C., Brown J., Leonardi N., Plater A. (2018). Flood Hazard Assessment for a Hyper-Tidal Estuary as a Function of Tide-Surge-Morphology Interaction. Estuaries and Coasts, 41, 1565–1586, DOI:10.1007/s12237-018-0384-9.

Matte, P., Secretan, Y., Morin, J. (2017). Hydrodynamic modeling of the St. Lawrence fluvial estuary. I: model setup, calibration, and validation. Journal of Waterway, Port, Coastal, and Ocean Engineering, 143 (5), DOI:10.1061/(ASCE)WW.1943-5460.0000397.

Miskevich I., Alabyan A., Korobov V., Demidenko N., Popryadukhin A. (2018). Short-term variability of hydrological and hydrochemical characteristics of the Kyanda estuary in Onega bay, the White sea (July 28–August 15). Oceanology, 58(3), 350–353, DOI: 10.1134/S000143701803013X.

Miskevich I., Korobov V., Alabyan A. (2018). Specificity of engineering-ecological surveys in small tidal estuaries of the western sector of the Russian Arctic. Engineering Survey, 12 (3-4), 50–61, DOI: 10.25296/1997-8650-2018-12-3-4-50-61(in Russian with English summary)

McDowell D., O'Connor B. (1977). Hydraulic behavior of estuaries. London: Macmillan Press.

Mikhailov V. (1971). Flow and channel dynamics in non-tidal river mouths. Moscow: Gidrometeoizdat. (in Russian)

Mills L., Janeiro J., Martins F. (2021). Effects of sea level rise on salinity and tidal flooding patterns in the Guadiana Estuary. Journal of Water and Climate Change, 12 (7), 2933–2947, DOI: 10.2166/wcc.2021.202.

Mohammadian A., Morse B., Robert J.-L. (2022). Calibration of a 3D hydrodynamic model for a hypertidal estuary with complex irregular bathymetry using adaptive parametrization of bottom roughness and eddy viscosity. Estuarine, Coastal and Shelf Science, 265, 107655, DOI: 10.1016/j.ecss.2021.107655.

Neill S., Reza Hashemi M. (2018). Fundamentals of Ocean Renewable Energy: Generating Electricity from the Sea. London: Academic Press. DOI: 10.1016/C2016-0-00230-9.

Panchenko E., Alabyan A., Demidenko N., Leummens M., Leummens L. (2020). Data from the research on hydrodynamic characteristics of the macrotidal estuary of the Semzha River (White Sea basin). Version 1, 4TU.ResearchData, dataset. DOI:10.4121/uuid:890d12be-ddc9-42dc-a889-752783670136.

Panchenko E., Alabyan A., Krylenko I., Lebedeva S. (2020). Modelling of hydrodynamic processes in the Onega and the Northern Dvina river mouths under different climate change scenarios. Proc. IX International Scientific and Practical Conference «Marine Research and Education (MARESEDU-2020)», 2, 72–75. (in Russian)

Panchenko E., Leummens M., Lebedeva S. (2020). Hydrodynamic modelling of the Onega river tidal estuary. E3S Web Conferences, 163, DOI: 10.1051/e3sconf/202016301008.

Panchenko E., Alabyan A. (2022). Friction factor evaluation in tidal rivers and estuaries. METHODSX, 9, 101669, DOI:10.1016/j.mex.2022.101669.

Panchenko E. (2023). Experience of one-dimensional hydrodynamic modeling in micro-, meso- and macrotidal estuaries of small rivers. Collection of articles on the materials of the XIII seminar of young scientists of universities, united by the council on the problem of erosion, channel and estuarine processes. Moscow: Your format. 94–100. (in Russian).

Rahbani M. (2015). A comparison between the suspended sediment concentrations derived from DELFT3D model and collected using transmissometer – a case study in tidally dominated area of Dithmarschen Bight. Oceanologia, 57, 44–49, DOI:10.1016/j.oceano.2014.06.002.

Rtimi R., Sottolichio A., Tassi P. (2021). Hydrodynamics of a hyper-tidal estuary influenced by the world's second largest tidal power station (Rance estuary, France). Estuarine, Coastal and Shelf Science, 250, 19, DOI: 10.1016/j.ecss.2020.107143.

Samarasinghe J., Basnayaka V., Gunathilake M., Azamathulla H., Rathnayake U. (2022). Comparing Combined 1D/2D and 2D Hydraulic Simulations Using High-Resolution Topographic Data: Examples from Sri Lanka—Lower Kelani River Basin. Hydrology, 9 (2), 39, DOI: 10.3390/hydrology9020039.

Savenije H. (2012). Salinity and tides in alluvial estuaries. 2nd completely revised ed. Delft: Delft University of Technology.

Veerapaga N., Azhikodan G., Shintani T., Iwamoto N., Yokoyama K. (2019). A three-dimensional environmental hydrodynamic model, Fantom-Refined: Validation and application for saltwater intrusion in a meso-macrotidal estuary. Ocean Modelling, 141, DOI: 10.1016/j.ocemod.2019.101425.

Ward, P., Couasnon A., Eilander D., Haigh I., Hendry A., Muis S., Veldkamp T., Winsemius H., Wahl T. (2018). Dependence between high sea-level and high river discharge increases flood hazard in global deltas and estuaries. Environ. Res. Lett. 13, 084012, DOI: 10.1088/1748-9326/aad400.

Yin Y., Karunarathna H., Reeve D. (2019). Numerical modelling of hydrodynamic and morphodynamic response of a meso-tidal estuary inlet to the impacts of global climate variabilities. Marine Geology, 407, 229–247, DOI: 10.1016/j.margeo.2018.11.005.

Zheng P., Li M., Wang C., Wolf J., Chen X., De Dominicis M., Yao P., Hu Z. (2020). Tide-Surge Interaction in the Pearl River Estuary: A Case Study of Typhoon Hato. Frontiers in Marine Science, 7, DOI:10.3389/fmars.2020.00236.

RESEARCH PAPER

SEASONAL STREAM WATER CHEMISTRY RESPONSE TO LONG-TERM FORESTRY DRAINAGE AND WILDFIRE: A CASE STUDY IN A PART OF THE GREAT VASYUGAN MIRE

Yulia A. Kharanzhevskaya[1*]
[1]Siberian Federal Scientific Centre of Agro-BioTechnologies of the Russian Academy of Sciences, Siberian Research Institute of Agriculture and Peat, Gagarin st., 3, 634050, Tomsk, Russia
***Corresponding author:** kharan@yandex.ru
Received: March 15th, 2023 / Accepted: November 12th, 2023 / Published: March 31st, 2024
https://DOI-10.24057/2071-9388-2023-2806

ABSTRACT. Recent research suggests that climate change is contributing to rising solute concentrations in streams. This study focuses on assessing the concentrations of major elements, nutrients, and dissolved organic carbon (DOC), and their release through the bog-river system in the taiga zone of Western Siberia. The research was carried out in the northeastern part of the Great Vasyugan Mire (GVM), the largest mire system that impacts the quality of river water in the Ob River basin. By using PCA and cluster analysis, we examined the long-term dynamics of the chemical composition of headwater streams of the GVM affected by drainage and wildfires. Our data from 2015-2022 revealed that the concentrations of Ca^{2+}, Mg^{2+}, K^+, Na^+, and HCO_{3-} in stream water from the drained area of the GVM were, on average, 1.3 times lower than those at the pristine site. Conversely, the concentrations of NH^+_4, Fe_{total}, Cl^-, SO_4^{2-}, NO^-_3, DOC, and COD were higher, indicating the influence of forestry drainage and the pyrogenic factor. Our findings also demonstrated that the GVM significantly impacts the water chemical composition of small rivers. We observed a close correlation in the concentrations of K^+, Na^+, Cl^-, Fe_{total}, NH^+_4, HCO_{3-}, and COD between the GVM and the Gavrilovka River waters. PCA analysis revealed that air temperature influences the concentrations of Ca^{2+}, Mg^{2+}, NH_4^+, NO_{3-}, HCO_{3-}, Fe_{total}, and DOC in the studied streams, with an inverse correlation with river discharge. The removal of major elements, nutrients, and DOC from the drained area of the GVM was most pronounced in April, being twice as high as in the pristine area. However, the total export from the drainage area of the Gavrilovka in April-September 2022 was 1.3 times lower than in the pristine area, amounting to 8487 kg/km^2, with DOC removal at 42%.

KEYWORDS: water chemistry, mire, drainage, wildfire, Western Siberia

CITATION: Y. A. Kharanzhevskaya (2024). Seasonal Stream Water Chemistry Response To Long-Term Forestry Drainage And Wildfire: A Case Study In A Part Of The Great Vasyugan Mire. Geography, Environment, Sustainability, 1(17), 44-53
https://DOI-10.24057/2071-9388-2023-2806

ACKNOWLEDGEMENTS: This study was supported by the Russian Science Foundation, project no. 22-27-00242.

Conflict of interests: The authors reported no potential conflict of interest.

INTRODUCTION

Western Siberia is a large peatland-dominated region in the northern hemisphere (Neishtadt 1971; Liss et al. 2001). Peatlands occupy vast areas on terraces and interfluves, playing an important role in the region's temperature and water balance. These peatlands also influence the water quality of the Ob River and its tributaries, thereby affecting the overall flow of mineral and organic substances into the Arctic Ocean (Kirpotin et al. 2009; Evseeva et al. 2012; Berezin et al. 2014; Pokrovsky et al. 2015; Terentiev et al. 2016; Savichev et al. 2016; Krickov et al. 2019; Dyukarev et al. 2019). Siberia experiences the highest rate of temperature change in the surface layers of the atmosphere (1.39°C/100 years), surpassing the average rate for Northern Eurasia and Northern Asia, the Arctic, and the entire northern hemisphere (Groisman et al. 2013). According to (Third Assessment Report of Roshydromet 2022), Western Siberia has seen a positive trend in average annual air temperature, with an increase of +0.42 °C/decade between 1976 and 2020. The region also experiences a growth in atmospheric precipitation with changes in its patterns, i.e. an increase in extremely heavy rainfall during summer and autumn (Kharyutkina et al. 2019).

The rise in air temperature, atmospheric precipitation, and the prevalence of wildfires can enhance the mobilization of mineral and organic substances from peatlands and accelerate their transport into surface waters and the Arctic Ocean (Frey 2005; Pokrovsky et al. 2015). Studies of river water chemistry in Western Siberia across climatic gradients (Krickov et al. 2019) revealed that under conditions of climate change, the greatest increase in dissolved organic carbon (DOC) occurs in streams with a catchment area of less than 1,000 km^2, particularly during summer and autumn.

Temperature rise contributes to more frequent wildfires in Siberia and other regions (Kharuk et al. 2021; Nelson et al. 2021), often associated with dry conditions in the summer period. Drained peatlands are particularly vulnerable to climate change and wildfires, as lower water table levels make them prone to burning, negatively impacting water quality. Various peatland use practices, such as forestry, agriculture, peat extraction, and peat fires, as well as their impact on water pollution, have been extensively studied (Nieminen et al. 2017; Marttila et al. 2018; Sulwiński et al. 2020, etc.). Peatlands drainage and fires lead to increased erosion, water pollution, eutrophication, and brownification, especially in headwater catchments (Broder, Biester 2017; Marttila et al. 2018; Ackley et al. 2021; Finér et al. 2021; Nieminen et al. 2020, 2021). Although water chemistry and substance removal from the medium-size river basins in the Middle Ob basin have been well-studied (Savichev 2007; Dubrovskaya and Brezhneva 2010; Savichev et al. 2016; Savichev et al. 2018), and some data on peatland-dominated streams are summarized in (Peatlands of Western Siberia 1976), there is a lack of detailed data on the effect of drainage and the pyrogenic factor on stream water chemistry in Western Siberia. Therefore, this study aims to assess the concentrations of major elements, nutrients, and DOC, as well as their release through the bog-river system in the taiga zone of Western Siberia.

MATERIALS AND METHODS

The study was carried out within the Gavrilovka River basin, a left-bank tributary of the Iksa River in the Middle Ob River basin (Fig. 1). Covering an area of 81 km^2, the Gavrilovka River basin is located in the drained area of the northeastern part of the Great Vasyugan Mire (GVM). The drainage network covers 39 km^2, while the peatlands account for approximately 75 km^2 or 93% of the catchment area. The bog was drained in the 1980s through a network of open ditches spaced 160–180 m apart (Maloletko et al. 2018). Currently, due to ditch overgrowth, self-restoration has been observed (Sinyutkina 2021). In 2016, a fire burned an area of 3.10 km^2 in the Gavrilovka River basin, with a burnt layer thickness of 5-15 cm (Sinyutkina et al. 2020). A similar pristine area of the GVM, located 3 km to the north within the 76 km^2 catchment area of the Klyuch River, a right-bank tributary of the Bakchar River, was selected as a background area. Peatlands in the Klyuch River basin cover around 60 km^2 or approximately 79% of the catchment area. The study area is characterized by poor infrastructure development, with the primary sources of pollution (industry, thermal power plants, etc.) located 200 km away.

River water sampling was conducted monthly from March to September between 2015 and 2022. In 2022, to assess spatial variation in water chemistry within the drained part of the GVM, simultaneous sampling was carried out at 6 key sites in the Gavrilovka River basin: pine dwarf-shrub *Sphagnum*, sedge *Sphagnum* communities, and the hummock-hollow complex. In the background watershed of the Klyuch River (a pristine part of the GVM), sampling was carried out in similar plant communities (Table 1). We measured water temperature, pH, O_2, and CO_2 immediately after sampling. Samples were preserved to determine Fe_{total}, NO^-_3, and NH^+_4. Dissolved O_2 was measured using a HI 9146-04 HANNA Instruments (Germany), pH was measured using a pH-200 field device from HM Digital (South Korea), and redox potential (Eh) was determined using ORP-200 from HM Digital (South Korea). The electrical conductivity (EC) was measured using a HI 8733 from HANNA Instruments (Germany) (Table 2). Dissolved carbon dioxide was measured by titrating samples with NaOH solution in the presence of Rochelle salt and the phenolphthalein indicator (FR.1.31.2005.01580).

The chemical analysis of water samples was carried out at the analytical laboratory of the Siberian Research Institute of Agriculture and Peat. Prior to analysis, water samples were filtered through a paper filter with a pore diameter of 1.0-2.5 µm. The concentrations of Ca^{2+}, Mg^{2+}, HCO_3^-, and Cl^- were determined using the titrimetric method, while Fetotal, NO^-_3, NH^+_4, and SO_4^{2-} were analyzed using the spectrophotometric method (Specol-1300, Analytik Jena AG, Germany). The concentrations of K^+ and Na^+ ions were determined using flame photometry (PFA-378, Russia). Chemical oxygen demand (COD) was estimated with potassium dichromate, and DOC was determined using the Tyurin method with potassium dichromate, along with photometric termination according to (STP 0493925-008-93) (Table 3). Total dissolved solids (TDS) were estimated by summing the concentrations of ions.

Statistical analysis of the chemical composition of water was performed using principal component analysis (PCA) and cluster analysis in Statistica 10. The chemical composition of water was analyzed using a cluster analysis with the classification of water samples based on homogeneity within classes (hierarchical method). The cluster analysis was carried out using the calculation of the Euclidean distance and the Ward method. Factor analysis was carried out using the principal component method (PCA), which is based on the calculation of vectors and eigenvalues of the covariance matrix of the initial data, along with the construction of a scree plot to determine the leading factors and the assessment of the factor loading matrix.

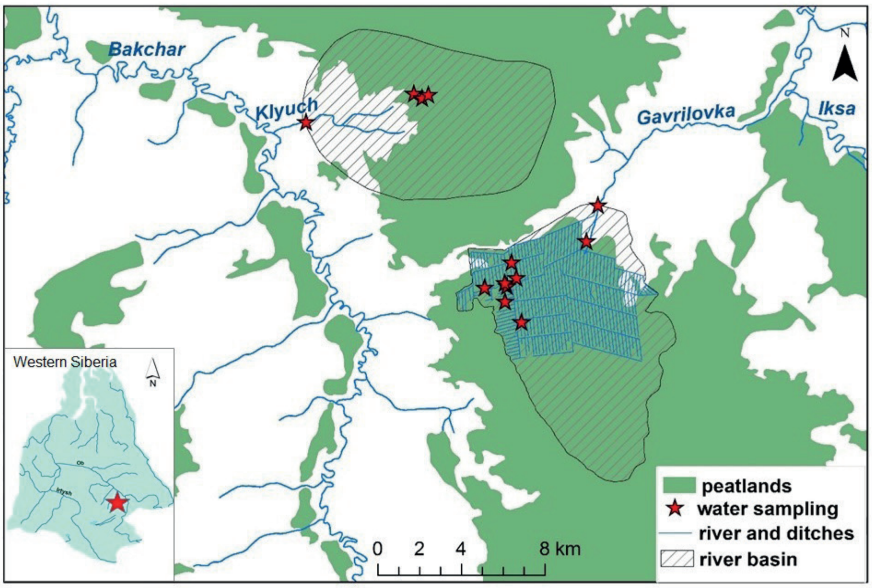

Fig. 1. Study area with sampling points in the Gavrilovka and Klyuch River basins

Table 1. Location, vegetation type, and water table level in the key sites of the Great Vasyugan Mire in March-September 2022

№	Vegetation type	Coordinates	Catchment	Land use type	Water table level, cm
1	Pine dwarf-shrub *Sphagnum* (RG)	N56°53′25,8″, E82°40′50,5″	Gavrilovka	Forestry drainage	-13
2	Pine dwarf-shrub *Sphagnum* (RG2)	N56°53′57,10» E82°41′05,95»	Gavrilovka	Forestry drainage	-41
3	Pine dwarf-shrub *Sphagnum* (RG3)	N56°53′32,7″ E82°41′19″	Gavrilovka	Forestry drainage	-18
4	Pine dwarf-shrub *Sphagnum* (PG2)	N56°53′18,6″ E82°40′36,7″	Gavrilovka	Forestry drainage and fire event area	-27
5	Sedge *Sphagnum* lagg (TG)	N56°52′23,6″, E82°41′30,1″	Gavrilovka	Forestry drainage	-10
6	Hummock-hollow complex (D2)	N56°53'18,8" E82°39′48,6″	Gavrilovka	Forestry drainage	-29
7	Pine dwarf-shrub *Sphagnum* (P3)	N56°58'24, 3", E82°36'41,2"	Klyuch	Forestry drainage	-13
8	Sedge *Sphagnum* lagg (P5)	N56°58'17, 3" E82°37′04,5″	Klyuch	Forestry drainage	-10
9	Hummock-hollow complex (D1)	N56°58′22,1» E82°37′22,4»	Klyuch	Forestry drainage	-8

Table 2. Instrument accuracy

№	Component	Instrument	Accuracy
1	O_2	HANNA 9146-04, Germany	±5 %
2	pH/T	PH200, HM Digital, South Korea	±0.1 ºC ±0.02pH
3	Eh	ORP200 HM Digital, South Korea	± 2мВ
4	EC	HANNA HI 8733, Germany	±1%

Water levels in Klyuch and Gavrilovka headwater streams were measured using Micro-Diver loggers (Eijkelkamp, Netherlands) every hour throughout the year. Discharge measurements were made using an acoustic current meter OTT Hydromet (Germany) at gauging stations set up at the Klyuch and Gavrilovka rivers, with measurements carried out every 5-10 days during typical water content periods in 2015-2022. The release of major elements, nutrients, and DOC was calculated in 2022 as the product of the total volume of river runoff and the concentrations of components in the Klyuch and Gavrilovka rivers obtained from the results of laboratory analysis of river water samples. On average, during spring flood and summer-autumn low water in 2022 (April-September), water flow was 0.35 m^3/s in the Klyuch River, and 0.24 m^3/s in the Gavrilovka River.

The average annual air temperature for the study period was 1.04 °C. Among the 8 years, 2015 and 2020 were the warmest, with average annual air temperatures of 2.05 and 3.03 °C, respectively (Table 4), marking the absolute maximum for the observation period from 1970 to 2022 at the Bakchar weather station. Throughout the study period, the annual precipitation averaged 537 mm, with decreases to 431-486 mm observed in 2016, 2019, and 2020. In 2018, the annual precipitation reached 677 mm, the highest value for a long period.

RESULTS AND DISCUSSION

Stream water chemistry

The pH values and concentrations of Ca^{2+}, Mg^{2+}, K^+, Na^+, and HCO_{3^-} in the waters of the Gavrilovka River, were 1.3 times lower than in the Klyuch River, which drains the pristine area of the GVM. Conversely, the waters of the Gavrilovka River exhibited high concentrations of NH^+_4, Fe_{total}, Cl^-, SO_4^{2-}, and NO^-_3, as well as DOC, COD, and CO_2 were revealed as indicators of forestry drainage. The increased concentrations of major elements in the Klyuch River are probably determined by the smaller peatland-dominated area (about 77%) and the removal of substances from the catchment area occupied by mineral soils or ion-rich groundwater supply. Similar findings were made by (Tokareva et al. 2022), whose research in the Yenisei River basin demonstrated that streams draining basins with a higher number of pristine ombrotrophic bogs (atmosphere-fed bogs) receive more atmospheric precipitation and have ion-poor runoff.

Analysis of the data revealed that, similar to previous studies (Kharanzhevskaya 2022a, b), the chemistry of river waters in the drained and pristine areas of the GVM may be similar in certain periods. Studies conducted in drained raised bogs in Canada also showed a slight effect of drainage on mire water chemistry. The differences in the

Table 3. Analytical methods

№	Component	Method	Standart	Accuracy,%
1	Ca^{2+}, Mg^{2+}	Titrometry	PNDF 14.1:2.98-97	±15
2	K^+	Flame photometry (PFA-378, Russia)	PNDF 14.1:2:4.138-98	±12
3	Na^+	Flame photometry (PFA-378, Russia)		±17
4	SO_4^{2-}	Spectrophotometry (Specol-1300, Analytik Jena, Germany)	PNDF 14.1:2.159-2000	±20
5	Cl^-	Titrometry	PNDF 14.1:2:4.111-97	±12
6	NH^+_4	Spectrophotometry (Specol-1300, Analytik Jena, Germany)	PNDF 14.1:2.1-95	±10
7	Fe_{total}	Spectrophotometry (Specol-1300, Analytik Jena, Germany)	PNDF 14.1:2:4.50-96	±15
8	HCO_{3-}	Titrometry	PNDF 14.2.99-97	±25
9	NO^-_3	Spectrophotometry (Specol-1300, Analytik Jena, Germany)	PNDF 14.1:2:4.4-95	±10
10	DOC	Spectrophotometry (Specol-1500, Analytik Jena, Germany)	STP 0493925-008-93	±10
11	COD	Titrometry	(Lurie, 1973)	±10
12	CO_2	Titrometry	FR.1.31.2005.01580	±10

Table 4. Hydrometeorological conditions according to the weather station near Bakchar village

Year	Annual precipitation, mm	Precipitation in April-September, mm	Average annual air temperature, ^{0}C	Sum
2015	616	382	2.05	T>10 ^{0}C
2016	486	347	0.72	
2017	566	419	1.30	1972
2018	677	495	-0.80	2162
2019	431	284	0.88	1891
2020	477	293	3.03	1781
2021	497	311	0.29	1860
2022	545	376	0.86	2136

Source: (http://meteo.ru/)

water chemistry between pristine and drained peatlands are influenced by the rate of decomposition of organic residues and biogeochemical processes in the region, which are largely dependent on the average annual air temperature (Harris et al. 2020).

Comparison of long-term data on Gavrilovka and Klyuch river waters using the nonparametric Mann-Whitney test revealed significant differences in the pH value (Z=-2.94, p=0.003), as well as in the concentrations of K^+ (Z=-2.26, p=0.024), Mg^{2+} (Z=-2.21, p=0.027), Fe_{total} (Z=2.63, p=0.009), NH^+_4 (Z=2.31, p=0.021), NO^-_3 (Z=2.52, p=0.012), HCO_{3-} (Z=-2.31, p=0.021), COD (Z=2.10, p=0.036), CO_2 (Z=2.10, p=0.036), and DOC (Z=3.05, p=0.002). These findings partially align with the results obtained in 62 small peatland-dominated watersheds in Finland (Marttila et al. 2018), which indicated increased concentrations, particularly of nitrogen and phosphorus, in headwater streams where peat extraction and peatland forestry were the main types of land use. While DOC, COD, and Fe concentrations in stream waters in Finland were at similar levels with near pristine sites, those sites exhibited lower pH levels in comparison to areas affected by peatland drainage (Marttila et al. 2018). However, our studies showed higher DOC content and concentrations of NO^-_3 and NH^+_4 in stream water of the GVM compared to data from Finland. On the contrary, the stream water pH in the drained part of the GVM was lower, which is determined by higher concentrations of DOC resulting from the decomposition of peat layers due to intensive drainage. Studies conducted in the Yenisei River basin (Tokareva et al. 2022) also showed lower pH values and elevated concentrations of NH^+_4 in stream water chemistry due to the input of highly acidic organic-rich solutes from a pristine peatland area within the basin and specific biogeochemical processes occurring directly in the stream channel.

Our data showed that differences in water chemistry between the Klyuch and Gavrilovka rivers varied from year to year, with no significant differences found in 2021. Differences were observed in the content of Fe_{total} (Z=2.56, p=0.011) in 2015, and of K^+ (Z=-2.04, p=0.041) and CO_2 (Z=2.87, p= 0.004) in 2016. In 2017 and 2018, there were differences in the content of NO_{-3} (Z=2.30, p=0.021), and also COD (Z=2.87, p=0.004) in 2018. In 2019, there were significant differences in SO_4^{2-} (Z=2.17, p=0.030) and DOC (Z=2.68, p=0.007). In 2020, significant differences were observed only in the pH value (Z=-2.30, p=0.021). Finally, in 2022 differences were found in the concentrations of DOC (Z=2.24, p<0.05), NO_{3-} (Z=-2.68, p<0.05), and Cl^- (Z=-2.81, p<0.05).

Cluster analysis showed that all the samples taken in the Klyuch River, except the ones from 2019 and 2022, and the samples taken in the Gavrilovka River in 2017, 2020, and 2021 belonged to the first cluster. The water samples taken in 2017 and 2021 stood out as a separate subcluster, as an indicator of the pyrogenic factor and the temperature regime. The second cluster included samples taken in 2015, 2016, 2018, 2019, and 2022. The first subcluster included the samples taken in the Gavrilovka River during high water in 2018 and low water in 2019, as well as in 2016 and 2022. The second subcluster included the water samples from the Gavrilovka River taken in 2015, as well as the samples from the Klyuch River taken in 2019 and 2022. Thus, under drought conditions, an increase in major element content was observed in the Gavrilovka River, and, as a result, water chemistry became comparable to the Klyuch River (Fig. 2).

Seasonal dynamics in stream water chemistry is characterized by an increase in pH, K^+, Na^+, Ca^{2+}, Mg^{2+}, NH_4^+, Fe_{total}, Cl^-, and HCO_{3^-} in March after the winter low water period, by 1.3-3 times. In winter, an increase in total dissolved solids is observed due to the displacement of ions during the formation of the ice cover on the river. The second maximum of ion content is achieved during the flood period (SO_4^{2-}, NO_{3^-}, DOC, NH_4^+, Cl^-) and at the end of the summer-autumn low water period (K^+, Na^+, Ca^{2+}, Mg^{2+}, HCO_{3^-}).

Differences are also observed in the long-term dynamics of river water chemistry. Our studies have shown that in the Gavrilovka River, it is determined by hydrometeorological conditions, forestry drainage, and the pyrogenic factor. The pH value of the Gavrilovka River waters was highest in 2016-2017 and 2022 (pH=6.53), with a decrease to the minimum values (pH=6.07) in the high-water year 2018 due to water supply from the GVM with high DOC content. In 2015, there was an increase in pH (6.93) in the Klyuch River due to high air temperature, while the minimum pH value (6.41) was observed in the dry year 2019. The Klyuch River catchment differs from the Gavrilovka River by a larger proportion of peatland area and regular groundwater discharge, factors contributing to higher content of main ions and pH in the Klyuch River.

Our data demonstrated that in 2017, following the fire, the waters of the Gavrilovka River showed an increase in the concentrations of K^+, Na^+, Ca^{2+}, Mg^{2+}, Fe_{total}, Cl^-, SO_4^{2-}, NO_3^-, and HCO_3^-, consistent with the results obtained for the GVM (Kharanzhevskaya and Sinyutkina 2021). In the high-water year 2018, there was a sharp decrease in concentrations of these elements due to dilution by atmospheric precipitation. Subsequent years saw an increase in the content of Ca^{2+}, Cl^-, NO_3^-, and HCO_3^- in 1.2-3 times in the Gavrilovka River, attributed to increased air temperatures in 2020 and further degradation of the pyrogenic layer. Studies (Lydersen et al. 2014; Rust et al. 2018; Stirling et al. 2019; Wu et al. 2022) showed that after a fire, there is an increase in pH and the concentrations of the main cations (Ca^{2+}, Mg^{2+}, Na^+, K^+), anions of strong acids (SO_4^{2-}, Cl^-, NO_3^-), ammonium ions, total nitrogen, phosphorus, and DOC. The greatest changes occur within three years after the fire, but the influence of the pyrogenic factor can persist for about 12 years (Sulwiński et al. 2020).

The water chemistry of the Klyuch River, draining the pristine part of the GVM, is mainly influenced by changing climatic conditions. As a result, in 2020, which was characterized by an absolute maximum of the average annual temperature, the Klyuch River waters showed increased concentrations of Ca^{2+}, Mg^{2+}, K^+, Na^+, HCO_3^-, and NO^-_3, except for Fe_{total}, NH^+_4, SO_4^{2-}, and Cl^-. In the dry year 2019, the content of Ca^{2+}, Mg^{2+}, K^+, SO_4^{2-}, Cl-, and HCO_3^- decreased due to the decomposition of organic matter in the active layer above the water table level. Its dissolution in water occurs when the water table level rises during precipitation events. Peatland drainage leads to increased leaching of nutrients over time because of the decomposition and degradation of peat deposits (Nieminen et al. 2017).

On the contrary, our studies have shown that, as a result of ditches' overgrowth, the river water chemistry of the drained area of the GVM becomes closer to the natural site. For example, in 2021, we did not find significant differences in major element, nutrient, and DOC concentrations. However, fires and elevated air temperatures impacted this trend. As a result, in 2020, with an absolute maximum air temperature over a long period, there was a sharp increase in major element and DOC content (Table 5). Similar results obtained in Finland showed positive correlations of organic matter (TOC, DOC, COD, LOI) and Fe with air temperature (Marttila et al. 2018). Additionally, a positive correlation between increasing nitrogen concentrations in waters discharging from drained boreal peatland forests in Finland and Sweden and temperature was noted (Nieminen et al. 2021). River waters exhibit concentrations of K^+, NH_4^+, Fe_{total}, Cl^-, SO_4^{2-}, and DOC similar to those in the waters of the GVM, with higher pH values of Na^+, Ca^{2+}, Mg^{2+}, NO_{3^-}, and HCO_{3^-}.

Mire water chemistry

Water samples taken in 2022 from the drained area (RG, RG2, RG3, PG2, TG, D2) of the GVM are characterized by a 1.5-3 times higher content of almost all components in comparison with the pristine area (P3, P5, D1). Conversely,

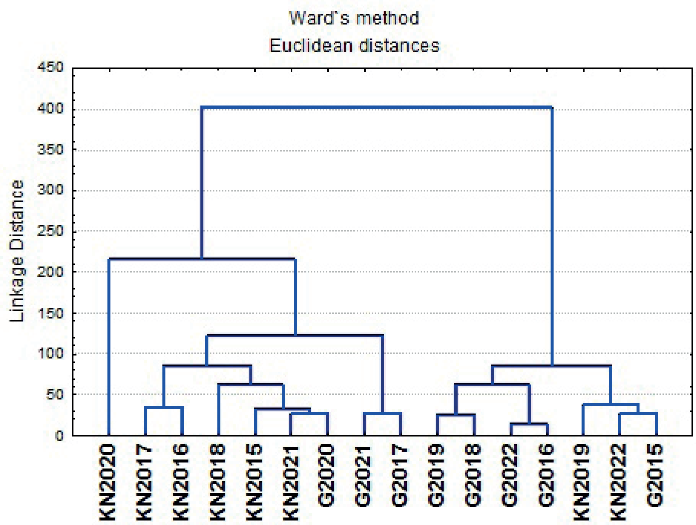

Fig. 2. Dendrogram of river water chemistry in March-September 2015-2022 of the Gavrilovka River (G) and the Klyuch River (KN)

Table 5. Long-term dynamics of the average concentrations in river waters (March-September 2015-2022)

		EC	pH	K^+	Na^+	Ca^{2+}	Mg^{2+}	NH_4^+	Fe_{total}	Cl^-	SO_4^{2-}	NO_{3-}	HCO_{3-}	DOC	TDS
2015	K	186	6.93	0.82	4.75	24.3	8.94	4.05	1.87	3.93	4.26	1.14	120.0	59.8	174
	G	138	6.25	0.48	4.44	19.2	7.56	5.07	4.21	3.31	3.87	1.55	87.6	69.8	137
2016	K	188	6.82	0.65	6.53	27.19	10.81	5.38	2.93	4.29	4.09	2.14	139.81	54.0	204
	G	113	6.53	0.31	4.49	18.6	6.93	6.64	4.88	3.98	5.16	2.07	76.4	65.0	129
2017	K	201	6.85	0.67	8.80	28.8	10.9	3.61	5.43	5.25	2.80	1.57	141.7	61.4	210
	G	151	6.53	0.79	7.96	27.3	9.14	4.29	8.27	4.71	7.71	3.61	110.4	71.4	184
2018	K	144	6.57	0.91	6.52	24.00	9.40	3.27	2.83	3.66	2.28	1.36	119.4	51.4	174
	G	125	6.07	0.57	5.71	21.4	7.62	4.28	8.48	4.28	3.60	3.50	85.7	74.6	145
2019	K	138	6.41	0.63	5.16	20.72	8.73	2.41	2.97	3.29	1.41	1.67	93.3	52.4	140
	G	143	6.23	0.48	5.77	23.3	8.07	3.57	4.58	4.11	2.22	2.19	91.1	71.7	145
2020	K	221	6.88	0.94	9.11	39.41	19.25	3.41	3.71	3.61	2.55	2.82	199.6	45.9	284
	G	182	6.44	0.66	7.46	28.9	7.37	4.85	4.49	4.48	2.91	3.65	117	60.4	182
2021	K	170	6.70	0.66	6.50	27.16	10.91	3.87	3.76	4.52	3.13	2.06	113.9	67.5	177
	G	165	6.37	0.65	6.13	26.9	8.88	4.90	7.48	5.16	4.07	4.54	108	79.3	177
2022	K	117	6.70	0.63	6.00	20.87	6.34	3.83	2.50	5.08	3.62	1.39	81.8	57.6	132
	G	113	6.56	0.57	6.21	21.34	6.86	5.18	3.53	6.79	5.07	3.81	70.50	75.9	130

there is a lower pH due to high organic substance content and minimal concentrations of HCO_3^-. Spatially, samples from the pine dwarf-shrub *Sphagnum* communities of the drained part of the GVM taken in 2022 (RG, RG2, RG3, PG2) had low pH and higher concentrations of K^+, Na^+, NH_4^+, Fe_{total}, Cl^-, NO_3^-, and DOC compared to the sedge *Sphagnum* community (TG) and the hummock-hollow complex (D2). At the same time, in the waters of the sedge *Sphagnum* community (TG), there was an increase in the content of Ca^{2+}, Mg^{2+}, HCO_{3-}, and pH, indicating deep groundwater supply. We also saw an increase in SO_4^{2-} and DOC in the waters of the hummock-hollow complex, indicating high peat decomposition rates due to a significant water level decrease (Table 6).

Principal component analysis (PCA) showed similarity in weather condition impact on the Klyuch and Gavrilovka rivers water chemistry. Air temperature (-0.42) and water temperature (-0.40) significantly affect the content of Ca^{2+} (-0,93), Mg^{2+} (-0,75), Na^+ (-0,78), HCO_{3-} (-0,96), and Fetotal (-0.78) in the Gavrilovka River (Fig.3). We see a direct correlation with the concentrations of NO_{3-} (0.42) and Gavrilovka River discharges (0.60). The second component is less significant, but it also reflects an increase of NH^+_4 (0.59) and DOC (0.51) in river waters with an increase in air (0.64) and water (0.81) temperatures. Similarly, the leading factors determining the concentrations of NO_{3-} (0.54), NH^+_4 (0.69), Fetotal (0.59), and DOC (0.65) in the Klyuch River are air (0.70) and water (0.79) temperatures. Klyuch River discharges (-0.63) are inversely correlated with nutrient content, indicating a dilution effect (Fig. 3). Thus, factor 1 characterizes the increase in the content of chemical substances in river waters as a result of an increase in air and water temperatures. Factor 2 mainly characterizes the dilution effect of river waters by precipitation.

Table 6. Spatial patterns in water chemistry of the drained (RG, RG2, RG3, TG, PG2, D2) and pristine (P3, P5, D1) areas of the GVM in April-September 2022, mg/l

	EC	pH	K^+	Na^+	Ca^{2+}	Mg^{2+}	NH_4^+	Fe_{total}	Cl^-	SO_4^{2-}	NO_{3-}	HCO_{3-}	DOC	TDS
RG	56	3.55	0.43	1.43	3.88	1.53	7.52	2.27	4.74	3.87	2.84	0.46	75.3	29.0
PG2	48	3.46	0.95	1.02	4.06	1.29	7.53	2.12	4.66	3.29	2.36	1.86	74.5	29
RG2	65	3.21	0.92	1.78	5.12	1.51	8.69	2.31	5.22	5.52	2.83	0.00	91.2	33.9
RG3	64	3.31	0.48	1.10	5.58	1.89	9.25	2.55	5.43	5.16	3.12	1.25	94.4	35.8
P3	47	3.46	0.47	0.90	2.33	0.76	6.11	1.83	4.39	3.16	1.86	0.56	52.7	22.4
TG	39	3.82	0.47	1.15	6.15	2.26	4.95	1.68	3.94	2.61	1.86	9.11	61.5	34.2
P5	29	3.70	0.57	0.92	2.71	1.15	3.55	1.03	3.05	1.28	1.18	4.75	41.6	20.2
D2	50	3.60	0.63	1.33	4.78	1.99	7.22	1.95	4.77	5.41	2.87	2.72	81.3	33.7
D1	31	3.92	0.55	1.30	3.70	1.43	4.28	1.45	3.30	2.81	1.42	7.76	53.0	28.0

To assess which key site of the drained part of the GVM had the most significant impact on the water chemistry of the Gavrilovka River, a correlation analysis was performed, which showed the closest positive relationship for the content of K^+, HCO_{3-}, NH^+_4, COD, and TDS in the Gavrilovka River and the GVM, and to a lesser extent for pH, Na^+, Cl^-, Fe_{total}, SO_4^{2-}, NO_{3-}, and DOC (Table 7). The pH value and the content of SO_4^{2-}, NO_{3-}, and DOC in the Gavrilovka River and the GVM were predominantly in an inverse relationship, which characterizes dry periods when river discharges are the lowest and the correlation in water chemistry is violated due to low hydrological connectivity of the river and the bog. The highest correlations in water chemistry were found between the Gavrilovka River and the sedge *Sphagnum* lagg (TG), where the river bed is formed. We also noticed that even 6 years after the fire, the pyrogenic factor still influences river water chemistry, with the highest correlation coefficients in the content of K^+, NH^+_4, HCO_{3-}, COD, DOC, and TDS in the waters of the Gavrilovka River and the post-fire area (PG2).

Our data showed that there was primarily an inverse correlation between the content of Na^+, Ca^{2+}, Mg^{2+}, Cl^-, HCO_{3-}, and SO_4^{2-} in the waters of the Gavrilovka River and river discharges, which indicates dilution and a subsequent decrease in the concentration of substances during the spring flood. In certain periods, there was a significant positive correlation between water discharges in the river and the content of K^+, NO_{3-} in April and June, DOC in June-July, and NH_{4+} in September (Table 8). The total removal of substances from the Gavrilovka River catchment area in April-September 2022 was 8487 kg/km^2, with DOC release equal to 42% or 3603 kg/km^2. Removal from the pristine part of the GVM was 1.3 times higher, totaling 11385 kg/km^2 in April-September 2022, with DOC flux at 37% (4243 kg/km^2). Generally, the higher removal of mineral components from the Klyuch River basin may be due to groundwater inflow into the river bed and the removal of substances from the part of the catchment area with mineral soils.

Export of major elements, nutrients, and DOC

The seasonal dynamics of major elements, nutrients, and DOC release from the studied watersheds is determined by differences in the hydrological regime. Thus, the largest flux of mineral and organic substances in the Gavrilovka River during the studied period was observed in April-May, coinciding with the spring flood. In June-September, substances removal decreased to 270-382 kg/km^2. The total flux of mineral and organic substances from the drained area of the GVM in April 2022 was 1.2-22.0 times higher than from the pristine area. Similar trends were observed in May, while in other months, removal from the pristine area was 3-5 times higher (Fig. 4). This aligns with findings from previous studies (Lepistö et al. 2014; Finstad et al. 2016) which link the leaching of nutrients and organic carbon to changes in seasonal weather conditions.

PCA indicates that with increasing precipitation and river water levels, the concentration of chemical components decreases. However, the total removal of major elements, nutrients, and DOC is greatest during periods of

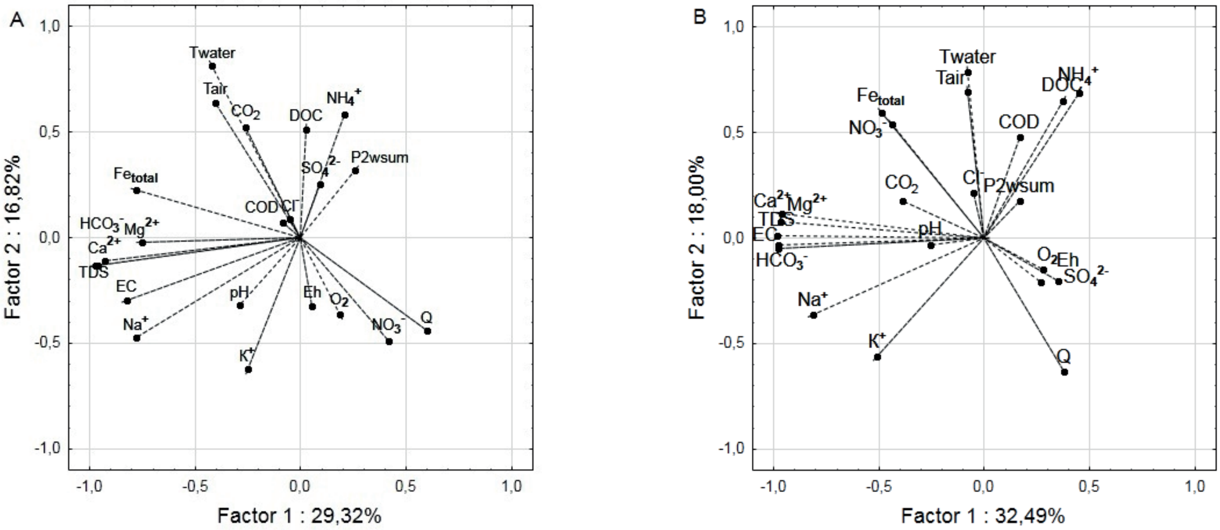

Fig. 3. PCA diagrams of the chemical composition of the waters of the Gavrilovka (A) and the Klyuch (B) rivers in April-September 2015-2022

(P_{2wsum} – total precipitation during 2 weeks before sampling, mm; T_{air} – air temperature at the sampling date, °C; T_{water} – water temperature at the sampling date, °C; Q – river discharge, m^3/s)

Table 7. Pearson correlation of the GVM and the Gavrilovka River water chemistry in 2022 (significance level p<5 %)

		Gavrilovka River														
	Key site	EC	pH	K^+	Na^+	Ca^{2+}	Mg^{2+}	NH4+	Fe_{total}	Cl^-	SO_4^{2-}	NO_{3-}	HCO_{3-}	COD	DOC	TDS
Great Vasyugan Mire	RG	-0.57	-0.48	0.51	-0.21	-0.02	0.05	0.85	-0.43	0.11	0.56	-0.11	0.98	0.76	-0.50	0.62
	PG2	0.10	-0.29	0.79	-0.16	0.46	0.24	0.84	-0.60	0.01	-0.09	-0.44	0.53	0.79	0.62	0.67
	RG2	-0.62	-0.18	0.53	0.43	0.02	0.27	0.75	0.59	0.18	-0.44	-0.54	0.93	0.61	-0.40	0.94
	RG3	-0.28	-0.03	0.48	0.88	-0.05	-0.12	0.81	0.25	-0.09	-0.53	-0.71	0.51	0.64	-0.15	0.92
	TG	0.33	-0.65	0.82	-0.25	-0.28	-0.13	0.65	0.69	0.74	-0.81	-0.64	-0.35	0.50	-0.44	0.27
	D2	-0.18	-0.10	0.50	0.11	-0.52	-0.14	0.81	0.35	0.90	0.44	-0.68	-0.66	0.64	0.47	-0.70

Table 8. Pearson correlation of Gavrilovka River water chemistry and river discharges in 2015-2022 (significance level p<5 %)

	Month	EC	pH	K^+	Na^+	Ca^{2+}	Mg^{2+}	NH_{4+}	Fe_{total}	Cl^-	SO_4^{2-}	NO_{3-}	HCO_{3-}	DOC	TDS
Gavrilovka River discharges	Apr	-0.32	0.39	0.54	-0.72	-0.89	-0.36	-0.55	-0.02	-0.43	-0.74	-0.28	-0.61	-0.54	-0.82
	May	-0.19	0.00	-0.34	0.18	-0.49	-0.32	-0.27	-0.31	-0.48	-0.13	0.24	-0.43	-0.07	-0.51
	Jun	-0.23	-0.64	0.59	-0.37	-0.06	0.11	0.14	0.46	-0.20	0.11	0.62	-0.29	0.72	-0.16
	Jul	-0.13	0.21	0.10	-0.14	-0.20	0.12	0.41	0.34	-0.45	-0.18	-0.05	-0.34	0.63	-0.28
	Aug	-0.45	-0.79	-0.48	-0.58	-0.65	-0.37	0.18	-0.70	0.29	-0.05	-0.01	-0.74	0.37	-0.73
	Sep	-0.64	-0.54	-0.31	-0.64	-0.70	-0.52	0.78	-0.57	-0.50	0.38	0.20	-0.59	-0.26	-0.62
	All data	-0.25	-0.08	0.31	-0.26	-0.48	-0.44	-0.15	-0.47	-0.21	0.01	0.58	-0.50	-0.13	-0.49

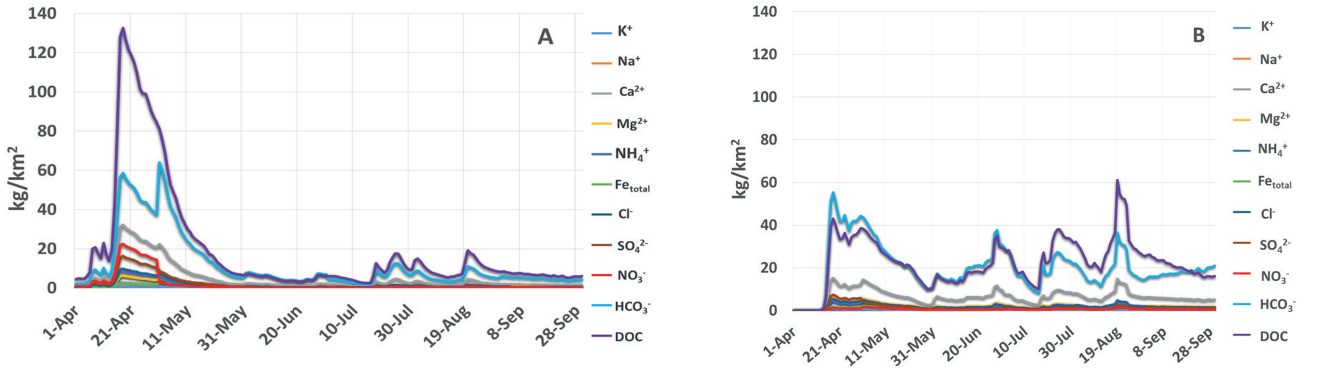

Fig. 4. Export of major elements, nutrients, and DOC by the Gavrilovka (A) and Klyuch (B) rivers in April-September 2022

high water levels, suggesting that a combination of high air temperatures and increased precipitation contributes to substance removal from river catchment areas.

CONCLUSIONS

The analysis revealed increased concentrations of NH^+_4, Fe_{total}, Cl^-, SO_4^{2-}, NO_{-3}, DOC, COD, and CO_2 in the waters of the Gavrilovka River, attributed to long-term forestry drainage. Additionally, a fire-related increase in pH, Ca^{2+}, Mg^{2+}, K^+, Na^+, Fe_{total}, SO_4^{2-}, and NO_{-3} was observed in the first year after the fire, with minimum concentrations of major elements registered mainly in 2015-2016, before the fire. Changes in water chemistry of the Gavrilovka River after the fire had a pulsating character, with extreme increase in air temperature in 2020 and the decomposition of the peat deposit's burnt layer leading to a repeated increase in Ca^{2+}, Na^+, and HCO_{3-}, and nearly a threefold increase in NO_{3-} concentration over the studied period. PCA analysis showed that air and water temperature affect the content of Ca^{2+}, Mg^{2+}, Na^+, Fe_{total}, NH_{4+}, NO_{3-}, and DOC in the studied streams and that there is an inverse correlation between them and river discharges.

Correlation analysis revealed the closest positive relationship between the content of K^+, HCO_{3-}, NH^+_4, COD, TDS in the Great Vasyugan Mire and the Gavrilovka River waters. There is an inverse correlation between the content of Na^+, Ca^{2+}, Mg^{2+}, Cl^-, HCO_{3-}, SO_4^{2-} in the waters of the Gavrilovka River and river discharges, which is a sign of dilution during spring floods. However, a significant positive correlation with river discharges was noted for K^+, NO_{3-} in April and June, DOC in June-July, and NH_{4+} in September.

The total export of major elements, nutrients, and DOC from the drained area of the Great Vasyugan Mire was 1.3 times lower in comparison to the pristine area, amounting to 8487 kg/km², with DOC flux at 42% or 3603 kg/km². Overall, our study suggests that climate change, alongside increased air temperature and precipitation in the region, will likely contribute to the removal of nutrients and organic substances from peatlands.

REFERENCES

Ackley C., Tank S.E., Haynes K.M., Rezanezhad F., McCarter C., Quinton W.L. (2021). Coupled hydrological and geochemical impacts of wildfire in peatland-dominated regions of discontinuous permafrost. Science of the Total Environment, Volume 782, 15 August, 146841 DOI: 10.1016/j.scitotenv.2021.146841

Berezin A.E., Bazanov V.A., Skugarev A.A., Rybina T.A., Parshina N.V. (2014). Great Vasyugan Mire: landscape structure and peat deposit structure features. International Journal of Environmental Studies, 71, No. 5, 618–623. https://doi.org/10.1080/00207233.2014.942537

Broder T. and Biester H. (2017). Linking major and trace element concentrations in a headwater stream to DOC release and hydrologic conditions in a bog and peaty riparian zone. Applied Geochemistry, 87, 188–201. doi:10.1016/j.apgeochem.2017.11.0

Dubrovskaya L.I., Brezhneva E.S. (2010) Composition and long-term dynamics of hydrochemical runoff in watersheds with oligotrophically associated landscapes. Bulletin of the Tomsk State Pedagogical University, Issue 3(93), 108-112. (in Russian)

Dyukarev E.A., Vyaizya A.A., Kiselev M.V. (2019). Differences in temperature regime of peat and mineral soil at Bakchar district of Tomsk region. Environmental dynamics and global climate change, V. 10, № 2, 100-109.

Eskelinen, R., Ronkanen, A.-K., Marttila, H., Isokangas, E., Kløve, B. (2016). Effect of soil frost on drained peat soils on snowmelt runoff and surface water quality. Boreal Environmental Research, 21, 556–570.

Evseeva, N. S., Sinyutkina A.A., Kharanzhevskaya, Yu.A. et al. (2012). Landscape of the mires in Tomsk Region. Tomsk: Publishing house of NTL. 400 p. (in Russian)

Finér, L., Lepistö, A., Karlsson, K., Räike, A., Härkönen, L., Huttunen, M., … Ukonmaanaho, L. (2021). Drainage for forestry increases N, P and TOC export to boreal surface waters. Science of The Total Environment, 762, 144098. doi:10.1016/j.scitotenv.2020.1440

Finstad, A.G., Anderson, T., Larsen, S., Tominaga, K., Blumentrath, S., de Wit, H.A., Tommervik, H., Hessen, D.O. (2016). From greening to browning: catchment vegetation development and reduced S-deposition promote organic carbon load on decadal time scales in Nordic lakes. Scientific Reports, 6, 31944. https://doi.org/10.1038/srep31944

Frey, K. E. (2005). Amplified carbon release from vast West Siberian peatlands by 2100. Geophysical Research Letters, 32(9). doi:10.1029/2004gl022025

Harris L.I., Moore T.R., Roulet N.T., Pinsonneault A.J. (2020). Limited effect of drainage on peat properties, porewater chemistry, and peat decomposition proxies in a boreal peatland. Biogeochemistry, 151, 43–62. DOI: 10.1007/s10533-020-00707-1

Kharuk V. I., Ponomarev E. I., Ivanova G. A., Dvinskaya M. L., Coogan S. C., and Flannigan M. D. (2021). Wildfires in the Siberian taiga. Ambio, 50, 1953–1974, https://doi.org/10.1007/s13280-020-01490-x, 2021.

Kharyutkina E.V., Loginov S.V., Usova E.I., Martynova Yu.V., Pustovalov K.N. (2019). Tendencies in changes of climate extremality in Western Siberia at the end of the XX century and the of the beginning of the XXI century. Fundamental and Applied Climatology, 2, 45-65.

Kharanzhevskaya Yu. A., Sinyutkina A. A. (2021). Effects of wildfire on the water chemistry of the northeastern part of the Great Vasyugan Mire (Western Siberia). IOP Conf. Series: Earth and Environmental Science, 928, 012006. doi:10.1088/1755-1315/928/1/012006

Kharanzhevskaya Yu. A. (2022a). Seasonal and long-term dynamics of water chemistry within the drained part of the great Vasyugan mire. Bulletin of the Tomsk Polytechnic University. Geo Assets Engineering, 333, № 8, 215-225. https://doi.org/10.18799/24131830/2022/8/3649

Kharanzhevskaya Yu. A. (2022b). Effect of Drainage on Spatio-Temporal Variation in Water Chemistry of the Great Vasyugan Mire. Geography and Natural Resources, Vol. 43, Suppl. 1, S36–S43. https://doi.org/10.1134/S1875372822050110

Kirpotin, S. N., Berezin, A., Bazanov, V., Polishchuk, Y., Vorobiov, S., Mironycheva-Tokoreva, N., Kosykh, N., Volkova, I., Dupre, B., Pokrovsky, O., Kouraev, A., Zakharova, E., Shirokova, L., Mognard,N., Biancamaria, S., Viers, J., Kolmakova, M., (2009). Western Siberia wetlands as indicator and regulator of climate change on the global scale. International Journal of Environmental Studies, 66, No. 4, 409–421. https://doi.org/10.1080/00207233.2014.942537

Krickov, I.V., Pokrovsky, O.S., Manasypov, R.M., Lim, A.G., Shirokova, L.S., Viers, J. (2019). Colloidal transport of carbon and metals by western Siberian rivers during different seasons across a permafrost gradient. Geochimica et Cosmochimica Acta, 265, 15 November 2019, 221-241. doi: https://doi.org/10.1016/j.gca.2019.08.041

Lepistö, A., Futter, M.N., Kortelainen, P. (2014). Almost 50 years of monitoring shows that climate, not forestry, controls long-term organic carbon fluxes in a large boreal watershed. Global Change Biology, 20 (4), 1225–1237. doi: 10.1111/gcb.12491

Liss O.L., Abramova L.I., Berezina N.A. (2001). Peatlands of Western Siberia and their conservation value. Tula: Grif and K0, 584 p.

Lurie Yu.Yu. Unified methods of water analysis. M.: Nauka, 1973. 376 p.

Lydersen E., Høgberget R., Moreno C.E. et al. (2014). The effects of wildfire on the water chemistry of dilute, acidic lakes in southern Norway. Biogeochemistry, 119, 109–124 https://doi.org/10.1007/s10533-014-9951-8

Maloletko A.A., Sinyutkina A.A., Gashkova L.P., Kharanzhevskaya Yu.A., Magur M.G., Voistinova E.S., Ivanova E.S., Chudinovskaya L.A., Khaustova A.A. (2018). Effects of long-term drainage on vegetation, surface topography, hydrology and water chemistry of north-eastern part of Great Vasyugan Mire (Western Siberia). IOP Conference Series: Earth and Environmental Science, Volume 211 (1). 012033 http://iopscience.iop.org/article/10.1088/1755-1315/211/1/012033

Marttila, H., Karjalainen, S.-M., Kuoppala, M., Nieminen, M. L., Ronkanen, A.-K., Kløve, B., & Hellsten, S. (2018). Elevated nutrient concentrations in headwaters affected by drained peatland. Science of The Total Environment, 643, 1304–1313. doi:10.1016/j.scitotenv.2018.06.2

Neishtadt M.I. (1971). The world natural phenomenon – swampiness of the West Siberian Plain. Proceedings of the Academy of Sciences of the USSR, Geographic series, No. 1, 21–34. (in Russian)

Nelson, K., Thompson, D., Hopkinson, C., Petrone, R., & Chasmer, L. (2021). Peatland-fire interactions: A review of wildland fire feedbacks and interactions in Canadian boreal peatlands. Science of The Total Environment, 769, 145212. doi:10.1016/j.scitotenv.2021.145212

Nieminen, M., Sallantaus, T., Ukonmaanaho, L., Nieminen, T.M., Sarkkola, S. (2017). Nitrogen and phosphorus concentrations in discharge from drained peatland forests are increasing. Science of The Total Environment, 609, 974–981. doi: 10.1016/j.scitotenv.2017.07.210

Nieminen, M., Sarkkola, S., Tolvanen, A., Tervahauta, A., Saarimaa, M., & Sallantaus, T. (2020). Water quality management dilemma: Increased nutrient, carbon, and heavy metal exports from forestry-drained peatlands restored for use as wetland buffer areas. Forest Ecology and Management, 465, 118089. doi:10.1016/j.foreco.2020.118089

Nieminen, M., Sarkkola, S., Hasselquist, E.M. et al. (2021). Long-Term Nitrogen and Phosphorus Dynamics in Waters Discharging from Forestry-Drained and Undrained Boreal Peatlands. Water Air Soil Pollution, 232, 371. https://doi.org/10.1007/s11270-021-05293-y

Peatlands of Western Siberia: their structure and hydrological regime. (1976). L.: Gidrometeoizdat, 447 p.

Pokrovsky, O.S., Manasypov, R.M., Loiko, S., Shirokova, L.S., Krickov, I.A., Pokrovsky, B.G., Kolesnichenko, L.G., Kopysov, S.G., Zemtzov, V.A., Kulizhsky, S.P., Vorobyev, S.N. &Kirpotin, S. N. (2015). Permafrost coverage, watershed area and season control of dissolved carbon and major elements in western Siberian rivers. Biogeosciences, 12, 6301–6320. https://doi.org/10.5194/bg-12-6301-2015.

Rust A. J., Hogue T. S., Saxe S., McCray J. (2018). Post-fire water-quality response in the western United States. International Journal of Wildland Fire, 27(3), 203. doi:10.1071/wf17115

Savichev O.G. (2007). Hydrochemical runoff in the Middle Ob basin. Bulletin of the Tomsk Polytechnic University. Geo Assets Engineering, V. 310, No. 1, 29-34.

Savichev, O.G., Mazurov, A.K., Pipko, I.I., Sergienko, V.I., Semiletova, I.P. (2016). Spatial patterns of the evolution of the chemical composition and discharge of river water in the Ob River basin. Doklady Earth Sciences, 466(1), 59-63. https://doi.org/10.1134/S1028334X16010141

Savichev O.G., Mazurov A.K., Rudmin M.A., Khvashchevskaya A.A., Dauletova A.B. Background indicators of the ecological and geochemical state of the waters of raised bogs in the taiga zone on the territory of the Russian Federation Bulletin of the Tomsk Polytechnic University. Geo Assets Engineering, 2018, Vol. 329, No 9, pp. 101-116.

Sinyutkina A. A., Gashkova L.P., Koronatova N.G., Maloletko A.A., Mironycheva-Tokareva N. P., Russkikh I.V., Serebrennikova O.V., Strel'nikova E.B., Vishnyakova E.K. Kharanzhevskaya Yu. A. (2020). Post-fire ecological consequences within the drained site of the Great Vasyugan Mire: retrospective water-thermal regime and pyrogenic disturbance estimation. IOP Conf. Ser.: Earth Environ. Sci., Vol. 408, 012037. doi: 10.1088/1755-1315/408/1/012037

Sinyutkina A. A. (2021). Drainage consequences and self-restoration of drained raised bogs in the south-eastern part of Western Siberia: Peat accumulation and vegetation dynamics. Catena, № 205, 105464. https://doi.org/10.1016/j.catena.2021.105464

Stirling E., Macdonald L.M., Smernik R.J., Cavagnaro T.R. (2019). Post fire litters are richer in water soluble carbon and lead to increased microbial activity. Applied Soil Ecology, 136, 101–105.

STP 0493925-008-93. Determination of dissolved organic carbon using the Tyurin method modified by SibNIIT. 1993. 20 p.

Sulwiński M., Mętrak M., Wilk M., Suska-Malawska M. (2020). Smouldering fire in a nutrient-limited wetland ecosystem: Long-lasting changes in water and soil chemistry facilitate shrub expansion into a drained burned fen. Science of The Total Environment, 746, 141142. doi:10.1016/j.scitotenv.2020.141142

Terentieva, I.E., Glagolev, M. V., Lapshina, E. D., Sabrekov, A. F., Maksyutov S. (2016). Mapping of West Siberian taiga wetland complexes using Landsat imagery: implications for methane emissions. Biogeosciences, 13, 4615–4626. https://doi.org/10.5194/bg-13-4615-2016

Third assessment report of Roshydromet on climate change and its consequences on the territory of the Russian Federation /edited by V. M. Kattsova; Roshydromet. St. Petersburg: High technology, 2022. 676 p.

Tokareva I.V., Korets M.A. and Prokushkin A.S. (2022). Nutrients in streams draining the different types of wetlands in Western Siberian Plain. IOP Conf. Ser.: Earth Environ. Sci. 1093, 012018. DOI 10.1088/1755-1315/1093/1/012018

Wu Yichen and Xu Xuebin and McCarter, Colin P.R. and Zhang, Nan and Ganzoury, Mohamed A. and Waddington, James Michael and de Lannoy, Charles-François (2022). Assessing leached TOC, nutrients and phenols from peatland soils after lab-simulated wildfires: Implications to source water protection. Science of The Total Environment, Volume 822, 153579 https://doi.org/10.1016/j.scitotenv.2022.153579

RESEARCH PAPER

RELEVANCE OF ERA5 REANALYSIS FOR WIND ENERGY APPLICATIONS: COMPARISON WITH SODAR OBSERVATIONS

Shestakova AnnaA.[1,2], Fedotova Ekaterina V.[3], Lyulyukin Vasily S.[1,4]
[1]Obukhov Institute of Atmospheric Physics of the Russian Academy of Science, Pyzhevskij 3, Moscow, 119017, Russia
[2]Research Computing Center of the Lomonosov Moscow State University, Leninskie Gory, 1, building 4, Moscow, 119234, Russia
[3]Moscow Power Engineering Institute, Krasnokazarmennaya 14, Moscow, 111250, Russia
[4]Bauman Moscow State Technical University, 2nd Baumanskaya street, 5, building 1, Moscow, 105005, Russia
*Corresponding author: shestakova.aa.92@gmail.com
Received: February 28th, 2023 / Accepted: February 6th, 2024 / Published: March 31st, 2024
https://DOI-10.24057/2071-9388-2023-2782

ABSTRACT. ERA5 reanalysis is one of the most trusted climate data sources for wind energy modeling. However, any reanalysis should be verified through comparison with observational data to detect biases before further use. For wind verification at heights close to typical wind turbine hub heights (i.e. about 100 m), it is preferable to use either in-situ measurements from meteorological towers or remote sensing data like acoustic and laser vertical profilers, which remain independent of reanalysis. In this study, we validated the wind speed data from ERA5 at a height of 100 m using data from four sodars (acoustic profilers) located in different climatic and natural vegetation zones across European Russia. The assessments revealed a systematic error at most stations; in general, ERA5 tends to overestimate wind speed over forests and underestimate it over grasslands and deserts. As anticipated, the largest errors were observed at a station on the mountain coast, where the relative wind speed error reached 45%. We performed the bias correction which reduced absolute errors and eliminated the error dependence on the daily course, which was crucial for wind energy modeling. Without bias correction, the error in the wind power capacity factor ranged from 30 to 50%. Hence, it is strongly recommended to apply correction of ERA5 for energy calculations, at least in the areas under consideration..

KEYWORDS: water chemistry, mire, drainage, wildfire, Western Siberia

CITATION: Shestakova A.A., Fedotova E.V., Lyulyukin V.S. (2024). Relevance Of Era5 Reanalysis For Wind Energy Applications: Comparison With Sodar Observations. Geography, Environment, Sustainability, 1(17), 54-66
https://DOI-10.24057/2071-9388-2023-2782

ACKNOWLEDGEMENTS: This study was supported by the Russian Science Foundation (project No. 18-79-10255) (reanalysis verification and correction; capacity factor estimation) and the state assignments of the A.M. Obukhov Institute of Atmospheric Physics RAS № FMWR-2022-0001 (preparation of reanalysis data; analysis of the daily course of reanalysis errors) and № FMWR-2022-0017 (sodar data processing).

Conflict of interests: The authors reported no potential conflict of interest.

INTRODUCTION

Nowadays, a rapid transformation in the energy sector implies making policy decisions for long-term energy planning under numerous uncertainties. Energy modeling is the key tool for providing evidence to support decision-making processes. A rapidly increasing share of the climate-governed renewable generation determines the demand for accurate climate data. At the same time, climate information is not only used for renewables but also for traditional energy sources. Energy models rely on climate data covering a wide spatial range, from point-wise observations for individual power plants to global energy system models that include all types of energy and require global-scale climate datasets. Among various energy problems that require climate information are the assessment of the renewable energy potential, the planning of new power plants and power grids, optimization cost evaluation of technology mix for energy systems, and the assessment of the climate change impact on existing power plants. Therefore, high-quality climate data for diverse energy applications is in great demand.

Modern reanalysis datasets belong to the most widely used sources of climate inputs for energy modeling. Reanalysis involves numerical simulations with atmospheric or Earth system models over a rather long period (>10 years, typically 40-70 years), initialized from past data and updated with observational data interpolated onto the model grid every few hours or days.

Reanalysis offers both advantages and disadvantages, and the latter primarily include inaccuracies in meteorological data compared to observed values, especially in areas with complex topography and surface types. These inaccuracies are associated with numerical model imperfections, errors in assimilated observational data, and coarse horizontal and vertical resolution. Reanalysis errors are usually associated with incorrect reproduction of orography (Dörenkämper et al. 2020) and underlying surface types (Gualtieri 2021). However, currently, there is no real alternative to reanalysis in terms of both spatial and temporal coverage.

In this study, we assessed the quality of climate information on wind, a critical climate input for various energy models. For correct work of energy models, climate information on wind should realistically reflect statistical wind characteristics, namely the probability distribution function of wind speed and seasonal and diurnal wind speed courses. The wind in the lower atmosphere is largely determined by the turbulent structure of the atmospheric boundary layer, which is tolerably reflected only in measurements with high vertical and temporal resolution (for example, in measurements on meteorological masts or using acoustic profilers), but is usually poorly reproduced by reanalysis. In this context, verification of wind data in reanalysis does not seem far-fetched, but a necessary task. However, utilization of the original (uncorrected) reanalysis data without verification and correction remains quite widespread in the energy modeling domain (Craig et al. 2022). Verification of reanalysis datasets is partly hampered by the rarity of the so-called independent data, i.e. those that are not assimilated in reanalysis. Independent data on wind includes local and typically short-term measurements on meteorological masts, sodars, and other means of ground-based remote sensing, ground-based networks of local stations, and some others.

Uncertainties associated with reanalysis data usage vary regionally, which means that the applicability of the reanalysis datasets should be assessed for specific regions of interest. Currently, research on reanalysis uncertainties is predominantly focused on Europe and the Americas (e.g., Molina et al. 2021; Thomas et al. 2021; Kubik et al. 2013; Santos et al. 2019; Staffell and Pfenninger 2016; Olauson 2018; Jourdier 2020; Dörenkämper et al. 2020). However, even for these regions, it is impossible to obtain unambiguous conclusions about the quality of wind data in particular reanalysis cases because quality evaluations depend on specific tasks, orographic complexity and land use of the site, and the verification method. At the same time, other areas of the world are much less studied at the time being. This knowledge gap is becoming crucial from the perspective of the global energy transition. The regions facing the most serious challenges in the implementation of renewable generation are least covered with the quality assessment of key climate inputs for energy planning studies.

The primary objective of this study is to assess the viability of using wind speed data at the 100 m level from the modern ERA5 reanalysis for energy modeling across European Russia. We selected ERA5 because of its popularity within the energy community and its use in creating other products, including both global (GWA) and European (NEWA) wind atlases, which use ERA5 as input data for mesoscale and microscale models to produce high-resolution outputs (Dörenkämper et al. 2020). However, the error in the initial data usually propagates further along the chain and can be found in the output fields. Therefore, we decided to validate the original ERA5 reanalysis to get a quantification of its performance in the context of energy modeling. Most comparative studies ((Ramon et al. 2019; Santos et al. 2019; Olauson 2018; Thomas et al. 2021), however, not all of them, e.g. (Calisir et al. 2021)) have shown that ERA5 outperforms other reanalyses in terms of wind speed and calculated wind power generation.

We compared ERA5 against measurements from acoustic locators (sodars) across central and southern parts of European Russia. Most sodar locations are situated in the southern regions, which are known for their high wind energy potential (Spravochnik 2007), where this industry is actively developing with new wind turbines being constructed. While ERA5 was previously verified against different sources of wind data in many regions across the world (Gualtieri 2021; Ramon et al. 2019; Santos et al. 2019; Olauson 2018; Molina et al. 2021; Calisir et al. 2021), its performance depends heavily on individual site characteristics and averaging periods. For instance, correlation coefficients of ERA5 with observations vary from 0.2-0.3 for stations with complex terrain to almost 1 for flat sites (Molina et al. 2021; Ramon et al. 2019; Santos et al. 2019; Jourdier 2020). Especially high correlation coefficients of 0.9-0.95 are obtained with increasing averaging time (Santos et al. 2019; Molina et al. 2021).

The spread of wind speed bias is very large across estimates reported by different studies: from -5 m s^{-1} to 4 m s^{-1} (Dörenkämper et al. 2020; Ramon et al. 2019; Molina et al. 2021; Jourdier 2020). Generally, the reanalysis performs better over the sea, while its quality is often not suitable for energy problems on land. This is explained, firstly, by the fact that the roughness of the sea surface depends on wind speed in a rather straightforward way, while the assessment of the land surface roughness is quite ambiguous. Secondly, reanalyses assimilate satellite wind observations only available over the ocean. Over the sea surface, ERA5 may slightly overestimate the wind speed (Ramon et al. 2019; Gualtieri 2021). Over the land, the wind speed, especially for strong winds, is underestimated and the frequency of weak winds is overestimated (Molina et al. 2021; Jourdier 2020; Santos et al. 2019; Gualtieri 2021). The only exception is forest areas, over which wind speed is overestimated (Gualtieri 2021), which is usually explained by the difficulty of determining the roughness length for a forest.

The hourly resolution of the ERA5 data allows us to consider the daily course of wind speed. Still, there is no clear dependence of the reanalysis quality on the time of day – at some stations, the error is greater at night, and at others during the day (Jourdier 2020). All these errors naturally affect the accuracy of wind power generation calculations, and, due to the nonlinear dependence of wind generation on wind speed, even with a small error in wind speed, the error in wind generation estimates becomes significant (Andersen et al. 2015; Gualtieri 2021). Wind power generation calculated from ERA5 data is usually slightly overestimated over the sea (e.g., Gualtieri 2021) and underestimated on the land by 5-20% in flat areas (except in forested areas, where it is overestimated (Gualtieri 2021)) and by more than 30% in areas with complex terrain (Dörenkämper et al. 2020; Gualtieri 2021; Jourdier 2020). However, with monthly averaging and in areas such as Scandinavia, great agreement can be achieved between reanalysis-calculated and observed power generation (Olauson 2018). Generally, the more estimates of reanalysis quality for sites in various natural conditions are obtained, the more complete picture of the quality of the reanalysis can be acquired and the higher the probability of finding the dependence of the error on these conditions.

Another aim of this study was to test the bias-correction method to correct the reanalysis of wind speed using sodar observations. The correction was performed in two ways: with and without the daily course of wind speed errors. The original and corrected wind speed series from the reanalysis were used to assess the relevance of the bias correction for quantifying the propagation of wind speed error into wind energy production, expressed as the capacity factor error. In general, the study is focused not on planning wind energy construction at specific locations, but on the development of the operation of universal methods that can be applied to any other area. The universality of the methods means that they can be applied to any region and reanalysis grid node. Although their application requires non-universal scaling factors that depend on local conditions, we assume that in the future it will be possible to obtain the dependence of these scaling factors on external conditions, which will make the bias correction method completely universal. This study also aims to supply energy modelers with a power-relevant estimation of uncertainty associated with errors of the modern reanalysis for natural conditions typical for various natural zones of Russia. Therefore, it is not of primary importance that not all sites we are considering are located in areas with high wind energy potential.

The rest of the article is organized as follows. The section Materials and Methods describes the sodar observations and ERA5 wind data, methods of reanalysis verification and correction, and capacity factor calculation. The Results and Discussion section presents the results of reanalysis verification and correction and considers the propagation of the wind speed error into errors in energy modeling. In conclusion, the main findings and limitations of the study are presented.

MATERIALS AND METHODS

Sodar data

Sodar (SOnic Detection And Ranging) is an acoustic locator providing vertical profiles of wind vector components within the lowest 500-m layer of the atmosphere. In this study, sodar observations from four locations were used (Table 1, Fig.1). Continuous measurements up to 300 m in height were carried out in the Zvenigorod area at the observation station of the Obukhov Institute of Atmospheric Physics (IAP) from 2009 to 2021. The IAP station is predominantly surrounded by mixed forest and occasional low-rise buildings (Fig.1b). Sodar measurements for steppe, arid, and coastal regions were obtained in short-term expeditions organized by the IAP (for Tsimlyansk and Kalmykia) and Lomonosov Moscow State University (for the Gelendzhik area). Measurements up to 200 m were conducted on the northern edge of Tsimlyansk (in a flat steppe area) in July-August, with a vertical resolution of 10 m . Measurements in dunes near Narynkhuduk in Kalmykia, 80 km northwest of the Caspian Sea, were carried out in late July–early August. In the Gelendzhik area, the measurements were carried out on the base of the Institute of Oceanology, at the end of a long pier, essentially over the sea surface (Fig.1e).

The Sodar LATAN-3, developed at IAP (Kuznetsov 2007), was employed in Zvenigorod, Kalmykia, and Tsimlyansk. The wind speed measurement accuracy was 0.3 m/s. In Gelendzhik, the measurements were carried out with a Scintec sodar (co-production of Germany, the USA, and some other countries), with a declared wind speed measurement accuracy of 0.1-0.3 m/s.

Data processing was performed to eliminate erroneous measurements. At the IAP base in Zvenigorod, trees and individual buildings contributed to the "blind zone" of the sodar, resulting in a higher occurrence of erroneous registrations of the echo signal from fixed objects ("fixed echoes"). To ensure maximum data availability at all levels, the lower measurement level ("blind zone") was set at 40 meters for Zvenigorod site and 30 meters for arid and steppe sites. The presence of "fixed echoes" led to

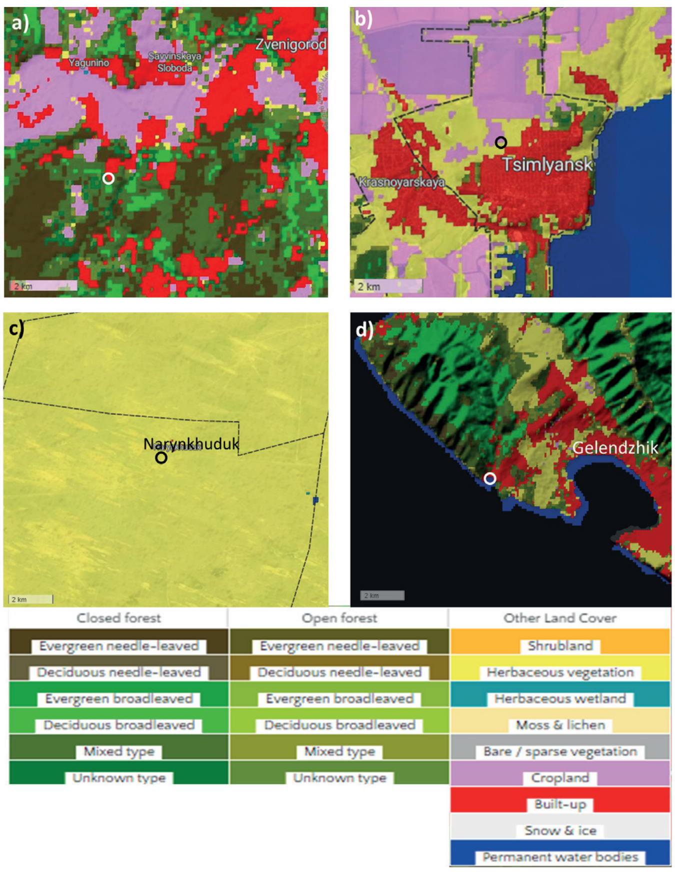

Fig. 1. Satellite image of the study area (a) and types of land cover (from Global Land Cover database, available at https://lcviewer.vito.be) around sodar locations (white and black circles) in Zvenigorod (b), Tsimlyansk (c), Kalmykia (d) and Gelendzhik (e)

an increase in the number of near-zero wind speeds at altitudes up to 300 m, significantly distorting wind statistics at this station. To remove the influence of obstacles from the data, a two-stage filtering algorithm was applied. In the first stage, instantaneous sounding profiles were analyzed, and intervals with zero wind speed at heights exceeding 40 meters and intervals with a significant excess of the echo signal level (> 3 dB) relative to adjacent intervals were excluded from averaging. Subsequently, in the second stage, the averaged data were filtered to eliminate sharp peaks in the vertical profiles. For this purpose, outliers in the vertical profiles of horizontal wind speed were filtered out if they exceeded 2 m/s compared to adjacent vertical levels.

Reanalysis and its processing

In this study, we compared the wind speed from ERA5 reanalysis (Hersbach et al. 2020) with observations taken at a 100-m height. This height is commonly used in wind energy studies, as it corresponds to the typical hub height of wind turbines. In reanalysis, wind speed values at heights of 100 m above ground level (a.g.l.) and below are considered diagnostic, meaning they are not directly calculated in the atmospheric model but rather interpolated from the lowest model level to the desired height using a wind profile approximation (logarithmic or power law). However, this approximation is valid only for neutral temperature stratification and moderate to strong wind. Vertical interpolation also requires the surface roughness length (or power law exponent), which is set constant on land (depending on the type of land cover) and dependent on wind speed over water. Thus, the values of the diagnostic wind speed contain errors associated with the deviation of the real wind profile from the approximation and with the inaccuracy in determining the roughness length/power law exponent.

The ERA5 reanalysis has 137 hybrid sigma levels from 10 m to 80 km above the surface, with 14 levels located in the lowest 500-m layer. This high resolution, coupled with the low placement of the lowest level (on average at 10 meters above ground level), minimizes errors in interpolation at both 10 and 100 meters, making ERA5 advantageous for wind generation studies compared to other reanalyses.

To compare observations with ERA5 reanalysis, we employed two approaches. The first one involved the interpolation of the reanalysis of 100-m wind horizontally to sodar locations. The series of observations were averaged over an hourly interval based on the following assumptions. The value in a reanalysis cell was the average over the area occupied by that cell. Since one reanalysis cell occupied 0.25°x0.25°, i.e. about 25 x 18 km at middle latitudes, then at an average speed of 5 m/s (characteristic speed for all the studied points), the airflow passed the entire cell in 1-1.5 h. This means that the reanalysis value averaged over the area of the cell could be compared with the 1-h mean of observations at one point.

The interpolation was carried out by the two most popular methods: the bilinear interpolation method and the nearest neighbor method. The latter implies that the reanalysis values are not interpolated, but are taken from the grid node closest to the observation station. Hence the verification results should significantly depend on how close the underlying surface in the reanalysis area is classified in comparison to the reality. In Zvenigorod, the nearest reanalysis nodes were occupied by forests (80% forest cover). The roughness coefficient in the reanalysis was plausibly high (around 0.9 m). For the Tsimlyansk station, land cover at the nearest node corresponded to crops (see Fig.1c), with a roughness length of around 0.3 m (which was quite high, since the roughness length for low grass is typically a few centimeters (Zilitinkevich 1972)). Other nodes to the east were partially occupied by water (Tsimlyansk reservoir). In Kalmykia, the land cover of nearby nodes was indicated as grass. The surrounding nodes were also classified as crops and sediments. The roughness coefficient was around 0.15 m, which was quite high for a relatively smooth dune surface. In Gelendzhik, the closest reanalysis node to the station was in the sea, and the cell that corresponded to it was 70% occupied by water. The cell average roughness coefficient was around 0.3 m. However, in reality, the land cover near the station was represented by a low pine forest, while the water roughness in the absence of waves is usually less than 1 cm. In Gelendzhik, the dependence of the reanalysis error on the wind direction (from the sea or land) was quite possible. In general, the surface types in the reanalysis nodes corresponded to reality.

The second approach to comparing reanalysis and observations involved averaging the reanalysis data over the area around the cell where the station point was located (hereafter, "averaging method"). Averaging was carried out over the area of 3 x 3 cells (approximately 75 x 55 km). An increase in the averaging area from 1 cell to 3 cells also led to an increase in the averaging period of observations from 1 h to 3 h. From general considerations, the verification results should improve with this approach, although the value of the obtained information decreases due to smoothing.

Table 1. Observation sites and characteristics of sodar measurements

	Coordinates, elevation	Land use; topography	Sodar system	Period	Vertical resolution; maximum height of measurements; averaging period
Zvenigorod	55.696ºN, 36.775ºE, 180 m a.g.l.	Mixed forest with few buildings	LATAN-3	2009-2021	20 m; 300 m; 30 min
Tsimlyansk	46.657ºN, 42.08ºE, 86 m a.g.l.	Steppe (low grass) with low-rise buildings to the south; flat topography	LATAN-3	2012, 2015-2021 (July-August)	10 m; 200 m; 30 min
Kalmykia	45.423ºN, 46.53ºE, -20 m a.g.l.	Dunes (desert); flat topography	LATAN-3	2016, 2020, 2021 (July-August)	10 m; 200 m; 30 min
Gelendzhik	44.575ºN, 37.979ºE, 4 m a.g.l.	Sea; mountains to the north	Scintec	2012 (June-July), 2012-2014 (January-February)	5 m; 300 m; 10-20 min

Verification methods

An interesting issue that requires further investigation is the problem of the criteria for the quality of wind data, specifically for wind energy applications. Since wind energy performance is very sensitive to wind speed, it can be expected that the quality criteria should also be quite strict. However, in the absence of such tailored criteria, we used a set of standard ones: bias, normalized bias (NB), mean absolute error (MAE), the standard deviation (scatter) of errors (SDE), normalized root mean square error (NRMSE), normalized standard deviation of wind speed in reanalysis (NSD), and correlation coefficient (CC), which are commonly used in practical energy-related climate data quality assessments. We also considered the empirical probability distribution function of errors, wind speed, and direction, and the dependence of the error on the wind speed and direction.

Typically, wind speed error is deemed acceptable if it does not exceed 10% of the value for speeds greater than 5 m/s, or if the error is less than 0.5 m/s for wind speeds less than 5 m/s (WMO 2014). Although these criteria were developed for standard wind measurements at ground-based weather stations, they can also be applied to assess the quality of wind in reanalysis when other strict criteria are lacking. We calculated the percentage of errors within acceptable accuracy (PEAA) based on these criteria, with a higher PEAA indicating better performance. Additionally, we used the ratio of the error value to the standard deviation of wind speed from observations (SDW) as a criterion for the reanalysis quality: if the error is comparable to or greater than SDW, which represents the natural variability of wind speed, then the quality of wind in the reanalysis is considered low.

Bias correction method

When systematic errors are detected in reanalysis data or climate model outputs, they are usually corrected using various methods. One commonly used method for correcting wind speed data is the Quantile Mapping based on the Weibull Distribution bias correction method (Haas et al. 2014). The method involves calculating the corrected wind speed u_{cor} using the following formula, which transforms the reanalysis's probability distribution function to match the observed distribution:

$$u_{cor} = c_o \left[-\ln \left(1 - \left(1 - e^{-\left(\frac{u_r}{c_r}\right)^{k_r}} \right) \right) \right]^{k_o^{-1}} \quad (1)$$

Here, the subscripts $_o$ and $_r$ mean observations and reanalysis, and the shape parameter k and scale parameter c are calculated from the mean μ and standard deviation σ of wind speed:

$$k = \left(\frac{\mu}{\sigma} \right)^{1.086} \quad (2)$$

$$c = \frac{\mu}{\Gamma\left(1 + \frac{1}{k}\right)} \quad (3)$$

where Γ is the gamma function.

In many studies (e.g., Li et al. 2019, Akperov et al. 2022, Akperov et al. 2023), the parameters *k* and *c* were calculated separately for each month. However, due to limited year-round data at stations (except Zvenigorod), we initially calculated these parameters for the entire data series rather than for each month. Subsequently, we further calculated these coefficients for each hour of the day and each month for Zvenigorod owing to the abundance of observations there, and for each hour of the day in July-August for Tsimlyansk. This approach was adopted to account for the daily (and annual in Zvenigorod) variation of the reanalysis wind speed error when performing corrections.

Capacity factor calculation

Wind speed dynamics affects wind generation performance most directly. This implies that uncertainties of the wind speed are being translated into uncertainties in wind power generation. A common method to convert wind speed into generated power is by using a so-called working curve of a wind turbine (Andresen et al. 2015). A wind turbine working curve is the relationship between the harnessed power and the wind speed. Typically, working curves are nonlinear, exhibiting higher sensitivity to speed variation at lower speed values. Working curves provided by manufacturers are derived from testing procedures conducted on a hub height under conditions reflective of wind generation unit operation.

We calculated the propagation of the ERA5 uncertainties on the operation of modern wind turbines using various approaches to bias correction. Calculations were performed based on the assumption of a realistic working curve of modern wind turbines. An example of such a curve is provided in Fig. 2.

The combination of a wind turbine power curve with actual wind speed values determines the wind power

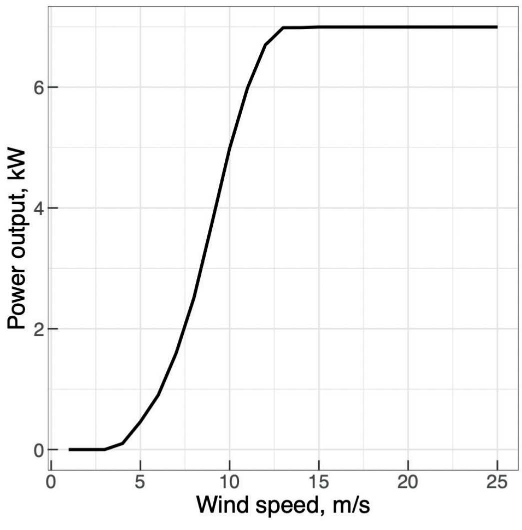

Fig. 2. A working curve for "Vestas V164" wind turbine

generation achievable at any particular location. The economic feasibility of wind generation can be roughly assessed using a capacity factor which is defined as the ratio of the actual harnessed power to the nominal power of a turbine. Additionally, we assumed that turbine construction is viable if its annual average capacity factor matches with typical values reported for wind generation.

Relevance of the wind speed values for wind power generation was addressed for each considered location using a linear scaling approach for the wind speed time series, which involved increasing wind speed values using a constant multiplier. This artificial approach aimed to account for the fact that the available measurement locations were not selected to maximize wind power output. Capacity factor values based on the "original" reanalysis data served as a reference point to match with a situation when the reanalysis data are utilized directly in energy simulations omitting any correction procedures. Indeed, the applied linear scaling procedure is a simplification intended only for a robust estimation of the broad effects that reanalysis errors may have on energy modeling outcomes. The scaling factor values were determined through a fitting procedure to achieve multiannual average capacity factors consistent with typical values for modern onshore wind generation, assumed to range from 0.25 to 0.35 based on global statistics (Boretti and Castelletto 2020; Jung and Schindler 2022).

The calculated capacity factors were averaged over the entire available observation period and compared against the assumed typical annual average values. To account for the nonlinear sensitivity of wind turbine performance to wind speed, the scaling factor was varied within the assumed typical capacity range. This scaling approach was applied to wind speed data for all considered stations except Gelendzhik. The ERA5-extracted wind speed values for Gerendzhik were high enough to yield capacity factors exceeding 0.35, the assumed upper boundary of the typical capacity factor range.

The range of the fitted scaling factor values depended primarily on the annual average wind speed and was found to be 1.15 to 1.30 for Zvenigorod and Tsimlyansk, and 1.25 to 1.43 for Kalmykia, with no scaling needed for Gelendzhik. These obtained scaling factor ranges were compared against wind speed values within approximately a 50 km radius around each station location, corresponding to the correlation length for wind speed aggregated with hourly time resolution and combined with a potential to vary the hub height between 70 and 200 m, following current standards.

RESULTS AND DISCUSSION

Verification

Statistical characteristics of the wind speed reanalysis error are shown in Table 2 and Figure 3. Notably, there is minimal difference between the verification results when using bilinear and the nearest neighbor interpolation methods. Previous studies (Ramon et al. 2019) also demonstrated the same independence of estimates from the interpolation method for ERA5, although the difference between methods arises for reanalyses with coarser spatial resolution. Therefore, we focus on the results obtained using the bilinear interpolation method.

It should be kept in mind that the amount of data available in Zvenigorod is several orders of magnitude higher than for other sites (Table 2), making the statistical estimates for Zvenigorod the most reliable. Systematic errors are observed at most stations (except for Gelendzhik). The Mean Absolute Error (MAE) varies from 1.4 to 2.1 m/s, with errors consistently lower than the standard deviation of the wind speed at all locations (Table 2). On average, 59% of errors fall within acceptable accuracy criteria. The average correlation coefficient between reanalysis and observations is 0.7. Across all locations except Zvenigorod, the reanalysis underestimates the frequency of wind speeds over 8-10 m/s (Fig. 4). The frequency of wind directions in the reanalysis roughly corresponds to the observed values (Fig. 5).

Variations in verification results among the stations can be attributed to the differences in the "complexity" of the areas where the stations are located. The highest errors are observed in Zvenigorod, despite its larger sample size, due to the presence of a high and heterogeneous forest which disrupts the logarithmic wind profile. At the same time, Tsimlyansk demonstrates the best results among all stations (i.e. the smallest MAE and SDE, the largest correlation coefficient), which is explained by the favorable location (the absence of significant obstacles nearby).

In Zvenigorod, the largest errors occur during weak winds of any direction (Fig.4a, 5a). In general, the wind speed probability distribution is shifted towards higher wind speeds in the reanalysis compared to observations (Fig. 4). This systematic overestimation may stem from the underestimation of roughness length and the deviation of the wind profile observed over the forest from the logarithmic profile, especially evident during weak winds.

In Tsimlyansk, there is a slight systematic underestimation of wind speed, particularly noticeable during the night (Fig.6b), possibly due to the absence of night low-level jet streams or an inaccurate description of momentum transfer processes under stable boundary layer stratification in the reanalysis. The largest underestimations, up to 7 m/s, are observed when the wind speed exceeds 7 m/s , and with errors reaching 5 m/s during weak winds. There is no clear dependence of the error on wind direction (Fig.5b).

In Kalmykia, the reanalysis similarly tends to underestimate wind speed, which can be explained with local effects, particularly the frequent sandstorms. During sandstorms, the roughness length becomes highly dependent on wind speed (Semenov 2020), similar to the sea surface, with values changing by four orders of magnitude. Additionally, flow acceleration may occur due to the influence of sand in the air, which disrupts the logarithmic wind profile (Semenov

Table 2. Statistical characteristics of wind speed reanalysis errors following bilinear interpolation method (BIM) and nearest neighbor method (NNM)

	Bias, m/s		MAE, m/s		SDE, m/s		SDW, m/s	CC		PEAA, %		Number of values
	BIM	NNM	BIM	NNM	BIM	NNM		BIM	NNM	BIM	NNM	
Zvenigorod	1.0	1.0	1.4	1.4	1.6	1.6	2.0	0.73	0.73	34	34	67352
Tsimlyansk	-0.8	-0.8	1.5	1.5	1.7	1.7	2.8	0.79	0.79	71	71	1765
Kalmykia	-1.1	-1.1	1.8	1.8	2.2	2.2	2.9	0.66	0.66	67	67	209
Gelendzhik	0.1	0.0	2.1	2.1	2.7	2.7	3	0.48	0.47	42	44	782

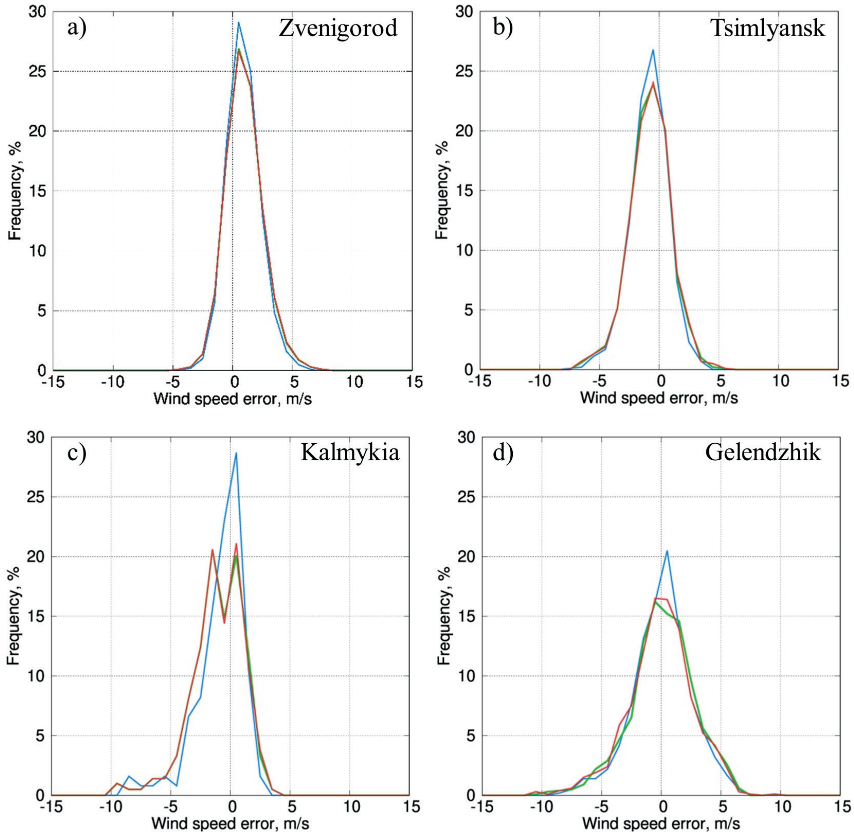

Fig. 3. Probability distribution of wind speed reanalysis errors when using bilinear interpolation (green line), nearest neighbor interpolation (red line), and averaging method (blue line) speed in Zvenigorod (a), Tsimlyansk (b), Kalmykia (c), and Gelendzhik (d)

2000). The largest errors, up to 10 m/s, correspond to strong southeast winds (Fig. 6c). However, there are insufficient observational data for a reliable assessment of reanalysis errors for different wind directions.

For the station in Gelendzhik, the largest spread of errors is observed due to the complexity of the surrounding orography and surface types (the combination of land and sea). This complexity leads to deviations of the wind profile from the logarithmic profile, which makes it impossible to accurately determine the roughness length in simplified parametrizations in the reanalysis. The largest errors, up to 11 m/s, occur at wind speeds exceeding 10 m/s with northeast, south, and southeast directions (Fig.5d). Strong northeastern winds in Gelendzhik are caused by the local Novorossiysk bora, a downslope windstorm (Shestakova et al. 2018). Strong southerly winds from the sea are also characteristic of the Gelendzhik area.

When using the "averaging method", the magnitude of MAE and SDE slightly decreases (by 0.2 m/s on average for all locations) compared to interpolation methods (Table 3). The error probability distribution becomes narrower for the "averaging method", with an increased frequency of small errors (Fig. 3). That error will continue to decrease with an increase in the area and period of averaging (Molina et al. 2021; Thomas et al. 2021), but this leads to a loss of useful information about the temporal variability of the wind field.

Our estimates of reanalysis's wind speed error are generally consistent with other similar estimates made previously for ERA5 (Gualtieri 2021; Ramon et al. 2019; Molina et al. 2021; Santos et al. 2019; Thomas et al. 2021; Dörenkämper et al. 2020; Jourdier 2020). According to the listed studies, the spread of the NSD varies from 0.3 to 2, the correlation coefficient from 0.2 to almost 1, and the bias from -5 to 3.8 m/s. Gualtieri (2021) examined the quality of the ERA5 reanalysis at several points on land, three of which can be compared with our points by land use type. For the Australian point Wallaby Creek situated in the forest, as well as in Zvenigorod, the reanalysis overestimated wind speed; the average NB and NRMSE practically coincided in Wallaby Creek and Zvenigorod. A point Humansdrop in South Africa, located on a flat grassland, can be compared with Tsimlyansk. The estimates for these two points also practically coincide, with the wind systematically being overestimated by 12-14% (Table 4). Conversely, the estimates for the point with desert land type in Iran (Ghoroghchi) do not coincide with our estimates for Kalmykia. The wind at the Iranian point, as well as in Kalymkia, is also underestimated by the reanalysis, but in higher proportions (the NB and NRMSE are 0.5 and 0.8 instead of 0.2 and 0.4 in Kalmykia, respectively).

Correction of reanalysis

Once the reanalysis had been verified, the next step was to evaluate how the obtained errors in wind speed propagated into wind energy modeling. However, we first needed to obtain "perfect" wind data so that we could compare it to the "original" reanalysis. To achieve this, we applied the bias correction method described earlier to the reanalysis data series.

Initially, we calculated the shape and scale parameters of the bias-correction method using formulas (2) and (3) for the entire data series due to its relatively small length. The wind speed probability distribution obtained after this correction is shown in Fig. 3 by a dotted line. Statistical analysis of the errors in the corrected wind speed (Table 4, 5) reveals that the correction not only eliminated the systematic error but also slightly decreased the MAE and NRMSE at most stations (Zvenigorod, Gelendzhik, and Tsimlyansk), with the standard deviation of wind speed in the corrected reanalysis being equal to the observed values. However, other statistical characteristics of the errors changed minimally, and the percentage of errors within acceptable accuracy for the corrected values even decreased.

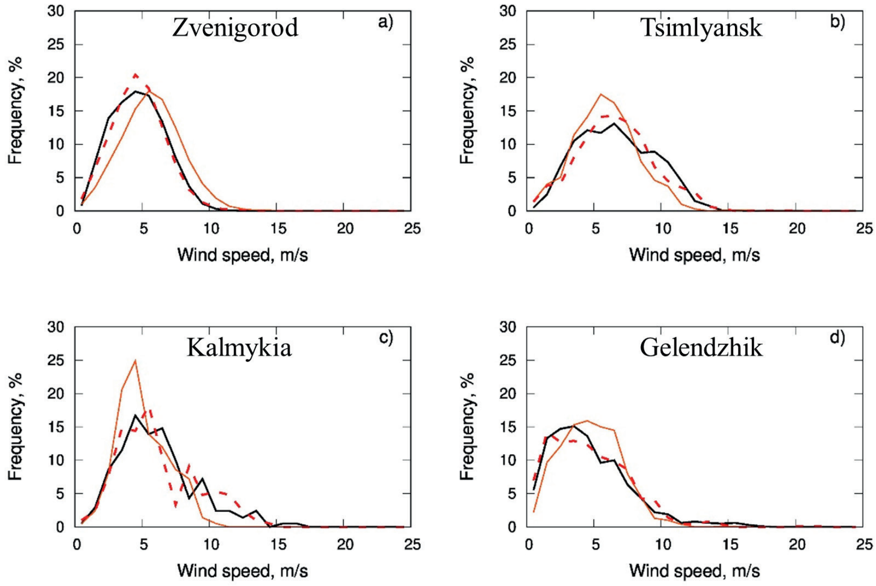

Fig. 4. Probability distribution of wind speed in Zvenigorod (a), Tsimlyansk (b), Kalmykia (c), and Gelendzhik (d) according to observations (black line), "original" reanalysis (red solid line) and corrected reanalysis (red dashed line)

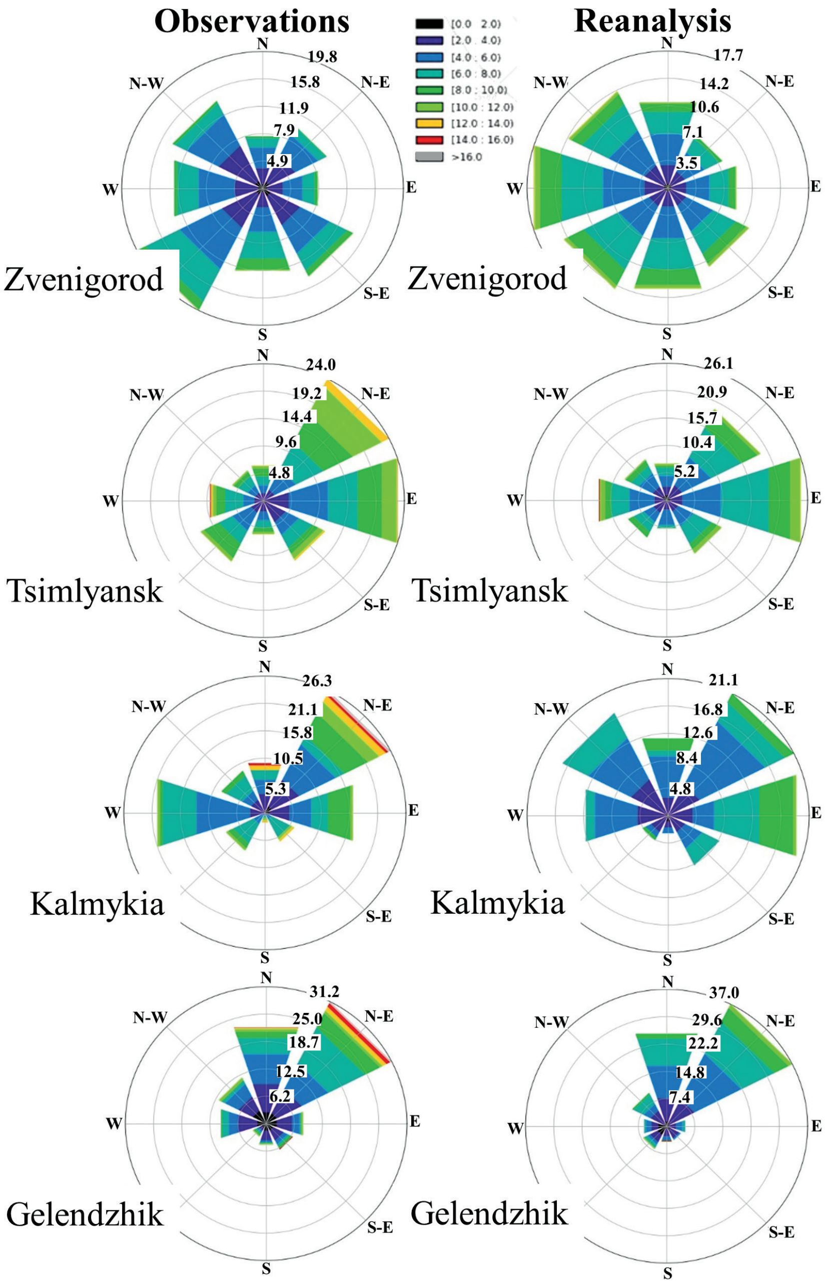

Fig. 5. Probability of wind of various speed categories from different directions in Zvenigorod , Tsimlyansk , Kalmykia, and Gelendzhik according to observations (left column) and reanalysis (right column)

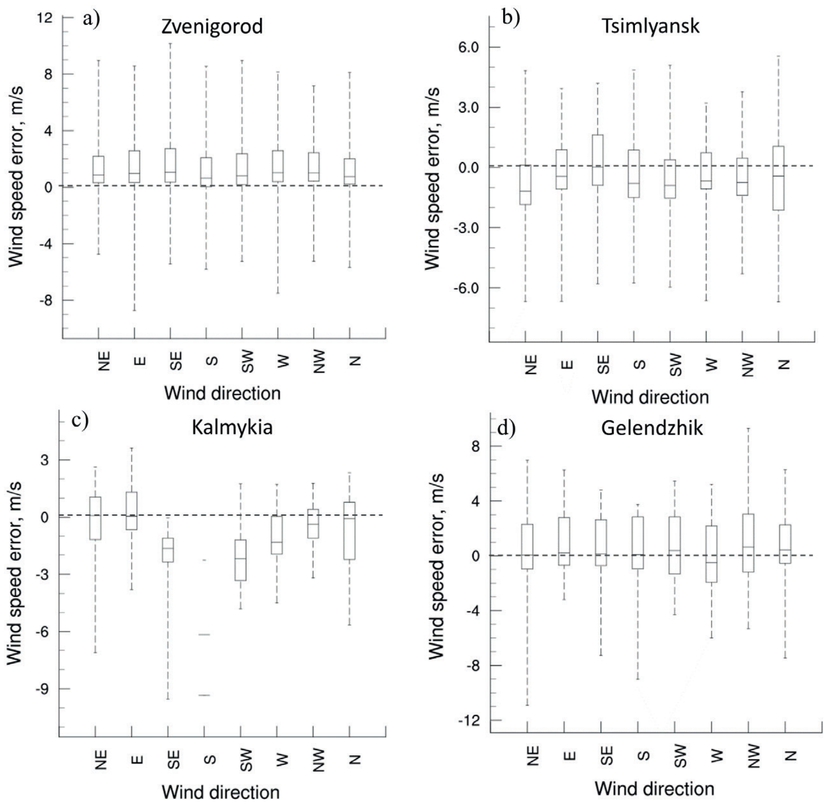

Fig. 6. The dependency of wind speed error of "original" reanalysis on wind direction in Zvenigorod (a), Tsimlyansk (b), Kalmykia (c), and Gelendzhik (d). Whiskers indicate minimum and maximum errors

Table 3. Statistical characteristics of wind speed reanalysis errors when using "averaging method"

	Bias, m/s	MAE, m/s	SDE, m/s	SDW, m/s	CC	PEAA, %	Number of values
Zvenigorod	0.9	1.3	1.4	1.8	0.77	35	55267
Tsimlyansk	-0.8	1.4	1.6	2.7	0.82	72	1468
Kalmykia	-0.8	1.4	2.0	2.5	0.59	70	122
Gelendzhik	0.0	1.9	2.4	2.5	0.45	43	649

Table 4. Comparison of NB, NRMSE and NSD before and after bias correction

	NB		NRMSE		NSD	
	original	corrected	original	Corrected	original	corrected
Zvenigorod	0.21	0	0.38	0.29	1.1	1
Tsimlyansk	-0.12	0	0.29	0.26	0.9	1
Kalmykia	-0.18	0	0.39	0.39	0.7	1
Gelendzhik	0.02	0	0.59	0.54	0.7	1

Table 5. Statistical characteristics of wind speed reanalysis errors after bias correction

	Bias, m/s	MAE, m/s	SDE, m/s	SDW, m/s	CC	PEAA, %	Number of values
Zvenigorod	0.0	1.1	1.4	2.0	0.73	53	67352
Tsimlyansk	0.0	1.4	1.8	2.8	0.79	58	1765
Kalmykia	0.0	1.8	2.4	2.9	0.67	53	209
Gelendzhik	0.0	2.3	3.0	3	0.49	41	782

Moreover, this correction method does not account for the features of the wind speed distribution associated with terrain features or intra-diurnal variability. For example, in Zvenigorod during summer, the reanalysis errors (namely, the overestimation of wind speed) are the smallest in the middle of the day and night. At this time of day, the regime of stratification and mixing of the boundary layer becomes more steady than in the transition hours. In the transition hours – in the morning and in the evening – the errors increase sharply (Fig 7.a), which is associated with the change from nighttime to daytime turbulence regime and vice versa (which may not occur simultaneously in reanalysis and observations). The transition from nocturnal to daytime boundary layers and vice versa is a rather subtle process, especially under conditions of a complex underlying forested surface, considering the low spatial resolution of the reanalysis and the complex nature of turbulence. Such features are typical for summer, when the differences between the daytime (convective) and nocturnal (stably stratified) boundary layers are highest, and hence the transitions between them are the sharpest. In addition, the change in the form of the daily course of wind speed in this region occurs at a height of about 100 m (Lokoshchenko 2014): the maximum speed is observed during the day below 100 m and at night above 100 m. This happens due to thermal stratification and features of the vertical transfer of momentum between the layers. In the reanalysis, this boundary (reversal of the daily course) can be higher or lower than the observed one, which adds to the reanalysis inaccuracy. After the correction procedure, morning and evening errors decreased, but at the same time a rather strong negative bias appeared in the middle of the day and night (Fig 7a).

The dependence of the reanalysis error on the time of day is not universal. There are small errors in the daytime in Tsimlyansk (Fig.7b), with the magnitude of errors significantly increasing at night, similar to the previously described underestimations. The correction procedure "spreads" the error evenly over the daily course, although the usefulness of such solution from the energy production point of view is questionable.

To address this, we performed another correction procedure for Zvenigorod and Tsimlyansk (at other stations, the length of the data series was insufficient for the calculation of the mean and standard deviation), considering the daily variation of wind speed error. After this correction, we eliminated biases in the reanalysis for both the entire series and individual hours. At both locations, MAE decreased by 0.1 m/s compared to the values in Table 5, and the correlation coefficient slightly increased, to 0.82 in Tsimlyansk and 0.76 in Zvenigorod. However, even with these corrections, the formal criteria of reanalysis quality outlined above were not fully met: the ratio of SDE to SDW was quite high, while PEAA was rather low. Such data are rarely "perfect". However, as demonstrated in the next section, even with bias correction alone, acceptable results for wind energy applications can be achieved.

Manifestation in energy modeling

Having evaluated the corrected reanalysis data, which we have assumed to be accurate, we could quantify the effects of the reanalysis uncertainties on the accuracy of the wind power modeling.

We assessed two main mechanisms for the propagation of the reanalysis uncertainty into energy modeling:

1. The difference in average capacity factors of the renewable generation on a long-term time scale associated with applying different approaches to the ERA5 bias correction. This uncertainty defines a difference between the wind power output values assumed by planning studies compared with values harnessed during the operation of real power systems.

2. Discrepancies between the power system regime parameters corresponding to the reanalysis-extracted wind speed values compared to the use of the "perfect" climate data.

Both climate-related energy modeling uncertainties were found to depend on the assumed wind speed scaling factor. Lower scaling values were linked to higher sensitivity of the energy modeling output to the underlying uncertainty of climate data. This effect should be expected and is explained by the nonlinear shape of the working curve mentioned earlier. It was shown that using the "original" ERA5 reanalysis data could lead to errors in the wind power capacity factor up to 0.10 to 0.15 on the "original" reanalysis data for all considered locations except Gelendzhik, where the errors could be up to 0.40. Keeping in mind that the typical capacity factor is about 0.3, the uncertainties associated with the reanalysis biases may seriously compromise the results of the investment planning if not corrected. The error value drops to as low as 0.01...0.02 when the proposed hourly-resolved bias correction procedure is applied (Fig. 8).

We considered several types of wind turbines (Vestas V80, Vestas V164, Siemens 82, Siemens 107, Repower 82, and Nordex N90) to ensure the obtained results are robust against wind turbine design. Power curves of each turbine type were approximated with a Weibull cumulative distribution function model (Bokde et al. 2018). The resulting relationship was used to compare the capacity factors of wind turbines corresponding to different approaches to climate data processing. Vestas 164, a 10 MW nominal class that is widely used in Russian wind farms, was selected for further calculations presented in the paper.

The obtained capacity factor errors (30-50%) when using the "original" ERA5 data as input are consistent with previously obtained estimates for different locations in Europe and the world (Staffell and Pfenninger 2016; Gualtieri 2021), although errors usually do not exceed ±10% on flat land or over the sea (Jourdier 2020; Gualtieri 2021). For some locations (for example, in regions with complex orography or forested areas), capacity factor errors calculated from ERA5 data can be even larger and reach 70-120% (Gualtieri 2021).

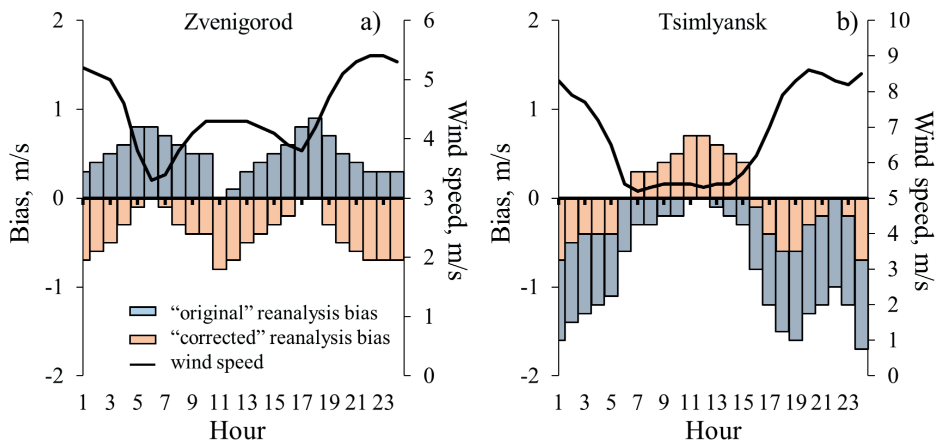

Fig. 7. Daily course of wind speed and wind bias in "original" and corrected reanalysis data series in Zvenigorod (a) and Tsimlyansk (b)

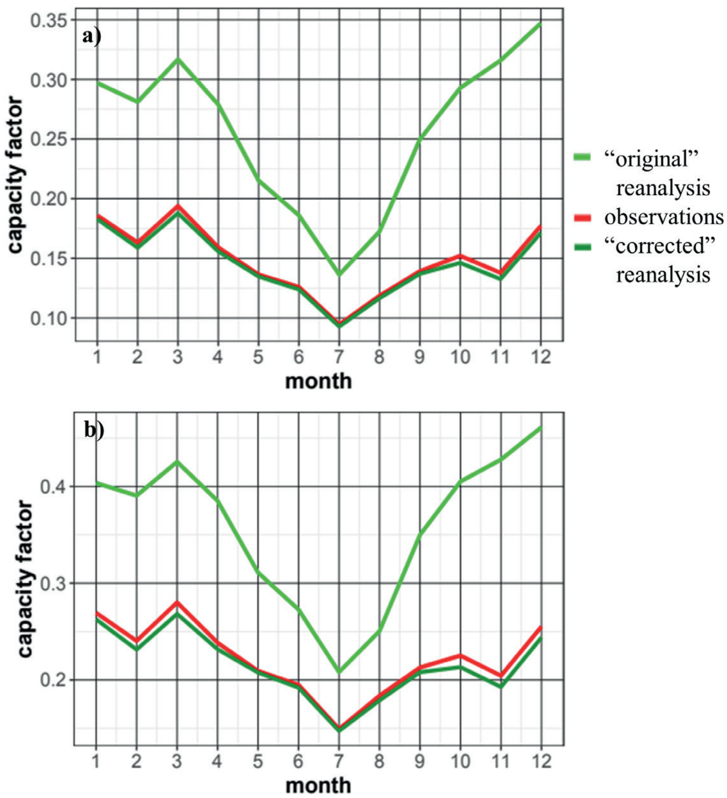

Fig. 8. The effect of ERA5 biases on the simulated multi-annual wind power capacity factor calculated using different approaches to the ERA5 biases correction with the average power capacity factor being 0.25 (a) and 0.35 (b) (Zvenigorod, turbine type «Vestas V164»)

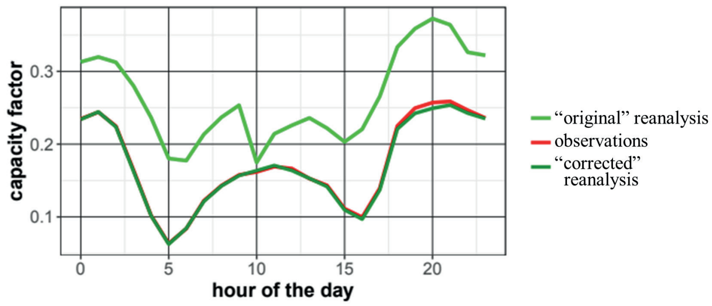

Fig. 9. Typical daily course of the simulated wind power capacity factor in May calculated using different approaches to the ERA5 biases correction (average power capacity factor on the reanalysis data is 0.30, Zvenigorod, scaling factor = 1.5, turbine type «Vestas V164»)

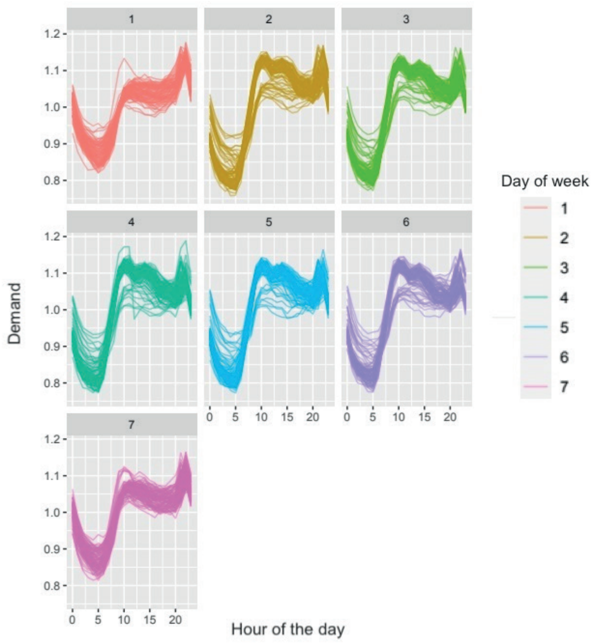

Fig. 10. Normalised daily power demand profiles for the Center power system in May for each day of the week (calculated using the System Operator data (so-ups.ru, 2005) data for 2000 – 2020)

It is worth emphasizing that the overestimation of harnessed wind power (as observed in Zvenigorod and Gelendzhik) by ERA5 may not be quite obvious from reviewing the current state-of-the-art of climate-energy research. Most published works report the underestimation of real wind potential by reanalysis data and consider energy simulation results obtained on original reanalysis data as conservative estimates of wind generation performance. This bias is linked to the fact that intensive wind generation development and applicable regional wing-energy research are currently concentrated in a few geographical regions of the world. Such a situation obviously leads to some research biases if a priori knowledge.

Diurnal patterns of reanalysis accuracy determine variations in climate-related uncertainties of simulated wind power throughout the day, particularly during peak demand hours when failing to provide the power needed to cover the actual electricity demand can lead to the most dramatic consequences for the power system. Inadequate modeling of the power system behavior during peak hours may lead to increasing risks for the power supply reliability. From this perspective, the local increase of reanalysis errors linked to the change of the boundary layer regime in the morning and evening hours poses a serious concern for energy modeling's practical use.

For example, in Zvenigorod during late spring (Fig. 8), the reanalysis error increases between 17:00 and 21:00 due to the transition between the daytime and nighttime boundary layer regimes. This timeframe is overlaid with the peak hours of the Center power system where Zvenigorod is located (see Fig. 10), which are typically between 19:00 and 21:00. If "original" reanalysis data are utilized to calculate the wind power available in the system, it can lead to an almost 50% overestimation of wind power for the evening load peak. Such discrepancy questions any conclusions which can be derived from energy models regarding power system reliability. Applying bias-corrected procedures significantly decreases this modeling error and is recommended for improving the reliability of energy models.

CONCLUSIONS

In this paper, we verified the wind speed and direction in the ERA5 reanalysis by comparing it with sodar measurements at 100 m above ground level. These measurements were carried out in various climatic zones and landscapes across European Russia. The presence of systematic errors in the reanalysis prompted us to correct the reanalysis data, considering the intradiurnal variation of wind speed error at each station. Since ERA5 reanalysis is often used as input climate data in energy modeling, we examined how wind speed bias translates into wind power capacity factor error and how this error can be eliminated with reanalysis bias correction.

Here are the main conclusions from the verification:

The systematic error of wind speed in ERA5 can be both positive and negative, ranging from -18% to 21% for the considered stations. The mean absolute wind speed error varies from 1.4 to 2.1 m/s, and the relative error ranges from 23% (on flat grassland in Tsimlyansk) to 45% (in the topographically complex area in Gelendzhik). The wind rose, representing the frequency and intensity of wind from different directions, is satisfactorily reproduced by ERA5.

There is no clear universal dependence of wind speed quality in ERA5 on a particular type of landscape and topography, as previously mentioned by other researchers (e.g., Molina et al. 2021). However, when comparing our results with those from other studies (Gualtieri 2021), ERA5 tends to overestimate wind speed over forest landscapes and underestimate it over steppe (grasslands) and desert landscapes.

There is a dependence of reanalysis error on the time of day, but this dependence varies among different stations.

In general, wind speed errors in ERA5 are significant, especially in Zvenigorod and Gelendzhik, where the percentage of errors within acceptable accuracy is less than 50%, and the absolute error approaches the standard deviation of wind speed. Therefore, reanalysis correction is necessary, especially if these data is used in energy modeling.

Bias correction not only eliminates the systematic error in wind speed but also slightly decreases the absolute error at most locations.

Our simplified wind energy modeling approach allowed us to assess the propagation of reanalysis biases into energy modeling. The energy modeling assumptions are based on the usage of working curves of wind turbines, which implies neglecting possible wake effects or the influence of mesoscale topography features. The analysis demonstrated that using "original" reanalysis data as inputs can produce misleading results. The main concerns include:

Reanalysis can both under and overestimate wind power capacity factors on a long-term time scale, depending on the area. Using "original" ERA5 data instead of observations can lead to capacity factor errors of 30-50%. This effect means that the wind energy modeling results can be misleading when used to support investment decisions. It should be recommended to assess the reanalysis uncertainty at least quantitatively, especially if an area is not well studied from the perspective of wind power development.

An important mechanism for the propagation of the reanalysis uncertainty into the energy model was identified when analyzing diurnal patterns of the reanalysis errors. High reanalysis errors associated with transient regimes of the atmospheric boundary layer can coincide with peak load periods of regional power systems. Failing to account for this effect in energy modeling can compromise power system reliability.

Utilizing the bias-correction approach is an effective measure to ensure meaningful energy modeling outputs. The capacity factor error is reduced by a factor of 10 compared to using original reanalysis data, and is less than 10% of its typical value. The developed bias-correcting approach accounting for the daily course of wind speed error was found to be an effective measure that allows to ensure a proper quality of climate inputs for energy modeling.

The main limitations of our study include the absence of wind measurements at a height of 100 m in southern European Russia during the cold season, when wind speed is highest. This limits a full assessment of reanalysis error over steppes and deserts, suitable areas for wind power plants. Additionally, the used correction method depends strongly on natural conditions, which may be unknown in advance. Further assessments of reanalysis quality for various natural conditions will help to obtain such dependences and apply them globally, not only for individual regions. Such in-depth assessments are crucial for accurate energy planning studies accommodating an increasing share of wind generation in power systems cost-effectively. ■

REFERENCES

Akperov M.G., Eliseev A.V., Mokhov I.I., Semenov V.A., Parfenova M., Koenigk T. (2022). Wind energy potential in the arctic and subarctic regions and its projected change in the 21st century according to regional climate model simulations. Russian Meteorology and Hydrology, 47(6), 428-426, DOI: 10.52002/0130-2906-2022-6-18-29

Akperov M., Eliseev A.V., Rinke A., Mokhov I.I., Semenov V.A., Dembitskaya M., et al. (2023). Future projections of wind energy potentials in the arctic for the 21st century under the RCP8. 5 scenario from regional climate models (Arctic-CORDEX). Anthropocene, V. 44, 100402, ISSN 2213-3054, https://doi.org/10.1016/j.ancene.2023.100402.

Andresen G. B., Søndergaard A. A., and Greiner M. (2015). Validation of Danish wind time series from a new global renewable energy atlas for energy system analysis. Energy, 93, 1074-1088, DOI: 10.1016/j.energy.2015.09.071.

Bokde N., Feijoo A., Villanueva D. (2018). Wind turbine power curves based on the Weibull cumulative distribution function. Applied Sciences, 8(10), 1757, DOI: 10.3390/app8101757.

Boretti A. and Castelletto S. (2020). Cost of wind energy generation should include energy storage allowance. Scientific Reports, 10, 2978, DOI: 10.1038/s41598-020-59936-x.

Çalışır E., Soran M.B., and Akpınar A. (2021). Quality of the ERA5 and CFSR winds and their contribution to wave modelling performance in a semi-closed sea. Journal of Operational Oceanography, 1-25, DOI:10.1080/1755876X.2021.1911126.

Craig M. T., Wohland J., Stoop L. P., Kies A., Pickering B., Bloomfield H. C., et al. (2022). Overcoming the disconnect between energy system and climate modeling. Joule, 6(7), 1405-1417, DOI:10.1016/j.joule.2022.05.010.

Dörenkämper M., Olsen B.T., Witha B., Hahmann A.N., Davis N.N., Barcons J., et al. (2020). The making of the new european wind atlas–part 2: Production and evaluation. Geoscientific model development, 13(10), 5079-5102, DOI: 10.5194/gmd-13-5079-2020.

Gualtieri G. (2021). Reliability of ERA5 reanalysis data for wind resource assessment: A comparison against tall towers. Energies, 14(14), 4169, DOI: 10.3390/en14144169.

Haas R., Pinto J.G., Born K. (2014). Can dynamically downscaled windstorm footprints be improved by observations through a probabilistic approach? Journal of Geophysical Research: Atmospheres, 119, 713–725, DOI: 10.1002/2013JD020882.

Hersbach H., Bell B., Berrisford P., Hirahara S., Horányi A., Muñoz-Sabater J., et al. (2020). The ERA5 global reanalysis. Quarterly Journal of the Royal Meteorological Society, 146(730), 1999-2049, DOI: 10.1002/qj.3803.

Jourdier B. (2020). Evaluation of ERA5, MERRA-2, COSMO-REA6, NEWA and AROME to simulate wind power production over France. Advances in Science and Research, 17, 63–77, DOI: 10.5194/asr-17-63-2020.

Jung C. and Schindler D. (2022). Development of onshore wind turbine fleet counteracts climate change-induced reduction in global capacity factor. Nature Energy, 7, 608–619, DOI: 10.1038/s41560-022-01056-z.

Kiseleva S.V., Shestakova A.A., Toropov P.A., and Myslenkov S.A. (2016). Evaluation of wind energy potential of the Black Sea coast using CFSR. Alternative Energy and Ecology (ISJAEE), 15-18, 75-85 (In Russian with English summary), DOI: 10.15518/isjaee.2016.15-18.075-085

Kubik M.L., Brayshaw D.J., Coker P.J., and Barlow J.F. (2013). Exploring the role of reanalysis data in simulating regional wind generation variability over Northern Ireland. Renewable energy, 57, 558-561, DOI: 10.1016/j.renene.2013.02.012.

Kuznetsov R. D. (2007). Sodar LATAN-3 for atmospheric boundary layer research. Optics of Atmosphere and Ocean, 20(8), 684-687 (in Russian).

Lokoshchenko M.A. (2014). Wind regime in the lower atmosphere over Moscow from the long-term acoustic sounding data. Russian Meteorology and Hydrology, 39, 218–227, DOI:10.3103/S1068373914040025

Li D., Feng J., Xu Z., Yin B., Shi H., and Qi J. (2019). Statistical bias correction for simulated wind speeds over CORDEX-East Asia. Earth and Space Science, 6, 200–211, DOI:10.1029/2018EA000493.

Molina M.O., Gutiérrez C., and Sánchez E. (2021). Comparison of ERA5 surface wind speed climatologies over Europe with observations from the HadISD dataset. International Journal of Climatology, 41(10), 4864-4878, DOI: 10.1002/joc.7103.

Olauson J. (2018). ERA5: The new champion of wind power modelling? Renewable energy, 126, 322-331, DOI: 10.1016/j.renene.2018.03.056.

Ramon J., Lledó L., Pérez-Zanón N., Soret A., and Doblas-Reyes F. J. (2020). The Tall Tower Dataset: a unique initiative to boost wind energy research. Earth System Science Data, 12(1), 429-439, DOI: 10.5194/essd-12-429-2020.

Ramon J., Lledó L., Torralba V., Soret A., and Doblas-Reyes F.J. (2019). What global reanalysis best represents near-surface winds? Quarterly Journal of the Royal Meteorological Society, 145(724), 3236-3251, DOI: 10.1002/qj.3616.

Santos J., Sakagami Y., Haas R., Passos J., Machuca M., Radünz W., et al. (2019). Wind speed evaluation of MERRA-2, ERA-interim and ERA-5 reanalysis data at a wind farm located in Brazil. In: Proceedings of the ISES Solar World Congress (pp. 1-10), DOI:10.18086/swc.2019.45.10. Available online at http://proceedings.ises.org.

Semenov O.E. (2000). On the flow acceleration during strong sand and dust storms. Hydrometeorology and Ecology, 3-4, 23-48 (in Russian).

Semenov O. E. (2020). Introduction to experimental meteorology and climatology of sandstorms. Dolgoprudny: Fizmatkniga Publishing House (in Russian).

Spravochnik po resursam vozobnovlyaemyh istochnikov energii Rossii i mestnym vidam topliva (pokazateli po territoriyam) (2007).- – M.: «IAC Energiya», 272 p. (in Russian).

Shestakova A.A., Toropov P.A., Stepanenko V.M., Sergeev D.E., and Repina I.A. (2018). Observations and modelling of downslope windstorm in Novorossiysk. Dynamics of Atmospheres and Oceans, 83, 83-99, DOI: 10.1016/j.dynatmoce.2018.07.001.

so-ups.ru (2005). System Operator Database. [online] Available at: https://www.so-ups.ru [Accessed 31 Aug. 2022]

Staffell I. and Pfenninger S. (2016). Using bias-corrected reanalysis to simulate current and future wind power output. Energy, 114, 1224-1239, DOI: 10.1016/j.energy.2016.08.068.

talltowers.bsc.es (2023). The Tall Tower Dataset website. [online] Available at https://talltowers.bsc.es/ [Accessed 21 Feb.2023]

Thomas S. R., Nicolau S., Martínez-Alvarado O., Drew D. J., and Bloomfield H. C. (2021). How well do atmospheric reanalyses reproduce observed winds in coastal regions of Mexico. Meteorological Applications, 28(5), e2023, DOI: 10.1002/met.2023.

Zilitinkevich S.S. (1972). The dynamics of the atmospheric boundary layer. National Lending Library for Science and Technology

RESEARCH PAPER

ENHANCING AGRICULTURAL PROTECTION AREAS UNDER SPATIAL RESTRICTIONS: A CASE STUDY OF MAJALENGKA REGENCY, INDONESIA

Adrian[1,4], Widiatmaka[2], Khursatul Munibah[2], Irman Firmansyah[3], Adrian[4]
[1]Graduate School of Natural Resources and Environmental Management Science, IPB University. IPB Dramaga Campus, Bogor 16680, West Java, Indonesia.
[2]Department of Soil Science and Land Resource, Faculty of Agriculture, IPB University.
[3]System Dynamics Center
[4]Departement of Education Geography, Islamic University 45 Bekasi, Bekasi 17113, West Java, Indonesia.
***Corresponding author:** psl13adrian@apps.ipb.ac.id
Received: June 20th, 2023 / Accepted: November 13th, 2023 / Published: March 31st, 2024
https://DOI-10.24057/2071-9388-2023-2939

ABSTRACT. The escalating trend of urbanization in Indonesia, accompanied by the conversion of agricultural land into urbanized areas, necessitates the implementation of zoning regulations. These regulations are crucial to protect agricultural land and safeguard the finite land assets of the country. To ensure the preservation of scarce land resources and guarantee food security, it is paramount for the Indonesian government to establish agricultural land protection areas. This paper presents an innovative approach and integrated methods to define agricultural land protection zones in spatial form. Results of studies landscape structure classification; core farmland accounts for 33.59% of the study region, whereas edge farmland accounts for 36.43%. Furthermore, the corridor farmland area is 0.30%, the discrete farming area is 12.26%, the Edge-Patch area is 3.54%, and the Perforated area is 13.89%. Geographically, the primary agricultural land is stretched out as a continuous area located on the outskirts of Majalengka city. By integrating Geographic Information Systems (GIS), remote sensing, landscape structure, prime farmland identification, and agricultural «land interest» could have a conservationist bent. It can mean protecting specific areas for environmental reasons (reach calculated), the study aims to create optimal farmland protection areas. The techniques outlined here can aid in determining PFPA from a geographical science standpoint, and the research's findings will be helpful for PFPA planning.

KEYWORDS: prime farmland protection area (PFPA), landscape structure classification, Geographic Information System (GIS), remote sensing, reach calculation, UrbanSCAD

CITATION: Adrian, Widiatmaka, K. Munibah, I. Firmansyah, Adrian. (2024). Enhancing Agricultural Protection Areas Under Spatial Restrictions: A Case Study Of Majalengka Regency, Indonesia. Geography, Environment, Sustainability, 1(17), 67-82
https://DOI-10.24057/2071-9388-2023-2939

ACKNOWLEDGEMENTS: The authors are grateful to BUDI-DN (LPDP) Indonesia Endowment Funds for Education and the Regional Development Planning and Research Agency for Majalengka Regency, who supported and funded this study. The authors are also grateful to all individuals and parties who assisted in completing this study, including the academic editor and the two anonymous reviewers.

Conflict of interests: The authors reported no potential conflict of interest.

INTRODUCTION

Agricultural land is crucial for sustaining life, ensuring national food security, safeguarding the environment, and enhancing the transition to renewable energy sources. Furthermore, it plays an important role in military and security activities (Bakker et al. 2011; Godfray et al. 2010; Qianwen et al. 2017; Sutherland et al. 2015). The ecological habitat surrounding urban areas tends to deteriorate due to socio-economic progress and the reduction of natural areas. Also, the conservation of regional ecological security increasingly relies on the ecological function of agricultural systems (Deslatte et al. 2017; Reid et al. 2010).

To safeguard agricultural land, policymakers, specifically the government, needs to consider its scope, quality, and ecological role. Also, the preservation of a unified agricultural landscape system can promote sustainable food production, especially lands dedicated to agricultural purposes (Sayer 2009; Sayer et al. 2013). The contradiction between farmland preservation and urban expansion poses a fundamental difficulty in planning the landscape systems. This is an important issue because it is the major link between agricultural scale, quality, and the ecosystem (Girvetz et al. 2008; Holmes 2014).

Disruptions to agricultural landscapes caused by non-agricultural activities, such as construction, and human development caused changes in the landscape configuration. These disturbances led to a deterioration in the overall quality of agricultural land usage (Jiang et al. 2018; Liang et al. 2015). Spatially, building activities related to urban expansion were observed to encroach upon agricultural land in a given area due to the increased demand for urban development and urbanization flows. The importance of striking a balance between protecting agricultural land and facilitating urban growth cannot be overstated, as these are basic conditions for driving sustainable economic growth and establishing resilient urban centre (Chen et al. 2019; Huang et al. 2019; T. Liu et al. 2015).

In Indonesia, particularly in Java, there has been a massive shift from farmland to urban development. The drastic reduction in the agricultural land area poses threat to regional food security, particularly in the Majalengka Regency. This situation arises from the on-ground changes in the conditions of agricultural land cover/use, in relation to development of infrastructure, such as the West Java International Airport Kertajati and the surrounding areas (Adrian et al. 2022).

The spatial regulation of agricultural land should safeguard sustainable agricultural land near urban areas while limiting the construction of buildings to accommodate urban expansion. Also, precise measures are imperative to demarcate critical agricultural land protection areas and outline clear-cut limits for urban development (Deng et al. 2015; Duan et al. 2019; Jiang et al. 2016). Establishing sustainable food agricultural land protection zones necessitates optimizing agricultural land spatial planning to facilitate the proximity of agricultural land, whether in a dense or concentrated arrangement. Furthermore, encouraging agricultural mechanization is essential for increasing output and quality (Deng et al. 2015; Qianwen et al. 2017).

According to (Jiang et al. 2018), the integration of farmland landscape structure could directly enhance the function of the agricultural system, with the agricultural land protection strategy gradually shifting from a quantity-based perspective to a landscape reorganization perspective. Therefore, protecting agricultural land in the suburbs through new forms of administration and maintaining the spatial continuity of landscapes are important considerations that have been discussed (Duan et al. 2019; Perrin et al. 2018). This study takes into account management difficulties and landscape structure in depth to establish sustainable food agricultural land protection zones in Majalengka Regency.

This study addressed a gap in the existing literature by examining the tension between protecting farmland and creating new economic zones in the Majalengka District. Also, leading agricultural land protected zones and the prime property were identified near the Special Economic Zones development region using a landscape structure categorization model for agricultural land. Specific limits for urban development were drawn to prevent unchecked urban encroachment into farmland. Policy guidance for managing the connection between building, agricultural land conservation, and sustainable agricultural food land protection was also determined. This was achieved by integrating urban development boundaries with key agricultural land conservation zones to establish spatial control boundaries for cultivated land.

MATERIALS AND METHODS

Study Area

This study was conducted in Majalengka Regency, located in West Java Province. Majalengka is comprised of 26 Districts, and geographically situated between 108°03′ and 108°25′ East Longitude and 6°36′ and 6°58′ South Latitude. It shares borders with Indramayu to the north, Garut, Tasikmalaya, and Ciamis to the south, Sumedang to the west, and Cirebon and Kuningan to the east, (see Fig. 1).

This study was inspired by the fact that the agricultural sector remains a vital aspect of the welfare and economic growth for the people of Majalengka Regency, where the sector's domestic revenue still holds the first position in the province (BPS 2018). (Sari and Kushardono 2019) showed a massive change in the use of agricultural land in Majalengka. This transformation was driven by the construction of Airport BIJB infrastructure in the Regency, which was part of the Rebana Special Economic Zone. The area occupied by the West Java International Airport expanded from

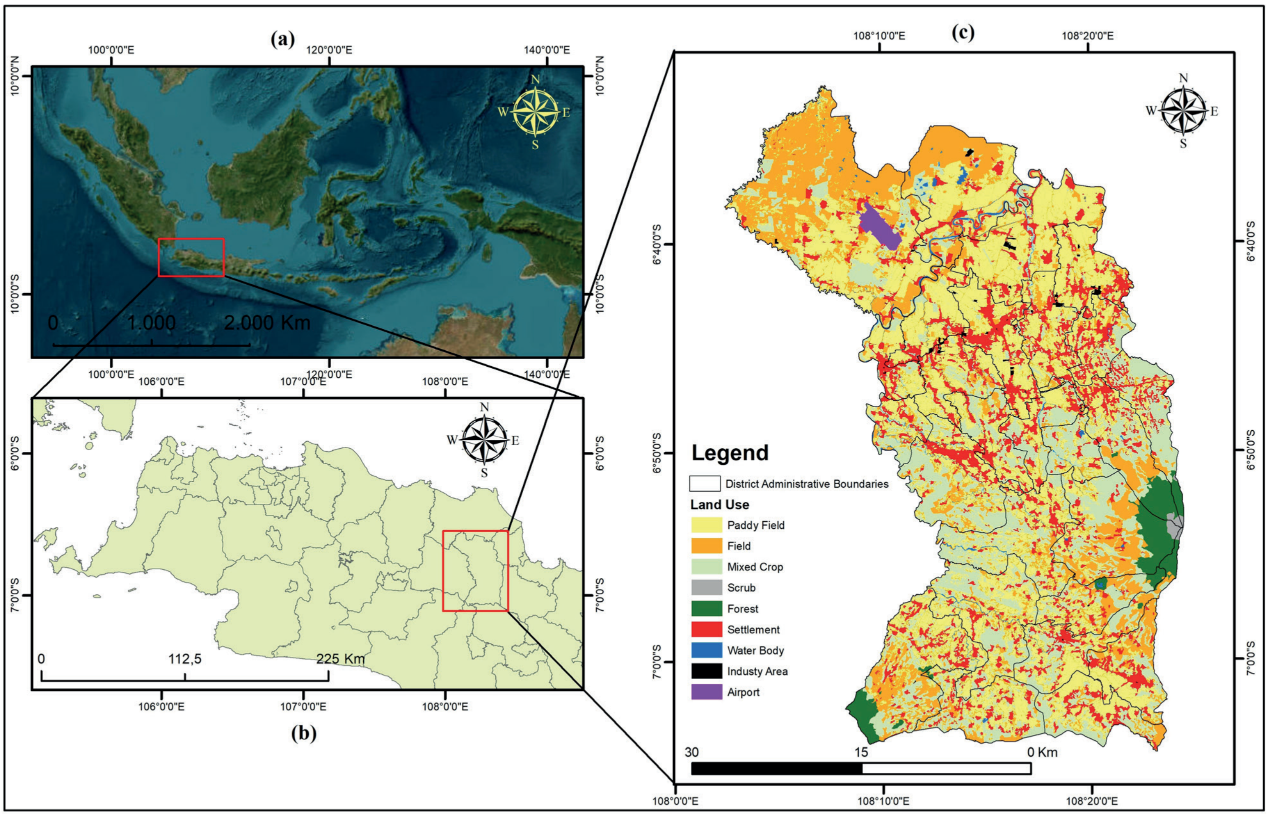

Fig. 1. Study Area

10.10 Ha in 2013 to 546.70 Ha in 2018. Furthermore, the area of paddy fields underwent a conversion of 413.30 Ha. This indicated the Rebana economic area in Majalengka Regency had a negative physical impact on land use change, primarily agricultural land on a large scale. It also significantly threatened regional food security, specifically in the area.

Data

This study utilized both primary and secondary data sources. The primary data included land use survey in the form of image interpretation in the field (using the results of field surveys), enabling the structural classifications of agricultural landscapes and providing essential data for planning agricultural land spatial regulations. The classification and gradation data on the quality of agricultural land served as the standard for evaluating high-quality agricultural land. In addition, secondary data comprised of several maps sourced from various regional and central agencies, as presented in Table 1.

-

Methodology

Agricultural land protection zoning model

Zoning protected farmland is one example of a more general problem known as land use planning, a series of questions on how to optimize space utilization. The study flow presented in (Fig.2) illustrates the procedure for agricultural land protection zoning. Remote sensing enables the acquisition of land use and urban development information, while GIS (Geographic Information System) provides spatial data analysis tools. Also, land interest was used to classify agricultural land based on factors like accessibility and proximity to public social facilities. It provided a probability of change, which helped to determine potential future changes to built-up land. This model was intended to protect agricultural land based on suitability and growth potential maps. The subsequent sections will delve into models for solving zoning protection problems.

This study proposes a method for protecting agricultural land, namely by using three sub-models: (a) the farmland landscape sub-model, namely the use of land landscape characteristic factors, which delineate the functional landscape of agricultural land based on the agricultural landscape structure classification model (b) the farmland quality sub-model, the quality of agricultural land is more comprehensive, then an integrated quality assessment of regional agricultural land is carried out using spatial analysis; (c) reach calculation sub-model, namely Proximity analysis, often used in spatial analysis and geographic information systems (GIS), involving assessing the relationship and distance between spatial features. In the context of calculating range in proximity analysis, in this case, the value of interest is to determine how far a particular feature is from a particular location or set of locations; (d) delineate protection zones of prime agricultural land, Interactions between protected areas and prime agricultural land often involve considerations related to land use planning, conservation, and sustainable development, the specific processes are described (see Fig. 2).

Land suitability map data and land use surveys (Table 1), were used to carry out structural classification of agricultural land landscapes and gather primary data for planning spatial regulations. This process enabled the classification and gradation of agricultural land quality, facilitating the assessments for selecting high-quality agricultural land (Jiang et al. 2018; Qianwen et al. 2017). Also, the configuration of the landscape was directly associated with agricultural land. Core farmlands had the most contiguous distribution, the most minor interference from non-farm activity, and the best agricultural productivity of all categories; Furthermore, edge farmland serves as an ecological transition zone between core farmlands and nonfarm ecosystems; it aids in the isolation of ecological interference and the ecological buffering of nonfarm habitats and nonfarm activities occurring on prime farmlands; Edge farmlands buffer and protect core farmland production functions, and the two farmland kinds complement each other; Corridor farmlands, on the other hand, are canals that connect farmlands and serve as barriers between farmlands and nonfarm habitats. We combined the core farmlands as contiguous farmlands and the edge patches of farmland, discrete patches of farmland, and perforation farmlands as discrete farmlands using the landscape structure classification results, functional segmentation, and pixel attribute reclassification, and defined corridor farmlands as connecting channels. Contiguous farmlands and linked canals were chosen as the ideal prime farmland conservation patches to provide consistency among farmland landscapes, based on the definitions of different farmland landscape types, the details of the farmland landscape structure classification process described (see Fig. 3).

Table 1. Data-collection used in the study

No	Data Name	Data Type	Data Source	Scale
1	Landuse Map	Vector	Classification of Spot 7 2021	1: 25k
2	Local Government Regulation Map	Vector	Local Government Majalengka Regency 2021	1: 25k
3	Cultivation intensity map	Vector	Local Government Majalengka Regency 2021	1: 25k
4	Land area map	Vector	Local Government Majalengka Regency 2021	1: 25k
5	land suitability for paddy map in Majalengka Regency	Vector	(Adrian et al. 2022)	1: 25k
6	Administrative map	Vector	Landuse Plan (RTRW) of Majalengka Regency 2021	1: 25k
7	Points Of Interest	Vector	Google (Gmaps Leads Generator)	1: 25k
8	Map of building geometries	Vector	Open Street map and vectorization from Spot 7	1: 25k
9	Location of Paddy Field	Point	Ground Truth Data 2022	-

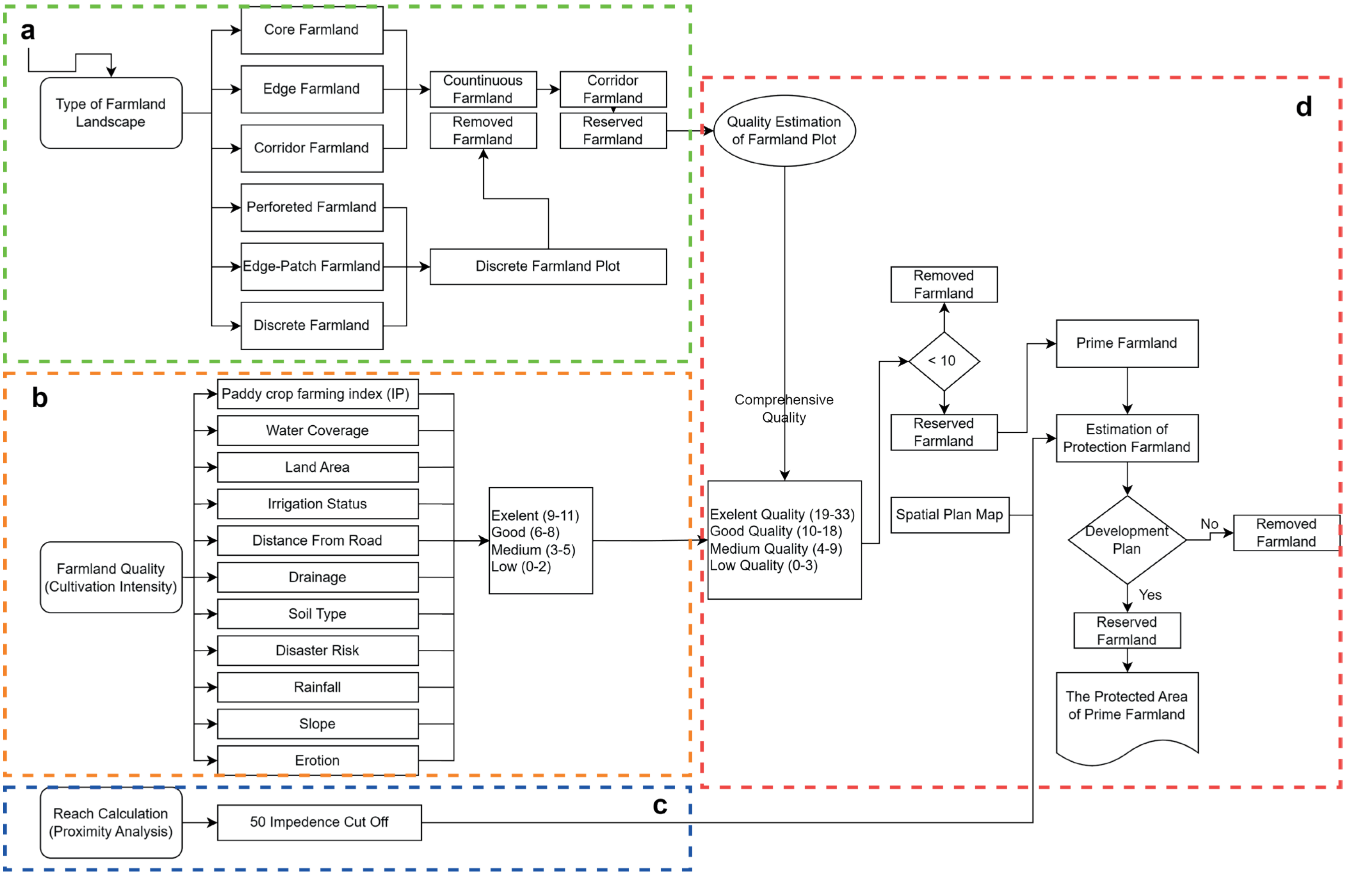

Fig. 2. Single-factor layer-by-layer exclusion procedure for identifying prime agricultural protection zones

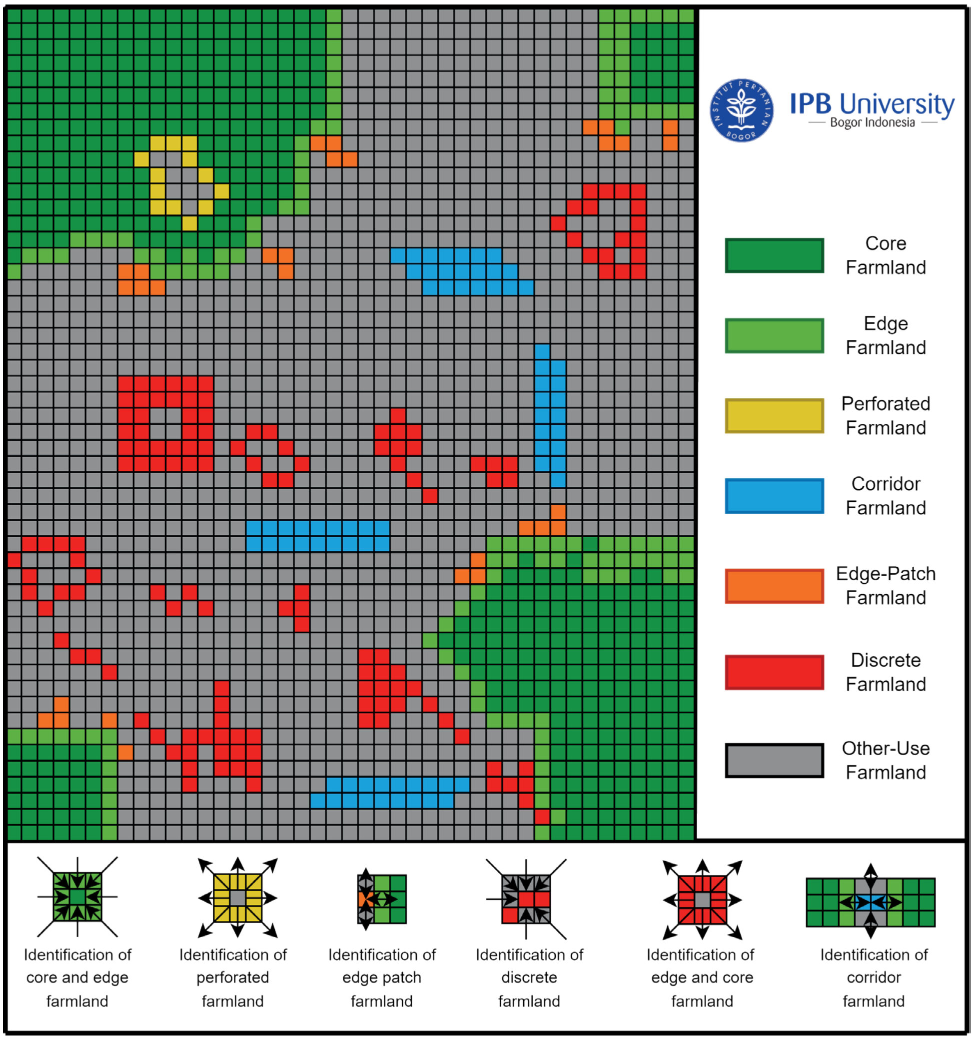

Fig. 3. Farmland landscape structure sketch map and farmland landscape categorization design

Excessive fragmentation necessitated greater precision in verifying the ecological role of agricultural land as a constituent of the landscape. It also led to noticeable mis-segmentation, focusing on the shared confusion among patches, edges, perforations, and corridors of agricultural land cartographic representation of a spatial plan (Jiang et al. 2020). Prime farmland (PF) protection area is described as high-quality farmland, A prime farmland protection area (PFPA) is a territory designated for the particular protection of PF, including accompanying roads, rivers, and facilities. The GIS spatial analysis process presented in (Fig.3) is as follows (1) Simplifying the polygonal form to delineate PF, (2) performing buffer analysis for each PF patch, and (3) conducting aggregation analysis to determine the boundaries of the PFPA.

The core farmlands were merged with adjacent ones, as well as edge and discrete patches, and perforated farmlands to form discrete using landscape structure classification, functional segmentation, and pixel attribute reclassification results. Corridor farmlands were selected to connect waterways. The adjacency of farmlands and connecting canals was considered to identify optimal farmland preservation patches and maintain the continuity of farmland landscapes.

Maximize Farmland Quality

Farmland quality refers to a piece of land's usefulness for agricultural purposes. Several factors influence farmland quality, and these factors have a significant impact on the success and productivity of agricultural activities. Data related to farmland quality include the paddy crop farming index (IP), land area, irrigation status, drainage, and soil type, which are data sourced from the Department of Agriculture of Majalengka Regency and processed in previous research (Adrian et al. 2022). The next step is to determine the weight of each driving factor in evaluating suitability and producing farmland quality classes (excellent, medium, good and low). The weighting of each attribute utilizes the calculation results of the AHP method, which involves six government stakeholders in the Majalengka Regency. In assessing the weighting of each farmland quality factor using the results of the AHP method calculation involving six government stakeholders in Majalengka Regency.

The analytic hierarchy process was used to rank the importance of different considerations. Furthermore, pairwise comparisons and expert opinions were used in this metric theory to establish ranking systems (T. L. Saaty 2003). Table 2 presents the weights assigned to various factors for assessing agricultural suitability and development potential. The suitability analysis process entailed considering numerous spatial variables or factors to assess the suitability score. A total of eleven variables were selected to analyze agricultural suitability. The incorporation of spatial factors into raster-based GIS software enabled the execution of spatial analysis using an overlay technique with a map algebra approach.

The primary objective of this endeavour was to safeguard valuable agricultural land. Agricultural fit can be determined through various geographic features obtained from *remote sensing data* (RS) combined with *Geographic Information System Data* (GIS). This integration proved invaluable in zoning agricultural land for protection. The Farmland Quality (Cultivation Intensity) method was based on the above spatial factors and the formula of the farming land quality conditions. The LS analysis incorporated criteria and subcriteria, as shown in (Fig.5):

The accuracy and availability of data have a significant impact on the results of this research. Therefore, extensive efforts are required to ensure a thorough review of important GIS datasets. This method is an integration of AHP and GIS-based farmland quality methods for paddy fields, as well as identification of suitable agricultural land. The AHP provided mathematical means to assess the consistency of judgment matrix. An accuracy ratio can be calculated based on the structure of the matrix, where the number of rows or columns is always greater than or equal to the number of rows or columns with the highest eigenvalue (max). The consistency index, which measures how well comparisons between two things match up, can be written as follows (T. Saaty, 1977; T. L. Saaty, 1988).

$$Ci = \frac{\lambda max - n}{n - 1} \tag{1}$$

Where *CI* is the consistency index, n is the number of elements in the compared matrix, and max is the largest or main eigenvalue. A random index table can be used to verify the consistency judgment for the right number of n to ensure the accuracy of the pairwise comparison matrix (T. L. Saaty, 1990).

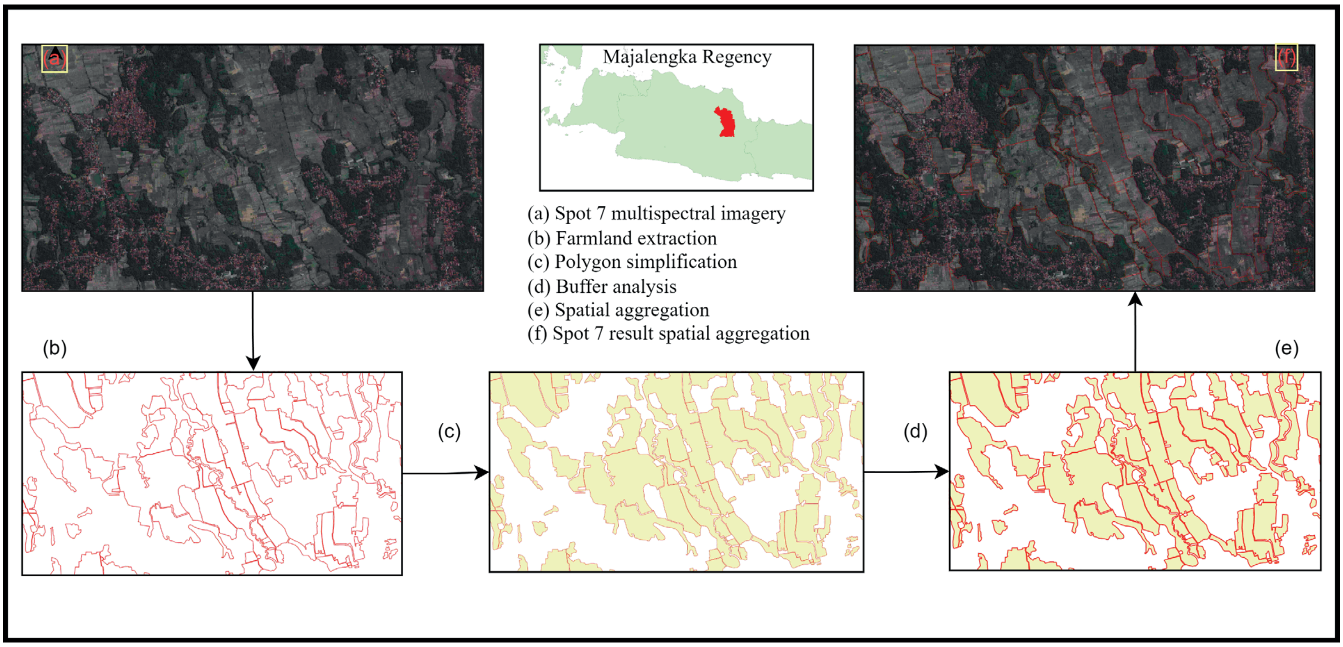

Fig. 4. Analysis Process GIS for Prime Farmland Protection Area

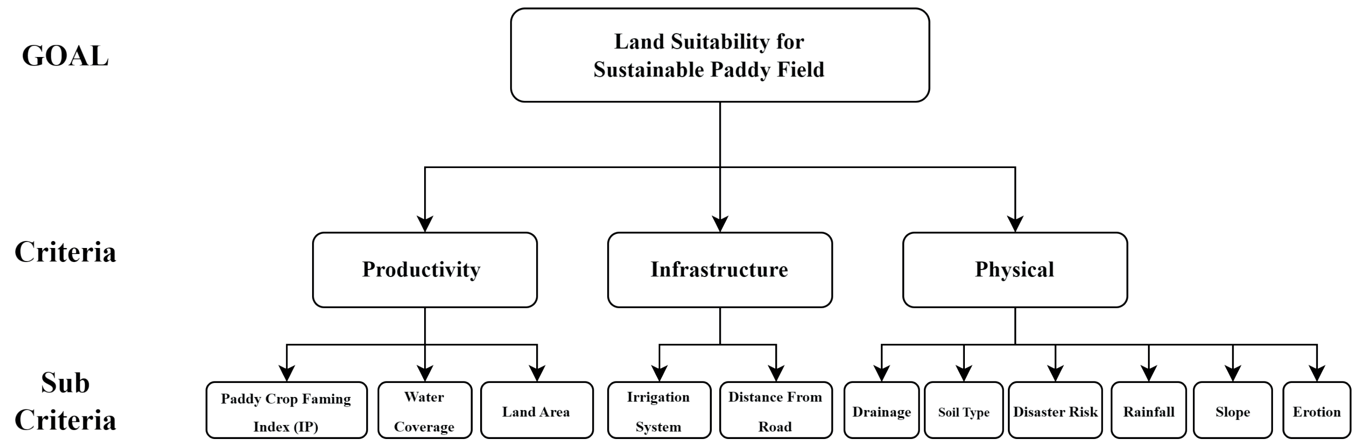

Fig. 5. Hierarchical Structure of Land Suitability

$$CR = \frac{CI}{RI} \tag{2}$$

Where *CR* is the consistency ratio, *CI* represents the consistency index, and *RI* denotes the randomness index. A consistency ratio below 0.1 indicates sufficient information to make an informed decision.

The aforementioned spatial factors are used to assess agricultural suitability using the Multicriteria Evaluation (MCE) approach (Eastman et al. 1995). Before the estimation, the factors should be standardized within the range of [0, 1]. A linear weighted combination approach generates the overall appropriateness score. The linear weighted combination method adopted the following equation to calculate the total fit score:

$$\begin{aligned} FQ\,(LS) &= W_1XPcf + W_2XWc + W_3XLa + \\ &+ W_4XIs + W_5XDfr + W_6XDr + W_7XSt + \\ &+ W_8XDis + W_9XRf + W_{10}XSl + W_{11}XErt \end{aligned} \tag{3}$$

where FQ(LS) is farm quality (*land suitability*), which represents land suitability, was calculated using the equation below, where (**Pcf**) paddy crop farming index, (**Wc**) water coverage, (**La**) land area, (**Is**) irrigation system, (**Dfr**) distance from road, (**Dr**) drainage, (**St**) soil type, (**Dis**) disaster risk, (**Rf**) rainfall, (**Sl**) slope and (**Ert**) Erosion. w_1, $w_2 w_3$, w_4, w_5, w_6, w_7, w_8, w_9, w_{10} *and* w_{11}, These are the weights for each factor, the sum of all the criterion weights is 1.

Reach Calculation

Reach and centrality are standard network analysis terms for transportation, social, and other interrelated systems. These notions are crucial for attractiveness analysis, which examines how network aspects affect attraction. Reach is the measure of the extent or range that something covers inside a network. Within the framework of attractiveness analysis, it frequently denotes the capacity of a particular node or element within the network to attract and engage the target audience, exert influence, or facilitate accessibility. Reach is crucial for understanding how far the influence of a particular element extends within a network. For example, in marketing, reach indicates the potential number points of interest who may be exposed to a paddy field persil.

Centrality analysis is a method used to discover the most essential pieces in a network that significantly impact connecting other nodes. These key aspects are frequently more appealing, be it in terms of social impact, transit hubs, or other variables. Utilize the Kernel Density Estimation (KDE) method on your spatial data to produce a smooth surface representing the estimated density of points throughout the study area. Utilize visualizations to analyze the data and create contour maps or heat maps that depict regions with varying levels of point density. The regions with higher KDE values imply areas of greater point concentration, suggesting a more significant "reach."

Table 2. Pairwise comparisons to score land suitability

	Normalization											Total Weight
Responden	Pcf	Wc	La	Is	Dfr	Dr	St	Dis	Rf	Sl	Er	
Bappeda	0,283	0,050	0,041	0,216	0,077	0,097	0,101	0,062	0,047	0,026	0,283	1.000
Distan	0,051	0,282	0,021	0,224	0,088	0,042	0,158	0,033	0,026	0,074	0,051	
Distan	0,289	0,044	0,021	0,224	0,088	0,031	0,158	0,033	0,036	0,076	0,289	
PUTR	0,089	0,244	0,024	0,216	0,093	0,030	0,152	0,038	0,039	0,075	0,089	
Setda	0,215	0,119	0,029	0,223	0,081	0,030	0,153	0,036	0,040	0,074	0,215	
BPN	0,188	0,146	0,018	0,218	0,097	0,036	0,155	0,023	0,031	0,088	0,188	
Weight	0,157	0,117	0,025	0,220	0,087	0,040	0,144	0,036	0,036	0,065	0,157	

W: Water Body R: Rock OutCrop,
(ymax) Max eigenvalue = 9,118 n = 9
(Ci) Consistency index = (ymax - n)/(n - 1) = 0,012
(Ri) Random index = 0,580
(Cr) Consistency ratio = Ci/Ri = 0,0210451
CR score = 0,0210451 less than 10% (CR<0.1), confirmed

Method of Kernel Density Estimation (KDE)

Kernel density estimation (KDE) was used to interpolate the POI distribution for food retail outlets and the three indices of road network centrality. Points represent service centers, reach zones could indicate areas with better service coverage, KDE results to make informed decisions about resource allocation, marketing strategies, or other relevant considerations. This reflected their spatial clustering characteristics within the study area. Furthermore, KDE facilitated the transformation of different spatial elements into the same spatial unit and enabled the study of their relationship. This technique was widely used in previous studies to investigate micro-spatial distributions (Evangelista and Beskow 2019; Zhang et al. 2021).

KDE uses data1, data2…, as independent, identically distributed samples of the population with the distribution density function f. f (x) can be defined as follows:

$$fn(y) = \frac{1}{nh}\sum_{i=1}^{n} p\left(\frac{c-ci}{q}\right) \tag{4}$$

where p (.) is the kernel function, q denotes the bandwidth, and c - ci represents the distance from estimation point c to sample ci. Also, the POI data for the location of public and social facilities were assessed for centrality in relation to the road network when conducting the analysis with ArcGIS software. Subsequently, the data were stored using KDE, considering 100 m polyline elements and a 100 m bandwidth, to transform the two data layers into spatial units, facilitating correlation analysis between them.

Network Approach (Reach Calculation)

Generally, the concept of a network was based on the relationship between entities, such as organizations or people. The network properties previously studied were related to the structure of relationships. According to (Knoke et al. 1996), the assumptions underlying the network emphasized structural relationships, which aligned with what (Scott 2020) discussed about relationships. In "Analyzing Social Networks," (Teshale 2016) presented at least three types of "basic" network analysis that can be used for measuring network analysis, namely centrality, subgraphs, and equivalence. Centrality refers to the "most important" actor often located strategically within a social network (Uitermark and van Meeteren 2021).

A referral model and regionalization approach was used in this study, considering spatial aspects, such as the distributions of settlement population, village office facilities, road data, travel time to facilities, and scoring results. These factors contributed to the spatial patterns of paddy field distribution in Majalengka Regency based on the probability of interest. The first step was to identify distribution patterns of activity and business centre locations using a network analysis technique (Zheng et al. 2020). Reach centrality refers to "the proportion of network nodes the focal node can reach in a given number of steps" (Henneberg et al. 2007). This metric is an alternative method for determining an actor's proximity to other actors in a network. The extent to which an actor can access information from other members can be determined by identifying the reachable portion of all other actors in one step, two steps, three steps, etc (Robins et al. 2007).

A *Reach'[i]* centrality approach is used for determining the importance of an entity in a link chart based on a knowledge graph. The centrality score ranks entities based on their position in the graph represented by the link diagram. This score identifies the link chart entities that play an essential role in the link chart. For instance, it can identify the most influential people in a social network, events contributing to the spread of disease, critical infrastructure nodes in an urban network, among others. The formula for this approach is as follows:

$$Reach^{r}[i] = f(x) = \sum_{j \in G-\{i\};\, d[i,j] \le r} W[j] \tag{5}$$

Where *d[i,j]* is the shortest path distance between nodes *i* and *j* in *G* the graph containing nodes and edges, and *W[j]* denotes the weight of the destination node *j*. The weights can represent any quantitative quality of the target structures, such as their total square footage or the number of residents. By incorporating weights, an analyst can determine how many of these features (paddy fields and public facilities) are accessible from each building within a specific network radius (Porta et al. 2012).

The reach centrality visually demonstrated how it operates. Starting from the paddy field of interest *i*, an accessibility buffer was extended in all directions along the street network until the limiting radius r was reached. The Reach index was subsequently calculated by counting the number of destinations within the radius. The aggregate of weights, rather than the number of destinations was considered when weights were specified. In (Fig.5), the radius of location encompassed twenty neighbouring locations. The output illustrated the surrounding built volume that could be accessed from each structure within a 50-meter radius. It was observed that areas with higher Reach values had more significant, densely spaced buildings and a denser street network.

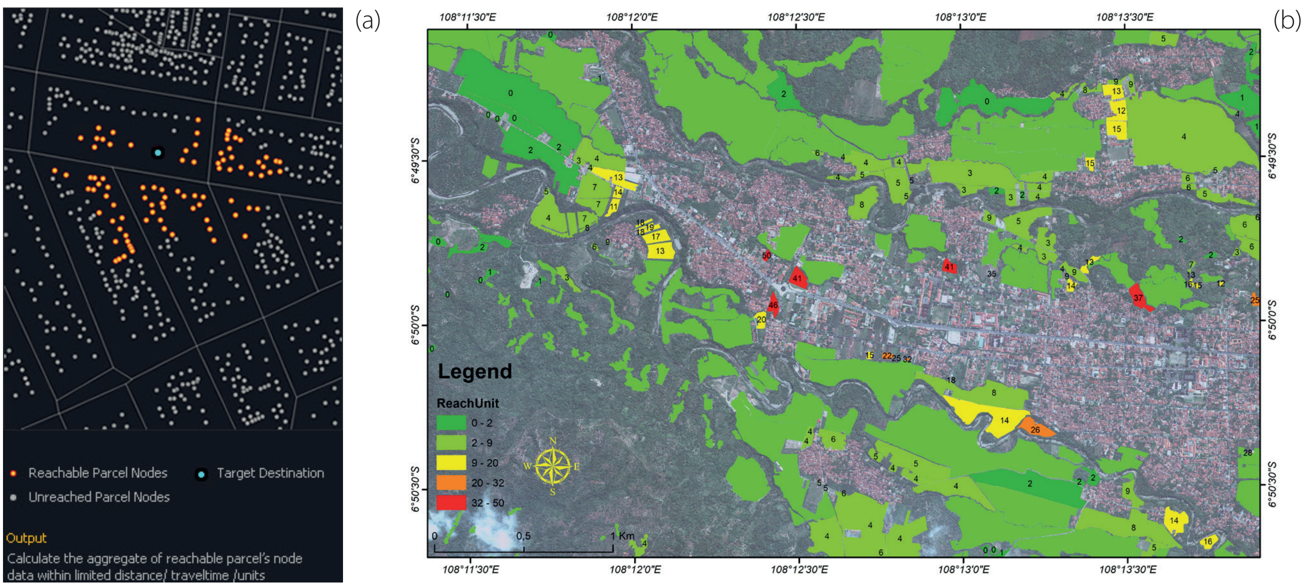

Fig. 6. (a) UrbanScad software tools, (b) Visual Illustration of The Reach Index

RESULTS AND DISCUSSION

Delineation of protection zones for precious farmland

The agriculturalfarmland landscape structure classification approach, as clearly shown in (Fig.6). In the study area, the core agricultural land occupied an area of 33.59%, while the Edge-Farmland covered 36.43 %. Furthermore, the Corridor area accounted for 0.30%, Discrete area of 12.26%, Edge-Patch area of 3.54%, and Perforated area of 13.89%. Spatially, the core agricultural land was predominantly distributed as a continuous area concentrated in the periphery outside the boundaries of the central urban area of Majalengka.

This peripheral area represented the historical agricultural land area in Majalengka Regency, which experienced a delay in urbanization and insignificant agricultural land segmentation due to road traffic, development areas, and other human activities. The agricultural land was segmented by other variables due to its dispersed nature on the outskirts of the city area, where regional development activities occurred daily, and non-agricultural activities encroached upon the limits of agricultural land. Most agricultural land was surrounded by built property, separating it as an ecological island in the heart of the city and reducing spatial proximity between different land uses. Compared to other land types, core farmlands exhibited superior functional qualities, such as strong connectedness, minimum disruption from non-agricultural activities, and optimal agricultural yield. This landscape was used for various agricultural purposes and significantly contributed to the quality of farmland landscapes. On the other hand, the edge farmland is a zone of ecological transition between core farmlands and non-farm ecosystems. Hence, implementing ecological conflict prevention methods enabled the coexistence of high-quality non-farm ecosystems and activities on arable lands while limiting their environmental impact. The peripheral agricultural lands functioned as a protective barrier, safeguarding the productive operations of central agricultural lands. The synergistic relationship between these two categories of agricultural land is noteworthy.

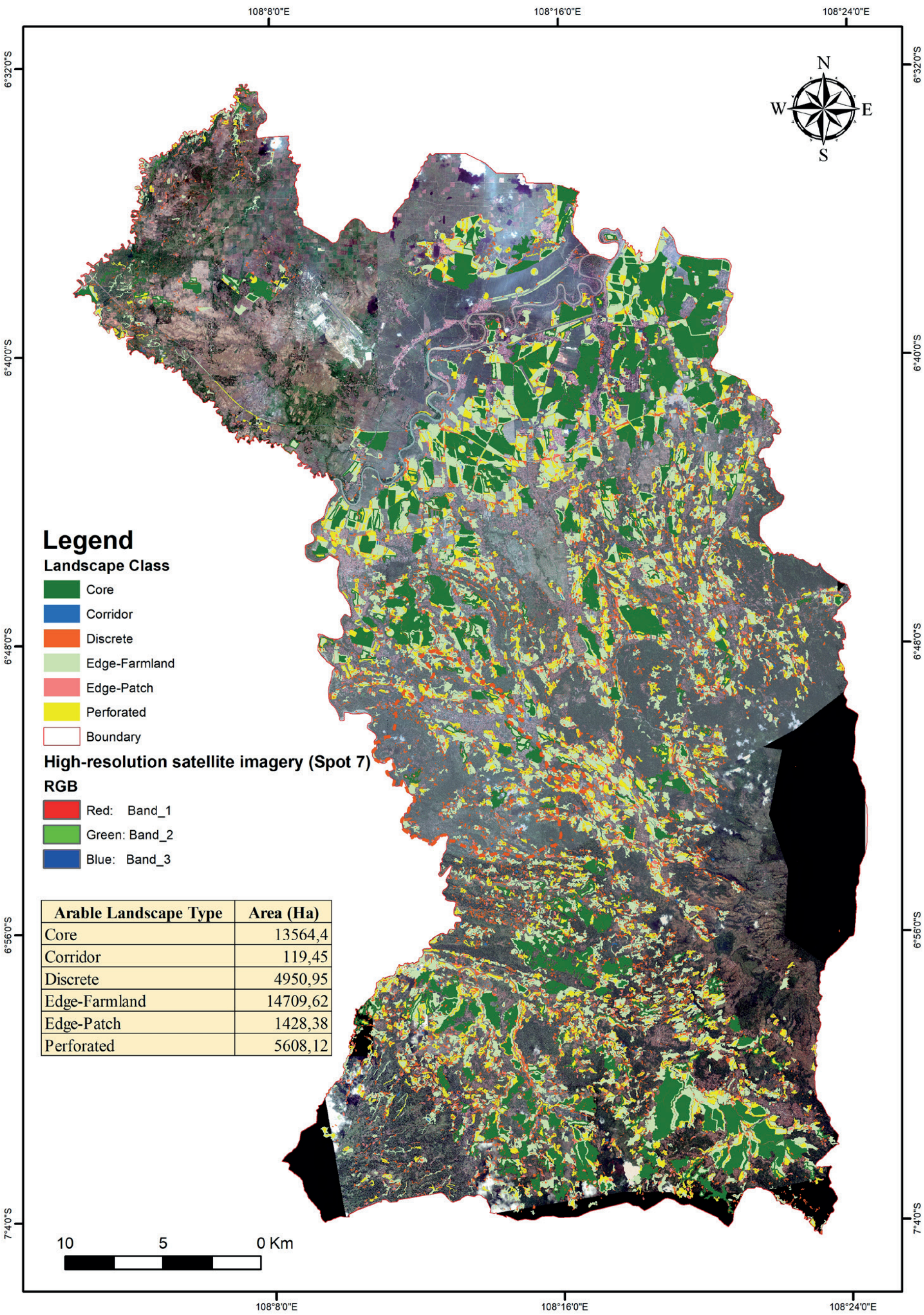

Arable Landscape Type	Area (Ha)
Core	13564,4
Corridor	119,45
Discrete	4950,95
Edge-Farmland	14709,62
Edge-Patch	1428,38
Perforated	5608,12

Fig. 7. Landscape class of agricultural land in Majalengka Regency

Corridor farmlands served as conduits linking agricultural lands, demarcating them from non-agricultural surroundings. The peripheries and fragments of agricultural land possessed diminutive habitats and exhibited mosaic patterns within non-agricultural landscapes. These factors frequently impacted the landscapes, potentially resulting in increased productivity. The objective of the aforementioned was akin to perforating farmlands, primarily exhibiting the temporal evolution of the spatial configuration of agricultural terrains. In the context of defining prime farmlands, it is imperative to consider both the peripheral and central farmlands as well as the continuity of the plot. The optimal utilization of prime farmlands can be achieved by adopting the core farmland as a prototype and demarcating the primary farming fields using the peripheries of the edge farmland.

Result Farmland Quality

Spatial variables were used to assess suitability scores during the analysis, it was important to categorize each variable based on the respective land suitability classification before applying the conformity overlay. The process of assessing and classifying a particular land region based on its intended purpose is called Land Suitability Classification (Fadlalla and Elsheikh 2016). The present study used the FAO (Food and Agriculture Organisation) land use suitability class to categorize agricultural land use. The classes in question were S1, S2, S3, and N1, denoting high suitability, sparse suitability, and unsuitability. This analysis utilized the values of each variable to ascertain the prospective land that could be used for sustainable food agriculture. The variables included physical factors that could be visually represented with spatial analysis. Some of the variables considered were agricultural index, water affordability and land area, irrigation system, drainage, soil type, disaster risk, rainfall, as well as slope and erosion hazard. Infrastructure sub-criteria, such as irrigation system analysis and road distance, were also considered. In addition, spatial analysis was carried out using the overlay technique.

As a result, the current study conducted a qualitative division of farmland by analyzing the quality of agricultural land at the block level in Majalengka Regency. Suitability analysis, which evaluated whether land properties were suitable for the intended use was a crucial part of the land use planning (Jayasinghe et al. 2019; Singha et al. 2019). The agricultural suitability study considered various spatial variables (factors) to determine the suitability score. A total of eleven parameters, including the water availability, land acreage, irrigation status, proximity to roads, drainage, soil type, disaster likelihood, precipitation, slope, and erosion, were selected, all of which contributed to the paddy crop farming index (IP). These spatial variables (factors) were incorporated into raster-based GIS software, and spatial analysis were performed using the overlay and map algebra methodology.

A land suitability calculation model and a modified algebra method raster analysis were used to create patterns of agricultural land protection. The estimated area required for protected agricultural land, based on strategic planning in the Majalengka district, was 40,380.92. This model offered alternative options for safeguarding agricultural land. The land suitability map was created using weighted spatial overlay analysis based on the AHP weights for 11 criteria, as shown in Fig. 8. The land quality grading for S1 (indicating high suitability for farming) was estimated to be 15,038.99 hectares, accounting for 11.31% of the total land area. Conversely, the estimated area of unsuitable land, mainly mountainous terrain and other land uses, was 80,764.05 hectares. The unsuitability of the land can be attributed to its current non-agricultural use and its lack of compliance with future suitability class requirements. In this case, the quality of farmland in Majalengka Regency was evaluated, encompassing a vast area of 39,190 hectares. The accessible land in Majalengka Regency was classified into two suitability ranges, namely S1 and S2. The total land area classified as *Highly Suitable* (S1) was 15,038.99 ha, while the *Suitable* (S2) group encompassed 23,745.42 ha, resulting in a total area of 38,784.41 hectares. The protection of this area against any change, particularly for development purposes is important to ensure its long-term viability.

Result Reach Calculation

Kernel Density *(Centrality Distributions Along Streets)*

The road network comprising 91,452 nodes (*intersections*) and 95,073 edges (*links between two intersections*), was obtained by merging the open street map data with Pleiades imagery. (Fig.9) shows the road length (*edge length*), while (Fig.10) illustrates the kernel density of the nodes, using kernel density estimation (KDE) on the street network, displaying the KDE of the nodes within a predetermined searching radius.

Point of Interest (POI)

The present investigation involved acquiring point-of-interest data in the Majalengka Regency from diverse sources, including Bappeda Majalengka. The data collection process was facilitated by utilizing G Map Scraper, which yielded 5,787 records. The Point of Interest (POI) was divided into 15 primary classifications, as illustrated in Fig. 9. The primary role of the urban center in the Majalengka District region was to furnish habitation and employment opportunities for its populace, alongside dispensing communal amenities. The most important land categories in terms of urban land functionality were commercial, residential, and industrial. Although the available POI dataset did not allow for a proper definition of industrial land within Majalengka Regency. Therefore, the POI data were classified into three, namely business facilities, commercial, residential locations, as well as public administration and services. The details of these categories are presented in (Fig. 11)

Reach Calculated

The reach analysis at each node was initially computed using the UrbanSCAD (https://circle.urbanesha.com/auth) urban network analysis tool. This study summarized the range analysis of edges by calculating the average centrality of the two connected nodes between points of interest (POI) and each paddy field (point). Furthermore, the paddy field data were processed from polygon data and converted into points using centroid tool in QGis software. The reach analysis was also computed to allocate point-of-interest amenities within a 50-meter constraint amidst the location markers of rice paddies. (Fig.12) shows the spatial distribution of the range analysis. Individuals may hold varying perspectives regarding the road network configuration as they traverse through. This study aimed to determine the effect of the road network index on the distribution of paddy fields and point of interest (POI) locations. In the study area, the reach estimates revealed

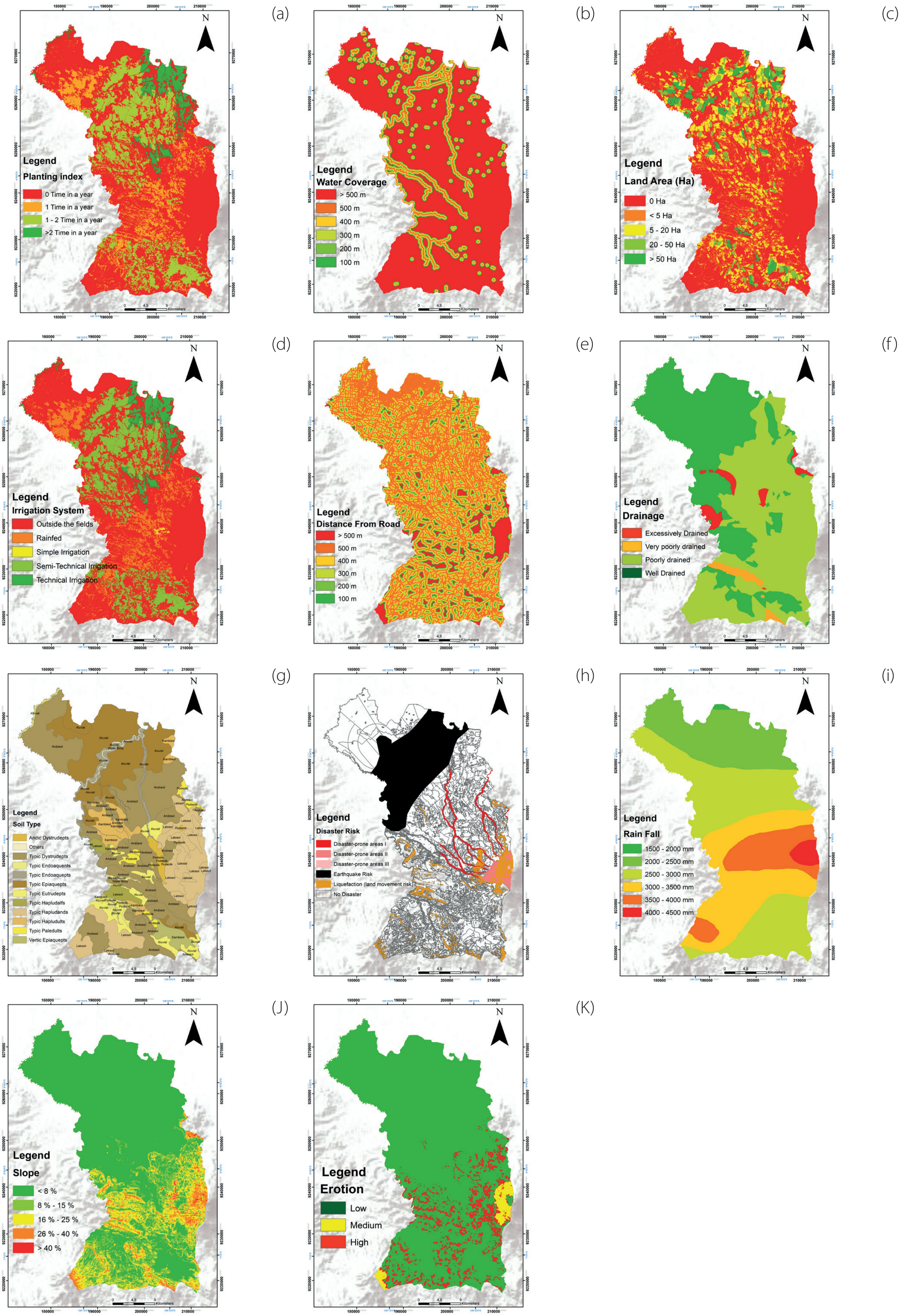

Fig. 8. Thematic Data Layer maps

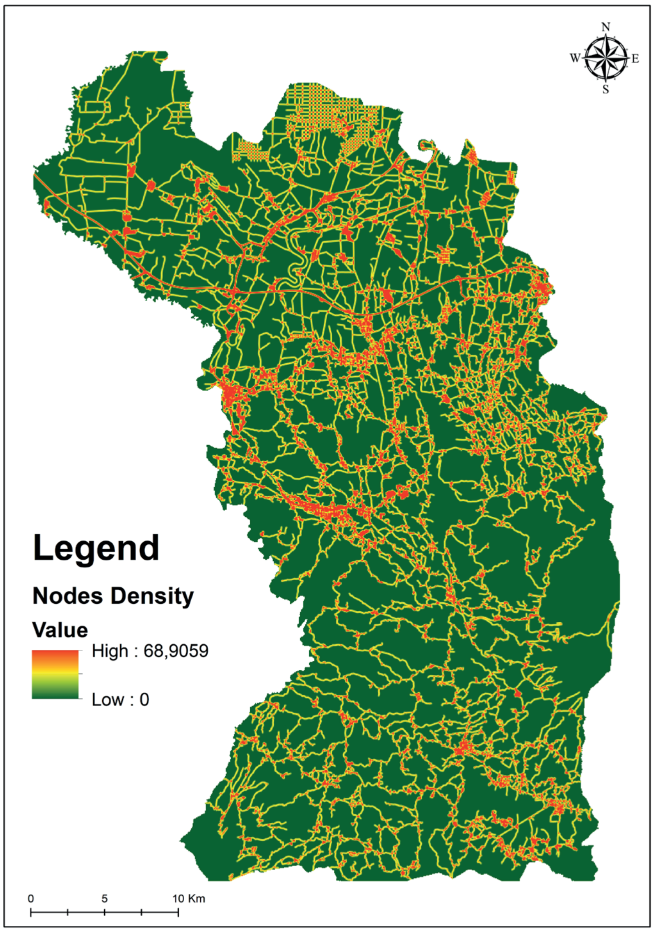

Fig. 9. Density of nodes in Majalengka Regency

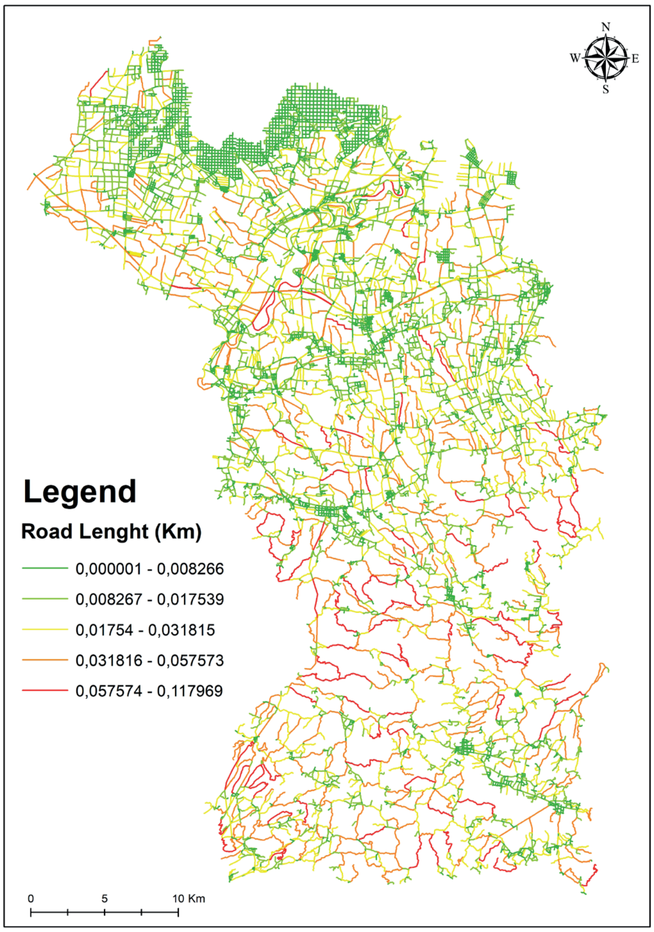

Fig. 10. oad lenght

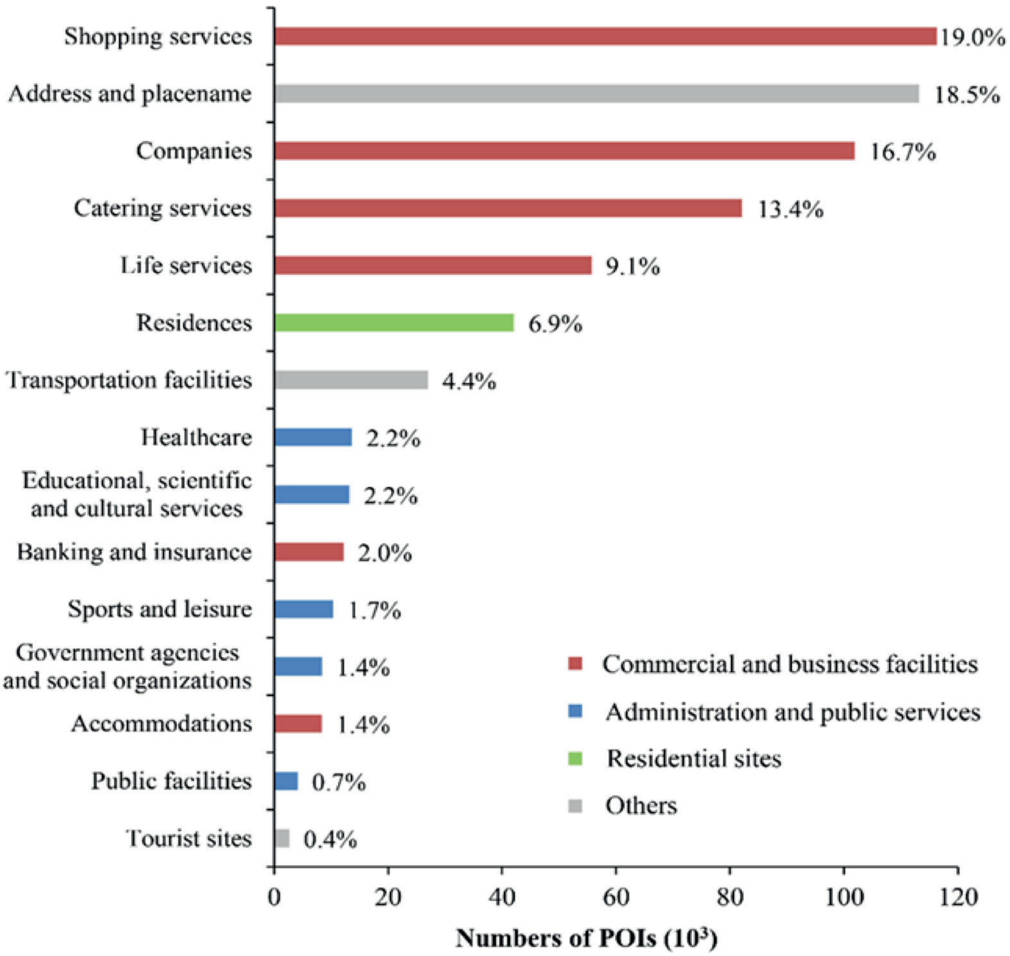

Fig. 11. Categories of Point of Interest (POI) in Majalengka Regency

varied spatial patterns, with a higher core concentration and a multipolar distribution in the suburbs. Also, the density of locations decreased from the downtown region to the outskirts. The proximity to geographical sites and the shorter average distance to the centre point implied easy accessibility (C. Liu et al. 2019; Van Duin et al. 2016).

Design of the spatial regulation of farmlands

This study developed a spatial arrangement structure for farmland, known as the 'two lanes, two zones' approach, based on the farmland protection principle. The approach aimed to manage and protect farmland while minimizing non-agricultural interference mechanisms. The term 'two lines' pertained to a pliant or inflexible boundary for urban development, while 'two zones' denoted a central zone for safeguarding agricultural land or an urban regulation zone with flexibility. The objective was to address spatial land use challenges arising from the tension between safeguarding agricultural land and accommodating urban growth. Results of the Reach Calculated calculation in (Fig.12) to implement this approach, Geographic Information Systems (GIS) spatial analysis technology was used to identify the factors that cause conflicts between agricultural land protection and urban expansion. A spatial diagnosis of land management policies was conducted using all available background information about the conflict areas. This step established the rules for the area, allowing for the definition of the final boundaries of the leading farmland protection zones, the flexible urban development boundaries, and the rigid urban development boundaries. This exclusion analysis from urban development boundaries identified areas that were flexible and adaptable to flexible or rigid urban development boundaries, also called urban spatial growth boundaries.

Delineation of the spatial regulation boundaries of farmlands

Establishing prime farmland conservation zones serves as the fundamental policy mechanism to mitigate the reduction of farmland due to urban expansion in the Majalengka Regency. The subject encompasses various components, including the structure of the storyline, the arrangement of physical spaces, the fertility of agricultural land, and the geographical characteristics of the location. Quantitative evaluations of landscape configuration indices are being conducted based on plot morphology and spatial layout, namely at the type, landscape, and patch scale. Quantitatively characterizing a single plot's spatial information and system functions is challenging. The assessment of farmland quality and regional geography mainly relies on extensive evaluations of multiple aspects and circumstances. The comprehensive review of regional farmlands' integrated productivity levels has some reference value; nonetheless, there needs to be clarity in determining the factors to be selected and weighted. Moreover, incorporating many elements tends to weaken the primary factor's significant impact on the quality of agricultural and environmental assessment, distorting the evaluation outcomes.

The conventional methodologies used in land-use planning and delineation in prime farmland preservation zones focus on the protected area's characteristics and the broader needs of regional socio-economic development (Qianwen et al. 2017; Xia et al. 2017). This approach creates numerous problems, such as a lowered quality of prime farmland protection zones, fragmented morphology, and high altitudes with highly gradient farmlands. Land morphology in the research area, namely Majalengka district, has an area of 400-2000 meters above sea level.

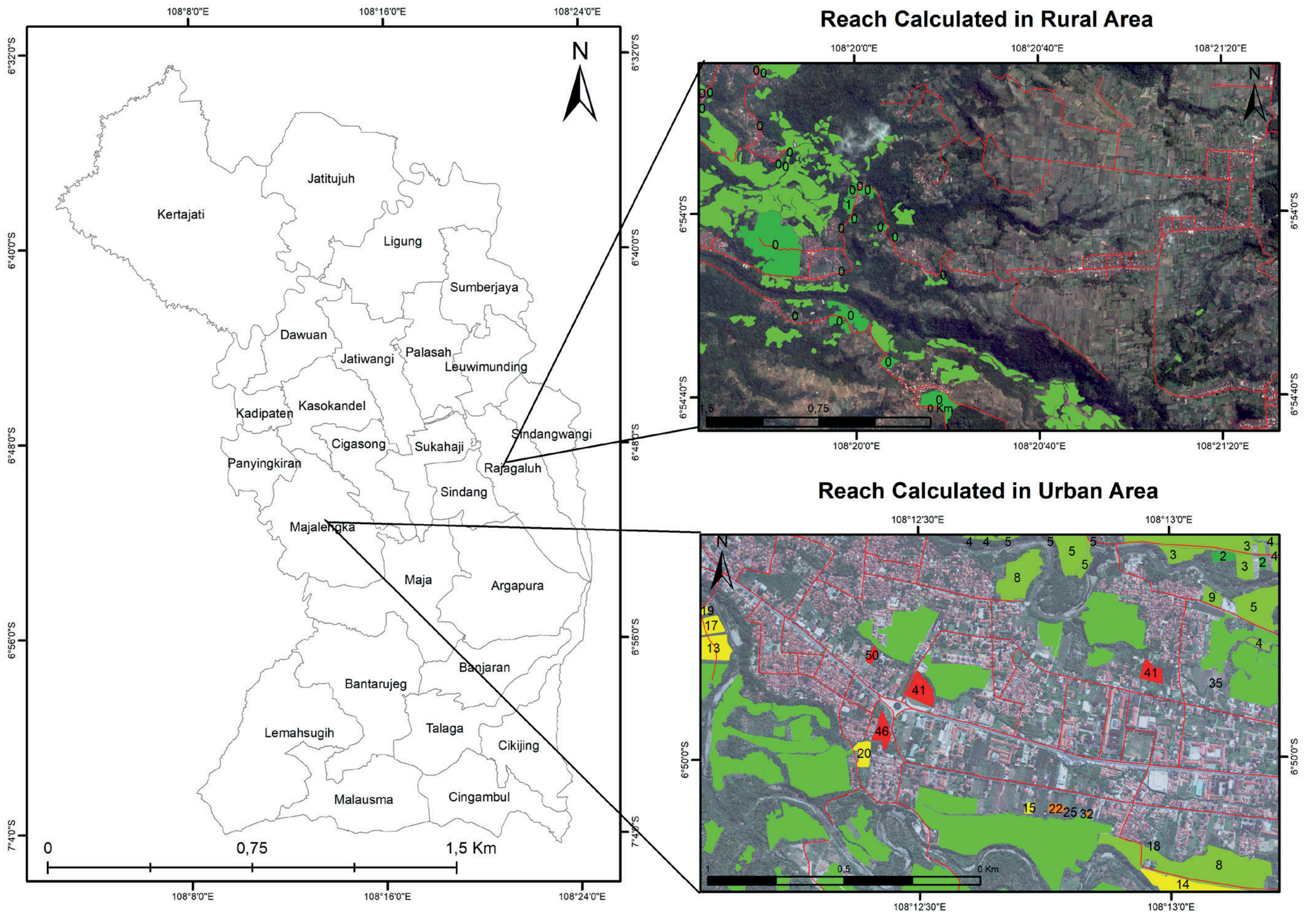

Fig. 12. Spatial Distribution of Paddy Field Reach Calculation to Point of Interest (POI)

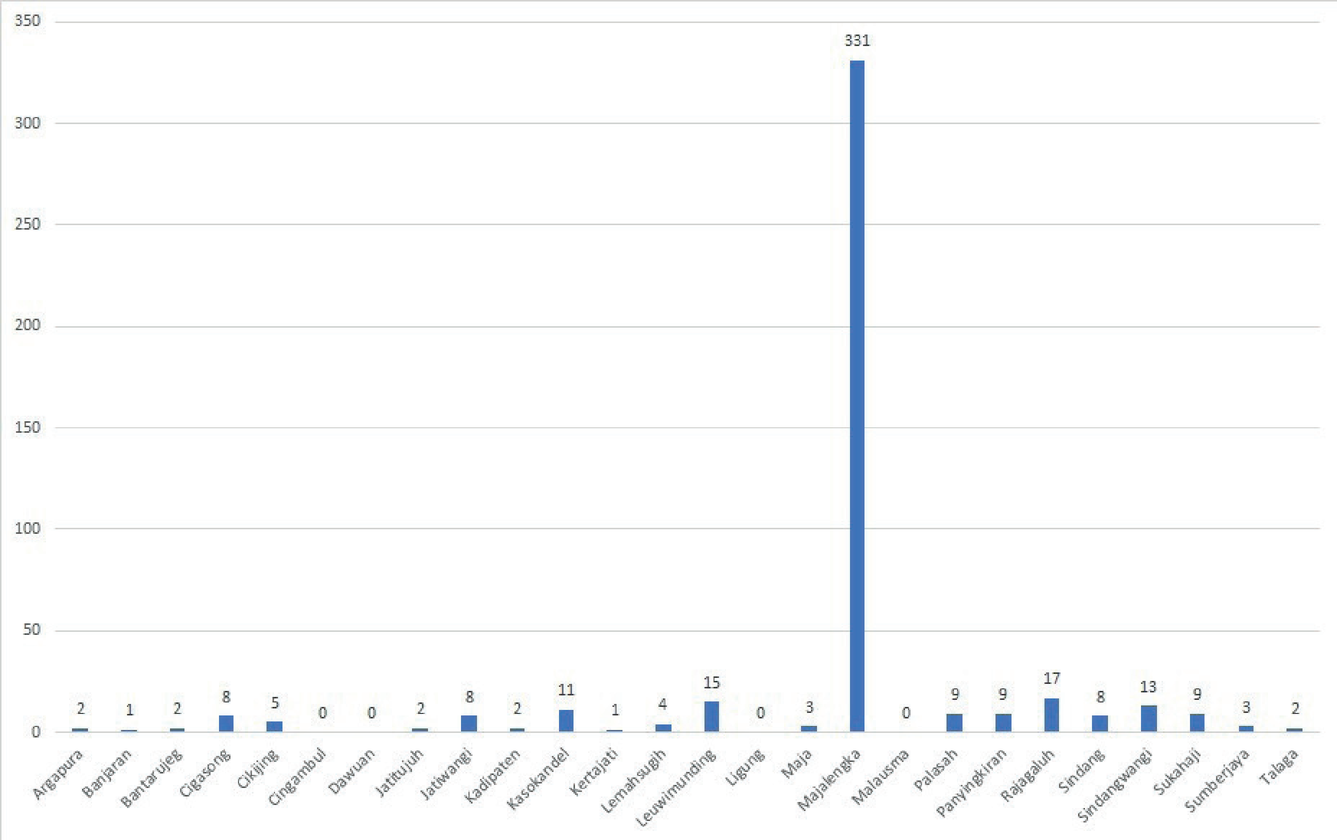

Fig. 13. Spatial Reach distribution data of district level

The total area of urban development boundaries, encompassing flexible and rigid boundaries, was 12,171.75 hectares. A flexible, adjustable zone of 998.22 hectares existed in this area. The demarcation resulted in the formation of two extensive areas, namely one situated north along the river and the other encompassing the majority of Majalengka Regency. The analysis, as depicted in (Fig.14), showed the protection zone covered a significant portion of the agricultural land, spanning an area of 13,564.39 hectares. This zone is situated in the northern region and comprised of two distinct patches in the central and eastern areas. The demarcation of the primary agricultural land conservation areas as well as the adaptable and inflexible urban expansion boundaries was established based on the outcomes of conflict resolution in these areas. The development of a two-lane, two-zone spatial regulation structure for agricultural land was informed by the range of flexible or rigid urban development boundary options and the identification of adaptable urban areas through spatial analysis. As previously mentioned, 'two lines' pertained to urban development boundaries that could either be flexible or rigid, while 'two zones' referred to zones primarily intended to protect agricultural land or regulate urban flexibility.

DISCUSSION

Due to the substantial overlap between agricultural land and urban development, Majalengka Regency has faced issues related to the widespread encroachment on valuable farmland caused by urban expansion. Agricultural land in Indonesia, particularly in Majalengka district, have diminished due to the following reasons (1) Agricultural lands were transformed into urban areas as people migrated and the number of people living in cities increased. The demand for homes, businesses, shopping centres and other urban infrastructure, necessitated more land, which often came at the expense of agricultural land. (2) Industries and Industrial Estates: The growth of industries and the establishment of industrial estates had also contributed to the reduction of agricultural land. Most factories, shops and other industrial buildings were constructed on land previously used for farming. (3) Infrastructural Development: Roads, bridges, airports, seaports and other infrastructure projects required land development, resulting in the conversion of agricultural land for other uses. (4) Improved Residential Land: Several agricultural lands were converted into residential areas to accommodate the growing population's housing needs.

Factors like threshold selection, data resolution, and landscape categorization size contribute to errors; future studies should investigate and resolve these issues. For instance, the regulations for gradation on agricultural land quality form the backbone of farmland quality classification in Indonesia. The regency-scale standard of farming, the land economic coefficient, and the land usage coefficient all play a role in determining this gradation. Setting up zones to protect good farmland was a primary policy tool for preventing shrinkage. This process involved various components, such as considering the shape of the rice field parcels, land layout, farming quality, and the geographical characteristics of the area. Landscape configuration indices were subjected to quantitative analysis based on factors, such as land type, landscape, and patch scale, to examine the shape and arrangement of parcels. Quantifying the spatial information and reach system functions of a single image required significant effort.

A comprehensive review can serve as a reference point for assessing the productivity of regional farmlands. However, determining which factors to use and how much weight to assign were sometimes unclear. Considering numerous factors tended to diminish the impact of the most pivotal factor on the quality of farmland and the assessment of the environment. This approach compromised the accuracy of evaluation results. Traditional techniques for safeguarding prime farmland through land-

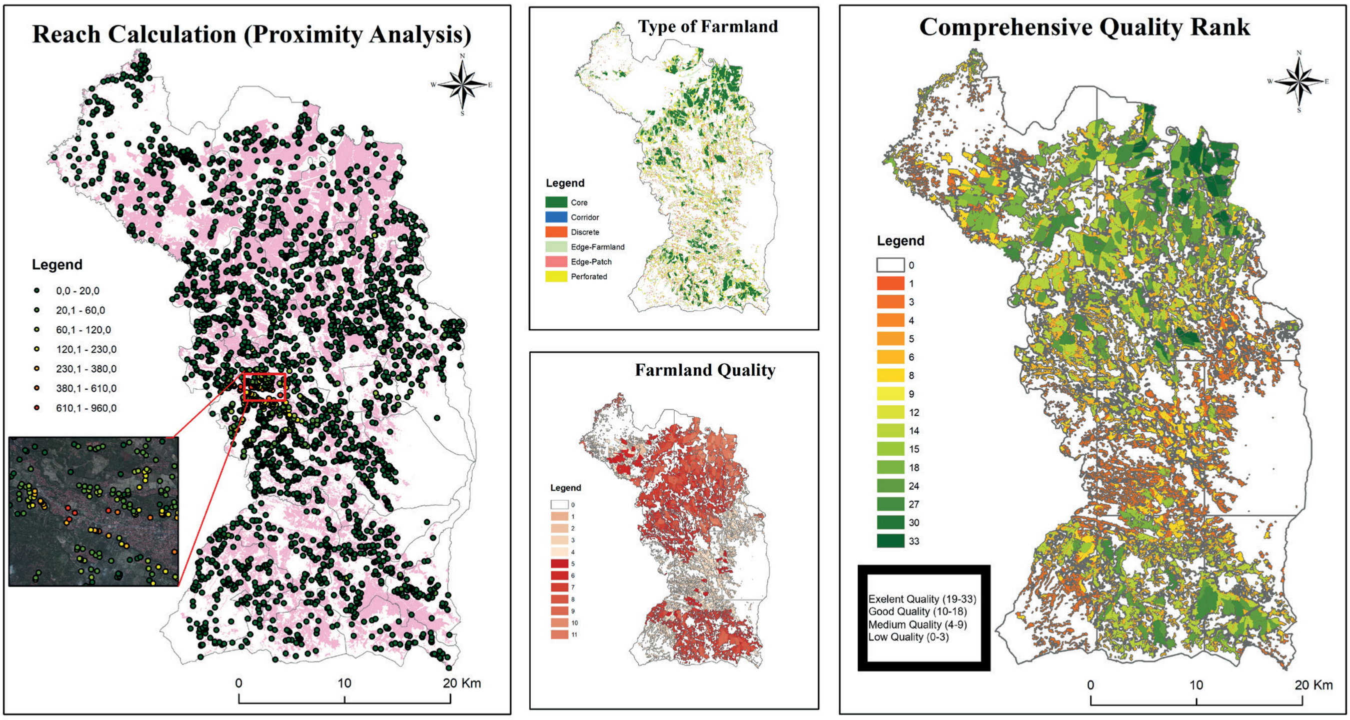

Fig. 14. Results of the Process of Optimizing Land Protection Patterns

use planning and delineation prioritized the characteristics of the preserved land and the broader requirements of socio-economic advancement in the region.

The present investigation employed a geographical spatial dimension deduction methodology, which entailed following a delineation sequence of "prime farmland protection plot, patch, and zone." Subsequently, spatial scaling and layer-by-layer aggregation were utilized to establish the prime farmland protection zones. The prime farmland protection patches were identified using a landscape structure classification model. This model used a proximity-based approach to identify clusters of plots and designated them as prime farmland protection patches. This study effectively screened prime farmland protection patches using a combination of quality grading of farmland plots, ownership information, and regional land development intensity. These patches were subsequently consolidated to form prime farmland protection areas, which were larger than patches but smaller than zones.

CONCLUSIONS

This study used the Landscape Structure Classification Model to analyze farmland and identify optimal areas for protection based on the functioning of different components. Furthermore, farmland quality grading and delineation were incorporated to determine the effectiveness of security patches on prime farms. This study used GIS spatial analytical techniques to investigate the causes of conflicts between farmland protection and urban development. A spatial diagnosis of the conflict areas was conducted, considering land-use spatial management policies and general background information. This step guided the regulatory direction of the conflict areas. The spatial boundaries of prime farmland protection zones, as well as the flexibility or rigidity of urban growth boundaries were also determined. implementing prime farmland protection zones was considered an effective strategy for managing and safeguarding farmland. The use of flexible buffer zones that could be modified as needed was the optimal approach for delineating farmland conservation areas within urbanized regions.

In the study area, core farmland has an area of 33.59%, while edge farmland has an area of 36.43%. Furthermore, the area of the corridor farmland is 0.30%, while the area of the discrete farmland is 12.26%, the Edge-Patch area is 3.54%, and the Perforated area is 13.89%. Spatially, the core agricultural land is mainly spread out as a continuous area concentrated on the outskirts outside the central area of Majalengka city. This study established a spatial regulatory framework for farmlands to reconcile the conflict between prime farmland protection zones and urban development boundaries. The establishment of this framework was aimed at addressing the construction and developmental requirements of the region, integrating spatial control of urbanized areas with the consolidation and protection of agricultural lands. This approach addressed the conflicts that arise from the need to preserve agricultural land while expanding urban areas. This has the potential to optimize the utilization of building land by enhancing both its spatial capacity and quality.

REFERENCES

Adrian, Widiatmaka, Munibah K. and Firmansyah I. (2022). Evaluate land suitability analysis for rice cultivation using a GIS-based AHP multi-criteria decision-making approach: Majalengka Regency, West Java Province. IOP Conference Series: Earth and Environmental Science, 1109(1), 012062. DOI: 10.1088/1755-1315/1109/1/012062

Bakker M.M., Hatna E., Kuhlman T. and Mücher C.A. (2011). Changing environmental characteristics of European cropland. Agricultural Systems, 104(7), 522–532. DOI: 10.1016/j.agsy.2011.03.008

BPS. (2018). Kabupaten Majalengka dalam angka tahun 2018. In: BPS Kabupaten Majalengka. Badan Pusat Statistik.

Chen Z., Zhang X., Huang X. and Chen Y. (2019). Influence of government leaders' localization on farmland conversion in Chinese cities: A "sense of place" perspective. Cities, 90, 74–87. DOI: 10.1016/j.cities.2019.01.037

Deng X., Huang J., Rozelle S., Zhang J. and Li Z. (2015). Impact of urbanization on cultivated land changes in China. Land Use Policy, 45, 1–7. DOI: 10.1016/j.landusepol.2015.01.007

Deslatte A., Swann W.L. and Feiock R.C. (2017). Three sides of the same coin? A Bayesian analysis of strategic management, comprehensive planning, and inclusionary values in land use. Journal of Public Administration Research and Theory, 27(3), 415–432. DOI: 10.1093/jopart/muw054

Duan Q., Tan M., Guo Y., Wang X. and Xin L. (2019). Understanding the spatial distribution of urban forests in China using Sentinel-2 images with Google Earth Engine. Forests, 10(9). DOI: 10.3390/f10090729

Eastman J.R., Weigen Jin, Kyem P.A.K. and Toledano J. (1995). Raster procedures for multi-criteria/multi-objective decisions. Photogrammetric Engineering & Remote Sensing, 61(5), 539–547.

Evangelista P.F. and Beskow D. (2019). Geospatial point density. R Journal, 10(2), 347–356. DOI: 10.32614/RJ-2018-061

Fadlalla R. and Elsheikh A. (2016). Physical Land Suitability Assessment Based On FAO Framework. IOSR Journal of Engineering (IOSRJEN) Www.Iosrjen.Org ISSN, 06(12), 1–36. www.iosrjen.org

Girvetz E.H., Thorne J.H., Berry A.M. and Jaeger J.A.G. (2008). Integration of landscape fragmentation analysis into regional planning: A statewide multi-scale case study from California, USA. Landscape and Urban Planning, 86(3–4). DOI: 10.1016/j.landurbplan.2008.02.007

Godfray H.C.J., Beddington J.R., Crute I.R., Haddad L., Lawrence D., Muir J.F., Pretty J., Robinson S., Thomas S.M. and Toulmin C. (2010). Food security: The challenge of feeding 9 billion people. In: Science , Vol. 327, Issue 5967, 812–818. DOI: 10.1126/science.1185383

Henneberg S.C., Jiang Z., Naudéc P. and Ormrod R.P. (2007). THE NETWORK RESEARCHERS ' NETWORK: A Social Network Analysis of the IMP Group 1984-2006. The IMP Journal, 3(1), 28–49.

Holmes G. (2014). What is a land grab? Exploring green grabs, conservation, and private protected areas in southern Chile. Journal of Peasant Studies, 41(4), 547–567. DOI: 10.1080/03066150.2014.919266

Huang Z., Du X. and Castillo C.S.Z. (2019). How does urbanization affect farmland protection? Evidence from China. Resources, Conservation and Recycling, 145, 139–147. DOI: 10.1016/j.resconrec.2018.12.023

Jayasinghe S.L., Kumar L. and Sandamali J. (2019). Assessment of potential land suitability for tea (Camellia sinensis (L.) O. Kuntze) in Sri Lanka using a gis-based multi-criteria approach. Agriculture (Switzerland), 9(7). DOI: 10.3390/agriculture9070148

Jiang P., Cheng Q., Gong Y., Wang L., Zhang Y., Cheng L., Li M., Lu J., Duan Y., Huang Q. and Chen D. (2016). Using Urban Development Boundaries to Constrain Uncontrolled Urban Sprawl in China. Annals of the American Association of Geographers, 106(6). DOI: 10.1080/24694452.2016.1198213

Jiang P., Cheng Q., Zhuang Z., Tang H., Li M., Cheng L. and Jin X. (2018). The dynamic mechanism of landscape structure change of arable landscape system in China. Agriculture, Ecosystems and Environment, 251, 26–36. DOI: 10.1016/j.agee.2017.09.006

Jiang P., Li M. and Sheng Y. (2020). Spatial regulation design of farmland landscape around cities in China: A case study of Changzhou City. Cities, 97. DOI: 10.1016/j.cities.2019.102504

Knoke D., Wasserman S. and Faust K. (1996). Social Network Analysis: Methods and Applications. Contemporary Sociology, 25(2), 275. DOI: 10.2307/2077235

Liang C., Penghui J., Wei C., Manchun L., Liyan W., Yuan G., Yuzhe P., Nan X., Yuewei D. and Qiuhao H. (2015). Farmland protection policies and rapid urbanization in China: A case study for Changzhou City. Land Use Policy, 48, 552–566. DOI: 10.1016/j.landusepol.2015.06.014

Liu C., Wang Q. and Susilo Y.O. (2019). Assessing the impacts of collection-delivery points to individual's activity-travel patterns: A greener last mile alternative? Transportation Research Part E: Logistics and Transportation Review, 121, 84–99. DOI: 10.1016/j.tre.2017.08.007

Liu T., Liu H. and Qi Y. (2015). Construction land expansion and cultivated land protection in urbanizing China: Insights from national land surveys, 1996-2006. Habitat International, 46, 13–22. DOI: 10.1016/j.habitatint.2014.10.019

Perrin C., Nougarèdes B., Sini L., Branduini P. and Salvati L. (2018). Governance changes in peri-urban farmland protection following decentralisation: A comparison between Montpellier (France) and Rome (Italy). Land Use Policy, 70, 535–546. DOI: 10.1016/j.landusepol.2017.09.027

Porta S., Latora V., Wang F., Rueda S., Strano E., Scellato S., Cardillo A., Belli E., Càrdenas F., Cormenzana B. and Latora L. (2012). Street Centrality and the Location of Economic Activities in Barcelona. Urban Studies, 49(7), 1471–1488. DOI: 10.1177/0042098011422570

Qianwen C., Penghui J., Lingyan C., Jinxia S., Yunqian Z., Liyan W., Manchun L., Feixue L., Axing Z. and Dong C. (2017). Delineation of a permanent basic farmland protection area around a city centre: Case study of Changzhou City, China. Land Use Policy, 60, 73–89. DOI: 10.1016/j.landusepol.2016.10.014

Reid W. V., Chen D., Goldfarb L., Hackmann H., Lee Y.T., Mokhele K., Ostrom E., Raivio K., Rockström J., Schellnhuber H.J. and Whyte A. (2010). Earth system science for global sustainability: Grand challenges. In: Science , Vol. 330, Issue 6006, 916–917. DOI: 10.1126/science.1196263

Robins G., Pattison P., Kalish Y. and Lusher D. (2007). An introduction to exponential random graph (p*) models for social networks. Social Networks, 29(2), 173–191. DOI: 10.1016/j.socnet.2006.08.002

Saaty T. (1977). [Saaty, 1977]. Journal of Mathematical Psychology, 15.

Saaty T.L. (1988). What is the Analytic Hierarchy Process? In: Mathematical Models for Decision Support , 109–121. DOI: 10.1007/978-3-642-83555-1_5

Saaty T.L. (1990). How to make a decision: The analytic hierarchy process. European Journal of Operational Research, 48(1), 9–26. DOI: 10.1016/0377-2217(90)90057-I

Sari N.M. and Kushardono D. (2019). Analisis Dampak Pembangunan Infrastruktur Bandara Internasional Jawa Barat Terhadap Alih Fungsi Lahan Pertanian Melalui Citra Satelit Resolusi Tinggi. Jurnal Geografi, 11(2), 146–162. DOI: 10.24114/jg.v11i2.13470

Sayer J. (2009). Reconciling Conservation and Development: Are Landscapes the Answer? In: Biotropica , Vol. 41, Issue 6, 649–652. DOI: 10.1111/j.1744-7429.2009.00575.x

Sayer J., Sunderland T., Ghazoul J., Pfund J.L., Sheil D., Meijaard E., Venter M., Boedhihartono A.K., Day M., Garcia C., Van Oosten C. and Buck L.E. (2013). Ten principles for a landscape approach to reconciling agriculture, conservation, and other competing land uses. In: Proceedings of the National Academy of Sciences of the United States of America , Vol. 110, Issue 21, 8349–8356. DOI: 10.1073/pnas.1210595110

Scott J. (2020). The History of Social Network Analysis. In: Social Network Analysis , 11–39. DOI: 10.4135/9781529716597.n2

Singha M., Dong J., Zhang G. and Xiao X. (2019). High resolution paddy rice maps in cloud-prone Bangladesh and Northeast India using Sentinel-1 data. Scientific Data, 6(1). DOI: 10.1038/s41597-019-0036-3

Sutherland L.A., Peter S. and Zagata L. (2015). Conceptualising multi-regime interactions: The role of the agriculture sector in renewable energy transitions. Research Policy, 44(8), 1543–1554. DOI: 10.1016/j.respol.2015.05.013

Teshale G.A. (2016). Analyzing Social Networks , by S. P. Borgatti, M. G. Everett, and J. C. Johnson . Journal of Community Practice, 24(3), 353–355. DOI: 10.1080/10705422.2016.1209400

Uitermark J. and van Meeteren M. (2021). Geographical Network Analysis. Tijdschrift Voor Economische En Sociale Geografie, 112(4), 337–350. DOI: 10.1111/tesg.12480

Van Duin J.H.R., De Goffau W., Wiegmans B., Tavasszy L.A. and Saes M. (2016). Improving Home Delivery Efficiency by Using Principles of Address Intelligence for B2C Deliveries. Transportation Research Procedia, 12, 14–25. DOI: 10.1016/j.trpro.2016.02.006

Xia N., Li M. and Cheng L. (2017). Demarcation of prime farmland protection areas from high-resolution satellite imagery. International Geoscience and Remote Sensing Symposium (IGARSS) 2017-July, 660–663. DOI: 10.1109/IGARSS.2017.8127040

Zhang H., Duan Y. and Han Z. (2021). Research on spatial patterns and sustainable development of rural tourism destinations in the yellow river basin of china. Land, 10(8). DOI: 10.3390/land10080849

Zheng Z., Morimoto T. and Murayama Y. (2020). Optimal location analysis of delivery parcel-pickup points using AHP and network huff model: A case study of shiweitang sub-district in Guangzhou city, China. ISPRS International Journal of Geo-Information, 9(4). DOI: 10.3390/ijgi9040193

RESEARCH PAPER

FUZZY INFERENCE SYSTEM FOR MAPPING FOREST FIRE SUSCEPTIBILITY IN NORTHERN RONDÔNIA, BRAZIL

Miqueias Lima Duarte[1*], Tatiana Acácio da Silva[2], Jocy Ana Paixão de Sousa[2], Amazonino Lemos de Castro[2], Roberto Wagner Lourenço[2]
[1]Federal University of Amazonas (UFAM), Institute of Education, Agriculture and Environment, 69800-000, Humaitá, Brazil
[2]Institute of Science and Technology, São Paulo State University (Unesp), 18087-180, Sorocaba, SP, Brazil.
*Corresponding author: miqueiaseng@hotmail.com
Received: May 24th, 2023 / Accepted: November February 6th, 2024 / Published: March 31st, 2024
https://DOI-10.24057/2071-9388-2023-2910

ABSTRACT. Forest fires are global phenomena that pose an accelerating threat to ecosystems, affect the population life quality and contribute to climate change. The mapping of fire susceptibility provides proper direction for mitigating measures for these events. However, predicting their occurrence and scope is complicated since many of their causes are related to human practices and climatological variations. To predict fire occurrences, this study applies a fuzzy inference system methodology implemented in R software and using triangular and trapezoidal functions that comprise four input parameters (temperature, rainfall, distance from highways, and land use and occupation) obtained from remote sensing data and processed through GIS environment. The fuzzy system classified 63.27% of the study area as having high and very high fire susceptibility. The high density of fire occurrences in these classes shows the high precision of the proposed model, which was confirmed by the area under the curve (AUC) value of 0.879. The application of the fuzzy system using two extreme climate events (rainy summer and dry summer) showed that the model is highly responsive to temperature and rainfall variations, which was verified by the sensitivity analysis. The results obtained with the system can assist in decision-making for appropriate firefighting actions in the region.

KEYWORDS: Fuzzy logic; GIS; forest fires; Amazon; fire control

CITATION: M. L. Duarte, T. Acácio da Silva, J. A. Paixão de Sousa, A. Lemos de Castro, R. W. Lourenço (2024). Fuzzy Inference System For Mapping Forest Fire Susceptibility In Northern Rondônia, Brazil. Geography, Environment, Sustainability, 1(17), 83-94
https://DOI-10.24057/2071-9388-2023-2910

ACKNOWLEDGEMENTS: This study was partially financed by the Coordenação de Aperfeiçoamento de Pessoal de Nível Superior – Brasil (CAPES) – Finance Code 001.

Conflict of interests: The authors reported no potential conflict of interest.

INTRODUCTION

Forest fires cause immeasurable environmental impacts. On top of economic damage and public health-related problems, which are commonly observed immediately after fires, later events such as climatic and environmental changes caused by large amounts of CO_2 emitted into the atmosphere lead to the increasing greenhouse effect, thus resulting in major ecological disturbances (Machado and Lopes 2014; Aragão et al. 2018; Venkatesh et al. 2020).

In the past, the occurrence of forest fires was naturally related to climatic fluctuations, such as changes in temperature and rainfall; however, in recent decades, anthropogenic activities have caused major alterations in the fire regime (Chuvieco et al. 2019) since changes in land use associated with climate change can increase the frequency and severity of these events (Aquilué et al. 2020). Thus, understanding their spatial and temporal distribution is not trivial (Machado and Lopes, 2014) since it includes a set of dynamic factors driven by the interaction of biotic and abiotic processes that depend on the geographic scale (Aragão et al. 2018; Mota et al. 2019; Pourghasemi et al. 2020; Ribeiro et al. 2020).

Data from the Fire Information for Resource Management System (FIRMS) indicates that between 2000 and 2018 there were about 7.27 million outbreaks of fire in South America (NASA, 2020). In Brazil, the occurrence fire outbreaks has significantly increased in recent years due to several factors, such as deforestation, agropastoral activities, and uncontrolled burning (Caúla et al. 2015; Barlow et al. 2019). Although the entire national territory suffers from these events, historical data shows that 80.66% of fires occur in the Amazon and Cerrado biomes, with an average of 170,000 fire outbreaks per year, predominantly between July and October (INPE, 2020).

The effective management of these events requires centralized planning, which includes identifying the locations with the greatest fire susceptibility. This identification can enable the management of critical areas and serve as a basis for developing more accurate fire warning systems and a consistent institutional program (Adab et al. 2013; Eugenio, 2016; White et al. 2016; Barlow et al. 2019). The methods usually employed in planning include integrating remote-sensing techniques, statistical methods, and GIS (Jaiswal et al. 2002; Adab et al. 2013; Mota et al. 2019; Pourghasem et al. 2020; Gizatullin and Alekseenko, 2022), which are employed through probabilistic, stochastic models, or a mixture of both.

Despite proving high effectiveness in studies at local scale, at regional scale the GIS and statistical methods have limitations due to multiple complex interactions related to the degree of subjectivity these events have, spatial distribution of the events, and uncertainties caused by spatial and temporal resolution of the ignition data. This makes it difficult to eliminate uncertainties regarding the inaccuracy of the data and, as a result, these models present difficulties when associating products with data inaccuracies in the GIS environment, thus resulting in errors in the final products (Bui et al. 2017; Moayedi et al. 2020; Sahiner et al. 2022). Therefore, it is necessary to develop new models that make it possible to deal with uncertainties and inaccuracies, while also improving the ability to predict these events.

As an alternative methodology, the fuzzy theory introduced by Zadeh (1965) provides a logical approach that is capable of dealing with complex systems, such as those observed in forest fire events that have spatial and temporal variability, as well as subjectivity, and providing an adequate mathematical treatment (Zadeh 1965; Araya-Muñoz et al. 2017; Bressane et al. 2020; Fernandes et al. 2023). Recent environmental applications that use the fuzzy approach integrated with GIS have shown advantages over traditional techniques in evaluating several phenomena, such as susceptibility to flooding (Sahana and Patel, 2019), landslides (Nwazelibe et al. 2023), drought (Nikolova et al. 2021), and soil erosion (Souza et al. 2019), and anthropic impact on watersheds (Lopes et al. 2021).

Considering that the fuzzy theory is used to analyze the causality of uncertain events (Román-Flores et al. 2020; Sahiner et al. 2022), including the causes of forest fires (Pourghasemi et al. 2020; Ribeiro et al. 2020), and that the fuzzy method can work with uncertainties related to the spatial and temporal data resolution (Lopes et al. 2021; Sahiner et al. 2022), this study presents a fuzzy inference system that considers climatic and anthropic variables as input variables for mapping fire susceptibility, with the study area of the northern region of the Rondônia state, Brazil, due to the high number of fires registered there in recent years.

MATERIALS AND METHODS

Study Area

The study was conducted in the north of the Rondônia state. It is an area of around 89,900 km^2 (Figure 1) that covers 14 municipalities and has a population density of 8.0 inhabitants/km^2. This region is mostly occupied by agricultural and cattle-ranching lands due to administrative and financial support from governmental colonization programs in the Brazilian Amazon that have taken place from the 1970s onwards (Alves et al. 2021). These programs are characterized by the implementation of colonization settlements, which are preceded by high deforestation rates due to the expansion of agricultural lands and cattle-ranching (Alves et al. 2021; Duarte et al. 2021), thus making the region a part of the "Arc of Deforestation" in the Brazilian Amazon.

In this region, fire is commonly used for clearing the land after deforestation and for pasture renewal (Caúla et al. 2015; Barlow et al. 2019). Consequently, around 70% of the fire outbreaks in Rondônia have occurred in its northern part, with 90% of them being registered between August and October during the dry season (SEDAM, 2020).

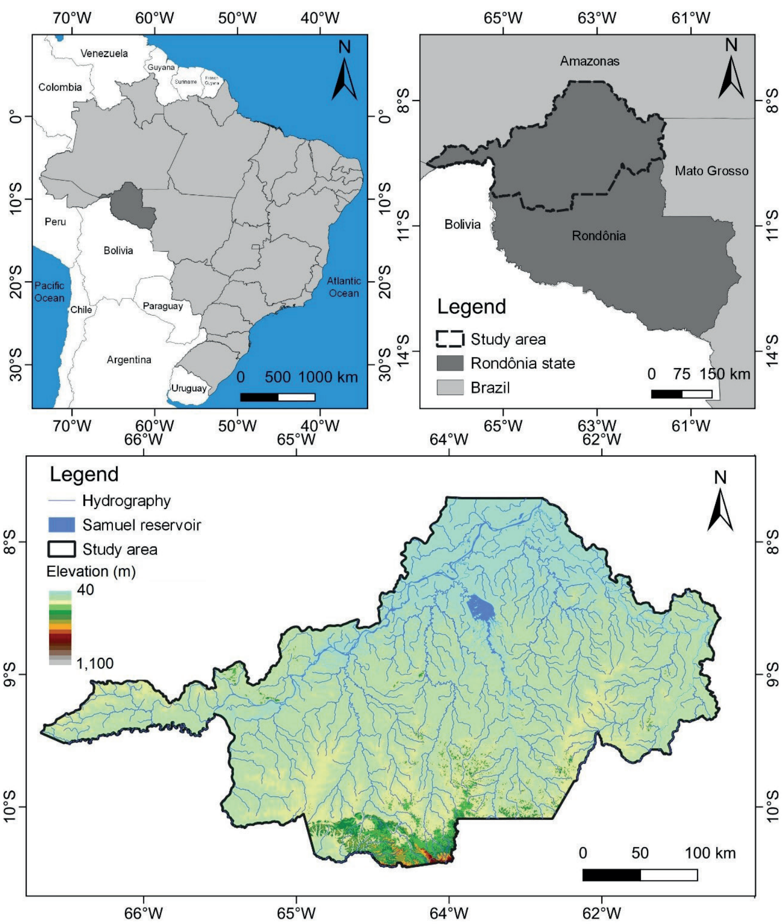

Fig. 1. Study area in northern Rondônia

According to the Köppen classification (Alvares et al. 2013), the region's climate is of the Aw type (Rainy Tropical Climate), with average annual precipitation of 2,250 mm. It has a well-defined dry period from June to August, with monthly precipitation below 50 mm, and a rainy period from November to April, with monthly precipitation above 220 mm. The average annual temperature in the region is 25.5 °C, with a maximum of 34.4 °C in August and a minimum of 19.2 °C in July (Silva et al. 2018).

The indigenous vegetation presents diverse characteristics, comprising open ombrophylous forests, dense ombrophylous forests, savannas, pioneer formations, and contact or transition forests. Additionally, there are areas of anthropogenic activity that are primarily occupied by pastures and family farming (SEMA, 2012; Schlindwein et al. 2012). In this region, deforestation occurs predominantly in areas that consist of open ombrophylous forests and dense ombrophylous forests, predominantly due to livestock farming.

Fuzzy System Proposal

Several previous studies propose the association of factors to indicate the spatial predisposition of forest fire occurrence (Jaiswal et al. 2002; Bonazountas et al. 2005; Parente and Pereira, 2016; Mota et al. 2019; Pourghasemi et al. 2020). However, methodological association of several factors is quite complicated, in addition to being impractical and possessing regional degrees of subjectivity (Carmo et al. 2011; Gralewicz et al. 2012). Furthermore, large-scale data are not always available, especially in remote areas like Brazilian Amazon.

This study gathered a set of factors mentioned in previous research that can be obtained from remote sensing data to compose a fuzzy inference model. This model is characterized by a Max-Min inference system proposed by Mamdani and Assilian (1975). This system is one of the most commonly used in geosciences since, besides being abstractly defined, it employs linguistic variables, which facilitates their application (Acaroglu et al. 2008).

The four main components of the fuzzy inference system are input fuzzification, fuzzy rule base, fuzzy inference method, and defuzzification. To "fuzzify" the input variables into a common range [0,1], each variable is transformed into linguistic variables (low, moderate, and high values) that can be calculated by Equations 1, 2 and 3, and represented by a triangular (Equation 4) and a trapezoidal (Equation 5) membership functions, which overlap and form fuzzy regions, thus allowing data to belong to more than one set (Cocconello et al. 2014; Román-Flores et al. 2020).

$$\mu_x(L) = f\left(x, a_{xL}, b_{xL}, c_{xL}, d_{xL}\right) \tag{1}$$

$$\mu_x(M) = f\left(x, a_{M}, b_{xM}, c_{xM}, d_{xM}\right) \tag{2}$$

$$\mu_x(H) = f\left(x, a_{xH}, b_{xH}, c_{xH}, d_{xH}\right) \tag{3}$$

where the function *f(x;a,b,c,d)* is given by Equations 4 or 5, x refers to the input variables, and the subscripts (*xL, xM, xH*) refer to the variables' membership function parameters for the low, medium, and high classes.

$$\mu(x;a,b,c) = max\left\{min\left\{\frac{x-a}{b-a}, \frac{c-x}{c-b}\right\}, 0\right\} \tag{4}$$

$$such\ that \backslash a, b, c \in R$$

$$\mu(x;a,b,c,d) = max\left\{min\left\{\frac{x-a}{b-a}, 1, \frac{d-x}{d-c}\right\}, 0\right\} \tag{5}$$

$$such\ that \backslash a, b, c, d \in R$$

where μ corresponds to the membership function, and the variables *a, b, c,* and d correspond to the parameters that represent the shape of the triangular and trapezoidal function. In this study, we chose functions of mixed relevance, employing trapezoidal functions for exact extensions and triangular functions for abrupt transitions.

The rule base comprises a set of IF … THEN rules that associate the inputs forming the fuzzy system outputs. These rules are based on the relationships between the variables, for instance: *IF temperature is low AND precipitation is low AND distance from highways is low AND land use and occupation is low, THEN fire hazard is very low*

The output variable comprising fire susceptibility was characterized by the following language terms: very low, low, moderate, high, and very high. Triangular membership functions represented these variables. Finally, the centroid method was used to transform the fuzzy output variable into a crisp numerical value (defuzzification). This method calculates the average of the areas representing the degrees of the fuzzy subset pertinence (Román-Flores et al. 2020).

Determining the Input Variables

The input variables selected for the fuzzy system referred to precipitation, temperature, distance from highways, and land use, and were obtained from open remote sensing products.

Land surface temperature for the study area (in Kelvin) was estimated from thermal images taken by the MODIS (Moderate Resolution Imaging Spectroradiometer) sensor, product MOD11 (Land Surface Temperature - LST) from Terra and Aqua satellites, at ~1 km spatial resolution. The data are available at the United States Geological Survey website (USGS, 2020). Data from the USGS were chosen for the calculations as their estimates were observed in situ for the Amazon region by Gomis-Cebolla et al. (2018). Monthly data were obtained between August and October 2018 at 1 km spatial resolution in GeoTIFF format using the Google Earth Engine platform. Then, the conversion from Kelvin to Celsius degrees was performed through the GIS environment.

Monthly precipitation (in mm) was obtained from the Global Precipitation Measurement (GPM), IMERG Version 6, with ~1 km spatial resolution, which was provided by the Japan Aerospace Exploration Agency (JAXA, 2020). These data are similar to the values observed by surface rainfall stations in the region (Santos et al. 2019). The monthly average data for August-October 2018 were obtained in GeoTIFF format using the Google Earth Engine platform and processed at a 1 km spatial scale.

Data on highways and minor roads in the region were obtained by joining the database of the National Department of Transport Infrastructure (DNIT, 2020) and crowdsource mapping data from OpenStreetMap (OSM Foundation, 2020). These data were pieced together, and the Euclidean distance of the vicinities was calculated, being spatialized with a spatial resolution of 1 km.

Land use data for the region were obtained from the database of the Annual Mapping of Land Cover and Land Use in Brazil (MapBiomas) project for 2018. These data were produced from the pixel-by-pixel classification of images from the Landsat satellite sensor series using machine-learning algorithms via the Google Earth Engine platform. They are available in GeoTIFF format for the entire country (MapBiomas, 2020). These data were processed with GIS with a spatial resolution of 1 km.

All data were treated and manipulated using ArcGIS 10.5 software (ESRI, 2016), adopting the Universal Transverse Mercator-UTM coordinate projection system, SIRGAS 2000 Datum, zone 20 south.

Fuzzy System

The variables were categorized according to the intervals defined in previous research. Thus, the temperature was categorized according to Melo et al. (2012), Mohammadi et al. (2014), and Assis et al. (2014). For precipitation, the studies by Oliveira et al. (2017), Silva and Pontes Jr. (2011), and Assis et al. (2014) were used. Land use was categorized following Venturi and Antunes (2007), Ribeiro et al. (2012), and Assis et al. (2013), while distance from minor roads was categorized according to intervals defined by Adab et al. (2013), White et al. (2016), and Gholamnia et al. (2020).

However, there is no consensus on the class interval definition for the assessed variables. As an example of subjectivity in class intervals, for temperature, Melo et al. (2012) defined the low class as <13 °C, moderate as between 13 °C and 24 °C, and high as >24 °C. Meanwhile, Mohammadi et al. (2014) defined them as <16 °C, between 16 °C and 30 °C, and >30 °C, respectively, whereas Assis et al. (2014) defined them as <23.4 °C, between 23.40 °C and 24.15 °C and >24.54 °C. Considering this subjectivity of the classes, fuzzy sets were built for each variable, and Table 1 presents the parameters compiled based on expert knowledge of the model's fuzzy association (μ(x;a,b,c,d)). It should be noted that this system's application in other climatic regions requires rule set adaptation since the model's response is intrinsically related to the variation of local environmental conditions.

According to the association functions presented in Table 1, each attribute has specific contributions that can imply increased or reduced susceptibility to fire. Temperature, for example, is important because, apart from influencing soil moisture, it is directly linked to the combustion of vegetation, so the higher the temperature, the greater the susceptibility to fire (Pourghasemi et al. 2020). On the other hand, high precipitation rates increase soil moisture content, decrease water stress, and hence reduce susceptibility to fire (Vadrevu et al. 2006; Venkatesh et al. 2020).

Highways and minor roads also contribute to fires since they help to clear up new areas for agriculture, cattle-ranching, and logging, thus facilitating fire outbreaks. The greater the proximity of highways and minor roads, the greater the susceptibility to fire (Ribeiro et al. 2012). The landscape's structure and the way land use patterns are organized strongly influence the fire occurrence because these dynamics are associated with the spatial distribution of the fuel load constituted by the type of vegetation and available biomass (Aquilué et al. 2020).

Model Sensitivity Analysis

Model validation is a crucial step as it tests the effectiveness and accuracy of the methodology used. In this case, we evaluated the ability of the model to map the areas with fire susceptibility. For this purpose, the data on fire outbreaks were obtained from the Fire Database of the National Institute for Space Research (INPE, 2010), and classified according to the number of observations per km^2. Fire occurrence was classified as very low (0 to 0.3), low (0.3 to 0.7), moderate (0.7 to 1), high (1 to 1.3), and very high (>1.3), as proposed by Nascimento et al. (2017).

Then, partitioning was performed through joint training (80%) and testing (20%) for the implementation of the fuzzy system, and the analysis of the ROC (receiver operating characteristic) and AUC (area under the curve) was performed to determine the accuracy of the proposed model. The ROC curve plots the true positive rate on the Y-axis and the false positive rate on the X-axis, with area under the curve (AUC) values ranging from 0.5 to 1.0, whereby the forecast accuracy can be classified as excellent (0.9-1.0), very good (0.8-0.9), good (0.7-0.8), average (0.6-0.7), or poor (0.5-0.6), as described by Chen et al. (2018).

To evaluate the efficiency of the fuzzy system, the model was tested considering the mapped fire susceptibility classes and the inventory of fire outbreaks in the region. This evaluation was carried out for the base year (2018) and two extreme climatic events, with a rainy summer period of 2001 and a dry summer period of 2007, according to the classification of extreme events described by Tejas et al. (2012) and França (2015).

Since fire susceptibility is highly dependent on the association of the input variables, evaluating the impact of the input association functions on the final result was of the utmost importance and was performed by Monte Carlo simulations

Table 1. Fuzzy membership function parameters compiled from specialized literature

Susceptibility Classes		Temperature (°C)	Precipitation (mm)	Distance from highways (m)	Land use Classes
Low	a	0	80	6,000	0
	b	0	80	6,000	0
	c	13	22	3,000	8
	d	24	10	2,000	12
Moderate	a	13	22	3,000	8
	b	24	10	2,000	12
	c	24	20	2,000	12
	d	30	2	1,000	20
High	a	24	10	2,000	12
	b	30	2	1,000	20
	c	50	0	0	30
	d	50	0	0	30

*Land-use classes defined by recategorization based on the number of «CAPTION CODES - COLLECTION 5» from the MapBiomas project.

(1,000 simulations). For comparison purposes, the input parameters were individually perturbed in an interval from -10% to +10%, considering their original value. The ±10% variation was adopted since it was compatible with the projections presented by the Intergovernmental Panel on Climate Change (IPCC), which indicated an increase in temperature of 1.5 °C and the intensification of extreme precipitation events (positive and negative anomalies) by 2050, and which could increase forest fires in the region (Hoegh-Guldberg et al. 2018). The individual sensitivity of the parameters was analyzed by considering the average percentual change in the fuzzy system's output.

The interaction of the four inputs of the proposed fuzzy system enabled the generation of 81 association rules. Figure 2 presents the schematic diagram of the fuzzy model implemented from the *R* software (R Core Team, 2020).

RESULTS

Model Input Data

Figure 3 presents the maps of the spatial distribution of the average observed temperature (a) and precipitation (b) between August and October 2018, as well as the distance from highways (c) and land use (d) for the respective period evaluated.

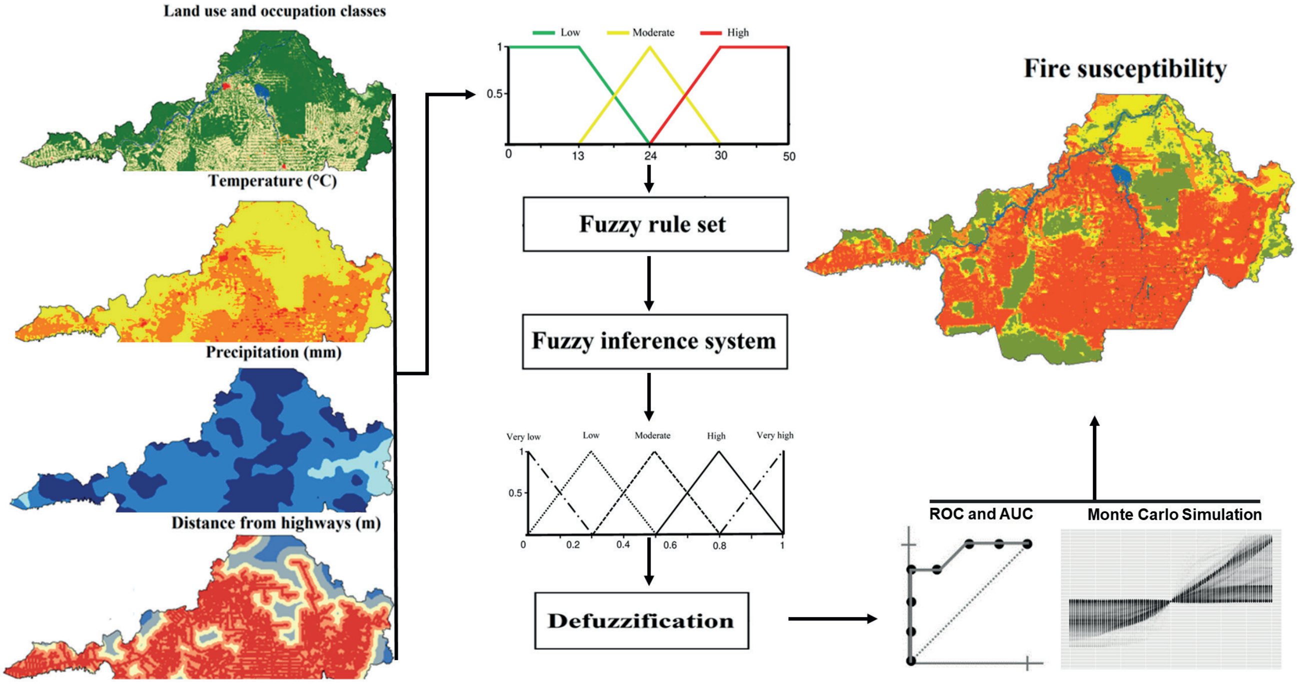

Fig. 2. Schematic diagram of the developed fuzzy inference system

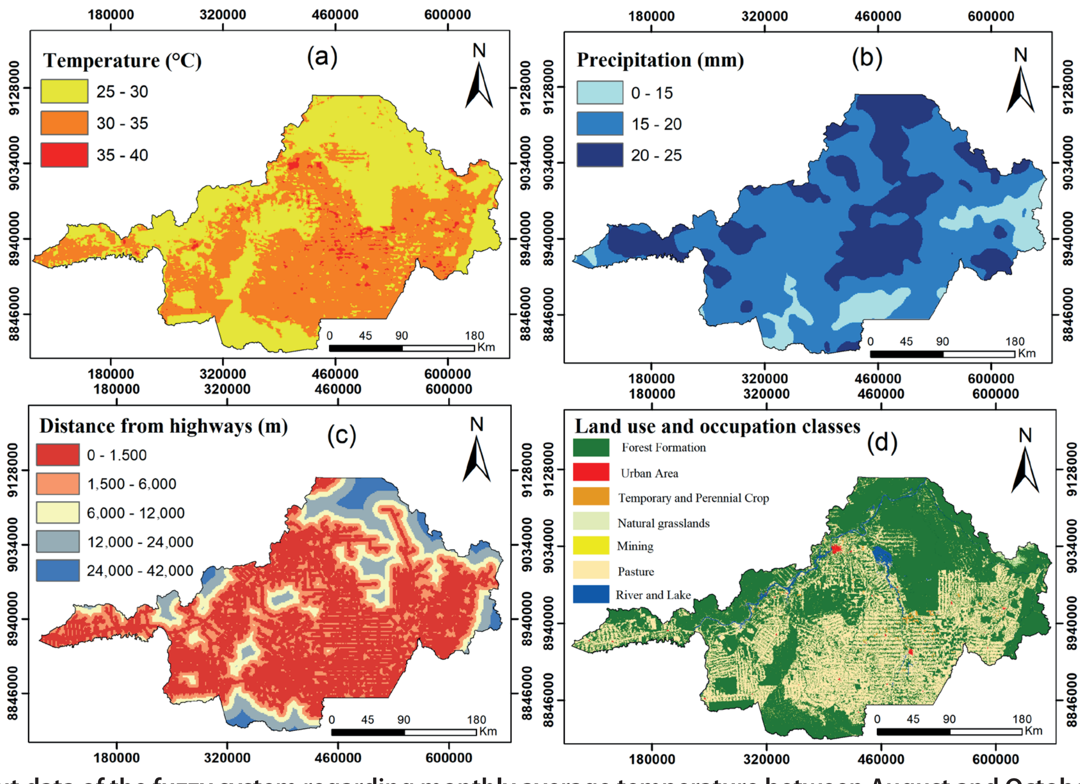

Fig. 3. Input data of the fuzzy system regarding monthly average temperature between August and October 2018 (a) retrieved via the MODIS satellite, monthly average precipitation between August and October 2018 (b) retrieved via the GPM satellite, distance from highways (c) obtained based on DNIT and OpenStreetMap data, and land use and occupation (d) obtained from MapBiomas

The surface temperature map obtained via the MODIS sensor (Figure 3 a) between August and October 2018 shows that the average values ranged from 25 °C to 40 °C, with the highest temperatures occurring in anthropized areas, mainly in urban and agricultural areas. Meanwhile, the lowest temperatures occurred in areas occupied by forests and natural grasslands. Regarding the average precipitation accumulated from August to October registered by the GPM sensor (Figure 3 b), it is evident that most of the study area had precipitation of 15-20 mm, with small areas in the central and extreme northern parts receiving 20-25 mm, and precipitation of 0-15 mm found in the outer eastern and southern parts.

Regarding the distance from highways and minor roads (Figure 3 c), the study area primarily presented high density of road network (dark red), especially in the south, where the majority of rural settlements are concentrated. This high density can also be observed on the land-use map (Figure 3 d), which illustrates the characteristic "herringbone" areas that correspond to deforestation advance around the minor roads.

The land-use map for 2018 shows the predominance of areas occupied by native forests (58.30%), followed by pasture areas (38.72%), rivers and lakes (1.88%), annual and perennial agriculture (0.46%), natural fields (0.41%) urban areas (0.21%), and mining areas (0.01%) during the studied period. Out of all areas occupied by forests, around 40% corresponded to areas protected by conservation units, and the other 10% protected by indigenous lands. In other words, 50% of the areas occupied by forests in the region were within protected areas, and the rest consisted of small forest fragments out of legal reserves and environmental protection areas. The predominance of anthropogenic pastures shows that the region was a part of the agricultural frontier, concentrating 34.02% of the cattle in Rondônia (IDARON, 2018).

Mapping of Fire Susceptibility

Figure 4 shows the fire susceptibility classification map generated by the fuzzy system for the north of Rondônia. 47% of the area were classified as having very high susceptibility, 16% as having high susceptibility, 18% as having moderate or low susceptibility, and just 0.17% as having very low susceptibility.

The reliability of the fuzzy system was evaluated using the overlap between the mapped fire susceptibility classes with the density of fire outbreaks that were observed by satellites between August and October 2018, as shown in Table 2.

It can be noted there is significant agreement between the fire susceptibility classes mapped by the fuzzy system and the density of fire outbreaks per km² observed between August and October 2018 in the region (Table 2). Notably, the very low and low susceptibility classes show a hotspot density of 0.01 and 0.09 per km². Meanwhile, the hotspots increase substantially in moderate, high, and very high susceptibility areas. The response of the model built by the fuzzy system was also evaluated by considering two extreme weather events (Figure 5). In the period corresponding to the rainy summer (Figure 5 a), the study area was predominantly classified as having low

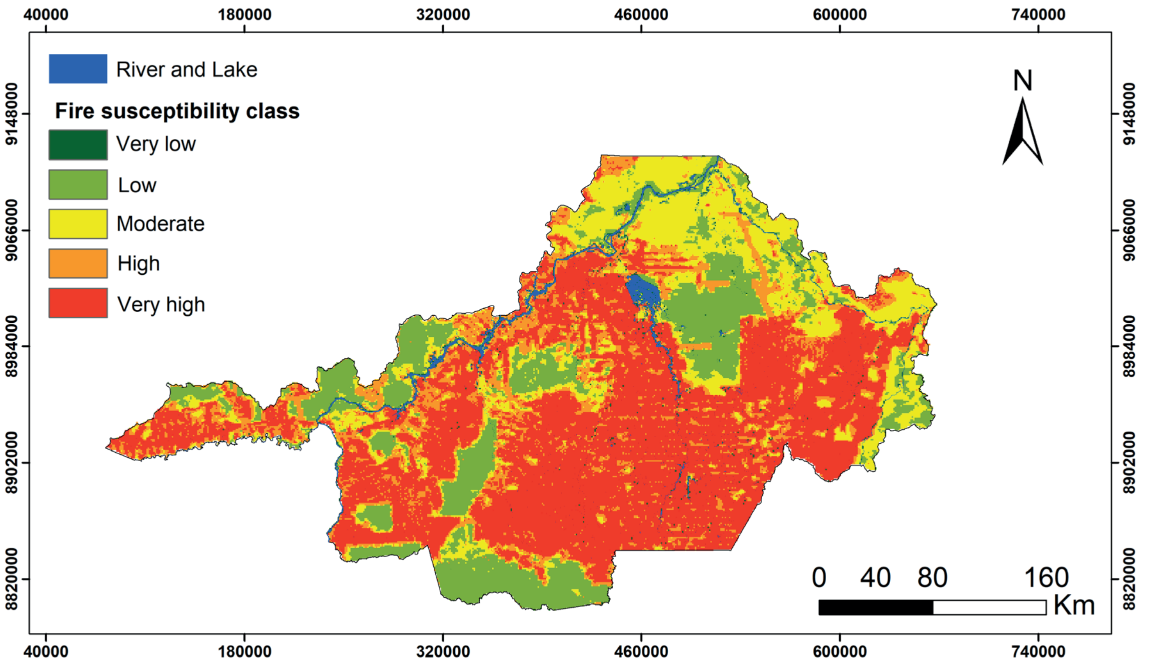

Fig. 4. Fire susceptibility map for the study area

Table 2. Relationship between the classes of fire susceptibility and observed fire outbreaks in 2018

Susceptibility Classes	Area (km²)	Area (%)	Number of outbreaks of fire	Density of fires/km²
Very low	1,731.74	0.17	15.00	0.01
Low	15,861.60	18.28	1,437.00	0.09
Moderate	16,059.00	18.29	9,890.00	0.62
High	14,248.90	16.27	23,514.00	1.65
Very high	41,789.80	47.00	59,910.00	1.43

susceptibility to fire. In contrast, for the dry summer period (Figure 5 c), the fuzzy system model classified the area as having a predominance of very high susceptibility.

Regarding the density of fire outbreaks per km^2, the rainy summer period showed low density (Figure 5 c), while the dry summer period showed high density (Figure 5 d). It is worth noting that the density of fire outbreaks aligns with the mapped susceptibility classes. The occurrence distribution is denser in areas classified with high and very high susceptibility and lower in areas classified with low and very low susceptibility, as shown in Figure 5 c and Figure 5 d.

To assess the accuracy of the results, which was a crucial step in the modelling process (Pourghasemi et al. 2020), the AUC and ROC were used. Figure 6 presents the AUC values for the ROC curve in 2018, as well as for 2001 and 2007. The AUC values for the proposed fuzzy model range from 0.709 to 0.879, thus indicating that the model has a good predictive capacity.

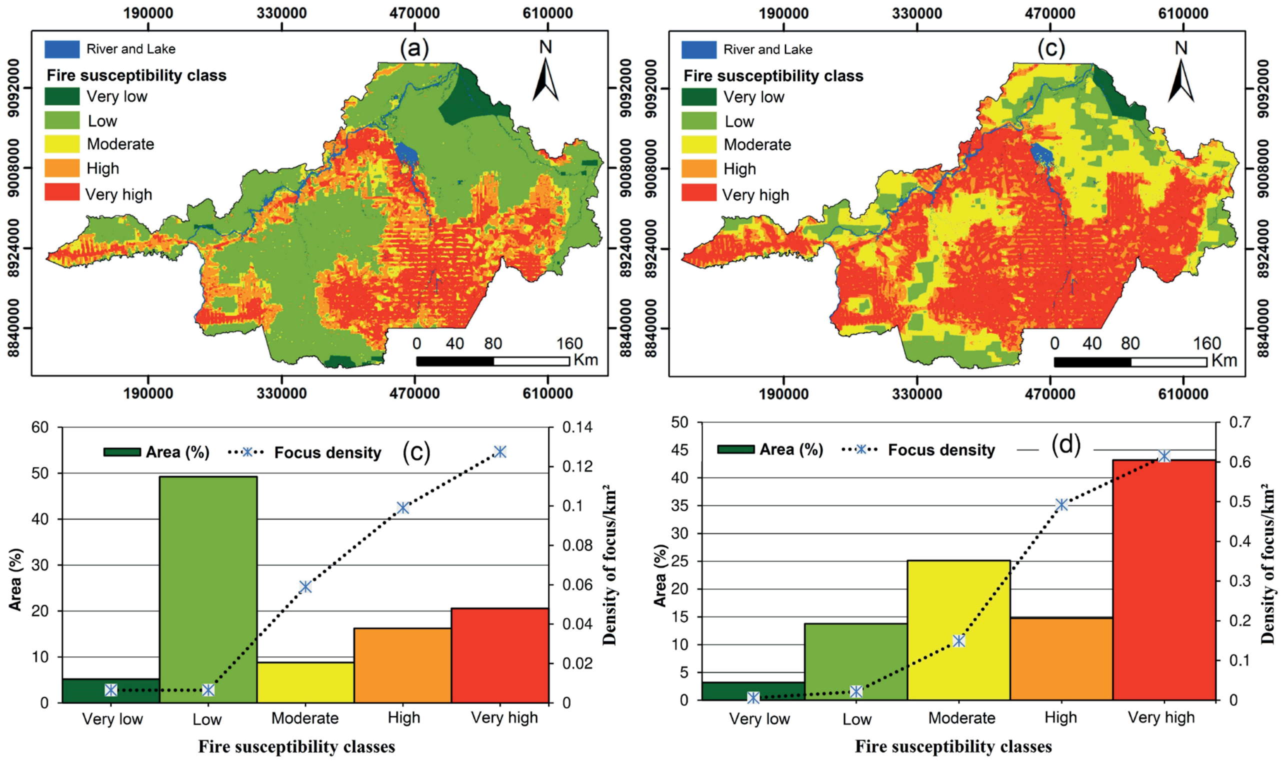

Fig. 5. Mapping of the fire susceptibility for a rainy (a) and dry (b) summer, and respective density of fire outbreaks per km^2 (c and d)

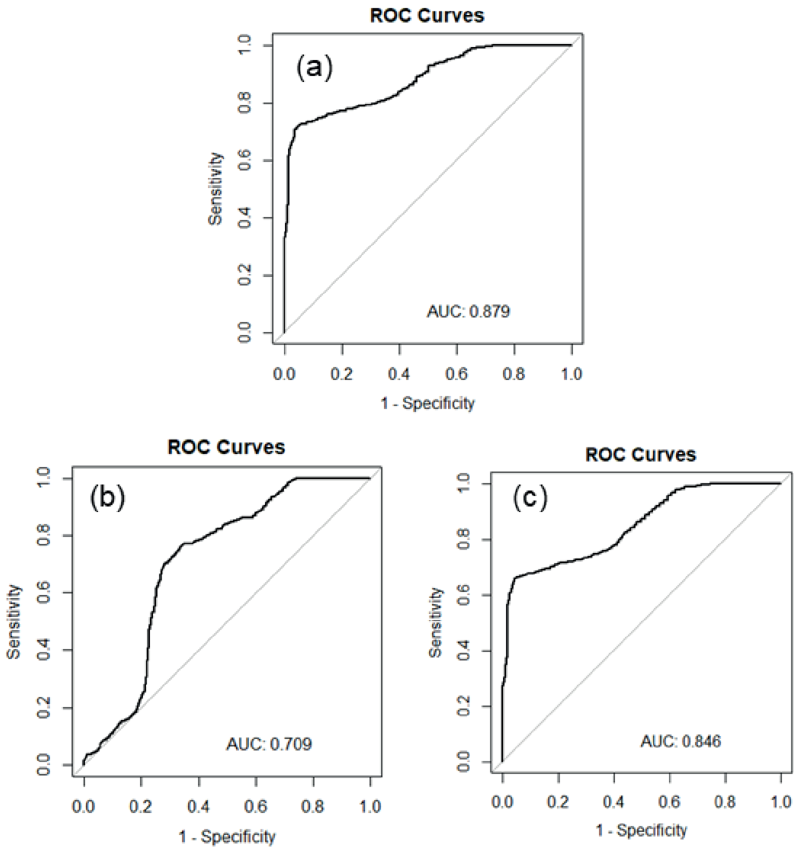

Fig. 6. Prediction rate curve of the forest fire susceptibility map using the fuzzy model for 2018 (a), 2001 (b) and 2007 (c)

Figure 7 represents the sensitivity analysis of the fuzzy system performed using 1,000 Monte Carlo simulations. The graphs show the percentage contribution of each variable to the model output when individually disturbed between -10% and +10%.

In random simulations of up to ±2.5% in temperature (Figure 7 a), fire susceptibility can be altered by an average of ±20%. In other words, a 2.5% increase in regional temperature can result in a 20% increase in fire susceptibility compared to what is normally observed. Meanwhile, precipitation showed considerably lower sensitivity when compared to temperature (Figure 7 b). Disturbances of up to ±2.5% of precipitation alter the average fire susceptibility by up to ±10%. Thus, a 2.5% reduction in precipitation can cause an average 10% increase in fire susceptibility to fire in the study area. Regarding the distance from highways and minor roads (Figure 7 c) and land use (Figure 7 d), the random simulations showed less significant variations in the proposed model.

DISCUSSION

Proper mapping of forest fire susceptibility is an important task within its management. However, this is still a complicated challenge due to the complexity and non-linearity of these fires (Moayedi et al. 2020; Sahiner et al. 2022). This study used the fuzzy inference system composed of four input parameters (temperature, precipitation, distance from roads, and land use and occupation), with a map output showing the spatial distribution of fire susceptibility. The used method made it possible to incorporate expert knowledge into the model and, with the use of linguistic variables and degrees of pertinence, to smoothen the transition from one class to another (Zadeh, 1965; Cheng et al. 2022). This allowed the values of the influencing factors to belong simultaneously to several levels of susceptibility with different degrees of association, thus better reflecting the real characteristics of the events.

The proposed fuzzy system applied in this study indicated the predominance of areas that were classified as having very high fire susceptibility in 2018. These areas were distributed mainly throughout the south of the study area, where most of the agricultural and cattle-ranching lands and the highest road network density could be found. When these factors were combined with low precipitation and high temperatures observed during the evaluated period, they contributed to the predominance of high and very high fire susceptibility, similar to Cardozo et al. (2014). On the other hand, the areas identified as having low and very low fire susceptibility corresponded to protected areas represented by conservation units and indigenous lands distributed throughout the north of the region. However, these areas have recently suffered from the advancement of anthropogenic activities due to the construction of unofficial minor roads and land grabbing, as also demonstrated by Fonseca et al. (2018). Although the study area had around 58.30% native forest coverage, 19.25% of them were classified as having high susceptibility to fire, and other 21% as having very high susceptibility. These areas corresponded to border zones with proximity to highways and unofficial minor roads. When road proximity is combined with the fuel stored in the forest litter, high temperatures, and low precipitation rates, it becomes a dominant component for the start of forest fires.

Furthermore, forest fires have become increasingly frequent because during intense dry seasons the Amazon Forest has become more flammable, and thus more susceptible to fires, as already described by Aragão et al. (2018) and Staver et al. (2020), and shown by the model results for the dry summer period in 2007. There is a high alignment between mapping results based on the proposed methodology and the recorded fire instance data both for 2018 and for 2001 and 2007 with extreme weather conditions. These results show that the developed fuzzy model system can adjust to climatic variations (temperature and precipitation) that occur during extreme weather events. This emphasizes the high adequacy of the applied method, which was confirmed by the AUC values of 0.879 for the year 2018, 0.709 for the rainy summer period, and 0.846 for the dry summer period.

The results achieved in this research are considered satisfactory when compared with the AUC values found in

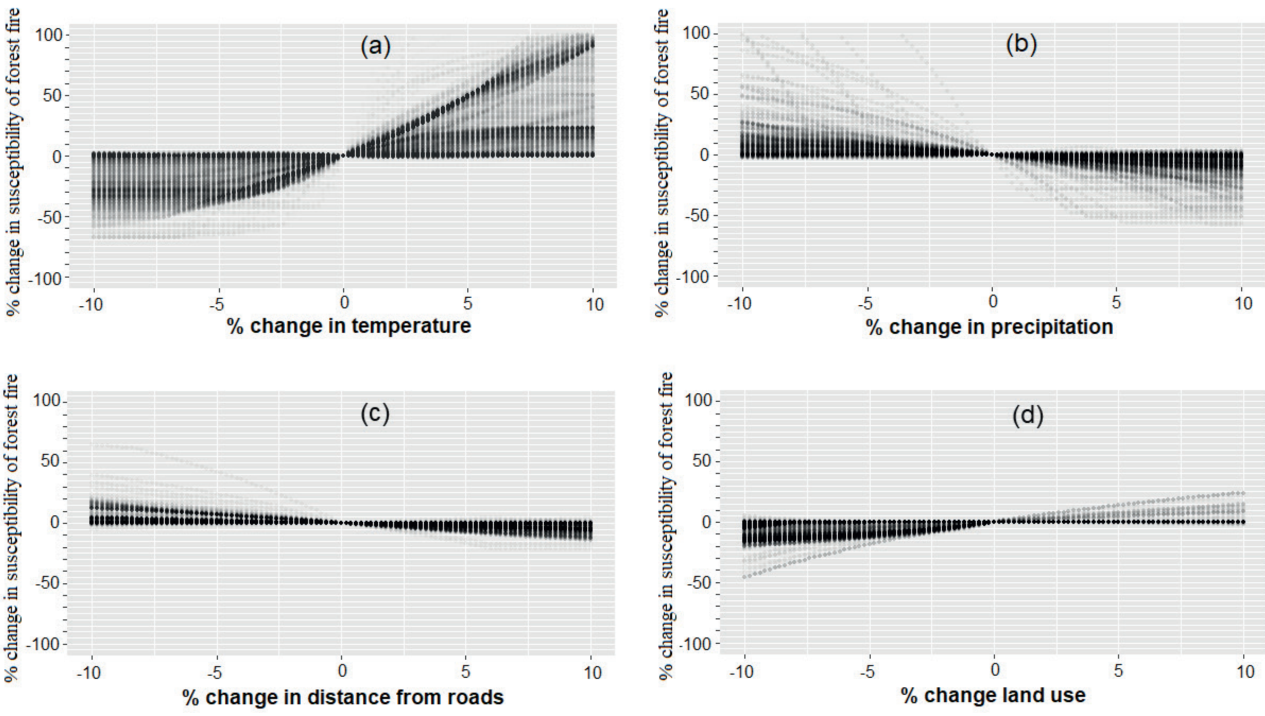

Fig. 7. Sensitivity analysis of the fuzzy system output with a disturbance at -10% and +10% of precipitation (a), temperature (b), distance from highways, and land use and occupation (d)

previous research. For example, Pourghasemi et al. (2020), when employing methods such as mixture discriminant analysis (MDA) and boosted regression tree (BRT), obtained AUC values ranging from 82.5% to 88.90%. By employing joint approaches, Eskandari et al. (2021) observed that the generalized additive model – multivariate adaptive regression spline – support vector machine (GAM-MARS-SVM) method achieved an AUC of 83.00%, which surpassed the individual models used by the authors. These findings are consistent with those of Mohajane et al. (2021), who observed an AUC of 98.90% for the forest random frequency ratio (RF-FR) method. In both cases, the models were considered satisfactory and appropriate for the mapping of fire susceptibility in the respective analysed areas.

Regarding the sensitivity of the input variables of the fuzzy inference system, the proposed model proved to be more sensitive to the factors that can alter the flammability of combustible materials, such as precipitation and temperature during seasonal changes. In variations of up to 2.5% in temperature, the model indicated an average 20% increase in fire susceptibility in the region, which is a worrisome scenario. According to the Intergovernmental Panel on Climate Change (IPCC), for the Amazon, there is a projected 1.5 °C increase in temperature by 2050 (Hoegh-Guldberg et al. 2018), which can result in an increase in fire susceptibility beyond what was calculated by the model.

It is worth mentioning the influence of anthropogenic activity on fire susceptibility. In this study, anthropogenic areas had an average temperature that was 5 °C higher than in natural areas (Figure 3a and 3d), which resulted in greater fire susceptibility, as reported in other studies (Oliveira et al. 2021; Silva et al. 2023).

Moreover, regional atmospheric conditions, such as strong anticyclones over the continent, for example, the South Atlantic Subtropical High, inhibit the formation of rain clouds north of the state of Rondônia. These conditions contribute to low precipitation between August and October in this region, which increases the flammability and burning potential of the combustible material (Tejas et al. 2012; França, 2015; Aragão et al. 2018; Ribeiro et al. 2020).

Thus, adopting an integrated command and control system that encompasses public policies and includes prevention techniques for fighting and controlling fires is essential for the region. As such, the methodology presented for fire susceptibility mapping, which integrates the fuzzy system with data obtained from remote sensing techniques and GIS, can provide the basis for local environmental planning.

It is worth noting that, although the Brazilian Forest Code, Law No. 12,651, of May 25, 2012, provides for the creation of the National Integrated Fire Management Policy (PNMIF), this system has not been completed yet (Brasil, 2020). The reflection of the absence of the system that centralizes firefighting efforts in Brazil makes these events historically excessive, such as those observed in the study area between August and October 2018, with about 94,766 registered fire outbreaks.

The absence of an effective fire control system, combined with the anthropogenic activity in the region, which includes deforestation for shifting agricultural practices and pastures and the practice of using fire to clear degraded pastures, and extreme droughts, are the main reasons for the high fire rates in this region (Cardozo et al. 2014; Aragão et al. 2018; Chuvieco et al. 2019; Barlow et al. 2019; Caúla et al. 2019; Staver et al. 2019; Ribeiro et al. 2020).

Advantages and Limitations

The ability of fuzzy inference systems to handle most inaccuracy sources in remote sensing data, such as uncertainties in sensor measurements, parameter variations due to limited sensor calibration, and class mixing due to limited spatial resolution, and other (Benz et al. 2004), gives the fuzzy system an advantage over other methods that are usually implemented for mapping forest fire susceptibility.

In this study, the uncertainties related to the disagreement between the expert class intervals were considered using fuzzy sets, which were defined by membership functions and allowed the incorporation of a combination of subjective data into a fuzzy domain, thus making it possible to build inference systems based on expert experience and deal with inaccurate data (Zadeh, 1965). In addition, it allowed influencing factors to belong simultaneously to more than one susceptibility class, however, with different degrees of association (Zadeh, 1965; Cheng et al. 2022) to better reflect the real characteristics of fire susceptibility that are observed in the region.

Nonetheless, it is worth mentioning that in a grid-type partition fuzzy inference system the number of rules is given by the combination of linguistic values, in other words, the number of rules can increase exponentially as a function of the number of input variables (Bressane et al. 2020; Fernandes et al. 2023). In this study, only four inputs were selected to compose the model; however, for cases in which a greater number of explanatory factors are introduced, this would negatively affect the transparency and interpretability of the fuzzy inference system, and, consequently, its replication (Ojha et al. 2019). One of the solutions would be the optimization of input factors using metaheuristics (Moayed et al. 2022).

CONCLUSIONS

The methodology presented for mapping fire susceptibility by integrating a fuzzy inference system with data obtained via remote sensing techniques and GIS tools proved to be highly effective, especially when implemented for precipitation, temperature, distance from highways, and land use as input variables. The findings indicate that the study area had a predominantly high fire susceptibility, especially when considering the climatic characteristics observed between August and October (during the dry season) and the land use patterns of the region.

The areas classified with very high susceptibility by the fuzzy system were located predominantly in the south of the study area, where agricultural and livestock activity prevails. On the other hand, the areas that had low and very low susceptibility were concentrated primarily in conservation units and indigenous lands, which shows the importance of these protected areas.

The comparison between the mapped fire susceptibility classes and the density of registered fire outbreaks showed a strong spatial coincidence, which reinforces the credibility of the fire susceptibility mapping based on the proposed methodology, and these results were confirmed by the AUC values (mean of 0.81), thus indicating an impressive predictive capacity of the model.

Thus, the results obtained in this study can be used to inform the community, fire departments, and local authorities about areas that are most susceptible to fires. The findings can also be used to highlight areas that are conducive to controlled burning, with the aim of reducing the accumulation of combustible material, contributing to the prevention of uncontrollable fires.

Finally, the obtained results can significantly contribute to land management and planning policies, including the possibility of integrating similar data in other regions. They can also assist the decision-making process when fighting fires. However, for implementation in other regions, it is necessary to incorporate sufficient information regarding local factors that can influence forest fires.

REFERENCES

Acaroglu, O.; Ozdemir, L.; Asbury, B. (2008). A fuzzy logic model to predict specific energy requirement for TBM performance prediction. Tunnelling and Underground Space Technology. v. 23, n. 5, p. 600-608. DOI: 10.1016/j.tust.2007.11.003

Adab, H.; Kanniah, K. D.; Solaimani, K. (2013). Modeling forest fire risk in the northeast of Iran using remote sensing and GIS techniques. Natural Hazards, v. 65, p. 1723–1743.DOI: 10.1007/s11069-012-0450-8

Alves, M. T.; Piontekowski, V. J.; Buscardo, E.; Pedlowski, M.; Sano,E. E.; Matricardi, E. A. T. (2021). Effects of settlement designs on deforestation and fragmentation in the Brazilian Amazon. Land Use Policy, v. 109. DOI: 10.1016/j.landusepol.2021.105710

Aquilué, N.; Fortin, M-J.; Messier, C.; Brotons, L. (2020). The Potential of Agricultural Conversion to Shape Forest Fire Regimes in Mediterranean Landscapes. Ecosystems. v. 23. p. 34-51. DOI: 10.1007/s10021-019-00385-7

Aragão, L.; Anderson, L.O.; Fonseca, M.G.; Rosan, T.M.; Vedovato,L.B.; Wagner, F.H.; Silva, C. V. J.; Silva Junior, C. H. L.; Arai, E.; Aguiar, A. P.; Barlow, J.; Berenguer, E.; Deeter, M. N.; Domingues, L. G.; Gatti, L.; Gloor, M.; Malhi, Y. Marengo, J. A.; Miller, J. B.; Phillips, O. L.; Saatchi, S. (2018). 21st Century drought-related fires counteract the decline of Amazon deforestation carbon emissions. Nature Communications, p. 1–12. DOI: 10.1038/s41467-017-02771-y

Araya-Muñoz, D.; Metzger, M.; Stuart, N.; Wilson, A. M. W.; Carvajal, D. (2017). A spatial fuzzy logic approach to urban multi-hazard impact assessment in Concepción, Chile, v. 576, p. 508-519. DOI: 10.1016/j.scitotenv.2016.10.077

Assis, F. R. V.; Mendonça, I. F. C.; Silva, J. E. R.; Lima, J. R. (2014). Uso de geotecnologias na locação espacial de torres para detecção de incêndios florestais no Semiárido Nordestino. Floresta. v. 44, n. 1, p. 133-142. DOI: 10.5380/rf.v44i1.32618

Barlow, J.; Berenguer, E.; Carmenta, R.; França, F. (2019). Clarifying Amazonia's burning crisis. Global Change Biology. v. 26, n. 2, p. 319-321. DOI: 10.1111/gcb.14872

Benz, U. C.; Hofmann, P.; Wilhauck, G.; Lingenfelder, I.; Heynen, M. (2004). Multi-resolution, object-oriented fuzzy analysis of remote sensing data for GIS-ready information. ISPRS Journal of Photogrammetry and Remote Sensing, v. 58, n. 3–4, 2004, p. 239-258. DOI: 10.1016/j.isprsjprs.2003.10.002

Bonazountas, M.; Kallidromitou, D.; Kassomenos, P. A.; Passas, N. (2005). Forest Fire Risk Analysis. Human and Ecological Risk Assessment: An International Journal. v. 11, n. 3. p. 617-626. DOI: 10.1080/10807030590949717

Brasil (2020). Projeto de Lei (PL): Institui a Política Nacional de Manejo Integrado do Fogo. Available at: http://www.planalto.gov.br/CCIVIL_03/Projetos/PL/2018/msg774-dezembro2018.htm [Accessed 25 Oct. 2022].

Bressane, A.; Silva, P. M.; Fiore, F. A.; Carra, T. A.; Ewbank, H.; Decarli, B. P.; Mota, M. T. (2020). Fuzzy-based computational intelligence to support screening decision in environmental impact assessment: A complementary tool for a case-by-case project appraisal. Environmental Impact Assessment Review, v. 85. DOI: 10.1016/j.eiar.2020.106446

Bui, D. T.; Bui, Q. T.; Nguyen, Q. P.; Pradhan, B.; H. Nampak, H.; Trinh, P. T. (2017). A hybrid artificial intelligence approach using GIS-based neural-fuzzy inference system and particle swarm optimization for forest fire susceptibility modeling at a tropical area. Agricultural and Forest Meteorology, v. 233, p. 32-44. DOI: 10.1016/j.agrformet.2016.11.002

Cardozo, F. S.; Pereira, G.; Shimabukuro, Y. E.; Moraes, E. C. (2014). Análise das mudanças dos parâmetros físicos da superfície derivados das queimadas no estado de Rondônia. Boletim de Ciências Geodésicas. v. 20, n. 4. p. 830-854. DOI: 10.1590/S1982-21702014000400047

Carmo, M.; Moreira, F.; Casimiro, P.; Vaz, P. (2011). Land use and topography influences on wildfire occurrence in northern Portugal. Landscape and Urban Planning. v. 100. n. 1-2. p. 169-176. DOI: 10.1016/j.landurbplan.2010.11.017

Caúla, R. H.; Oliveira-Júnior, J. F. Lyra, G. B.; Delgado, R. C.; Filho, P. F. L. (2015). Overview off fire foci causes and localitions in Brazil based on meteorological satellite data from 1998 to 2011.Enviromental Earth Science. v. 74. p. 1497-1508. DOI: 10.1007/s12665-015-4142-z

Chen, W., Zhang, S., Li, R., & Shahabi, H. (2018). Performance evaluation of the GIS-based data mining techniques of best-first decision tree, random forest, and naïve Bayes tree for landslide susceptibility modeling. Science of the Total Environment, 644, 1006– 1018. DOI: 10.1016/j.scitotenv.2018.06.389

Cheng, H.; Zhu, L.; Meng, J. (2022). Fuzzy evaluation of the ecological security of land resources in mainland China based on the Pressure-State-Response framework. Science of The Total Environment, v. 804. DOI: 10.1016/j.scitotenv.2021.150053

Chuvieco, E.; Mouillot, F.; Werf, G. R. V.; Miguel, J. S.; Tanase, M.; Koutsias, N.; García, M.; Yebra, M.; Padilla, M.; Gitas, L.; Heil, A.; Hawbaker, T. J.; Giglio, L. (2019). Historical background and current developments for mapping burned area from satellite Earth observation. Remote Sensing of Environment, v. 225, p. 45-64. DOI: 10.1016/j.rse.2019.02.013

Cocconello, M. S.; Bassanezi, R. C.; Brandão, A. J. V.; Leite, J. (2014). On the stability of fuzzy dynamical systems. Fuzzy Sets and Systems. v. 248, n. 1. p .106-121. DOI: 10.1016/j.fss.2013.12.009

Duarte, M. L. Sousa, J. A. P.; Castro, A. L.; Lourenço, R. W. (2021). Dynamics of land use in a rural settlement in the Brazilian Legal Amazon. Brazilian Journal of Environmental Sciences, v. 56, n. 3, p. 375–384. DOI: 10.5327/Z217694781005

DNIT - Departamento Nacional de Infraestrutura de Transportes. (2020). Rodovias do Brasil (Shapefiles). Available at: http://www.dnit.gov.br/mapas-multimodais/shapefiles [Accessed 23 Oct. 2022].

Eugenio, F. C.; Santos, A. R.; Fieldler, N. C.; Ribeiro, G. A.; Silva, A. G.; Juvanhol, R. J.; Schettino, V. R.; Marcatti, G. E.; Domingues, G. F.; Santos, G. M. A. A.; Pezzopane, J. M.; Pedra, B. D.; Banhos, A.; Martins, L. D. (2016). GIS applied to location of fires detection towers in domain area of tropical forest. Science of The Total Environment. v. 562, n. 15. p. 542-549. DOI: 10.1016/j.scitotenv.2016.03.231

ESRI (2016). Software ArcGis 10.5

Eskandari, S.; Pourghasemi, H. R.; Tiefenbacher, J. P. (2021). Fire-susceptibility mapping in the natural areas of Iran using new and ensemble data-mining models. Environmental Science and Pollution Research, v. 28, p. 47395–47406. DOI: 10.1007/s11356-021-13881-y

Fonseca, A.; Salomão, R.; Ribeiro, J.; Souza Jr. C. (2018). Ameaça e pressão de desmatamento em Áreas Protegidas: SAD agosto de 2017 a julho de 2018. Instituto do Homem e Meio Ambiente da Amazônia – IMAZON. 2p. Available at: https://imazon.org.br/ [Accessed 27 Oct. 2022].

França, R. R. (2015). Climatologia das chuvas em Rondônia – período 1981-2011. Revista Geografias. v. 11, n. 1. p. 44-58.

Fernandes, P. H. De Godoy.; Silva, T. A.; Duarte, M. L.; Sousa, J.; Dupas, F. A. (2023). Fuzzy inference system for environmental vulnerability assessment of protected areas: a case study of the Itupararanga environmental protection area in southeastern Brazil. International Journal of River Basin Management, p. 1–16. DOI: 10.1080/15715124.2023.2260361

Gizatullin, A. T.; Alekseenko, N. A. Prediction of Wildfires Based on the Spatio-Temporal Variability of Fire Danger Factors. Geography, Environment, Sustainability, 2(15), p 31-37. DOI: 10.24057/2071-9388-2021-139

Gholamnia, K.; Nachappa, T. G.; Gorbanzadeh, O.; Blaschke, T. (2020). Comparisons of Diverse Machine Learning Approaches for Wildfire Susceptibility Mapping. Symmetry. v. 12, n. 4. DOI: 10.3390/sym12040604

Gomis-Cebolla, J.; Jimenez, J. C.; Sobrino, J. A. (2018). LST retrieval algorithm adapted to the Amazon evergreen forests using MODIS data. Remote Sensing of Environment, v. 204, p. 401-411. DOI: 10.1016/j.rse.2017.10.015

Gralewicz, N. J.; Nelson, T. A.; Wulder, M. A. (2012). Factors influencing national scale wildfire susceptibility in Canada. Forest Ecology and Management. v. 265, n. 1. p. 20-29. DOI: 10.1016/j.foreco.2011.10.031

Hoegh-Guldberg, O.; Jacob, D.; Taylor, M.; Bindi, M.; Brown, S.; Camilloni, I.; Diedhiou, A.; Djalante, R.; Ebi, K. L.; Engelbrecht, F.; Guiot, J.; Hijioka, Y.; Mehrotra, S.; Payne, A.; Seneviratne, S. I.; Thomas, A.; Warren, R.; Zhou, G. (2018). Impacts of 1.5ºC Global Warming on Natural and Human Systems. In: Global Warming of 1.5°C. Available at: https://www.ipcc.ch/sr15/ [Accessed 23 Oct. 2022].

IDARON. (2022). Agência de Defesa Sanitária Agrosilvopastoril do Estado de Rondônia. Gerencia Animal. Campanha de Vacinação 2018. Available at: http://www.idaron.ro.gov.br/index.php/gerencia-animal/ [Accessed 23 Oct. 2022].

INPE-Instituto Nacional de Pesquisas Espaciais. (2022). Monitoramento dos Focos Ativos por Países. Available at: http://queimadas.dgi.inpe.br/queimadas/portal-static/estatisticas_paises/ [Accessed 04 Oct. 2022].

Jaiswal, R. K.; Mukherjee, S.; Raju, K. D.; Saxena, R. (2002). Forest fire risk zone mapping from satellite imagery and GIS. International Journal of Applied Earth Observation and Geoinformation. v. 4, n. 1, p. 1-10. DOI: 10.1016/S0303-2434(02)00006-5

JAXA - Japan Aerospace Exploration Agency. (2022). Global Satellite Mapping of Precipitation. Available at: https://global.jaxa.jp/policy.html [Accessed 04 Oct. 2022].

Lopes, E. R. N.; Souza, J. C.; Sousa, J. A. P.; Filho, J. L. A.; Lourenço, R. W. (2021). Anthropic Exposure Indicator for River Basins Based on Landscape Characterization and Fuzzy Inference. Water Resources, 48, 29-40. DOI: 10.1134/S0097807821010140

Machado, J. A.; Lopes, A. M. (2014). Analysis of Forest Fires by means of Pseudo Phase Plane and Multidimensional Scaling Methods. Mathematical Problems in Engineering. v. p. 1-8. DOI: 10.1155/2014/575872

Mamdani, E. H.; Assilian, S. (1975). An experiment in linguistic synthesis whit a fuzzy logic controller. International Journal of Man-Machine Studies. v. 7, n. 1, p. 1-13. DOI: 10.1016/S0020-7373(75)80002-2

MapBiomas - Projeto MapBiomas Alerta - versão 4.1 (2020). Sistema de Validação e Refinamento de Alertas de Desmatamento com Imagens de Alta Resolução. Available at: https://mapbiomas.org/ [Accessed 04 Oct. 2022].

Melo, A. S.; Justino, F. B.; Melo, E. C. S.; Vale Silva, T. L. (2012). Índices de risco de fogo de Haines e Setzer em diferentes condições climáticas. Mercator. v. 11, n. 24. p. 187-207. DOI: 10.4215/RM2012.1124. 0012

Moayedi, H. Mehrabi, M.; Bui, D. T.; Pradhan, B.; Foong, L. K. (2020). Fuzzy-metaheuristic ensembles for spatial assessment of forest fire susceptibility. Journal of Environmental Management, v. 260. DOI: 10.1016/j.jenvman.2019.109867

Mohammadi, F.; Bavaghar, M. P.; Shabanian, N. (2014). Forest Fire Risk Zone Modeling Using Logistic Regression and GIS: An Iranian Case Study. Small-scale Forestry, v. 13, p. 117-125. DOI: 10.1007/s11842-013-9244-4

Mohajane, M.; Costache, R.; Karimi, F.; Bao Pham, Q.; Essahlaoui, A.; Nguyen, H.; Laneve, G.; Oudija, F. (2021). Application of remote sensing and machine learning algorithms for forest fire mapping in a Mediterranean Área. Ecological Indicators v. 129, 107869. DOI: 10.1016/j.ecolind.2021.107869

Mota, P. H. S.; Rocha, S. J. S. S.; Castro, N. L. M.; França, L. C. J.; Schettini, B. L. S.; Villanova, P. H.; Santos, H. T.; Santos, A. R. (2019). Forest fire hazard zoning in Mato Grosso State, Brazil. Land Use Policy. v. 88, p. 1-6. DOI: 10.1016/j.landusepol.2019.104206

NASA (2020). Fire Information for Resource Management System (FIRMS). Available at: https://firms.modaps.eosdis.nasa.gov/download/ [Accessed 09 Oct. 2022].

Nascimento, O. S.; Souza, I. R.; Nascimento, W. P. S.; Nascimento, J. S. (2017). Análise espaço-temporal dos focos de calor no município de Parnaguá Piauí, entre 2008 a 2015. Revista Brasileira de Gestão Ambiental. v.11, n.1, p.193 -199.

Nikolova, N. Zlateva, P.; Todorov, L. (2021). Fuzzy Logic Approach to Complex Assessment of Drought Vulnerability, IFIP Advances in Information and Communication Technology, v. 622. DOI: 10.1007/978-3-030-81469-4_24

Nwazelibe, V. E.; Unigwe, C. O.; Egbueri, J. C. (2023). Testing the performances of different fuzzy overlay methods in GIS-based landslide susceptibility mapping of Udi Province, SE Nigeria, CATENA, v. 220. DOI: 10.1016/j.catena.2022.106654

Ojha, V.; Abrahan, A.; Snásel, V. (2019). Heuristic design of fuzzy inference systems: A review of three decades of research. Engineering Applications of Artificial Intelligence, v. 85, p. 845-864. DOI: 10.1016/j.engappai.2019.08.010

Oliveira, A. L. S.; Nero, M. A.; Júnior, J. R. T.; Candeias, A. L. B.; Nóbrega, R. A. A. (2017). Comparação e validação da modelagem espacial de risco de incêndios considerando diferentes métodos de predição. Bulletin of Geodetic Sciences. v. 23, n. 4, p. 556-577. 2017. DOI: 10.1590/S1982-21702017000400037

Oliveira, A. B. F.; Bottino, M. J.; Nobre, P.; Nobre, C. A. (2021). Deforestation and climate change are projected to increase heat stress risk in the Brazilian Amazon. Communications Earth & Environment, v. 2, p. 1–8. DOI: 10.1038/s43247-021-00275-8

OSM Foundation. (2020). OpenStreetMap Foundation. United Kingdom. Available at: https://www.openstreetmap.org/copyright [Accessed 04 Oct. 2022].

Parente, J.; Pereira, M. G. (2016). Structural fire risk: the case of Portugal. Science of the total Environmental. V. 573, n. 15. P. 883-893. DOI: 10.1016/j.scitotenv.2016.08.164

Pourghasemi, H. R.; Gayen, A.; Lasaponara, R.; Tiefenbacher, J. P. (2020). Application of learning vector quantization and different machine learning techniques to assessing forest fire influence factors and spatial modelling. Environmental Research. v. 184, p. 1-12. DOI: 10.1016/j.envres.2020.109321

R Core Team (2020). R: A language and environment for statistical computing. R Foundation for Statistical Computing, Vienna, Austria. Available at: https://www.r-project.org/ [Accessed 03 Oct. 2022].

Ribeiro, L.; Soares, R. V.; Bepller, M. (2012). Mapeamento do risco de incêndios florestais no município de Novo Mundo, Mato Grosso, Brasil. Cerne, v. 18, n. 1, p. 117-126. DOI: 10.1590/S0104-77602012000100014

Ribeiro, T. M.; Mendonça, B. A. F.; Oliveira-Júnior, J. F.; Fernandes-Filho, E. I. (2020). Fire foci assessment in the Western Amazon (2000–2015). 2020. Environment, Development and Sustainability. DOI: 10.1007/s10668-020-00632-1

Román-Flores, H.; Chalco-Cano, Y.; Figueroa-García, J. C. (2020) A note on defuzzification of type-2 fuzzy intervals. Fuzzy Sets and Systems. DOI: 10.1016/j.fss.2019.06.011

Sahana, M.; Patel, P. P. (2019) A comparison of frequency ratio and fuzzy logic models for flood susceptibility assessment of the lower Kosi River Basin in India. Environmental Earth Sciences, 78. DOI: 10.1007/s12665-019-8285-1

Sahiner, A.; Ermiş, E.; Karakoyun, M. H.; Awan, M. W. (2022) Determining the most effective way of intervention in forest fires with fuzzy logic modeling: the case of Antalya/Türkiye. Natural Hazards. DOI: 10.1007/s11069-022-05763-4

Santos, L. O. F.; Querino, C. A. S.; Querino, J. K. A. S.; Junior, A. L. P.; Moura, A. R. M.; Machado, N. G.; Biudes, M. S. (2019). Validation of rainfall data estimated by GPM satellite on Southern Amazon region. Revista Ambiente & Água, v.14, n.1.DOI: 10.4136/ambi-agua.2249

Schlindwein, J. A.; Marcolan, A. L.; Fioreli-Perira, E. C.; Pequeno, P. L. L.; Militão, J. S. T. L. (2012). Solos de Rondônia: usos e perspectivas. Revista Brasileira de Ciência da Amazônia, v. 1, n. 1. p. 213-231.

SEDAM - Secretaria de Estado do Desenvolvimento Ambiental. (2020). Relatório de Alerta de Focos de calor. Available at: http://coreh.sedam.ro.gov.br/focos-de-queimada/ [Accessed 17 Oct. 2022].

SEMA-Secretaria Municipal de Meio Ambiente. (2012). Revisão do Plano de Manejo do Parque Natural Municipal de Porto Velho. 244pp. Available at: https://sema.portovelho.ro.gov.br//artigo/23660/protecao-integral [Accessed 10 Oct. 2022].

Silva, I. D. B.; Pontes Jr. A. C. F. (2011). Elaboração de um fator de risco de incêndio florestal utilizando lógica fuzzy. Biomatemática. v. 21, p. 113-128.

Silva, M. J. G.; Querino, C. A. S.; Neto, L. A. S.; Machado, N. G.; Militão, J. S.; Biudes, M. S. (2018). Efeito da ocupação do solo sobre o clima de Porto Velho, Rondônia, Brasil. RA'EGA, v. 43, p. 232-251. DOI: 10.5380/raega.v43i0.48753

Silva, R. M. Da.; Lopes, A. G.; Santos, C. A. G. (2023). Deforestation and fires in the Brazilian Amazon from 2001 to 2020: Impacts on rainfall variability and land surface temperature. Journal of Environmental Management, v. 326, p. 116664, 2023. DOI: 10.1016/j.jenvman.2022.116664

Souza, J. C.; Sales, J. C. A.; Lopes, E. R. N.; Roveda, J. A. F.; Roveda, S. R. M. M.; Lourenço, R. W. (2019). Valuation methodology of laminar erosion potential using fuzzy inference systems in a Brazilian savanna. Environmental Monitoring and Assessment, v. 191. DOI: 10.1007/s10661-019-7789-1

Staver, A.; Brando, P. M.; Barlow, J.; Morton, D. C.; Piane, C. E.; alhi, Y.; Murakami, A. A.; Pasquel, J. d. A. (2020). Thinner bark increases sensitivity of wetter Amazonian tropical forests to fire. Ecology Letters. v. 23, n. 1, p. 99-106. DOI: 10.1111/ele.13409

Tejas, G. T.; Souza, R. M. da S.; França, R. R.; Nunes, D. D. (2012) Estudo da variabilidade climática em Porto Velho-Brasil no período de 1982-2011. Revista de Geografia. v. 29, n, 2. p. 63-82.

USGS - United States Geological Survey (2020). MODIS/Terra Land Surface Temperature/Emissivity 8-Day L3 Global 1. Available at: https://doi.org/10.5067/MODIS/MOD11A2.006 [Accessed 15 Oct. 2022].

Vadrevu, K. P.; Eaturu, A.; Badarinath, K. V. S. (2006). Spatial distribution of forest fires and controlling factors in Andhra Pradesh, India using spot satellite datasets. Environmental Monitoring and Assessment, v. 123, n. 1–3, p. 75-96. DOI: 10.1007/s10661-005-9122-4

Venkatesh, K.; Preethi, K.; Ramesh, H. (2020). Evaluating the effects of forest fire on water balance using fire susceptibility maps. Ecological Indicators. v. 110, p. 1-14. DOI: 10.1016/j.ecolind.2019.105856

Venturi, N. L.; Antunes, A. F. B. (2007). Determinação de locais ótimos para implantação de torres de vigilância para detecção de incêndios florestais por meio de Sistema de Informações Geográficas. Floresta. v. 37, n. 2, p. 159-173. 2007. DOI: 10.5380/rf.v37i2.8647

White, L. A. S.; White, B. L. A.; Ribeiro, G. T. (2016). Modelagem espacial do risco de incêndio florestal para o Município de Inhambupe, BA. Brazilian Journal of Forestry Research. v. 36, n. 85, p. 41-49. DOI: 10.4336/2016.pfb.36.85.850

Zadeh, L. A. (1965) Fuzzy sets. Information and Control, v. 8, n. 3, p. 338-353. DOI: 10.1016/S0019-9958(65)90241-X

RESEARCH PAPER

PREDICTING THE IMPACT OF LAND USE CHANGES ON THERMAL ENVIRONMENT IN LAHORE, PAKISTAN: IMPLICATIONS FOR URBAN PLANNING

Muhammad Jabbar[1*], Muhammad Nasar-u-Minallah[2*], Mariney Mohd Yusoff[1]
[1]Department of Geography, University of Malaya, Kuala Lumpur, Malaya
[2]Institute of Geography, University of the Punjab, Lahore, 54000, Pakistan
***Corresponding author:** jabbar.lhr@gmail.com; Nasarbhalli@gmail.com
Received: April 15th, 2023 / Accepted: November February 6th, 2024 / Published: March 31st, 2024
https://DOI-10.24057/2071-9388-2023-2862

ABSTRACT. Land use changes significantly threaten urban areas, especially in developing countries such as Pakistan, impacting the thermal environment and comfort of human life. The ongoing transformations in cities such as Lahore, the second largest and rapidly expanding urban center in Pakistan, are alarming due to the removal of green cover and the disruption of ecological structures. In response to these concerns, this study was conducted to assess and predict the implications of observed land use changes in Lahore. The analysis employed three Landsat images from 1990, 2005, and 2020, using ArcGIS and Idrisi Selva software. The results show that the built-up area increased almost 100% (16.44% to 32.48%) during the last three decades. Consequently, a substantial shift from low to medium and medium to high degrees of LST was observed. The projections indicate a further 50% expansion of the built-up area, encroaching upon green cover until 2050, shifting more areas under a higher LST spectrum. So, the study concludes that Lahore is facing imminent threats from rapid land use changes caused by higher land surface temperature in the study area, necessitating prompt attention and decisive action. The study area is at risk of losing its conducive environment and the desirable uniformity of the thermal environment. Therefore, it is recommended that green cover be strategically enhanced to offset the rise in built-up areas and ensure a sustainable thermal environment.

KEYWORDS: Land Surface Temperature; Land Use Changes; Urban Green Cover; Thermal Environment; Urbanization

CITATION: M. Jabbar, M. Nasar-u-Minallah, M. M. Yusoff (2024). Predicting the Impact of Land Use Changes on Thermal Environment in Lahore, Pakistan: Implications for Urban Planning. Geography, Environment, Sustainability, 1(17), 95-109
https://DOI-10.24057/2071-9388-2023-2862

ACKNOWLEDGEMENTS: The author expresses sincere gratitude for the support and collaboration of co-authors, as well as for the valuable contributions of the editor and reviewers in transforming this manuscript into a scientific research endeavor.

Conflict of interests: The authors reported no potential conflict of interest.

INTRODUCTION

Urbanization is one of the most critical human-caused changes to land use and land cover (LULC) on the earth (Gallo and Owen 1999; Guo 2015; Zhao et al. 2020). Land use and land cover changes are essential when studying global dynamics and how they respond to thermal environments and socio-economic factors (Zhao et al. 2020). A growing global environmental concern is the changes in land use and land cover and how they affect Land surface temperature. Although "land cover" and "land use" may be used interchangeably, they have different meanings. The term "land use" describes how land is used for various objectives, including housing, agriculture, education, and recreation. In contrast, land cover describes the kinds of covering on the earth, such as water, bare rock, or forests (Anderson 1976; Zhang et al. 2019; Siddique et al. 2020). LULC are highly significant for managing the urban environment, heterogeneity of landscapes, human life functions, and socio-economic activities (Schott 2007). Urban greenness has appeared significant for understanding, managing, and enhancing its multiple services under the highly fragmented urban landscapes affected by rapid urbanization (Benedict & McMahon 2012; Hanif et al. 2022). Therefore, balanced urban landscapes are highly significant for a sustainable urban environment where green spaces are vital for ecological services (Nasar-u-Minallah et al. 2023). It has been analyzed that green cover in an urban area is increasingly uneven due to the rapid increase in unplanned urbanization. The availability of green spaces currently does not meet the requirements of suitable landscapes for human beings (Ernstson 2013; Wolch et al. 2014). Therefore, the importance of green spaces with their spatial distribution and functioning has increased, and it has been accepted that every element of the green landscape has its specific importance. For instance, trees have more cooling effects than a grassy landscape, but the grassy landscape may be more effective for its aesthetic values (Jabbar et al. 2021; Jabbar & Yusoff 2022). Assessing inequality in urban landscape settings can improve land usage and environmental status.

LULC change analysis provides valuable and essential information for several applications in the geospatial field. Environmental management and monitoring urban and regional planning are prime examples (Bhalli and Ghaffar 2015; Liu et al. 2017; Zhang et al. 2019; Zia et al. 2022). The information produced by land use changes can also be used for socio-economic challenges, climate change effects, food security, and disaster risk management (Stürck et al. 2015). Land use mapping on satellite-based data provides up-to-date information on Earth surface changes. Accordingly, multi-temporal analysis of land use changes can be monitored in land surface dynamics (Hansen et al. 2013; Nasar-u-Minallah et al. 2021) and urban growth (Taubenböck et al. 2012; Minallah et al. 2016). LULC change predictions are a process through which we can estimate the future scenario of any area for future planning to avoid its adverse consequences. As such, several studies use a variety of approaches for LULC change predictions. The approaches vary based on their purposes, location, methodologies, source of data, and type (Michetti & Zampieri 2014). The Markov chain system uses chain analysis techniques to predict land use changes (Eastman 2006). The land use planning of urban areas should be approached according to the socio-economic and physio-ecological attributes that may be present. Vegetation on a landscape increases its socio-economic value, and land-use changes collectively affect the environment and economy (Riaz et al. 2017; Fu et al. 2018). Sustainable development in a compact city is also related to the price of land, and many researchers have used three dimensions of sustainability (social, economic, and environmental) during land-use studies (Gonzalez-Redin et al. 2019; Parveen et al. 2019).

The presence of urban green spaces (UGSs) and their spatial distribution is essential for assessing and measuring their expected impacts on human beings and the city environment (Kuo et al. 2011). A standard number of UGSs required to sustain an ecologically healthy environment for human beings can be judged under World Health Organization (WHO) guidance. The standard set by WHO is 9 m^2 per person, which is the minimum benchmark per person (UN-Habitat 2013). Availability typically refers to the quantity of UGSs in an urban area, whereas accessibility indicates the location and distance humans must travel for green space. The term accessibility in this context refers to the spatial nearness of UGSs for humans (Koohsari et al. 2015). The existence and ease of access to green spaces have been outlined and evaluated under spatial equity matters (Zhou et al. 2017). It has been demonstrated that UGSs, such as parks enhance active lifestyles, mental health, and social cohesion.

The availability of open or green spaces for humans also contributes to more dynamic behavior, social responsibility, and care for public resources. It improves inhabitants' co-existence, tolerance, health, and quality of life (Ward 2013; Jabbar & Mohd Yusoff 2022). The accessibility and vegetation structure, location, shape, and scale are vital in recreational activities and ecological resources. If an urban green space has more potential for recreational facilities, it will be considered a more attractive place for children and parents (Lachowycz & Jones 2013). Thus, urban green spaces play a pivotal role in fostering sustainable cities by offering diverse benefits to both human and animal populations. Scientists emphasize their significance in regulating the environment and enhancing socio-economic values. However, a critical need arises to quantify the requisite green area for a specific population. Concurrently, the escalating conversion of green cover into built-up environments in rapidly urbanizing cities exacerbates challenges, such as heightened temperatures and urban heat islands (Gull et al. 2019). Lahore, the second most populated city in Pakistan, is currently undergoing rapid land use changes, and the absence of robust environmental regulations intensifies the conversion of green spaces in the city context (Jabbar et al. 2023; Nasar-u-Minallah 2018). This ongoing transformation poses environmental and socio-economic concerns, warranting a comprehensive scientific assessment.

This study aims to ultimately assess and predict the impact of land use changes on the thermal environment of Lahore until the year 2050. The significance of this research lies in its potential to inform evidence-based urban planning strategies, addressing the implications of land use changes on thermal dynamics. By scientifically examining the trajectory of these changes, the study can extract and contribute valuable insights for sustainable urban development in Lahore. However, it is essential to note that limitations and gaps in the existing literature may influence the study outcomes. These could include data constraints, variations in methodologies, and the dynamic nature of urban systems. Acknowledging and addressing these limitations enhances the robustness of the study. The study hypothesizes that the ongoing land use changes in Lahore will substantially increase built-up areas, contributing to elevated temperatures and urban heat islands. The lack of environmental regulations exacerbates these challenges. The study aims to provide quantifiable projections and insights through scientific analysis, hoping to ultimately facilitate informed urban planning decisions to mitigate the adverse impacts on the thermal environment.

MATERIALS AND METHODS

The Study Area

Lahore, located in the Punjab province of Pakistan on the bank of the river Ravi, has been chosen as the focus area of this study. As the second largest metropolitan city in Pakistan in terms of population, it faces significant and unique environmental pressures that are relevant to the study. With a population of 13.98 million people (GOP 2023) and a density of 6278/km^2 (GOP 2017), Lahore is the most rapidly growing city in Pakistan and covers an area of 1,772 km^2 and located between 31° 15′ to 31° 45′ N and 74° 01′ to 74° 39′ E. The city is divided into ten administrative units, as shown in Figure 1. The research area's climate is semi-arid, with five distinct seasons: (i) a foggy winter with some rainfall from western depressions from mid-November to mid-February; (ii) a pleasant spring from mid-February to mid-May; (iii) a warm and humid summer with dust and rainy storms from mid-May to end-June; (iv) a rainy monsoon from July to mid-September; and (v) dry autumn from mid-September to mid-November. In Lahore, June has the highest temperature, July the wettest, and January the lowest, with an annual maximum of 48.3ºC and a minimum of -2.2ºC, as illustrated in Figure 2.

As a vibrant and historically rich city, Lahore boasts a diverse socio-economic and physio-environmental setup reflecting the dynamic tapestry of urban life. On the socio-economic front, Lahore stands as a bustling economic hub with a thriving business community, diverse industries, and a robust informal sector. Its cultural richness is mirrored in the plethora of markets, heritage sites, and a lively street life that characterizes its social landscape. Simultaneously, the physio-environmental aspects of Lahore present a complex urban scenario. The city faces rapid urbanization, characterized by an expanding population, extensive land use changes, and the conversion of green spaces into built-up or industrialized areas. These transformations contribute to challenges such as rising temperatures, urban heat islands, heavy waves, and smog, necessitating a nuanced approach to balance economic growth with environmental sustainability in Lahore evolving urban fabric.

Data Acquisition and Pre-preparation

The Landsat images were acquired using the Path/Row 149/38 from the Earth Explorer website (https://earthexplorer.usgs.gov/). The spring season was selected to acquire Landsat images due to the fully green cover and the ideal land use classification time. Therefore, based on availability and clear weather conditions, the study obtained Landsat images from March 16, 1990, April 2, 2005, and March 18, 2020. All the images obtained have a resolution of 30 meters, and they are sensed by different sensors at different times; the details are provided in Table 1. After band composition, the study area was extracted by applying the "extract by mask" function in ArcGIS.

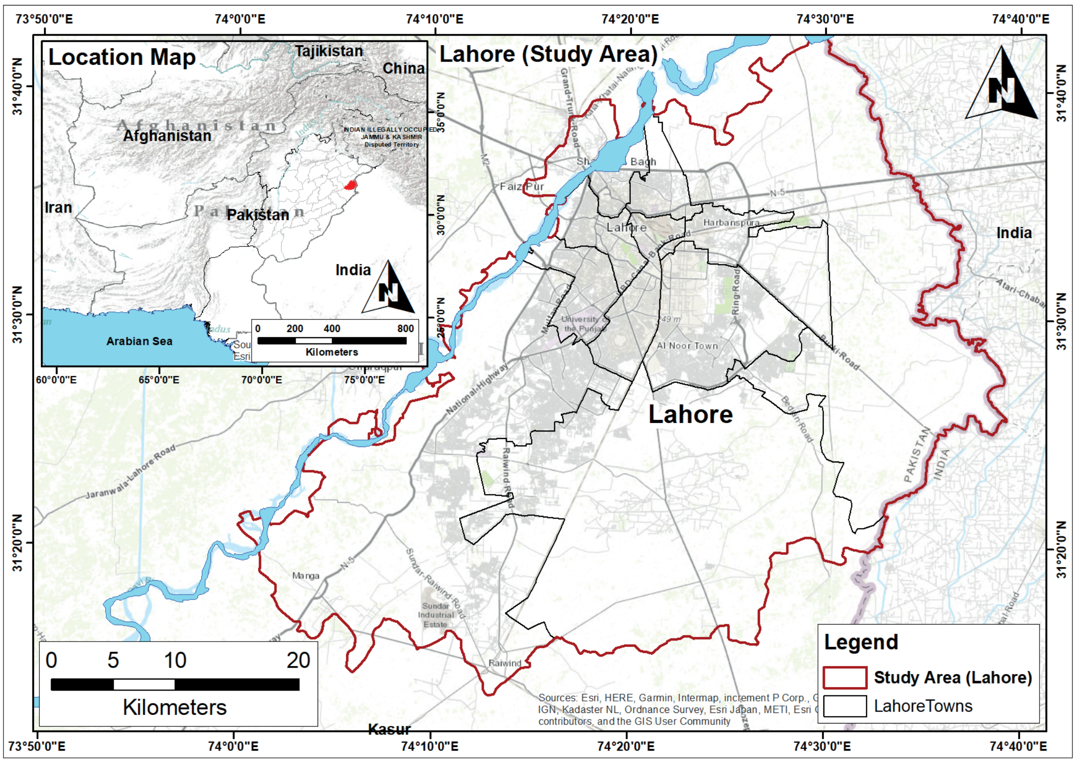

Fig. 1. Geographical Location of the Study Area (District Lahore)

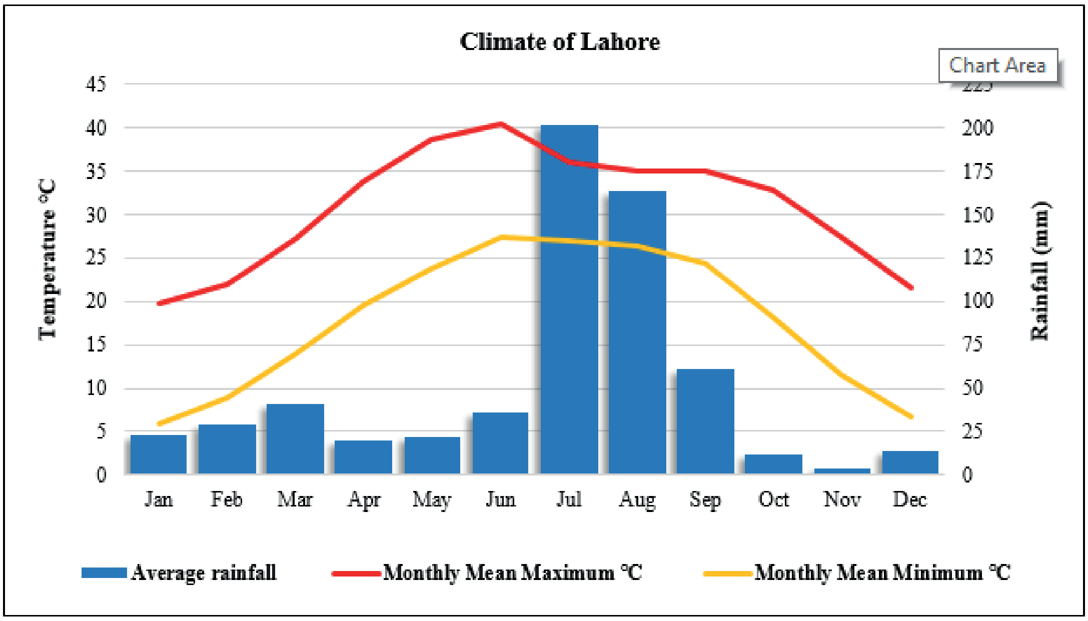

Fig. 2. Climate of the Study Area (District Lahore)

Table 1. Landsat Image Characteristics Used in the Study

Years	Satellite	Sensor	Path/Row	Resolution (m)	Acquisition Day
1990	Landsat-5	TM	149/38	30	16-03-1990
2005	Landsat-7	ETM+	149/38	30	02-04-2005
2020	Landsat-8	OLI/TIRs	149/38	30	18-03-2020

LU/LC Classification

The study utilized the supervised image classification technique to classify the study area. Supervised image classification is a well-recognized Landsat image classification technique aimed at achieving maximum accuracy (Anwar and Bhalli 2012; Bhalli et al. 2012a; Bhalli et al. 2012b; Barman et al. 2016; Iqbal & Iqbal 2018; Naeem et al. 2021; Mazhar et al. 2023). Four main land use classes are used to categorize the research area: bare land, built-up area, green cover, and water bodies.

Accuracy Assessment

The accuracy of the classified images was assessed by generating 450 random reference points. The following equations were applied in this process, and the obtained accuracy is presented in Table 2.

$$Producer'\ Accuracy\ (\%) = \left(\frac{x_{kk}}{x_{+k}}\right) \times 100 \quad (1)$$

$$User'\ Accuracy = \left(\frac{x_{kk}}{x_{k+}}\right) \times 100\,\% \quad (2)$$

$$Overall\ Accuracy\ (OA) = \frac{1}{N}\sum\nolimits_{k=1}^{\gamma} n_i \quad (3)$$

$$Kappa - coefficient\ (k) = \frac{n\sum_{k=1}^{r} x_{kk} - \sum_{k=1}^{r}\left(x_{k+}\cdot x_{+k}\right)}{N^2 - \sum_{k=1}^{r}\left(x_{k+}\cdot x_{+k}\right)} \quad (4)$$

LU and LC Change Detection

The study employed a post-classification comparison approach to identify changes between two classified images. Similarly, three self-classified images were used to detect LULC changes during the study period (Bhalli et al. 2013a; Bhalli et al. 2013b; Bhalli et al. 2012b). The change (C) in land use classes was calculated using Equation 5.

$$C_i = L_i - B_i \quad (5)$$

Next, using equation 6, the study determined the percentage of changes in land cover (C%).

$$Pi = (Li - Bi)/Bi \times 100 \quad (6)$$

Computation of LST

For Landsat-5 and 7

Chen et al. (2002) state that band 6 for Landsat 5 and 7 is used in the investigation to measure LST. First, the study used equation 7 to transform the digital numbers (DNs) of band 6 into radiation luminance. In this equation, LMAX and LMIN have values of 1 and 255, respectively, while QCALMIN has a value of 1 and QCALMAX has 255. QCAL represents DN.

$$Radiance = \frac{LMAX - LMIN}{QCALMAX - QCALMIN}(QCAL - QCALMIN) + LMIN \quad (7)$$

Secondly, the LST was calculated in Kelvin using equation 8.

$$T = \frac{K2}{In\,(K1/L\gamma + 1)} \quad (8)$$

Lastly, 'Kelvin (A)' temperature values were converted into 'Degree Celsius (B)' using equation 9.

$$B = A - 273.15 \quad (9)$$

For Landsat 8

The following metadata values were applied to Landsat 8 images for LST in the study: In terms of Radiance, add bands 10 and 11, which have 0.10000, 0.0003342 for Radiance Mult Band 10 and 11, 774.8853 for K1 constant band 10, 1321.0789 for K2, 480.8883 for K1 constant band 11, and 1201.1442 for K2. The Landsat 8 LST in five phases using the values mentioned above:

(i) Equation 10 was used in the study to transform thermal infrared digital numbers into TOA (Top of Atmosphere) spectral radiation.

$$L\lambda = ML \times QCAL + AL \quad (10)$$

(ii) Spectral radiance data were converted into TOA brightness temperature using equation 11.

$$BT = K2/In\,(k1/L\lambda + 1) - 272.15 \quad (11)$$

(iii) NDVI was calculated using equation 12 and suggested by Shah et al. 2022.

$$NDVI = NIR - RED/NIR + RED \quad (12)$$

(iv) Average Land Surface Emissivity (LSE) was calculated using equations 13 and 14, in which PV shows the proportion of vegetation, and E shows Land Surface Emissivity.

$$PV = (NDVImax - NDVImin/NDVImax + NDVImin)\ \hat{}2 \quad (13)$$

$$E = 0.004 \times PV + 0.986 \quad (14)$$

(v) LST was calculated by using the following equation 15.

$$LST = (BT/1) + W \times (BT/14380) \times In\,(E) \quad (15)$$

The areas of each LST range were computed in QGIS 3.14, creating the LST maps.

Table 2. Accuracy of classified images

	1990		2005		2020	
Class Name	UA	PA	UA	PA	UA	PA
Barren Land	89.83%	88.13%	86.91%	88.23%	93.21%	90.25%
Built-up Area	83.08%	90.01%	88.41%	86.76%	90.36%	93.35%
Green Cover	90.65%	88.81%	92.14%	94.65%	93.57%	93.54%
Water Bodies	91.92%	100%	100%	100%	100%	100%
	OA = 87.76% KC = 0.83		OA = 90.57% KC = 0.87		OA = 92.76% KC = 0.91	

Note: UA = User's Accuracy, PA = Producer's, OA = Overall Accuracy, KC = Kappa-coefficient

Quantification of NDVI and NDBI

Equation 12 was used to quantify NDVI, while Equation 16 was utilized to quantify NDBI, as suggested by Shah et al. 2022.

$$NDBI = (SWIR - NIR) / (SWIR + NIR) \quad (16)$$

Next, using Fishnet Polygons to extract data from LST, NDVI, and NDBI maps, the correlations between LST and NDVI and NDBI were examined.

Prediction of Land Use/Land Cover

LULC change prediction analysis was conducted in IDRISI software (version 17), utilizing the CA-Markov Model. The model integrates cellular automata and the Markov chain to forecast future LULC (Tegene 2002; Yang et al. 2014). For LULC change prediction analysis, LULC maps of 1990 and 2005 served as inputs for transition probability images. The CA-Markov model simulated the land use and land cover map for 2020, and a transition suitability image was generated by applying a multi-criteria evaluation model. Subsequently, a cross-classification between the predicted map of 2020 and the detected map of 2020 was analyzed, as shown in Figure 3. Finally, LULC prediction maps for 2035 and 2050 were generated using transition probability images.

Prediction of Land Surface Temperature

LST prediction analysis was carried out using the MOLUSE Plugin in QGIS 2.18. This Plugin operates based on an artificial neural network (ANN), a widely accepted method for predicting LST (Imran & Mehmood 2020; Alam et al. 2021; Fattah et al. 2021; Jafarpour Ghalehteimouri et al. 2022). Figure 4 illustrates the architecture of the LST prediction model.

RESULTS AND DISCUSSION

Land use Changes (1990 – 2020)

LULC classification of the study area for 1990 is depicted in Figure 5(A), revealing that bare land accounted for 13.77%, built-up area for 16.44%, Green Cover for 66.04%, and water bodies for 3.75%. Thus, in 1990, the study area boasted nearly two-thirds green cover, rendering it an environmentally friendly urban space in Pakistan, often

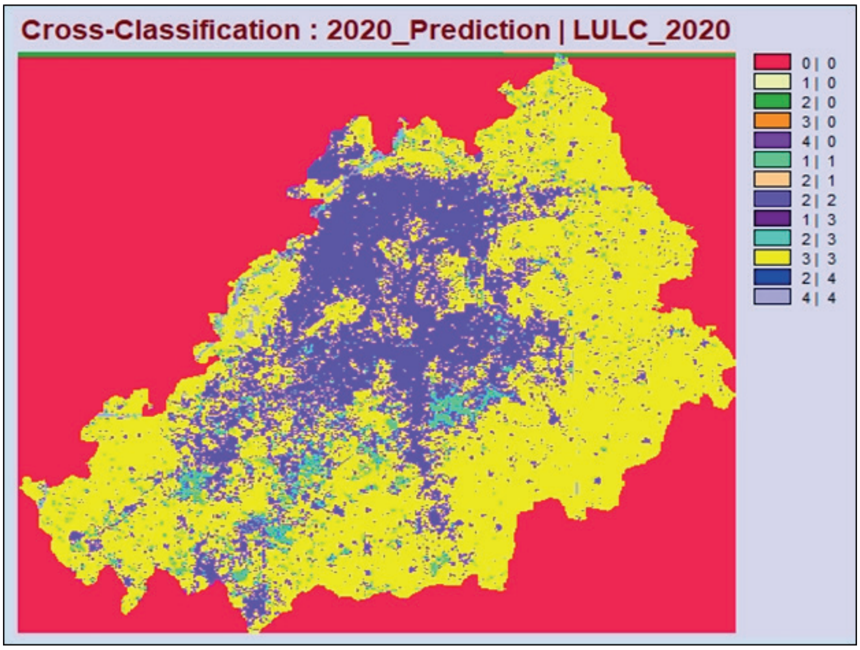

Fig. 3. Cross-classification of Images

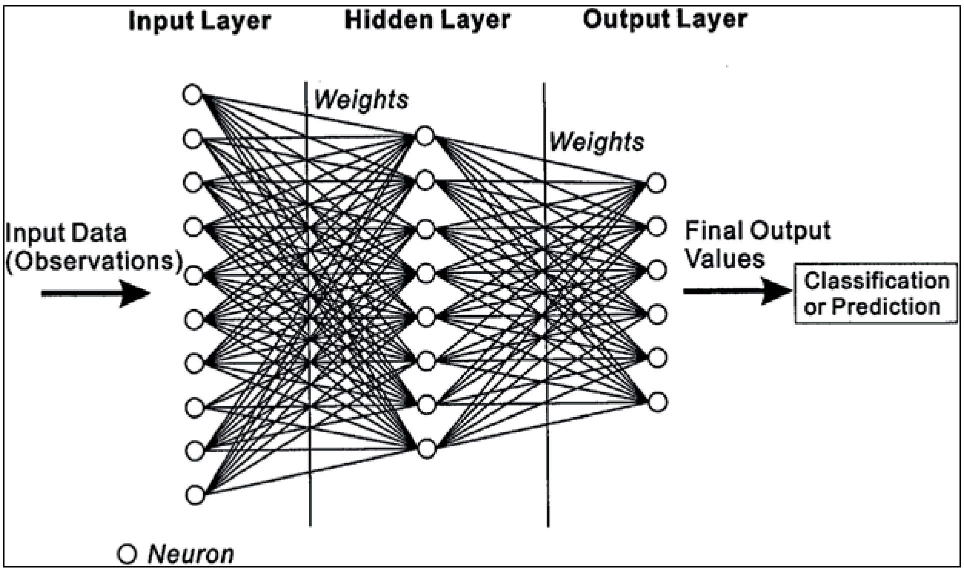

Fig. 4. LST Prediction Model Architecture

referred to as the city of gardens. Similarly, Figure 5(B) illustrates the LULCs of the study area for 2005, indicating Bare Land at 13.20%, built-up Area at 20.65%, Green Cover at 62.68%, and Water Bodies at 3.52%. Furthermore, Figure 5(C) displays the LULCs for 2020, wherein Bare Land occupied 4.04%, built-up area 32.48%, Green Cover 60.86%, and water bodies 0.68%. The area covered by all land types for 1990, 2005, and 2020 is presented in Figure 5(D). According to 2020 data, Lahore boasted a green cover area of 12.98 m^2 per person across the entire district. However, this value is anticipated to decrease due to current land use patterns.

Land Use Gains and Loss (1990 – 2020)

Gains and losses of the land use are evident in Figure 6, facilitating easy comparison. It reveals that bare land lost over 200 km^2 and gained nearly 50 km^2 of the area. Similarly, built-up areas experienced a gain of almost 400 km^2 while only losing 90 km^2. Green cover saw an increase of almost 220 km^2 but also suffered a loss of nearly 300 km^2 of its area. Similarly, water bodies gained nearly 10 km^2 but lost 60 km^2 of their area.

The net change in land use of the study area is illustrated in Figure 7, highlighting the significant area lost by bare land and gained by the Built-up area. Similarly, green cover and water bodies also experienced almost equal losses. While the "Gains and Losses of land covers (1990 - 2020)" section visually depicts the rates of loss and gain of classified land types, it is understood that readers may desire a more detailed understanding of the specific land cover classes contributing to the observed increases. The study indeed delves into this aspect, examining the percentage ratio of classes that have transformed into built-up areas, water bodies, and other categories.

The rapid growth of built-up areas is a significant concern of the study and the developing world in general because it accelerates several environmental issues. Urbanization is an essential feature of human development that directly affects urban ecology and ecosystem services (Larson et al. 2016). The rapid urban expansion puts pressure on biodiversity and other ecological patterns of urban landscapes (Song & Wang 2015; Nasar-u-Minallah et al. 2023). An increase in the population of urban areas demands more ecological services due to urban expansion.

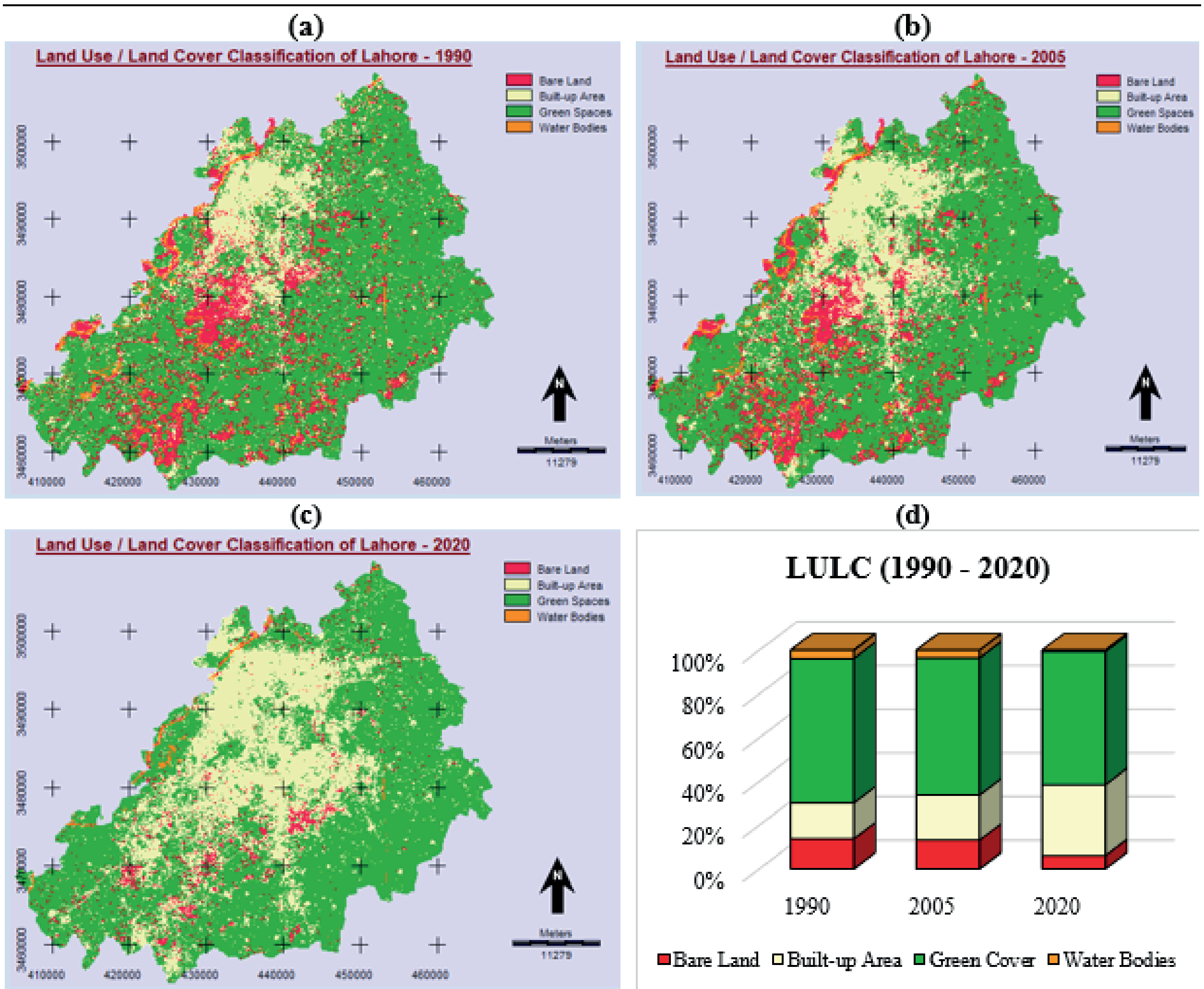

Fig. 5. Observed Land Use Changes in Lahore from 1990 to 2020

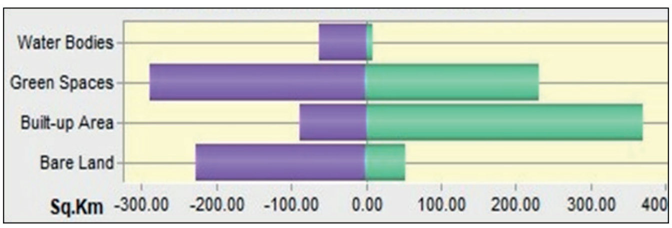

Fig. 6. Land Use Gain and Loss from 1990 to 2020

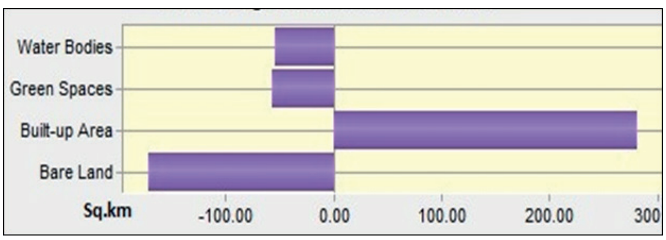

Fig. 7. Net Change in Land Use from 1990 to 2020

The ecological carrying capacity of UGSs has been reduced by urban population pressure (Daneshvar et al. 2017; Hanif et al. 2023). Land use changes pose severe challenges for urban management due to their significant ecological resource effects (Mustard et al. 2012). Therefore, studying land use changes is essential for effectively managing natural and environmental resources (Thilagavathi et al. 2015). The study area suffers from severe environmental issues due to decreasing UGSs and increasing built-up areas. The results demonstrate that the ratio between green and built-up areas was almost 71:29 in 1990, which was found to be 49:51 in 2020 after a 22.17% loss of green areas in 2020. So, 22.17% of the study area has been transformed from green to built-up areas, which may accelerate environmental issues.

Forests also play a critical role in the livelihoods of millions of individuals and are a significant contributor to the national economic growth of many countries. Forests are essential for carbon sinks and contribute to climate change rates, soil development, and water control. The forestry industry also has direct employment estimated at 10 million people (FAO 2010). Apart from providing livelihoods for millions more, approximately 410 million people depend on forests for their livelihood and income, with 1.6 billion people relying on forests for a living (Köhl et al. 2015). Research conducted by UNEP, FAO, and UNFF (Köhl et al. 2015) found that the world forests have declined due to a growing human population. Unfortunately, in the last 50 to 100 years, the deforestation rate (0.5%) has risen significantly in emerging nations.

Predicting LULC Changes (2020 – 2050)

LULC changes will be one of the significant reasons for future challenges for the study area because the last 30-year trend shows a rapid expansion in built-up areas by removing the green spaces. Therefore, the study projected an LULC classification of the study area for 2035, as shown in Figure 9, which shows that the study area will consist of 3.30% bare land, 40.09% built-up areas, 56.13% in green spaces, and 0.49% in water bodies. The continuation of the current LULC changing trend will also accelerate current environmental issues. Thus, the study projected LULC classification for 2050 (Figure 10), showing that the study area will contain 2.44% bare land, 51.73% built-up area, 45.47% green spaces, and 0.37% water bodies.

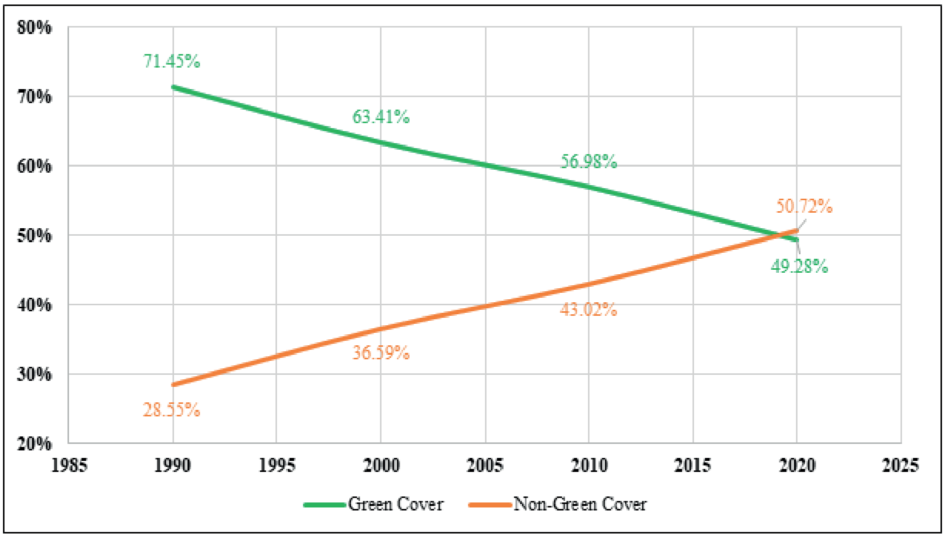

Fig. 8. Changes in Green and Non-green Covers in Lahore from 1990 to 2020

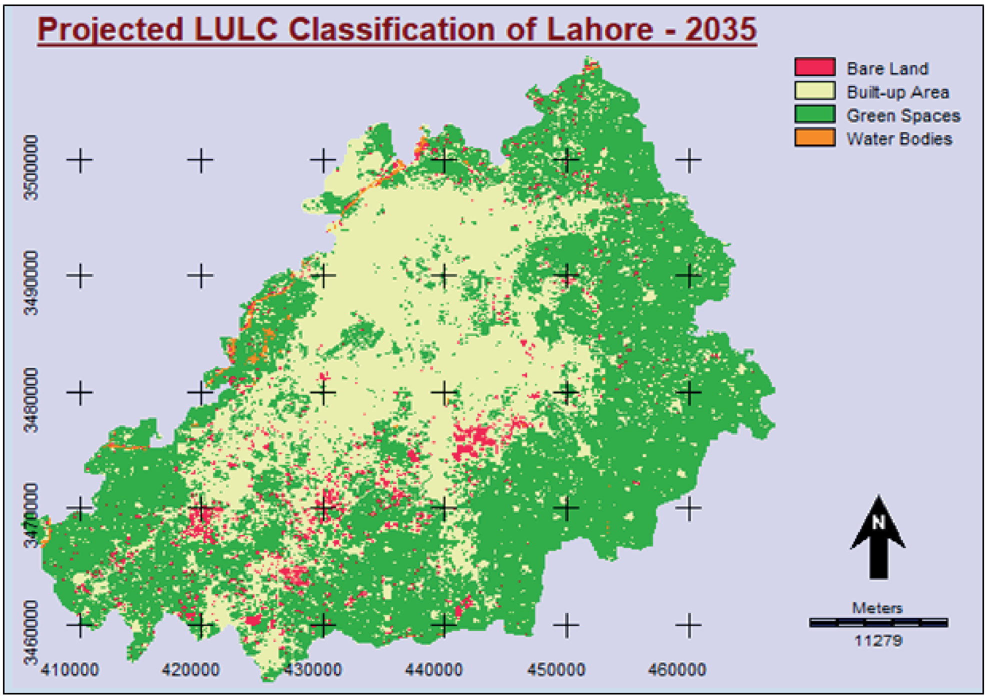

Fig. 9. Projected Land Use of Lahore in 2035

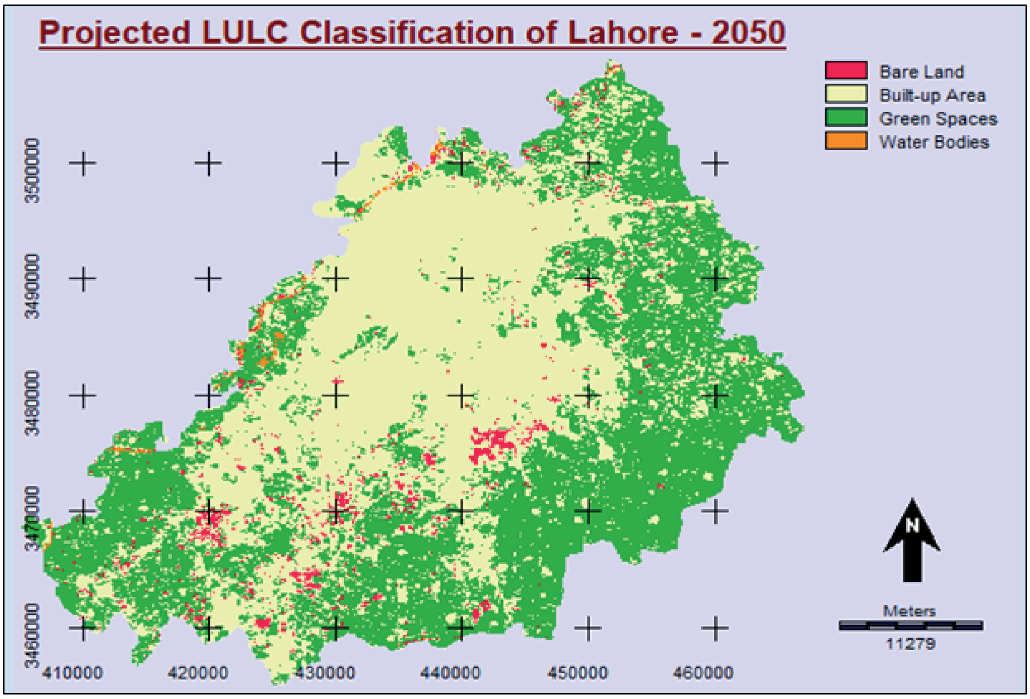

Fig. 10. Projected Land Use of Lahore in 2050

The LULC of the study area from 1990 to 2020 (observed) and 2020 to 2050 (predicted) are shown in Figure 10. It has been analyzed that green spaces are shrinking rapidly, whereas built-up areas are expanding rapidly (Figure 11). So, this change in land use will reduce the number of green spaces from 60.86% (2020) to 45.51% by 2050. Similarly, the expanding trend of the built-up area will increase over 51.76% from 32.48% (2020) till 2050. Moreover, the decrease in bare land and water bodies will continue, and both landforms will be found at 2.45% and 0.34%, respectively, till 2050.

Figure 12 displays the anticipated increases and decreases in land cover types within the study area. The figure shows that the maximum loss (more than 300 km^2) will occur in green spaces, whereas the maximum gain will occur in the built-up areas of the study area. Therefore, it is projected that they will expand at the expense of green areas in the future, which is a significant concern. Similarly, Figure 13 shows the net change in land covers, where it can also be seen that a significant net change will occur in the green cover and built-up areas. The built-up areas will replace the green spaces, and more than half a portion of the study area will be transformed into impermeable surfaces by 2050. Similarly, the green surface will reduce to less than half of the study area. So, the figure indicates that the study area will face a massive loss of urban green cover, and it will have to bear urban built-up areas on more than half of its portion by 2050.

The behavior of LULC changes raises various environmental issues, among others. LULC changes are significant concerns in the developing world, where countries experiencing rapid population growth also face a corresponding increase in urban population. The situation becomes more problematic when scholars observe that this trend continues unabated (Adedeji et al. 2020; Hamad et al. 2018; How et al. 2020). Similar trends are evident in Lahore, signaling an alarming situation for future environmental hazards. Therefore, it is imperative to reinvigorate management efforts and take swift measures to ensure the environmental sustainability of the study area.

Similarly, the green areas will decrease to less than half of the study area. Moreover, section C illustrates the net contribution of green spaces in future land cover classification, indicating that the green cover will lose a substantial area (more than 300 km^2) by 2050. Consequently, the figure suggests that the study area will experience a significant loss of urban green cover, with urban built-up areas occupying more than half of its total area by 2050. The expansion of built-up areas leads to a reduction in

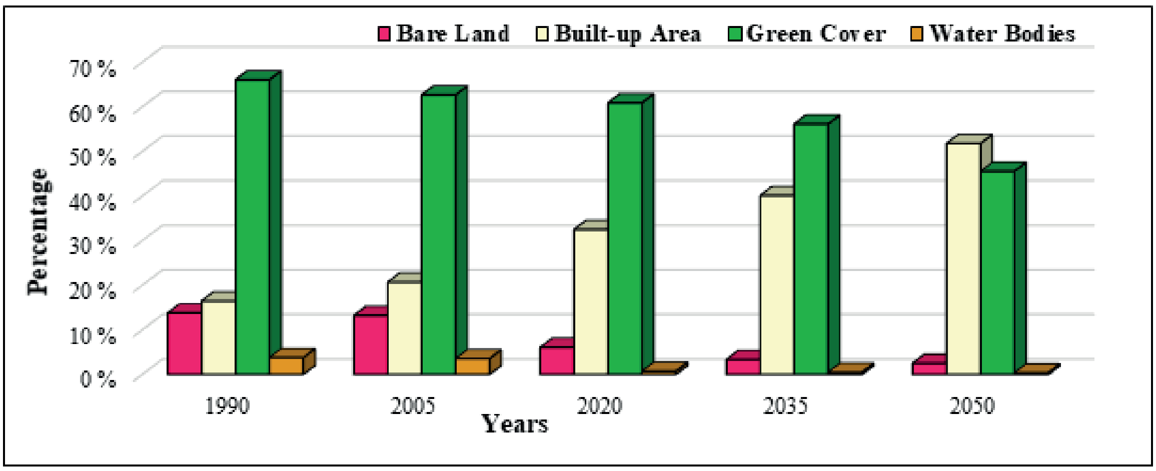

Fig. 11. Land Use Changes in Lahore from 1990 to 2050

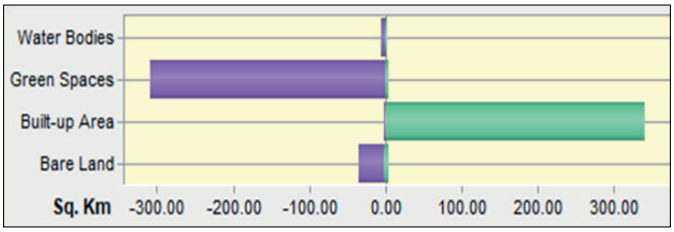

Fig. 12. Land Covers Gain and Loss in Lahore from 2020 to 2050

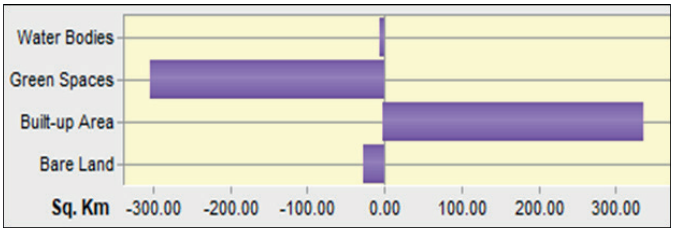

Fig. 13. Net Change within Land Covers in Lahore from 2020 to 2050

agricultural land and the decline of the ecosystem in the area. Increased built-up areas also demand more energy consumption and water resources, contributing to water pollution and urban heat island effects. The rapid increase in the built-up environment is a significant contributor to environmental issues in urban areas (Adedeji et al. 2020; Shao et al. 2021).

The projected LULC classification for 2050 predicts extreme environmental issues in the study area, negatively impacting human well-being (Karimi et al. 2018; Samie et al. 2020). The projection for 2050 indicates that more than half of the study area will be covered by built-up areas, while green cover will occupy less than half of the total land area. The rapid expansion of built-up areas has been observed in various urban settings in the developing world, leading to several environmental issues such as high LST and urban heat island effects, air and water pollution, increased air temperatures, and decreased thermal comfort (Adedeji et al. 2020; Shao et al. 2021).

Observing LST Changes (1990 – 2020)

The LST (Land Surface Temperature) of the study area in 1990, 2005 and 2020 is depicted in Figure 14. The year 1990, shows that the study area had 3.58 km^2 area with the lowest temperature range (8°C – 21°C), 205.48 km^2 with lower temperature (22°C), 515.99 km^2 with low temperatures (23°C), 650.81 km^2 with medium temperatures (24°C), 317 km^2 with high temperatures (25°C), 57.26 km^2 with higher temperatures (26°C), and 9.67 km^2 with highest temperature range (27°C - 32°C). Similarly, in 2005, the LST of the study area encompassed 147.28 km^2 with the lowest temperatures range (8°C – 21°C), 470.64 km^2 with lower temperatures (22°C), 357.92 km^2 with low temperatures (23°C), 239.87 km^2 with medium temperatures (24°C), 352.67 km^2 with high temperatures (25°C), 156.57 km^2 with higher temperatures (26°C) and 35.76 km^2 with highest temperature range (27°C - 32°C) of LST. Likewise, in 2020, the LST of the study area encompassed 118.37 km^2 with the lowest temperatures range (8°C – 21°C), 362.22 km^2 with the lower temperatures (22°C), 341.44 km^2 with low temperatures (23°C), 154.96 km^2 with medium temperatures (24°C), 361.06 km^2 with high temperatures (25°C), 250.24 km^2 with higher temperatures (26°C) and 172.46 km^2 with highest temperature range (27°C - 32°C) of LST.

Relationships between LST and NDVI

Normalized Difference Vegetation Index (NDVI) measures surface reflectance and quantifies vegetation growth and biomass. Therefore, the negative relationships of LST and NDVI authenticate that UGSs caused low LST.

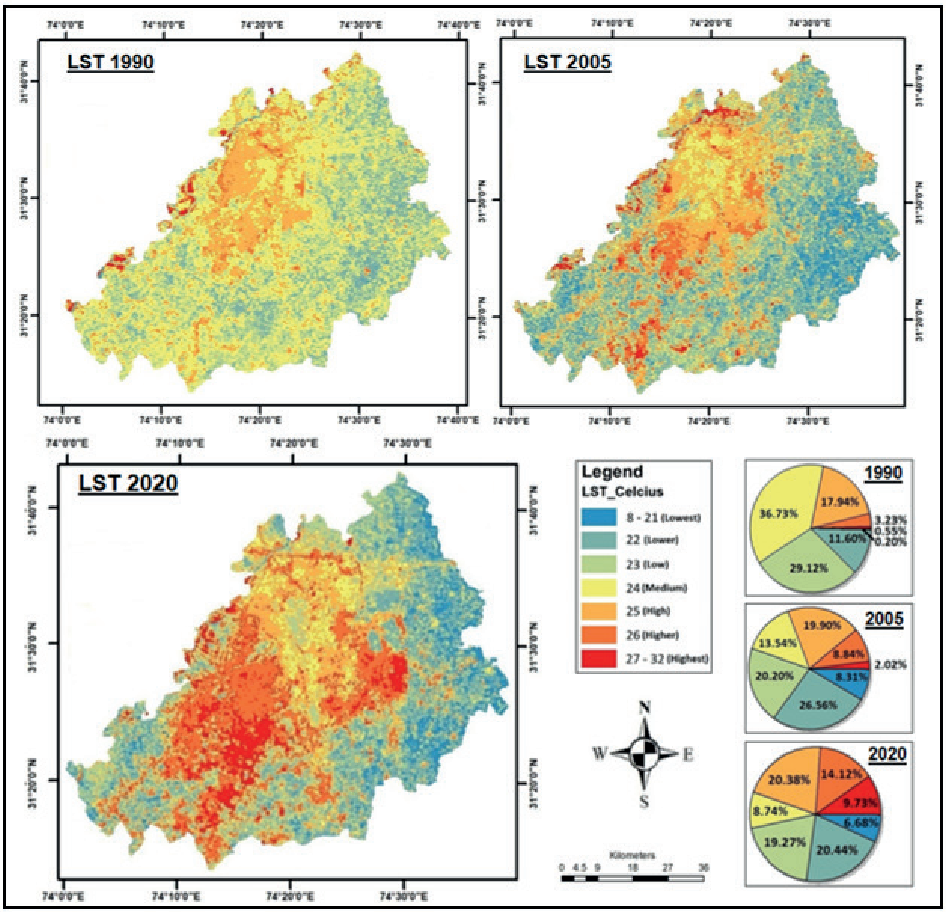

Fig. 14. Land Surface Temperature in Lahore from 1990 to 2020

Figure 15 shows relationships between LST and NDVI in the study area, in which negative relations were found. Moreover, it can be observed that a5.5°C LST decreases from -0.05 to 0.55 NDVI, which indicates that greenness reduces LST.

Relationships between LST and NDBI

Normalized Difference Built-up Index (NDBI) measures surface reflectance and quantifies built-up area and impermeable surface. The mounting of positive NDBI values indicates the increase of built-up and impermeable surfaces (Wu et al., 2016). Relationships between LST and NDBI of the study area are shown in Figure 16, which was found positive. Therefore, it can be assessed that LST 5°C increases from -0.35 to 0.1 NDBI. So, the positive relation between LST and NDBI indicates that the built-up surface increase caused LST and UHI expansion.

Prediction of Land Surface Temperature

An increase in LST is one of the common issues in urban areas caused by the expansion of the built-up structure. Urban expansion alters land into an impermeable surface, the primary cause of rising LST in urban areas, especially in cities that expand and violate environmental rules (Land Surface Temperature - an Overview | ScienceDirect Topics, n.d.; Yan et al. 2020). Similar conditions have been analyzed in the study area in the last 30 years. The study has analyzed the LST of the study area for 1990, 2000, 2010, and 2020. Similarly, the study projected the LST of the study area for 2035 and 2050, which is given below in detail.

The growth of the urban built-up area caused expansion in the impermeable surface. It is a natural phenomenon that the expansion of impermeable surfaces causes the expansion of high LST and urban heat island effects (Uddin & Swapnil 2021). As the study has analyzed, the area under

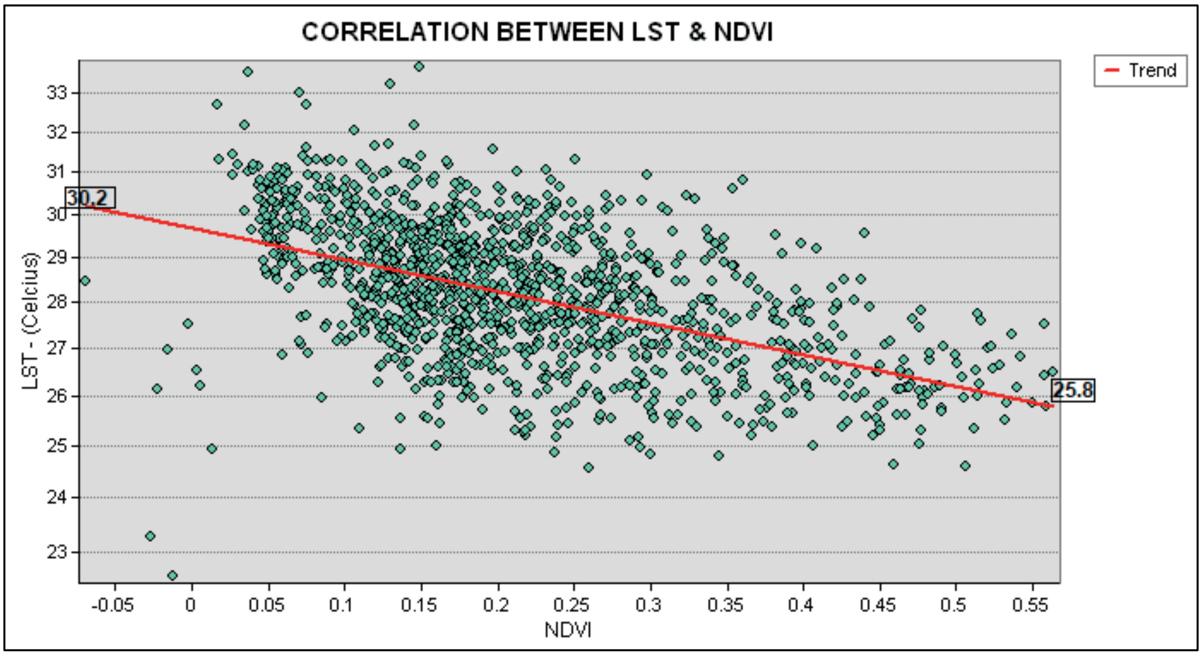

Fig. 15. Relationships between LST and NDVI

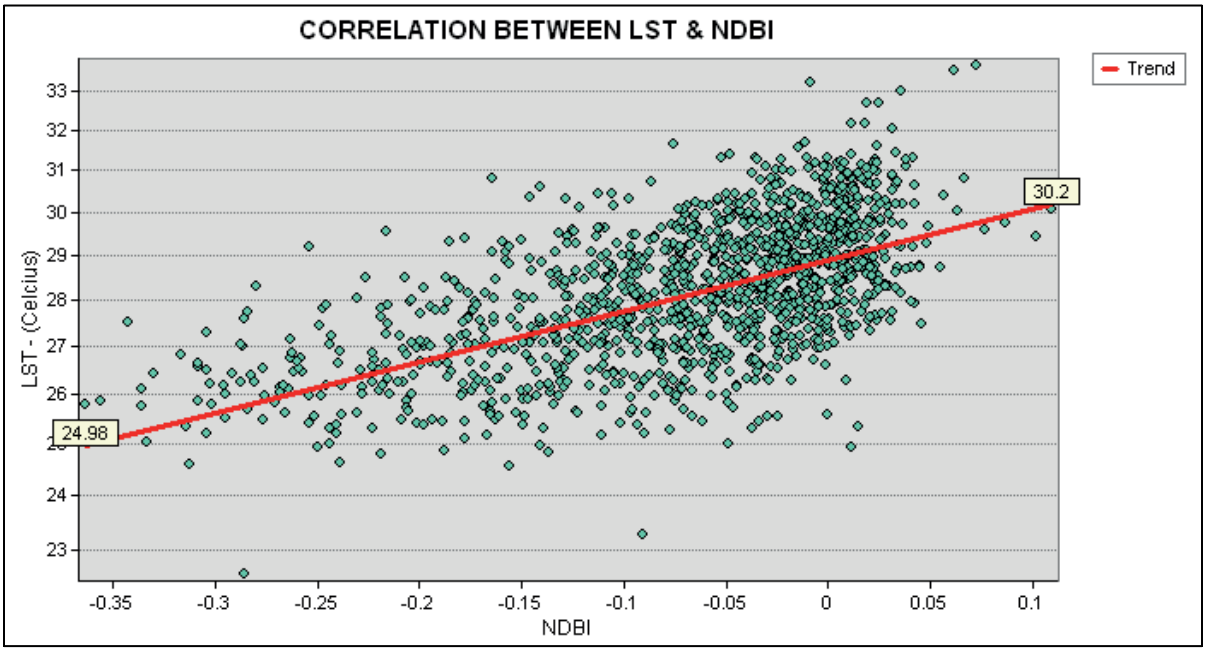

Fig. 16. Relationships Between LST and NDBI

a lower degree of LST decreases with the increase of built-up area, and the area under a higher degree of the land surface increases alternatively. In this way, as demonstrated by the trend over the last three decades, the study generated a projection of LST for 2035 and found that the expansion of the higher range of LST will expand towards the eastern and southern part of the study area as well as more areas will enter from lower degree of LST to higher degree. Therefore, the study projected that the area would face higher LST on projected built-up land, from east to southward. All the details of the LST projection for 2035 can be observed in Figure 17.

Several studies have found that land use changes green surfaces into built-up areas, transforming urban areas into hazardous places. Decreased green covers and expanded built-up land by violating environmental land caused various environmental issues (Tran et al. 2017). The study found a similar situation in Lahore, which is facing several environmental issues. The study analyzed the LST of the study area from 1990 to 2020 and found that the study area faces a continuous expansion in a higher zone of LST. Similarly, the study projected an LST for the study area in 2050 and found that more than half of the study area would enter the high, higher, and highest zones of LST. The areas with lower LST will decrease significantly, and urban heat island effects will expand more. If the same trend of land use changes continues, then it is projected that a higher range of LST will be found over more than 55% of the study area by 2050. A detailed map of projected LST for 2050 can be analyzed in Figure 18 for a more comprehensive understanding. The projected results highlighted that the study area would face higher LST due to the present behavior of land use changes. Therefore, the attention of all responsible authorities and stakeholders is critical to preventing and resolving the expected hazardous conditions in the study area.

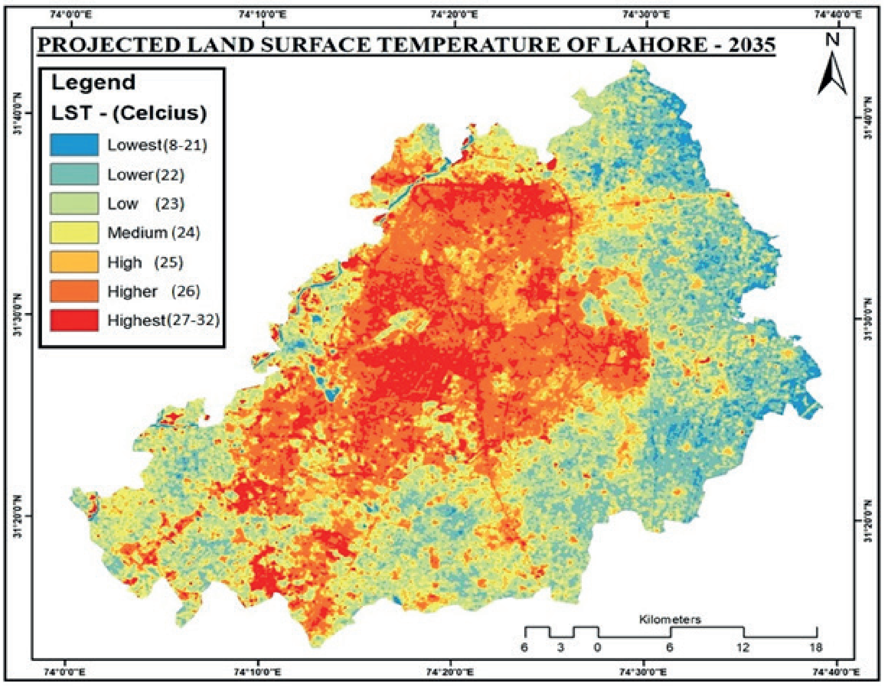

Fig. 17. Projected of Land Surface Temperature in Lahore for 2035

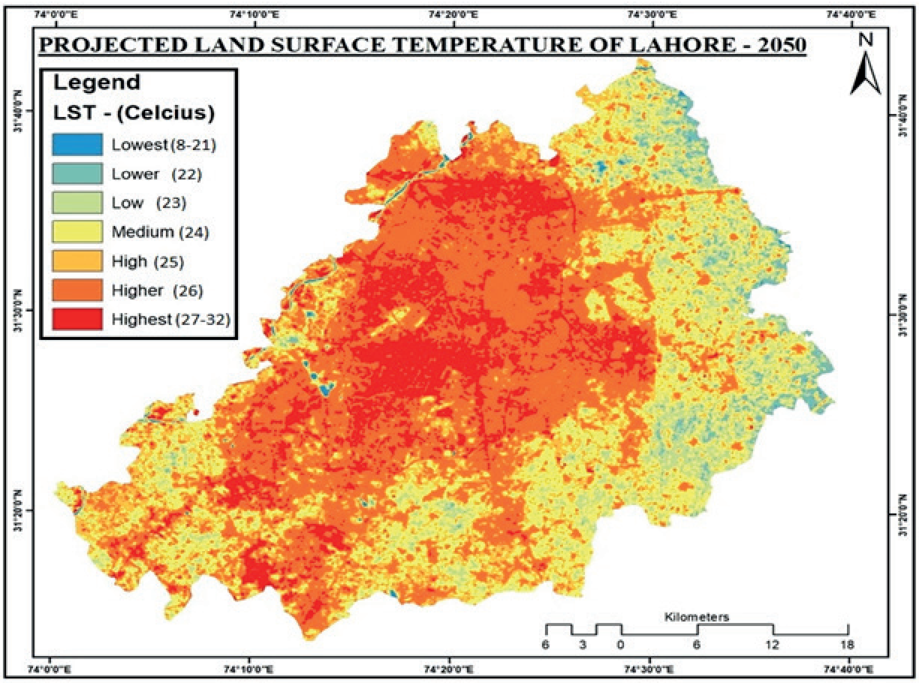

Fig. 18. ojected of Land Surface Temperature in Lahore for 2050

Observed and Predicted LST (1990 – 2020 - 2050)

As the study showed, seven auto-generated (by ArcGIS 10.8) degrees of LST for 2035 and 2050 were ranked as; (i) 8°C - 21°C, (ii) 22°C, (iii) 23°C, (iv) 24°C, (v) 25°C, (vi) 26°C and (vii) 27°C - 32°C. By using these rankings for the LST of the study area, the study did not find any significant change in the lowest (8°C - 21°C) degrees. However, a significant change was found in the shift of 22°C to 23°C LST. The figure shows that the study area had its maximum portion under the 23°C of LST in 1990, which shifted toward the 24°C LST till 2020. Similarly, when the study projected LST for 2035 and 2050, the maximum portion of the study area will be found under the 25°C of LST in 2050. Therefore, the found change indicates that the current LULC changing trend will shift maximum portion of the study area under the High, Higher, and Highest degrees of LST till 2050. The study findings indicate that the study area will push its more than 55% area under the high degree of LST in the next 30 years (till 2050). All the details are given in Figure 19 to understand the readers better.

LST is a crucial variable for climate change and environmental studies (Mundia & James, 2014) and describes the earth's skin temperature, which varies with land use type change. It came from the energy and water balance of the earth's surface (Rozenstein et al. 2014). Several studies have used LST as an essential parameter for monitoring vegetation, global warming, and built-up changes. It is a well-known parameter for environmental issues (Kayet et al. 2016). Lahore (the study area) faces several environmental issues in highly polluted cities worldwide. The analysis demonstrates that the study area is expanding toward the high-temperature zone.

Similarly, a study by Buyadi et al. (2013) on urban expansion found that the expansion of built-up areas was caused by vegetation reduction and microclimatic changes (Buyadi et al. 2013). In recent years, Henao et al. (2020) found that rapid urbanization has considerably replaced green spaces with built-up areas, which has caused environmental problems (Henao et al., 2020). It is analyzed that the most common urban environmental problems are caused by urbanization, like urban thermal discomfort (Feizizadeh et al. 2013). Significant deforestation in Kedah and Perak, located in Malaysia, has reduced forest cover from 39% to 35% in Kedah and from 58% to 49% in Perak. This deforestation caused an increase in LST, whereas areas with vegetation and forest had lower LST (Jaafar et al. 2020). So, the studies demonstrate that reducing or removing green spaces is the leading cause of the increase in LST.

Likewise, the study indicates that the expansion of built-up and barren areas has increased LST. The removal of green spaces has also contributed to higher LST in the study area. Interestingly, adjacent green areas have been observed to exhibit similar LST levels. LST increases with the increase of built-up areas because built-up areas convert permeable land into an impermeable surface, which causes high LST (Ahmed et al. 2013; Tran et al. 2017; How et al. 2020). Therefore, the projected LST of the study area shows that the study area will face the expansion of built-up areas, which will increase the impermeable surface and cause an expansion of the high LST zone. As a result, it is projected that the high, higher, and highest zones of LST will increase in the study area, of which almost half of the study area will be under the influence of high LST. The expansion of high LST can be controlled by providing green spaces within the built-up areas and maintaining existing green spaces because only green spaces are the most suitable and cheapest way to mitigate the expansion of high LST (Rahman et al. 2017; Sun & Chen 2017).

LIMITATIONS

Despite the comprehensive nature of this study on assessing and predicting the impact of land use changes on the thermal environment in Lahore, certain limitations should be acknowledged. First, the reliance on Landsat images from 1990, 2005, and 2020 introduces potential limitations regarding image resolution and temporal frequency, impacting the precision of land use change assessments. Additionally, the predictive modeling for 2050 assumes a linear progression of land use changes, neglecting the impact of potential non-linear trends influenced by unforeseen factors. The study primarily focuses on physical and environmental aspects, overlooking socio-economic factors that intricately contribute to land use changes. The exclusion of detailed analysis of existing and potential future environmental policies and regulations in Lahore limits the understanding of policy dynamics and their impact on mitigating thermal challenges. Furthermore, the single city focus on Lahore

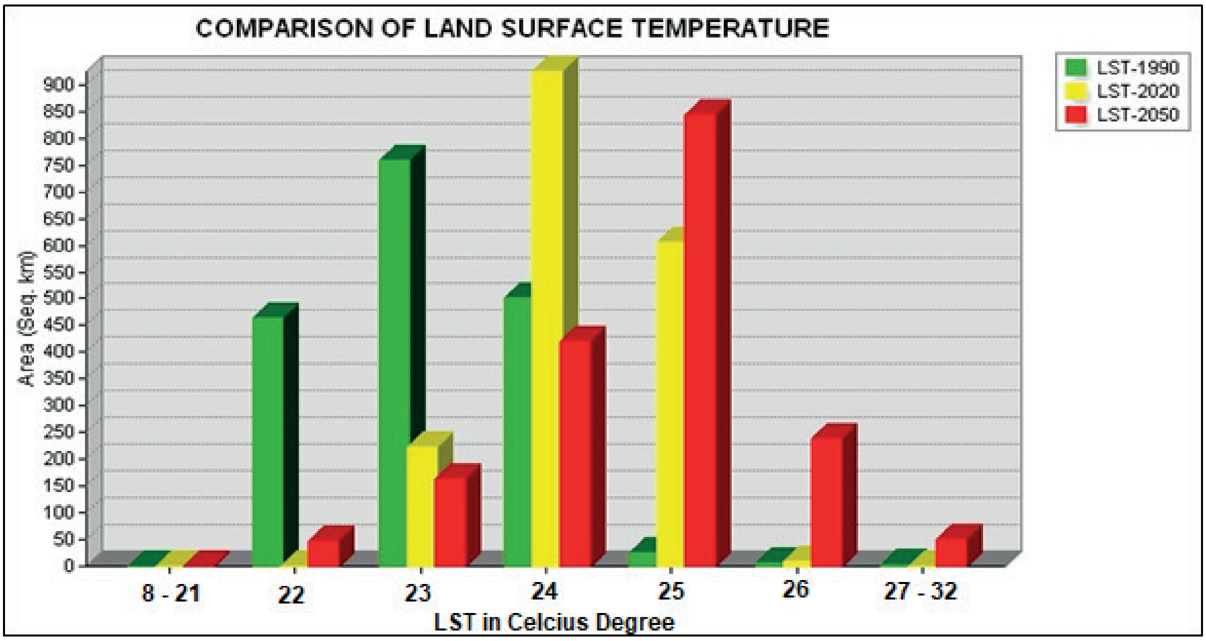

Fig. 19. Predicted Changes in Land Surface Temperature in Lahore from 1990 to 2050

may restrict the universal applicability of findings to other urban contexts, emphasizing the need for caution in extrapolating these results. Finally, uncertainties related to climate change and the simplifications in the land use change modeling process contribute to the limitations of the study, highlighting areas for improvement in future research endeavors.

CONCLUSION

The study area faces rapid land use change and the spread of built-up areas, which is a primary concern of the study. According to the observed land use changes (1990 – 2020), the study area has increased its built-up land cover by almost 100%, pushing its maximum area from the Low to Medium range of LST. Similarly, according to the predicted land use changes (2020 – 2050), the built-up area will spread over more than 50% of the study area by decreasing its green cover by less than 50%. As a result, the maximum area will be found under the High LST range instead of Medium. Therefore, the observed land use changes in Lahore are highly sensitive to its LST, which will affect its urban heat island and other climatic elements because the study area is also found in a country (Pakistan) nominated as one of the top ten impacted by climate change. Therefore, in these circumstances, the increase in a built-up area and LST is highly significant, negatively affecting the environmental sustainability and residents' health. Hence, it is concluded that the study area is threatened by rapid land use changes and its impacts on its LST increase, which demands serious attention and quick action against such activities; otherwise, the study will lose its suitable environment and acceptable homogeneousness of LST. The conservation and expansion of green cover are recommended with increased built-up areas if management aims to maintain the required ecosystem quality for the residents. As demonstrated in the study, urban forest using Miyawaki may be one of the best options to handle the urban thermal environment. Therefore, integrated urban planning that balances built-up areas and green spaces should be promoted. Resources should be allocated for green infrastructure projects, and zoning regulations favoring mixed land use and green area preservation should also be enforced. Furthermore, climate-responsive design practices should be encouraged in conjunction with raising public awareness and fostering community engagement on these issues. Other valuable recommendations include developing green corridors, implementing adaptive land use policies, establishing a robust monitoring system, and encouraging stakeholder collaboration to better inform policy measures. Investing in capacity-building programs for urban planners to better understand and address the complex relationship between land use changes and thermal environments can ultimately address their growing issues. Upon reflecting on the findings of the study and these subsequent recommendations, I realized that such comprehensive measures could ultimately assist in creating a sustainable, resilient, and aesthetically pleasing urban landscape in Lahore, Pakistan.

REFERENCES

Adedeji, O. H., Adeofun, C. O., Tope-Ajayi, O. O., & Ogunkola, M. O. (2020). Spatio-temporal analysis of urban sprawl and land use/land cover changes in a suburb of Lagos and Ogun metropolises, Nigeria (1986-2014). Ife Journal of Science, 22(2), 27–42.

Ahmed, B., Kamruzzaman, M., Zhu, X., Rahman, M. S., & Choi, K. (2013). Simulating Land Cover Changes and Their Impacts on Land Surface Temperature in Dhaka, Bangladesh. Remote Sensing, 5(11), Article 11. https://doi.org/10.3390/rs5115969

Alam, N., Saha, S., Gupta, S., & Chakraborty, S. (2021). Prediction modelling of riverine landscape dynamics in the context of sustainable management of floodplain: A Geospatial approach. Annals of GIS, 27(3), 299–314.

Anderson, J. R. (1976). A land use and land cover classification system for use with remote sensor data (Vol. 964). US Government Printing Office.

Anwar, M. M. and Bhalli, M. N. (2012) Urban Population Growth Monitoring and Land Use Classification by using GIS and Remote Sensing Techniques: A Case Study of Faisalabad City, Asian Journal of Social Science & Humanities, 1(1), 05-13.

Bhalli, M. N., Ghaffar, A., and Shirazi, S. A. (2012a). Spatio-temporal Patterns of Urban Growth in Faisalabad-Pakistan: A GIS Perspective. Journal of Research Society of Pakistan, 49(1), 115-134.

Bhalli, M. N., Ghaffar, A., Shirazi, S. A., Parveen, N. and Anwar, M. M. (2012b) Change Detection Analysis of Landuse by using Geospatial Techniques: A Case Study of Faisalabad- Pakistan, Science International, 24(4), 539-546.

Bhalli, M. N., Ghaffar, A. and Shirazi, S. A. (2012c) Remote Sensing and GIS Applications for Monitoring and Assessment of the Urban Sprawl in Faisalabad-Pakistan, Pakistan Journal of Science, 64(3), 203-208.

Bhalli, M. N., Ghaffar, A., Shirazi, S. A., and Parveen, N. (2013a). An analysis of the normalized difference vegetation index (NDVI) and its relationship with the population distribution of Faisalabad-Pakistan. Pakistan Journal of Science, 65 (3), 496-502.

Bhalli, M. N., Ghaffar, A., Shirazi, S. A., and Parveen, N. (2013b), Use of Multi-Temporal Digital Data to Monitor LULC Changes in Faisalabad-Pakistan. Pakistan Journal of Science, 65 (1), 58-62.

Bhalli, M. N. and Ghaffar, A. (2015). Use of Geospatial Techniques in Monitoring Urban Expansion and Land Use Change Analysis: A Case of Lahore, Pakistan. Journal of Basic & Applied Sciences, 11, 265-273.

Buyadi, S. N. A., Mohd, W. M. N. W., & Misni, A. (2013). Impact of land use changes on the surface temperature distribution of the area surrounding the National Botanic Garden, Shah Alam. Procedia-Social and Behavioral Sciences, 101, 516–525.

Daneshvar, M. R. M., Khatami, F., & Zahed, F. (2017). Ecological carrying capacity of public green spaces as a sustainability index of urban population: A case study of Mashhad city in Iran. Modeling Earth Systems and Environment, 3(3), 1161–1170.

Eastman, J. R. (2006). Eastman: Guide to GIS and Image Process. Clark Labs, Clark University.

Ernstson, H. (2013). The social production of ecosystem services: A framework for studying environmental justice and ecological complexity in urbanized landscapes. Landscape and Urban Planning, 109(1), 7–17.

FAO (2010) Global forest resource assessment. In: FAO Forestry paper 163, Main Report, Rome, Italy—Google Search. (n.d.). Retrieved July 2, 2021.

Fattah, M., Morshed, S. R., & Morshed, S. Y. (2021). Multi-layer perceptron-Markov chain-based artificial neural network for modelling future land-specific carbon emission pattern and its influences on surface temperature. SN Applied Sciences, 3(3), 1–22.

Feizizadeh, B., Blaschke, T., Nazmfar, H., Akbari, E., & Kohbanani, H. R. (2013). Monitoring land surface temperature relationship to land use/land cover from satellite imagery in Maraqeh County, Iran. Journal of Environmental Planning and Management, 56(9), 1290–1315.

Fu, W., Lü, Y., Harris, P., Comber, A., & Wu, L. (2018). Peri-urbanization may vary with vegetation restoration: A large scale regional analysis. Urban Forestry & Urban Greening, 29, 77–87.

Gallo, K. P., & Owen, T. W. (1999). Satellite-based adjustments for the urban heat island temperature bias. Journal of Applied Meteorology, 38(6), 806-813. 488.

Gonzalez-Redin, J., Gordon, I. J., Hill, R., Polhill, J. G., & Dawson, T. P. (2019). Exploring sustainable land use in forested tropical social-ecological systems: A case study in the Wet Tropics. Journal of Environmental Management, 231, 940–952.

Gull, N., Adeel, M., Waseem, L. A., Hussain, D., Abbas, N., Elahi, A., Hussain, Z., Jan, B., Nasar-u-Minallah, M., and Naqvi, S. A. A. (2021). Computing Spatio-temporal variations in land surface temperature: A case study of Tehsil Murree, Pakistan. Journal of Geography and Social Sciences, 3(1), 17-30.

Guo, G., Wu, Z., Xiao, R., Chen, Y., Liu, X., & Zhang, X. (2015). Impacts of urban biophysical composition on land surface 489 temperature in urban heat island clusters. Landscape and Urban Planning, 135, 1-10.

Hanif, A., Nasar-u-Minallah, M., Zia, S., and Ashraf, I., (2022). Mapping and Analyzing the Park Cooling Intensity in Mitigation of Urban Heat Island Effect in Lahore, Pakistan. Korean Journal of Remote Sensing, 38(1), 127-137. https://doi.org/10.7780/kjrs.2022.38.1.10.

Hanif, A., Shirazi, S. A., Jabbar, M., Liaqat, A., Zia, S., & Yusoff, M. M. (2023). Evaluating The Visitors' Perception and Available Ecosystem Services in Urban Parks of Lahore (Pakistan) Research Paper. Geography, Environment, Sustainability, 15(4), 32–38.

Hamad, R., Balzter, H., & Kolo, K. (2018). Predicting land use/land cover changes using a CA-Markov model under two different scenarios. Sustainability, 10(10), 3421.

Hansen, M. C., Potapov, P. V., Moore, R., Hancher, M., Turubanova, S. A., Tyukavina, A., Thau, D., Stehman, S. V., Goetz, S. J., Loveland, T. R., Kommareddy, A., Egorov, A., Chini, L., Justice, C. O., & Townshend, J. R. G. (2013). High-Resolution Global Maps of 21st-Century Forest Cover Change. Science, 342(6160), 850–853. https://doi.org/10.1126/science.1244693

Henao, J. J., Rendón, A. M., & Salazar, J. F. (2020). Trade-off between urban heat island mitigation and air quality in urban valleys. Urban Climate, 31, 100542.

How Jin Aik, D., Ismail, M. H., & Muharam, F. M. (2020). Land use/land cover changes and the relationship with land surface temperature using Landsat and MODIS imageries in Cameron Highlands, Malaysia. Land, 9(10), 372.

Imran, M., & Mehmood, A. (2020). Analysis and mapping of present and future drivers of local urban climate using remote sensing: A case of Lahore, Pakistan. Arabian Journal of Geosciences, 13(6), 1–14.

Jabbar, M., Yusoff, M. M., & Shafie, A. (2021). Assessing the role of urban green spaces for human well-being: A systematic review. GeoJournal. https://doi.org/10.1007/s10708-021-10474-7

Jabbar, M., & Mohd Yusoff, M. (2022). Assessing and modelling the Role of Urban Green Spaces for Human Well-being in Lahore (Pakistan). Geocarto International. 1–21.

Jabbar, M., & Yusoff, M. M. (2022). Assessing The Spatiotemporal Urban Green Cover Changes and Their Impact on Land Surface Temperature and Urban Heat Island in Lahore (Pakistan). Geography, Environment, Sustainability, 15(1), 130–140.

Jabbar, M., Ghous, M., Hanif, A., Ali, Z., Ghaffar, A., & Munir, S. (2023). Assessing The Impact of Land Use Changes on Air Pollution Removal Capacity: A Three-Decade Analysis Applying The I-Tree Eco Model. Bulletin of Business and Economics (BBE), 12(2), 188–194.

Jafarpour Ghalehteimouri, K., Shamsoddini, A., Mousavi, M. N., Binti Che Ros, F., & Khedmatzadeh, A. (2022). Predicting spatial and decadal of land use and land cover change using integrated cellular automata Markov chain model based scenarios (2019–2049) Zarriné-Rūd River Basin in Iran. Environmental Challenges, 6, 100399. https://doi.org/10.1016/j.envc.2021.100399

Kayet, N., Pathak, K., Chakrabarty, A., & Sahoo, S. (2016). Urban heat island explored by co-relationship between land surface temperature vs multiple vegetation indices. Spatial Information Research, 24(5), 515–529.

Köhl, M., Lasco, R., Cifuentes, M., Jonsson, Ö., Korhonen, K. T., Mundhenk, P., de Jesus Navar, J., & Stinson, G. (2015). Changes in forest production, biomass and carbon: Results from the 2015 UN FAO Global Forest Resource Assessment. Forest Ecology and Management, 352, 21–34. https://doi.org/10.1016/j.foreco.2015.05.036

Lachowycz, K., & Jones, A. P. (2013). Towards a better understanding of the relationship between greenspace and health: Development of a theoretical framework. Landscape and Urban Planning, 118, 62–69.

Lahore Population 2024. (n.d.). Retrieved January 10 2024, from https://worldpopulationreview.com/world-cities/Lahore-population

Land Surface Temperature—An overview | ScienceDirect Topics. (n.d.). Retrieved December 30, 2021, from https://www.sciencedirect.com/topics/earth-and-planetary-sciences/land-surface-temperature

Larson, L. R., Jennings, V., & Cloutier, S. A. (2016). Public parks and well-being in urban areas of the United States. PLoS One, 11(4).

Liu, X., He, J., Yao, Y., Zhang, J., Liang, H., Wang, H., & Hong, Y. (2017). Classifying urban land use by integrating remote sensing and social media data. International Journal of Geographical Information Science, 31(8), 1675–1696. https://doi.org/10.1080/13658816.2017.1324976

Michetti, M., & Zampieri, M. (2014). Climate–human–land interactions: A review of major modelling approaches. Land, 3(3), 793–833.

Minallah, M. N., Rafique, M., Anwar, M. M., and Mohsin, M. (2016). Assessing the Urban Growth and Morphological Patterns of Gojra City, Pakistan. Sindh University Research Journal (Science Series), 48(2), 393-398.

Mohsin M. and Bhalli, M. N. (2015). Rapid Urban Growth and Change in Urban and Municipal Limits of Bahawalpur City, Pakistan: A Spatio-Periodical Discourse. Journal of Basic & Applied Sciences, 11,528-538.

Mundia, C. N., & James, M. M. (2014). Dynamism of land use changes on surface temperature in Kenya: A case study of Nairobi City.

Mustard, J. F., Defries, R. S., Fisher, T., & Moran, E. (2012). Land-use and land-cover change pathways and impacts. In Land change science (pp. 411–429). Springer.

Mazhar, N., Nasar-u-Minallah, M., Shirazi, S.A. et al. (2024). Spatio-temporal patterns and dynamics of sensitivity to sandification, in the Drylands of South Punjab, Pakistan. GeoJournal, 89, (15). https://doi.org/10.1007/s10708-024-11014-9.

Naeem, M., Nasar-U-Minallah, M., Tariq, B., Tariq, N., and Mushtaq, K. (2021). Monitoring Land-use Change and Assessment of Urban Expansion of Faisalabad, Pakistan using Remote Sensing and GIS. Pakistan Geographical Review, 76(1), 174-190.

Nasar-u-Minallah, M., Haase, D., Qureshi, S., Zia, S. and Munnaza, F. (2023). Ecological monitoring of urban thermal field variance index and determining the surface urban heat island effects in Lahore, Pakistan. Environ Monit Assess 195, 1212. https://doi.org/10.1007/s10661-023-11799-1.

Nasar-u-Minallah, M., Zia S., Rahman A., and Riaz O. (2021). Spatio-Temporal Analysis of Urban Expansion and Future Growth Patterns of Lahore, Pakistan. Geography, Environment, Sustainability. 14(3):41-53. https://doi.org/10.24057/2071-9388-2020-215.

Nasar-u-Minallah, M. (2019). Retrieval of Land Surface Temperature of Lahore through Landsat-8 TIRS Data. International Journal of Economic and Environmental Geology, 10 (1), 70-77. https://doi.org/10.46660/ijeeg.Vol10.Iss1.2019.220

Nasar-u-Minallah, M. (2018). Spatial and Temporal Change Assessment in Land Surface Temperature of Lahore using GIS and Remote Sensing Techniques. Proceedings of the Pakistan Academy of Sciences: A. Physical and Computational Sciences, 55 (3): 67–75.

National Oceanic and Atmospheric Administration. (n.d.). Retrieved October 5, 2020, from https://www.noaa.gov/

Pakistan Meteorological Department PMD. (n.d.). Retrieved October 5, 2020, from http://www.pmd.gov.pk/index-old.html

Parveen, N., Ghaffar, A., Nasar-u-Minallah, M., and Ali, M. (2019). Analytical Study on Urban Expansion using the Spatial and Temporal Dynamics of Land Use Change in Faisalabad City, Pakistan. International Journal of Economic and Environmental Geology (IJEEG). 10 (3) 102-108. https://doi.org/10.46660/ijeeg.Vol10.Iss3.2019.318

Rahman, M. T., Aldosary, A. S., & Mortoja, M. G. (2017). Modeling Future Land Cover Changes and Their Effects on the Land Surface Temperatures in the Saudi Arabian Eastern Coastal City of Dammam. Land, 6(2), Article 2. https://doi.org/10.3390/land6020036

Riaz, O., Munawar, H., Nasar-u-Minallah, M., Hameed, K.,and Khalid, M., (2017). Geospatial Analysis of Urbanization and its Impact on Land Use Changes in Sargodha, Pakistan. Journal of Basic & Applied Sciences, 13, 226-233. https://doi.org/10.6000/1927-5129.2017.13.39

Rozenstein, O., Qin, Z., Derimian, Y., & Karnieli, A. (2014). Derivation of land surface temperature for Landsat-8 TIRS using a split window algorithm. Sensors, 14(4), 5768–5780.

Schott, J. R. (2007). Remote sensing: The image chain approach. Oxford University Press on Demand.

Shao, Z., Sumari, N. S., Portnov, A., Ujoh, F., Musakwa, W., & Mandela, P. J. (2021). Urban sprawl and its impact on sustainable urban development: A combination of remote sensing and social media data. Geospatial Information Science, 24(2), 241–255. https://doi.org/10.1080/10095020.2020.1787800

Shah, S. A., Kiran, M., Nazir, A., & Ashrafani, S. H. (2022). Exploring NDVI and NDBI relationship using Landsat 8 OLI/TIRS in Khangarh taluka, Ghotki. Malaysian Journal of Geosciences (MJG), 6(1), 08-11.

Siddique, M. A. et al. (2020). Assessment and simulation of land use and land cover change impacts on the land surface temperature of Chaoyang District in Beijing, China. PeerJ 8, e9115.

Song, J., & Wang, Z.-H. (2015). Impacts of mesic and xeric urban vegetation on outdoor thermal comfort and microclimate in Phoenix, AZ. Building and Environment, 94, 558–568.

Stürck, J., Schulp, C. J. E., & Verburg, P. H. (2015). Spatio-temporal dynamics of regulating ecosystem services in Europe – The role of past and future land use change. Applied Geography, 63, 121–135. https://doi.org/10.1016/j.apgeog.2015.06.009

Sun, R., & Chen, L. (2017). Effects of green space dynamics on urban heat islands: Mitigation and diversification. Ecosystem Services, 23, 38–46. https://doi.org/10.1016/j.ecoser.2016.11.011

Taubenböck, H., Esch, T., Felbier, A., Wiesner, M., Roth, A., & Dech, S. (2012). Monitoring urbanization in mega cities from space. Remote Sensing of Environment, 117, 162–176. https://doi.org/10.1016/j.rse.2011.09.015

Thilagavathi, N., Subramani, T., & Suresh, M. (2015). Land use/land cover change detection analysis in Salem Chalk Hills, South India using remote sensing and GIS. Disaster Adv, 8, 44–52.

Tran, D. X., Pla, F., Latorre-Carmona, P., Myint, S. W., Caetano, M., & Kieu, H. V. (2017). Characterizing the relationship between land use land cover change and land surface temperature. ISPRS Journal of Photogrammetry and Remote Sensing, 124, 119–132. https://doi.org/10.1016/j.isprsjprs.2017.01.001

Uddin, M. J., & Swapnil, F. J. (2021). Land Surface Temperature (LST) Estimation at Kushtia District, Bangladesh. Journal of Civil Engineering, Science and Technology, 12(2), 213–227.

Wan Mohd Jaafar, W. S., Abdul Maulud, K. N., Muhmad Kamarulzaman, A. M., Raihan, A., Md Sah, S., Ahmad, A., Saad, S. N. M., Mohd Azmi, A. T., Jusoh Syukri, N. K. A., & Razzaq Khan, W. (2020). The influence of deforestation on land surface temperature—A case study of Perak and Kedah, Malaysia. Forests, 11(6), 670.

Ward, C. (2013). Probing identity, integration and adaptation: Big questions, little answers. International Journal of Intercultural Relations, 37(4), 391–404.

Wolch, J. R., Byrne, J., & Newell, J. P. (2014). Urban green space, public health, and environmental justice: The challenge of making cities' just green enough. Landscape and Urban Planning, 125, 234–244. https://doi.org/10.1016/j.landurbplan.2014.01.017

Yan, Y., Mao, K., Shi, J., Piao, S., Shen, X., Dozier, J., Liu, Y., Ren, H., & Bao, Q. (2020). Driving forces of land surface temperature anomalous changes in North America in 2002–2018. Scientific Reports, 10(1), 6931. https://doi.org/10.1038/s41598-020-63701-5

Zia, S., Mohsin, M., Nasar-u-Minallah, M., and Hanif, A. (2022). Site Suitability Analysis for Urban Settlements along River Jhelum, Pakistan using GIS and Remote Sensing Techniques. Indonesian Journal of Geography, 54(2), 22–239. https://doi.org/10.22146/ijg.72354.

Zhang, C., Sargent, I., Pan, X., Li, H., Gardiner, A., Hare, J., & Atkinson, P. M. (2019). Joint Deep Learning for land cover and land use classification. Remote Sensing of Environment, 221, 173–187. https://doi.org/10.1016/j.rse.2018.11.014

Zhao, M., Zhou, Y., Li, X., Cheng, W., Zhou, C., Ma, T., Huang, K., 2020. Mapping urban dynamics (1992–2018) in Southeast Asia using consistent nighttime light data from DMSP and VIIRS. Remote Sens. Environ. 248, 111980 https://doi.org/10.1016/j.rse.2020.111980.

Zhou, W., Wang, J., & Cadenasso, M. L. (2017). Effects of the spatial configuration of trees on urban heat mitigation: A comparative study. Remote Sensing of Environment, 195, 1–12.

ges.rgo.ru/jour/

ISSN 2542-1565 (Online)